Atomic Scale Study of Oxygen Loss and Structural Degradation in Oxide Cathodes and a Mitigation strategy

BY

Seyyed Soroosh Sharifi Asl

B.S., Imam Khomeini International University, Qazvin, Iran, 2012
M.S., University of Tehran, Tehran, Iran, 2014

THESIS

Submitted as partial fulfillment of the requirements
for the degree of Doctor of Philosophy in Mechanical Engineering
to the Graduate College of the
University of Illinois at Chicago, 2020

Chicago, Illinois

Defense Committee:

Reza Shahbazian-Yassar, Chair and Advisor
Jeremiah Abiade
Jordi Cabana, Chemistry
Fengyuan Shi, Electron Microscopy Core
Jason Croy, Argonne National Laboratory
Perla Balbuena, Texas A&M University

To parents, to my lovely wife, Tara
and to my brother, Soheil

ACKNOWLEDGMENTS

I am deeply thankful for the great support and supervision of my advisor, Dr. Shahbazian-Yassar throughout my PhD research. Without his great guidance, encouragement and provision, this thesis could not be written. I also thank all my friends and colleagues at the NanoEngineerig Laboratory, specially Hasti Asayesh-Ardakani, Anmin Nie and Yifei Yuan for their great mentorship and collaboration. I would like to thank the scientists of Electron Microscopy Facility at Research Resource Center (RRC) at UIC, specially Alan Nichols and Fengyuan Shi, for their great contribution in training and educating students. I am highly grateful to my doctoral defense committee for their insightful feedbacks and comments on this thesis. I am deeply thankful to all my collaborators who contributed to this thesis, specially Fernando A. Soto and Vitaliy R. Yurkiv. I would like to thank my parents who nurtured me with their great sacrifices and always supported me in each and every step of my life. My deepest gratitude goes to my wife, colleague and friend, Tara Foroozan that not only provided technical assistance in this thesis but supported me to pass through numerous challenges in many years and never ceased her compassion and optimism.

CONTRIBUTION OF AUTHORS

The contribution of authors in every chapter of this thesis is listed below. The discussions and results presented in each chapter in taken from my published and submitted journal articles. The permissions are attached to the appendix.

Authors' Contributions in Chapter 4 (from reference [[1]]). S Sharifi-Asl and R. Shahbazian-Yassar initiated the idea and designed the experimental protocols. S. Sharifi-Asl and A. Nie performed TEM experiments. S. Sharifi-Asl, Y. Yuan and H. Asayesh-ardakani carried out EELS data analysis. S. Sharifi-Asl and T. Foroozan carried out sample preparation, ICP measurement and thermal analysis. F. A. Soto carried out the AIMD simulations and the simulation results were discussed and written in collaboration with P, B. Balbuena, F. A. Soto, S. Sharifi-Asl, and R. Shahbazian-Yassar. B. Song and V. Yurkiv draw the schematic figures. All the authors contributed to the writing and discussion of the manuscript.

Authors' Contributions in Chapter 5 (from reference [[2]]). S. Sharifi-Asl and R. Shahbazian-Yassar initiated the idea and designed the experimental protocols. S. Sharifi-Asl and T. Foroozan carried out the graphene-coating and the characterization efforts. S. Sharifi-Asl and Y. Yuan performed the electrochemical cycling experiments. S. Sharifi-Asl carried out *in-situ* TEM/EELS experiments and subsequent data analysis. M. Asadi and X. Bi carried out the DEMS experiments, and the results were discussed and written in collaboration with A. Salehi-Khojin and J. Lu. B. Song draw the schematic figure. All the authors contributed to the writing and discussion of the manuscript.

Authors' Contributions in Chapter 6 (From reference [[3]]). S. Sharifi-Asl, A. Gutierrez and V. Yurkiv contributed equally to this work. S. Sharifi-Asl and R. Shahbazian-Yassar initiated the idea and designed the experimental protocols. A. Gutierrez., J. Croy. and M. Balasubramanian, synthesized the sample and carried out the electrochemical cycling experiments. S. Sharifi-Asl performed STEM experiments and conducted the data analysis. V. Yurkiv and F. Mashayek carried out the DFT calculations. M. Cheng drew the schematic figure. All the authors contributed to the writing and discussion of the manuscript.

SUMMARY

This thesis presents the identification of nano-scale degradation mechanisms associated with the layered oxide cathode materials of Li-ion batteries (LIBs), and our novel approach in tackling some of the uncovered challenges. Layered oxide cathodes with the general formula of $LiMO_2$ (M= Co, Ni, Mn) are the prime member of positive LIB electrodes, widely used in commercial applications. However certain challenges such as structural instability that leads to rapid capacity fade, voltage polarization and even thermal runaway and ignition of the batteries are not fully comprehended and are remaining to be addressed.

Oxygen release from the oxygen-containing positive electrode materials is one of the major structural degradations resulting in rapid capacity/voltage fading of the battery and triggering the parasitic thermal runaway events. This thesis summarizes the recent progress in understanding the mechanisms of the oxygen release phenomena and corelative structural degradations observed in four major groups of cathode materials: layered, spinel, olivine and Li-rich cathodes.

Utilizing *in-situ* scanning transmission electron microscopy (STEM) and electron energy loss spectroscopy (EELS) at high temperatures, we show that Li_xCoO_2 cathode crystals undergo inhomogeneous oxygen loss that are localized at the surface of individual particles. Using atomic resolution imaging and electron diffraction analysis, we correlated the oxygen release from Li_xCoO_2 to the surface-originated phase conversions such as layered to spinel and rock salt phases at elevated temperatures. Corroborating the experimental findings with ab-initio molecular dynamics (in collaboration with Prof. Balbuena's group from Texas A&M University) we proposed the facet-dependent thermal instability of $LiCoO_2$ cathodes for the first time.

Next, we show that the surface-originated structural decomposition can be hindered by depositing a conformal coating of 2D reduced graphene oxide on individual Li_xCoO_2 particles. By conducting various electrochemical tests, thermal analysis and *in-situ* heating transmission electron microscopy the effectiveness of the graphene-coating on the structural stability of Li_xCoO_2 was evaluated. Through computational calculations and modeling (by Prof. Balbuena's group from Texas A&M University) it was shown that the rGO layers could suppress O_2 formation more effectively due to the strong $C\text{-}O_{cathode}$ bond formation at the interface of rGO/LCO where

low coordination oxygens exist. This systematic investigation uncovered a reliable approach for hindering the oxygen release reaction and mitigating the thermal instability of battery cathodes.

Layered oxide cathodes that are the dominant positive electrodes in current commercial LIB technologies, are reaching to their intrinsic capacity limits, restraining the advancement of the batteries. Therefore, Li- and Mn-rich layered cathodes with capacities of ~300 $mAhg^{-1}$ are considered as the next generation of LIB cathodes. Despite their high energy densities, Li- and Mn-rich, layered-layered, $xLi_2MnO_3•(1-x)LiTMO_2$ (TM=Ni, Mn, Co) (LMR-NMC) cathodes require further development in order to overcome issues related to bulk and surface instabilities such as Mn dissolution, impedance rise, and voltage fade. One promising strategy to modify LMR-NMC properties has been the incorporation of spinel-type, local domains to create 'layered-layered-spinel' cathodes. However, precise control of local structure and composition, as well as subsequent characterization of such materials, is challenging and elucidating structure-property relationships is not trivial. Therefore, detailed studies of atomic structures within these materials are still critical to their development. Herein, aberration corrected scanning transmission electron microscopy (AC-STEM) is utilized to study atomic structures, prior and subsequent to electrochemical cycling, of LMR-NMC materials having integrated spinel-type components. The results demonstrate that strained grain boundaries with various atomic configurations, including spinel-type structures, can exist. These high energy boundaries appear to induce cracking and promote dissolution of Mn by increasing the contact surface to electrolyte as well as migration of Ni during cycling, thereby accelerating performance degradation. These results present insights into the important role that local structures can play in the macroscopic degradation of the cathode structures and reiterate the complexity of how synthesis and composition affect structure-electrochemical-property relationships of advanced cathode designs.

TABLE OF CONTENTS

LIST OF TABLES

LIST OF FIGURES

LIST OF ABBREVIATIONS AND NOMENCLATURE

LIB: Li-ion battery

V_{OC}: open circuit voltage

HOMO: highest occupied molecular orbitals

LUMO: lowest unoccupied molecular orbitals

fcc: face centered cubic

SEI: solid/electrolyte interface

EIS: electrochemical impedance spectroscopy

LLO: Li-rich layered oxide

EELS: electron energy loss spectroscopy

STEM: Scanning transmission electron microscopy

DFT: density functional theory

AIMD: Ab initio molecular dynamics simulations

DSC: differential scanning calorimetry

TEM: transmission electron microscopy

SAEDP: Selected area electron diffraction pattern

FFT: fast Fourier transform

SRL: surface reconstruction layer

ICP-OES: inductively coupled plasma optical emission spectroscopy

SEM: Scanning electron microscopy

XPS: X-ray photoelectron spectroscopy

TGA: thermogravimetric analysis

TR-XRD: time resolved x-ray diffraction

DEMS: differential electrochemical mass spectroscopy

XAS: x-ray absorption spectroscopy

SOC: state of charge

CCP: cubic close packed

XANES: X-ray absorption near edge spectroscopy

EXAFS: extended X-ray absorption fine structure

LCSU: local coordination structure units

LFT: ligand field theory

LMR: Li-Mn rich cathodes

DOS: density of states

RIXS: resonance inelastic X-ray spectroscopy

HAADF: high angle angular dark field

RDF: radial distribution function

ZLP: zero loss peak

DLS: dynamic light scattering

VASP: Vienna ab-initio Simulation Package

rGO: reduced graphene oxide

OTR: oxygen transfer rate

HRTEM: high-resolution transmission electron microscopy

LMR-NMC: Li- and Mn-rich, layered-layered, $xLi_2MnO_3 \bullet (1-x)LiTMO_2$ (TM=Ni, Mn, Co)

AC-STEM: aberration corrected-scanning transmission electron microscopy

EDS: electron dispersive spectroscopy

GPA: geographic phase analysis

CSTR: continuously-stirred-tank-react

Chapter 1: Introduction

1.1. Layered Oxide Cathode Materials and Their Application in Li-ion Batteries

1.1.2 An Overview of Li-ion Batteries

Rechargeable batteries are essential constituents of the modern energy-sustainable societies, therefore there is an ever-growing thrust in improving the quality and functionality of the battery systems. The most developed and utilized rechargeable battery system is the Li-ion battery (LIB) that has been discovered nearly 4 decades ago in 1976[3]. Thereafter, LIBs revolutionized many fields and have been integrated in various-scale devices ranging from microelectronic systems to electric transportation vehicles. As schematically shown in *Figure 1*, Li-ion battery is an electrochemical cell consisting of two solid electrodes and an electrolyte that keeps the electrodes apart. The electrolyte that is ion conducting and electron insulating, can be either in solid or in liquid state, in which case it should be used together with a liquid permeable separator. Reversible chemical reactions at both electrodes results in release/storage of Li ions, which are the charge carriers that travel through the ionic conducting electrolyte in between the electrodes. Simultaneously, the electronic charge is transferred through the outer circuit supplying the electric energy[4]. Contemporary Li-ion batteries are composed of a layered graphite as the anode and a Li-containing oxide or sulfide as the cathode that allow for reversible Li (de)intercalation. The difference between the chemical protentional (μ) of the anode and the cathode is defined as the open circuit voltage (V_{OC}).

$$V_{OC} = \mu_{Anode} - \mu_{Cathode} \quad (1)$$

During the charge process, where the Li ions are extracted from the cathode host and intercalated into the graphite anode, the V_{OC} increases as the result of applied current and the battery resistance ($\eta = I_{Charge}R_{battery}$). So, the operating voltage (V_{Charge}) increases during the charge. During the

discharge the reactions at the electrodes are inversed and the operating voltage decreases gradually[5].

$$V_{\substack{charge \\ discharge}} = V_{OC} \pm \eta_{\substack{charge \\ discharge}} \quad (2)$$

The energy density of the battery is defined as the product of the total charge per unit volume (Q) and the operating voltage of the battery.

$$Q_{Theoretical} = \frac{nF}{3600 \times Mw} \quad (3)$$

$$Q_{experimental} = \int_0^{\Delta T} Idt \quad (4)$$

$$\text{Energy density} = Q.V = \int_0^{\Delta T} IVdt \quad (5)$$

Where, n is the number of charge carriers, F is the Faraday constant and Mw is the molecular weight of the active material. The experimental value for Q is dependent on the applied current rate as kinetically-limited ion diffusion reactions can limit the charge transfer at high current rates. The operating voltage is restricted by the stable voltage window of the electrolyte, which is the range between the highest occupied molecular orbitals (HOMO) and the lowest unoccupied molecular orbitals (LUMO), outside of which the electrolyte will decompose and cause rapid degradation of the battery (*Figure 2*). The operating voltage can also be limited by the top of anionic p-bands of the cathodes, beyond which the cathode materials instability results in decomposition, phase transition and failure of the battery[5] (detailed discussion is presented in the Chapter 3).

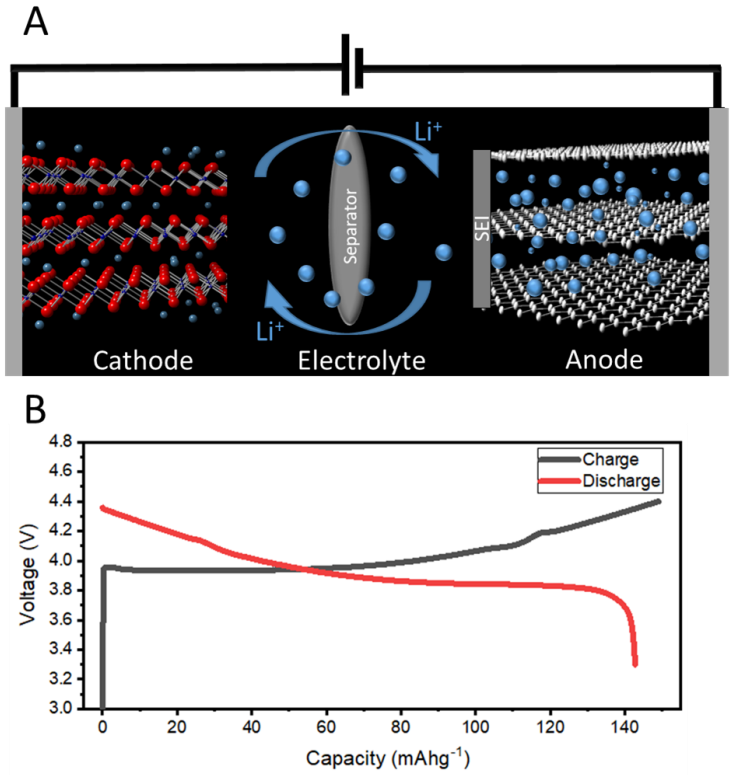

Figure 1. (A) schematic representation of a conventional Li-ion battery and its components. (B) 1st charge and discharge profiles of a $LiCoO_2$/Li battery.

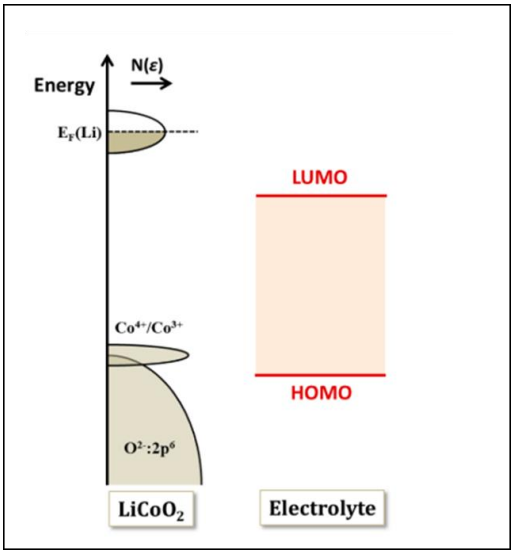

Figure 2. Schematic energy band diagrams of Li and $LiCoO_2$ with respect to the HUMO and LUMO bands of liquid electrolyte. Reproduced with permission[5]. Copyright 2010, American Chemical Society.

1.1.2 Introduction to Li-ion Battery Cathodes

The cathode is the positive electrode of the battery that stores Li ions in the discharged state. According to an early review article by Whittingham[6], LIB cathodes should meet a number of prerequisites such as, (1) presence of a redox active centers such as transition metals, (2) being able to reversibly react with Li; the number of intercalating Li ion should be high to induce high capacity, the reaction should happen at high energies to have high energy density and the reaction should be possible at high rates to have high power density, (3) good ionic and electronic conductivity to ensure good electrochemical activity and (4) good stability, low cost and environmental benignity of the materials are the also among important factors in designing a cathode material. It was in early 80s that Goodenough demonstrated that layered oxide materials such as $LiCoO_2$ can be used as a reversible intercalation compound for the first time[7]. It was soon realized that the layered transition metal oxides satisfy many of the above requirements and since then a tremendous research has been carried out on these materials[8–10].

Atomic structure: Crystallographic structure of the layered oxide cathodes consists of close-pack oxygen sublattices that host the alternative transition metal and alkali ion in the octahedral sites in alternating layers[9]. The transition metal layers form MO_2 sheets and Li-ions can intercalate into and out of the crystal structure between these sheets (*Figure 3A*). Partial deintercalation of the layered oxides, results in thermodynamic instability of the structure, which can transform to spinel or disordered rock-salt phase[11]. Since the layered, spinel and the disordered rock-salt phases share the common oxygen face centered cubic (fcc) framework, the phase transition from original layered structure to spinel and rock-salt phases depends only on the migration of transition metals and the alkali ions and can readily occur with small energy barriers[11]. For instance, transformation from the layered phase to the spinel phase occurs by the migration of ¼ of transition metals to Li

octahedral sites forming a cubic symmetry and forcing the Li ions to either occupy the vacant transition metals octahedral or the available tetrahedral sites[12]. In the disordered rock-salt structure, transition metals are occupying Li octahedral sites, but both cations are intermixed in the slabs and do not exhibit a long-range order (*Figure 3B*)[13,14]. The rock-salt structure contains less oxygen in its stoichiometry and thus layered to rock-salt phase transition is accompanied by oxygen release and densification of the crystal structure, which can pose a safety concern[15,16]. Such phase transitions to spinel and rock-salt phases are irreversible and can result in electrochemical inactivity of the cathode and lead to capacity degradation of the battery. The thermodynamic feasibility of this reactions is determined by the extent of Li deintercalation[17,18]. As such, if the deintercalation extent is limited to ~50%, kinetic barrier for metal diffusion and oxygen release reaction can hinder such irreversible phase transitions. In addition to TM migration-induced phase transitions, a change in the stacking that occurs due to glide MO_2 layers can induce some alterations in the crystal structure of the layered oxide cathodes[13,19].

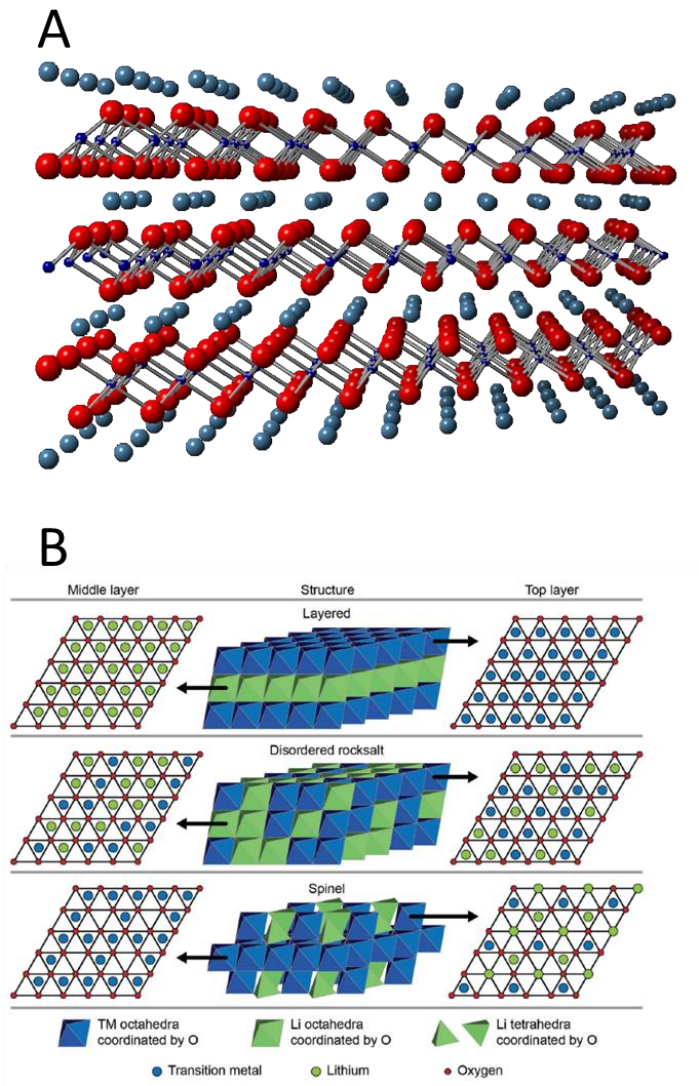

Figure 3. (A) Schematic representation of $LiCoO_2$ structure. (B) Schematic representation of layered oxide cathodes phase transition to spinel and rock-salt phases. Reproduced with permission[11]. Copyright 2017, Wiley-VCH

Synthesis methods: $LiCoO_2$ can be synthesized with a variety of different methods such as solid-state reaction[20–22], microwave heating synthesis[23–25], sol-gel method[26–30], molten salt technique[31,32] and hydrothermal synthesis[33–36]. Solid state reaction which is known as the first route to obtain $LiCoO_2$ with desired hexagonal structure, requires pre-treatment mechanical mixing followed by heating at 800-1000 °C. Although this conventional method is reliable and scalable, it does not

allow for controlled morphology and homogenous particle size distribution and is very costly due to high temperature requirements. Therefore, early research on $LiCoO_2$, has been devoted on exploring different synthesis techniques to reduce the cost of synthesis and to better control the morphology. As such, microwave heating was proposed at early stages to reduce the time of synthesis, however, it introduced more complexity to the procedure and was not highly scalable. Sol-gel method was then proposed as a more cost-effective synthesis technique that results in fine particles size of about 50 nm with a better homogeneity. In this technique, metal nitrate containing polyacrylic acid is used to form aqueous solution as a chelating agent, gel precursor is then formed using the prepared solvent. The gel will finally decompose to $LiCoO_2$ powder. The decomposition occurs at around 350 °C and pure HT-$LiCoO_2$ can be obtained after calcination at 600 °C. Similarly, another proposed method was molten salt technique which utilizes salt with low melting temperature such as KNO_3 as the reaction medium. In this technique, which is favorable due to its simplicity, cobalt oxide (Co_3O_4) and hydrated Lithium hydroxide ($LiOH \cdot H_2O$) are mixed in a molten-salt medium and then calcinated in a furnace at about 700 °C for about 8 hours. Hydrothermal synthesis method, however, is one of most promising techniques that enables the control of particle size and morphology with a better oxygen stoichiometry and also requires lower temperatures of around 200 °C. In one recipe, pure $LiCoO_2$ can be obtained from CoOOH and LiOH precursors using a hydrothermal autoclave heated at 150 °C in less than an hour, particle size can be controlled by varying the duration of reaction. Advantageously, hydrothermal synthesis allows for introducing dopants into $LiCoO_2$ structure simply with varying the concentration of precursors[34]. This technique also enables the *in-situ* control of the morphology through preferred formation of facets by varying pOH in the synthesis medium or with a post annealing in reducing or oxidizing environments[37,38].

Intercalation mechanism: Li-ion transfer occurs due to the difference in the chemical potential of the anode and the cathode. As Li+ ions are extracted from the $LiMO_2$ cathode during the charge process, the valence state of the transition metal changes from +3 to +4, which is known as the oxidation process. In the discharge the reverse process is ideally happening. As a result, electronic properties and chemical potential of the cathode changes as a function of Li concentration in the cathode. For instance, Li_xCoO_2 which is an insulator at $x > 0.95$ becomes metallic at $x < 0.75$[39,40]. In addition, the voltage of the cathode changes as a function of Li concentration based on which, the thermodynamics of Li-ion (de)intercalation can be derived. Specifically, sloped voltage profile corresponds to a solid solution intercalation mechanism and a flat voltage profile denotes to a two-phase reaction (Figure 1.4)[11]. Diffusion of Li ions in the layered structure of the cathodes is limited to the 2-D planes in between the MO_2 slabs and occurs through the hopping of Li ions into the adjacent Li octahedral vacancies[41]. Their hopping follows a curved trajectory that passes through a neighbor tetrahedral site in order to maximize the distance from the oxygen ions[41]. Therefore, the local Li ordering has a large effect on the Li diffusion kinetics. For instance, at the Li concentration where Li ordering in the structure happens, drastic increase in the Li diffusion barrier can be observed[42,43]. In addition, when a large fraction of Li ions is removed out of the Li_XCoO_2 structure the diffusion coefficient of the Li migration rapidly decrease due to phase transitions and unavailability of free interlayer hopping sites[13,44]. The diffusion process of Li-ions is a result of chemical gradient potential in the cathode particles. As a result, the surface of cathode particles is under a local Li deficiency during the charge process and a local accumulation of Li ion during the discharge process[45]. Therefore, as chemical potential of the cathode is a function of Li concentration, there is a shift in the chemical potential of the surface with respect to the average chemical potential. Hence, there is a polarization in the voltage, since the measured and plotted

voltage does not represent the Li concentration at the surface, rather it corresponds to the average Li concentration of the particle. Voltage polarization can also prevent the extraction of the full capacity of the cathode because if the surface layer reaches the full concentration, the measured voltage will reach to the cut-off voltage and stop the lithiation although the full intercalation of the particle is not realized yet[11]. Such phenomena will be more predominant at higher rates of cycling, where limited diffusion kinetics of the Li ions will induce a larger concentration gap between the surface and core of particles. Ion transfer through the solid/electrolyte interface (SEI) is also another kinetic limitation can that define the electrochemical properties of cathode materials. Such interface may be composed of SEI only, or the SEI layer together with the surface spinel or rock-salt atomic layers that are generally referred to as the charge transfer resistance[46]. Both surface film resistance and the bulk diffusion resistance can be measured experimentally by electrochemical impedance spectroscopy (EIS), which utilizes an AC current to measure the resistance of the Li-ion transfer.

Degradation mechanisms: Capacity/voltage degradation are among the major issues of the Li-ion batteries, and tremendous efforts have been focused to understand the underlying mechanism for cathodes degradation. With the advancement of the characterization techniques, several degradation mechanisms for the failure of layered oxide cathodes have been discovered in recent years[47,48] such as; transition metal migration and phase transition[12,49–51]; transition metal dissolution[52–54]; surface film formation and lithium consumption[55]; parasitic oxygen release reaction[56]; mechanical degradation through cracking and disintegration of cathode particles[57–59]. Some of the captured mechanisms are shown in the *Figure 4*. Noteworthy, such mechanisms can occur independently or as a chain of events and their occurrence are highly dependent on the

electrochemical cycling conditions, chemical composition and particle morphology, which are discussed in detail in Chapter 3.

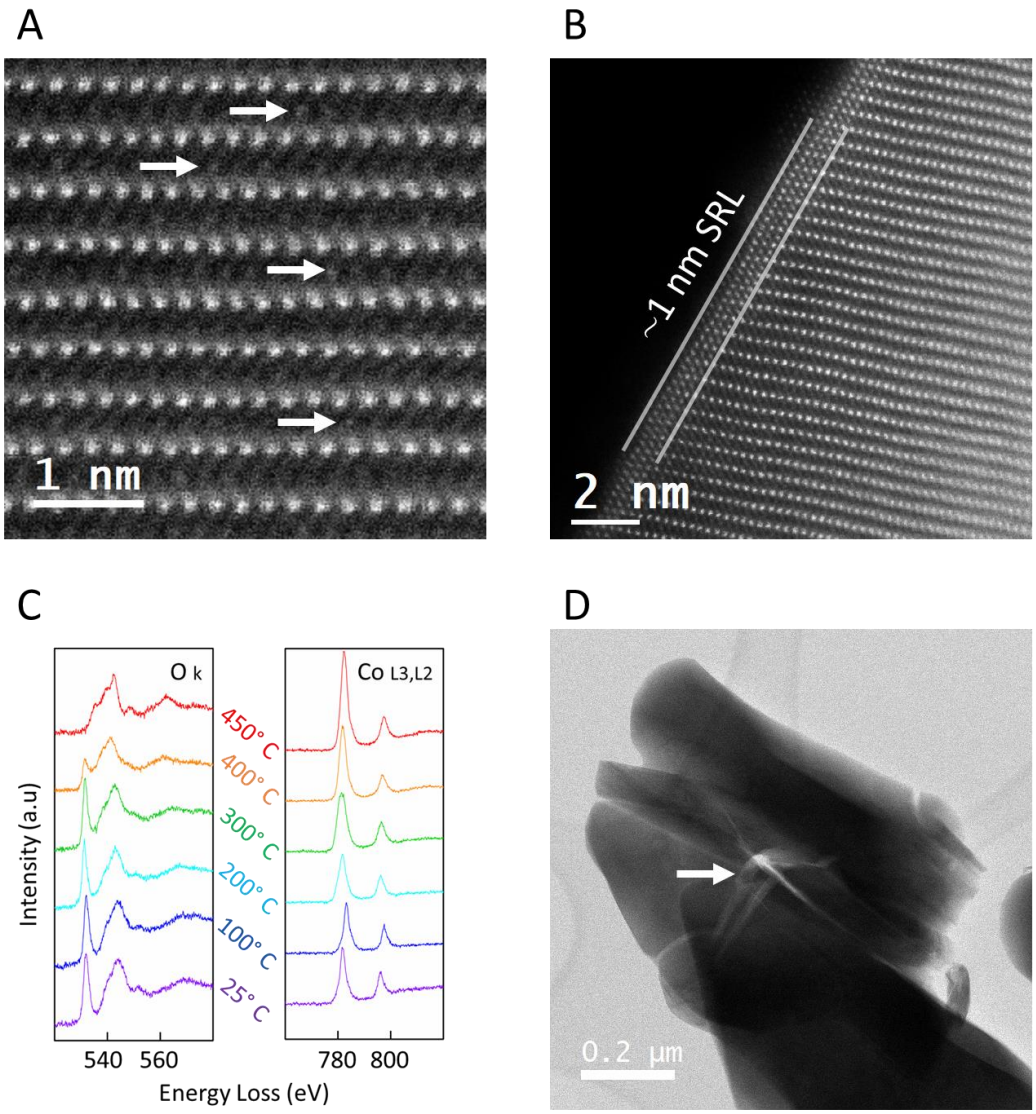

Figure 4. (A) Atomic resolution HAADF image from a cycled cathode sample, where anti-site transition metal defects can be detected. (B) Detection of rock-salt type surface reconstruction layer on a layered cathode sample. (C) *in-situ* heating electron energy loss spectroscopy (EELS) results showing the thermally induced oxygen release reaction. Reproduced with permission[1].

Copyright 2017, American Chemical Society. (D) Low magnification ABF image demonstrating the cracking and fracture of cycled cathode particles.

Transition metals migration to Li vacancies is one of the initial degradation mechanisms that occur via diffusion of transition metals through the tetrahedral sites into Li octahedral vacancies (*Figure 4A*). Formation of such point defects can hinder the in-plane diffusion of Li ions leading to increased cell impedance, decreased Coulombic efficiency, and eventually phase transition to spinel/rock-salt [60–62]. The layered to spinel/rock salt phase transition can be observed on the surface structure of almost all the layered oxide cathode materials (*Figure 4B*)[63]. The effect of such phases on the cathode performance is still ambiguous as it is suggested that such cubic structures disrupt the Li diffusion and increase to cell impedance and hinder the high rate cycling, on the contrary some argue that the thin layers of dense phases act as the protective layer of the cathode contributing to reversibility of the cathode[11]. Non uniform Li deintercalation leading to surface Li deficiency[45], the cathode/electrolyte reactions[64] and environmental reactions are the underlying causes for the formation of the surface reconstruction layers. Cathode/electrolyte reaction can also result in formation of surface films such as LiF and Li_2CO_3, which degrade the capacity by consuming Li ions and increasing cell impedance[65]. HF generation in the electrolyte due to moisture contamination reaction with $LiPF_6$ salt that can attack the cathode surface and cause transition metal dissolution is another degradation method caused by electrolyte interaction with cathode surface[65]. Oxygen release is another major degradation mechanism that can cause catastrophic failure and is a safety concern for Li-ion batteries (*Figure 4C*). The parasitic O_2 release can be induced in two circumstances, which are overcharging[66] and overheating[62]. In general, the hybridization of undercoordinated oxygen atoms that leads to O_2 formation and evolution accompanied by phase transitions is regarded as the triggering mechanism for cathodes oxygen release. This is discussed in detail in Chapter 3. Finally, fracture and disintegration of cathode

particles are another degradation mode in cathode materials (*Figure 4D*). Cracking has observed both at the grain boundaries (intergranular cracking) and inside the grains of cathode particles (intragranular cracking)[67]. Intergranular cracking can occur due to accumulated strain in the grain boundaries during the repeated expansion/extraction cycles of adjacent electrochemically active grain. The intragranular cracking is proposed to be the result of formation of dislocations in the grains that can evolve into premature cracks during repeated cycling and eventually result in fragmentation of the particles[57].

1.2. The Role of Layered Cathode Materials in the Parasitic Thermal Runaway Reaction

Thermal runaway is the uncontrolled release of heat and energy that normally leads to ignition or explosion of Li-ion batteries, which is a major safety issue in Li-ion batteries. Thermal runways have been observed in several Li-ion battery powered systems ranging from laptop and cell phones to electric vehicles[68,69]. The thermal runaway is induced by a series of self-progressive exothermic events, that are initiated by various events such as temperature rise, mechanical damage and short circuit or non-equilibrium electrochemical cycling[70,71]. The detailed description of the thermal runaway events is discussed in Chapter 3.1. Regardless of the initial stimulus of a thermal runaway, the chain of exothermic events leads to a local temperature rise. Therefore, when the temperature reaches to above 150 °C, the oxide cathode material decomposes and releases a large amount of oxygen that can ignite the flammable electrolyte/combustible gases in presence of the accumulated heat and triggers the thermal runaway of the battery[72]. Therefore, it is suggested that the highly exothermic final step of the thermal runaway reaction that triggers the ignition of the battery is induced by the cathode decomposition and oxygen release. It should be noted that the pristine oxide cathodes are stable up to 900 °C, however Li deintercalation leads to under-coordination of oxygen atoms, that can readily form O-O bonds and release as O_2 gas below 200 °C [73]. Different

scenarios of thermal runaway reaction, the parameters that influence the oxygen release thermodynamics and kinetics in the cathode materials and proposed solution to hinder such parasitic reaction are discussed in length in Chapter 3.

1.3.Next Generation Li-rich Cathode Materials; Challenges and Issues

Layered oxide cathodes played a key role in the development of Li-ion batteries and are still the dominant cathode materials in most Li-ion batteries. Despite numerous advantages such as high electrochemical voltage vs Li/Li^+, good rate capability and cycling stability, their limited capacity is a major drawback. This is because only about half of the theoretical capacity of the layered oxide cathode materials can be reversibly extracted because as the cathodes potential reaches to the O-2p molecular orbitals, peroxo like $(O_2)^{2-}$ ions form at the particle surface and release as O_2 gas[5]. In addition, excessive Li extraction can induce transition metal migration to Li vacancies and cause irreversible phase transitions and activate the discussed degradation mechanisms. Therefore, the ever-growing demand in improving the capacity of LIBs cannot be satisfied due to such intrinsic limits in the capacity of conventional cathode materials.

Advancement of layered oxide cathodes was initiated by the development of solid solution layered oxide cathodes with the composition of $Li(Ni_xMn_yCo_z)O_2$ (NMC) and $Li(Ni_{0.8}Co_{0.15}Al_{0.05})O_2$ (NCA), which extended the capacity and improved the cycling stability. In these cathodes the Co^{3+} cations are replaced with Ni^{2+}, Mn^{4+} and Al^{3+} ions. Therefore, since the redox reaction of Ni proceeds through the less stable e_g orbital (*Figure 5A*) the redox reaction of Ni^{2+}/Ni^{3+} and the Ni^{3+}/Ni^{4+} occur first, followed by the high voltage redox reaction of Co^{3+}/Co^{4+} that involves more stable t_{2g} electrons (*Figure 5B*)[11]. Mn^{4+} and Al^{3+} do not participate in the redox reactions and act as the structural stabilizers[74]. These materials have superior properties such as better Li-stoichiometry (decreased cation mixing in Li layer), improved electrochemical performance and

higher thermal stability compared to $LiNiO_2$ and $LiCoO_2$[75–77]. Therefore, they are dominating the market of high capacity and large scale Li-ion batteries, such as electric vehicles[9,78,79].

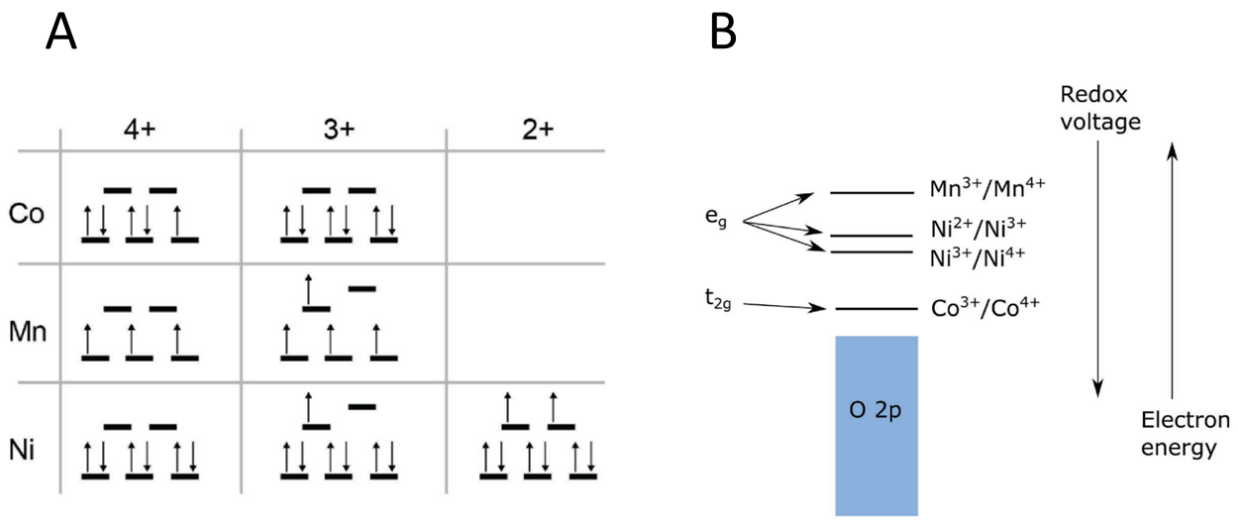

Figure 5. (A) Electron configuration in transition metals cations in NMC cathodes. (B) Schematic electron energy levels in NMC cathodes. Reproduced with permission[11]. Copyright 2017, Wiley-VCH.

A breakthrough was made recently by partial substitution of transition metals in a solid solution layered oxide cathode with Li-ions, which gave birth to the concept of Li-rich layered oxide (LLO) cathodes[80]. Although there is only less than 20% excess Li in the layered cathodes composition, their capacity has significantly increased to about 300 $mAhg^{-1}$ [81]. Since the enormous 50% increase in the capacity of the Li-rich cathodes cannot be explained by the 20 % extra Li-ions, scientist proposed a different mechanism for generation of the extra capacity. Overall, it is accepted that the source of extra capacity of LLOs is the anionic redox reaction that activates subsequent or concurrent to cationic redox reaction[81]. The anionic redox reaction is suggested to occur by formation of Li-O-Li bonds that are only probable in LLOs, which is due to the presence of Li ion in the TM layers. The Li-O-Li bond has extra (orphan) electrons, that are closer to the valence

band compared to Li-O-TM electrons[82]. Therefore, such electrons can be extracted readily at lower voltages, allowing the participation of oxygen anions in the redox reaction and increasing the capacity considerably. This phenomenon is called anionic redox reaction and is the accepted cause for increased capacity of LLO cathodes[83–86]. However, despite the great specific capacity, poor cycling stability and rapid capacity/voltage fade has hindered the practical application of Li-rich cathodes. To understand the origins of such rapid degradation, the atomic structure of Li-rich cathodes should be fully comprehended. However, there is still an ongoing debate on the atomic structure of pristine Li-rich cathodes and their structure have been denoted in three opposing ways; (1) original ($R\bar{3}m$) $LiTMO_2$ layered structure solid solution, where the extra Li ions are taking the transition metal sites[87], (2) C2/m Li_2TMO_3 solid solution phase with random Li/TM mixture (Figure 1.6)[88], (3) a nano-composite of the $R\bar{3}m$ $LiMO_2$ and the C2/m Li_2MnO_3 that is denoted as of xLi_2MnO_3-(1-x)$LiMO_2$[89] (*Figure 6*). The underlying reasons for the rapid voltage fade and capacity degradation have also remained very elusive and controversial and are the topics of vast scientific studies[90–94]. Our atomic resolution scanning transmission electron microscopy and electron energy loss spectroscopy (STEM/EELS) investigations coupled with density functional theory (DFT) calculations on the structural degradation of LLO cathodes are discussed thoroughly in Chapter 6.

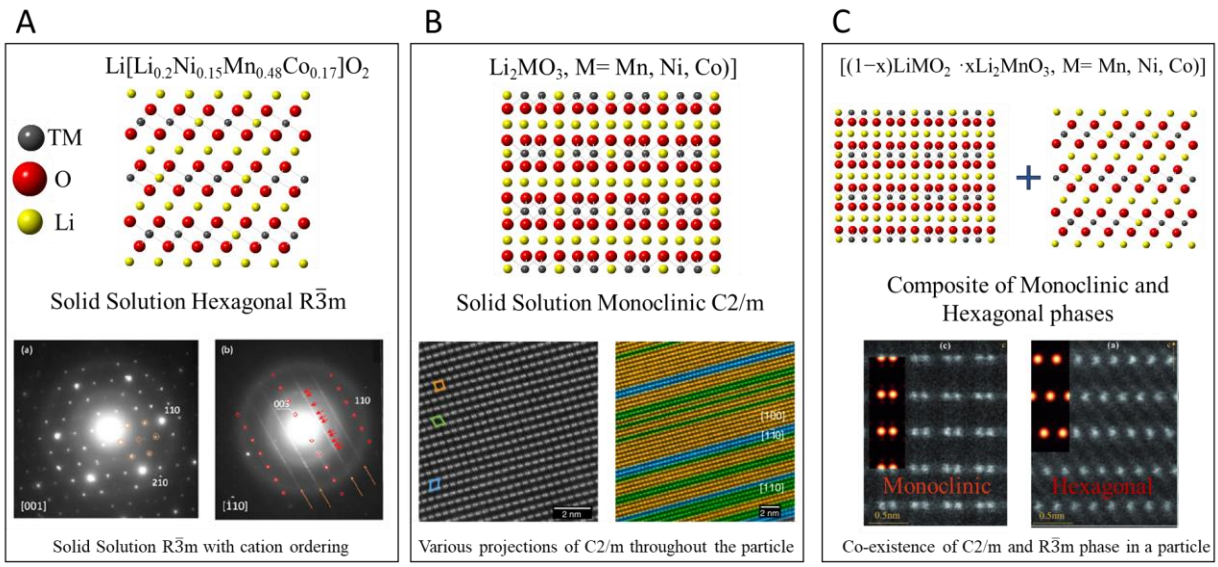

Figure 6. Schematics of proposed atomic structures of Li-rich layered oxide cathodes together with the representative results. (A) Solid solution hexagonal layered structure, where extra Li ions occupy the transition metal sites. Reproduced with permission[87]. Copyright 2013, American Chemical Society. (B) Solid solution monoclinic structures with extra transition metals in Li sites[88] and (C) nano composite structure of hexagonal/monoclinic phases. Reproduced with permission[89]. Copyright 2017, Wiley-VCH.

1.4.Order of Chapters

This dissertation is ordered based on the flow of my research progress on the understanding and controlling the heat/overcharge-induced degradation of $LiCoO_2$ cathodes and our atomic resolution study aiming to resolve the structural ambiguities of the next generation Li-rich cathode materials.

The presented chapter 1 is designed as a brief overview of the Li-ion battery and the layered oxide cathode materials. Furthermore, the general atomic structure, Li (de)intercalation mechanism, degradation modes and contribution of layered oxide cathodes in the thermal runaway events are discussed. Finally, the next generation Li-rich cathodes are introduced, and their advantages, drawbacks and scientific challenges are briefly discussed.

Chapter 2 presents the experimental methods that have been utilized throughout this thesis.

Chapter 3 is a comprehensive review on the oxygen release degradation of Li-ion battery cathodes. Oxygen release from oxygen-containing positive electrode materials is one of the major structural degradations resulting in rapid capacity/voltage fading of the battery and triggering the parasitic thermal runaway events. In this chapter, I summarized the recent progress in understanding the mechanisms of the oxygen release phenomena and corelative structural degradations observed in four major groups of cathode materials: layered, spinel, olivine and Li-rich cathodes. In addition, the engineering and materials design approaches that improve the structural integrity of the cathode materials and minimize the detrimental O_2 evolution reaction have been summarized. We believe that this review can guide researchers on developing mitigation strategies for the design of next generation oxygen-containing cathode materials where the oxygen release is no longer a major degradation issue.

Chapter 4 presents our efforts in understanding the oxygen release reaction from the Li_XCoO_2 cathode under heating conditions. Utilizing *in-situ* aberration-corrected scanning transmission electron microscopy (STEM) and electron energy loss spectroscopy (EELS) at high temperatures, we show the inhomogeneous oxygen loss from Li_xCoO_2 crystals for the first time. The oxygen evolution from Li_xCoO_2 structure was correlated with local phase transitions spanning from layered to spinel and then to rock salt structure upon exposure to elevated temperatures. Ab initio molecular dynamics simulations (AIMD) results show that oxygen release is highly dependent on the Li_xCoO_2 facet termination. While the [001] facets are stable at 300 °C, oxygen release is observed from the [012] and [104] facets, where under-coordinated oxygen atoms from the delithiated structures are able to combine and eventually evolve as O_2.

Chapter 5 describes our novel nano-coating design of individual $LiCoO_2$ nanoparticles that mitigates the oxygen evolution reaction. In this research we have performed electrochemical cycling, differential electrochemical mass spectroscopy (Done by Dr. Salehi-khojin's at UIC), differential scanning calorimetry (DSC), and *in-situ* heating transmission electron microscopy to characterize the effectiveness of the graphene-coating on the abusive tolerance of Li_xCoO_2. Additionally, density functional theory and *ab-initio* molecular dynamics calculations (done by Dr. Soto and Dr. Balbuena as a collaboration) were carried out. The results show that there is a strong $C\text{-}O_{cathode}$ bond formation at the interface of rGO/LCO, which suppresses the O-O bond formation from low coordination oxygens thus the O_2 evolution is suppressed. This systematic investigation uncovers a reliable approach for hindering the oxygen release reaction and mitigating the thermal instability of battery cathodes.

Chapter 6 presents our detailed atomic resolution studies on the atomic structure of the Li-rich cathode materials. In this research, we have identified the hexagonal/monoclinic and monoclinic/monoclinic grain boundaries of Li-rich cathode materials, which provides the first direct proof of the nano-composite structure of the LLO materials. Our results demonstrate that the grain boundaries have a cubic spinel structure and are highly strained. During cycling the high energy grain boundaries are depleted from Mn cations and are enriched with Ni cations, which deteriorates the capacity by consuming the active redox centers. The mechanism of Ni diffusion to grain boundaries are investigated through DFT modeling by Dr. Yurkiv and Dr. Mashayek at UIC, in a collaborative research. In addition, crack initiation was detected to occur on the tip of such grain boundaries, which is identified as a newly discovered degradation mechanism of LLO cathodes.

Chapter 7 discusses some aspects of our collaborative research, where transmission electron microscopy techniques were utilized to (1) identify the atomic configuration and structure of the engineered cathode materials and (2) uncover the correlation of cell-design and cathodes chemistry on failure mode and degradation extent of the cathode materials.

Chapter 2: Experimental Methods

Details of the experimental procedures that were carried out in this thesis are described in this chapter. Details of transmission electron microscopy (TEM) characterizations, graphene-coating of $LiCoO_2$ particles, utilized materials characterization techniques and electrochemical tests are discussed in the following sections.

2.1. Transmission Electron Microscopy (TEM)

Transmission electron microscopy can achieve ~ 10^4 times higher resolution than conventional optical microscopes due to the ultra-small wavelength of the electrons. Therefore, in this research TEM (JEOL JEM-3010) was utilized to study the decomposition mechanism of the layered oxide cathodes at the single particle level. Selected area electron diffraction pattern (SAEDP), which is the result of elastic interaction of electron wave with the crystal lattice of the sample was utilized to identify the phase transitions during the thermal decomposition of $LiCoO_2$ particle. SAEDPs can be obtained from particle agglomerates or can be obtained from a limited area within a single particle, therefore can carry local information.

Based on the Bragg's Law and the schematic image in *Figure 7A*;

$$\frac{R}{L} = \tan 2\theta \sim 2\theta \tag{6}$$

$$n\lambda = 2\mathrm{d}\sin\theta \sim \mathrm{d}2\theta \tag{7}$$

therefore,

$$d = \frac{L\lambda}{R} \tag{8}$$

where, R is the distance from the diffraction spot in pixels, L is the average cameral length which is calibrated for each microscope to pixels, λ is the electron wavelength and d is the lattice spacing of the crystals, which is calculated based on this equation

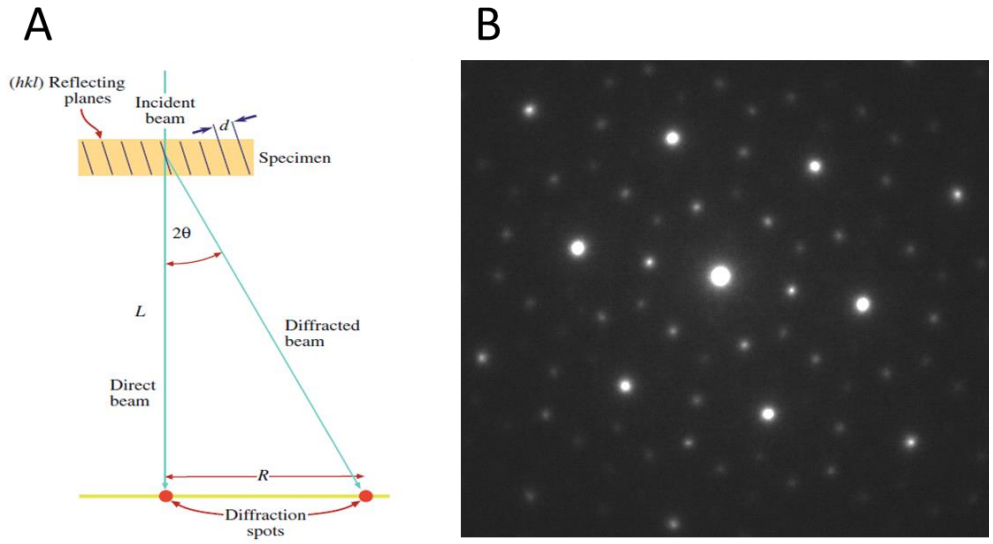

Figure 7. (A) Schematic diagram showing the electron diffraction pattern formation mechanism. Reproduced with permission Copyright 2009[95], Springer Nature. (B) An example of an SAEDP.

Conventional bright field TEM images are collected by placing the objective aperture of the microscope on the direct beam. On the other hand, dark field TEM images can be collected by placing the objective aperture on the diffracted beam based on the SAEDP pattern. This technique allows for identification of the location of each phase in multi-phase specimens. This method is utilized in chapter 4 for identification of surface-originated phase transition during thermal decomposition of $LiCoO_2$ cathodes.

Scanning transmission electron microscopy (STEM), which uses a highly focused beam to scan over a specimen has also been utilized in this research. Unlike TEM that is a phase contrast imaging technique and is based on the wave-like characteristics of electrons, STEM utilizes the particle-

like characters of electron for image formation. STEM utilizes annular detectors with various range of angles and each one carries specific information. High angle annular dark field detector with 90 mrad inner detector angle, allows for Z-contrast imaging mode which can distinguish between the atoms based on their atomic number. Low angle annular dark field detector with 45 mrad inner detector angle, is sensitive to defects and crystalline irregularities. Annular bright field detector with detector diameter of 7-14 mrad is utilized to resolve light elements such as O and S. In this thesis STEM experiments were performed using a JEOL JEM-ARM200CF equipped with a cold field emission gun and a spherical aberration corrected that allows for atomic resolution imaging with 0.78 Å spatial resolution.

Lattice plane measurement can be directly carried out on atomic resolution images or based on the fast Fourier transform (FFT) of the images. FFT images that are similar to diffraction patterns, represent the frequency of atomic arrangement sequence in an image. In FFT images the inverse of the distance between each bright dot to the center dot, corresponds to a resolved lattice plane. Outer product of two identified plane vectors indicate the zone axis of the image, which is parallel with the direction of e-beam travel through the sample. By identification of the lattice planes and the zone axis of the image the crystal structure of a sample can be identified, which is the procedure that was carried out to identify the spinel/rock-salt phase in chapter 4 and the hexagonal/monoclinic interphases in chapter 6. In addition, FFT images can be utilized to reconstruct color-coded image from the atomic resolution images. To reconstruct color coded images, using Digital Micrograph, indicated spots of FFT image which corresponds to each phase are masked and inverted to form separate images from each phase and then combined with various color constrsts to reconstruct color coded images. Such procedure is also utilized in Chapters 4, 6 and 7 to identify various phases in a single image.

Electron energy loss spectroscopy (EELS) which carries information about the electronic structure of the material was also utilized in this thesis. EELS is the analysis of the energy distribution of inelastic scattered electrons that can be interpreted to valence information, bonding and nearest neighbor atoms, sample thickness, etc. In this thesis, EELS experiments were carried out using the JEOL JEM-ARM200CF microscope and Gatan Enfina and GIF Quantum EELS detectors with 0.1-0.5 eV/channel dispersion and with a 2 mm detector aperture. Full-width half maximum of zero loss peak was measured 0.5-0.75 eV, which determines the energy resolution of the obtained spectra.

The layered oxide cathode samples are electron beam sensitive and both radiolysis and knock-on damage mechanisms are active since the samples are semi-conductive material, containing light elements such as Li and O. Based on the conducted experiments, the radiolysis damage is more predominant in TEM mode as the total electron dose can be higher, especially when high resolution imaging is attempted. In STEM mode the knock-on damage is the predominant damage mechanism, where the dose rate is higher compared to TEM mode experiments. However, in STEM mode the radiolysis is still an active mechanism (since the phase transition is observed as well as hole formation as a result of knock-on damage). Therefore, using the microscope in 80 kV was not very helpful since by reducing the extent of knock-on damage, the radiolysis damage would increase in 80 kV.

Beam damage was controlled and minimized throughout the (S)TEM experiments. We control the electron beam dosage, by (1) decreasing the gun current, (2) by changing the spot size, (3) by using various condenser lens apertures and (4) by controlling the pixel dwell time. Before collecting data in every experiment, we gather a series of data to find out the best of set of parameters that yield the highest signal to noise ratio and does not induce beam-damage artifacts.

In the presented experiment shown in *Figure 8*, a layered oxide cathode sample is imaged from the [100] zone axis. The area from which the beam damage measurement will be carried out is shown in the blue box, the area of interest in digitally magnified and shown as the inset in *Figure 8A*. Then an EELS map is obtained from the area of interest and the sample is imaged again subsequent to obtaining the EELS map. Again, the area of interest is digitally magnified for a better observation. In this experiment the pixel size is 0.5 nm, the dwell time is 0.2 s and the beam current is set to 35 pA, which results in the dose rate of 8×10^{6} $e.A^{-2}s^{-1}$. Normally the 2D EELS maps are summed into a line scan and each column of spectrums are added up for higher signal quality and represent the valence state of transition metal at a certain distance from the cathode surface[1,92,96,97]. As can be seen from the corresponding EELS spectrum that represents the top surface region of the sample (*Figure 8D*), the signal to noise ratio is very high and the results quality is totally acceptable for publication. Here the O-K edge signal is magnified and the ΔE ($E_{pre\text{-}peak} - E_{main\text{-}peak}$) value is measured to be 11 eV, which corresponds to the value expected from a pristine NMC cathode[98]. Any decrease in this value corresponds to valence reduction of transition metals and oxygen release phenomena[99]. Therefore, as can be seen from the atomic resolution image and the EELS spectrum the effect of the electron beam after obtaining such a good quality EELS signal is very minimal. The layered structure is totally preserved and the thickness of the surface reconstruction layer (SRL) has grown only by about 0.2 nm which is very far from the scale of our measurements in the manuscript. Then we increased the pixel dwell time from 0.2 to 1 s and obtained another EELS map from the same area. The area of interest is imaged after obtaining this EELS map and shown in *Figure 8C*. It can be observed that the layered structure is totally disrupted, and cation disorder can be clearly detected in the area that EELS map was obtained from. Although the EELS signal to noise ratio is slightly improved and the intensity has increased

by 5 folds, the beam damage has induced artifacts in the results. By looking at the O-K edge it can be concluded that reduction of transition metals' valence state and oxygen release has occurred, due to knocked off oxygen atoms and broken oxygen- metal bonds. In general, it can be concluded that, although beam damage is a serious issue in any electron microscopy/spectroscopy experiments, by taking proper yet simple cautions it can be avoided without compromising the quality of data.

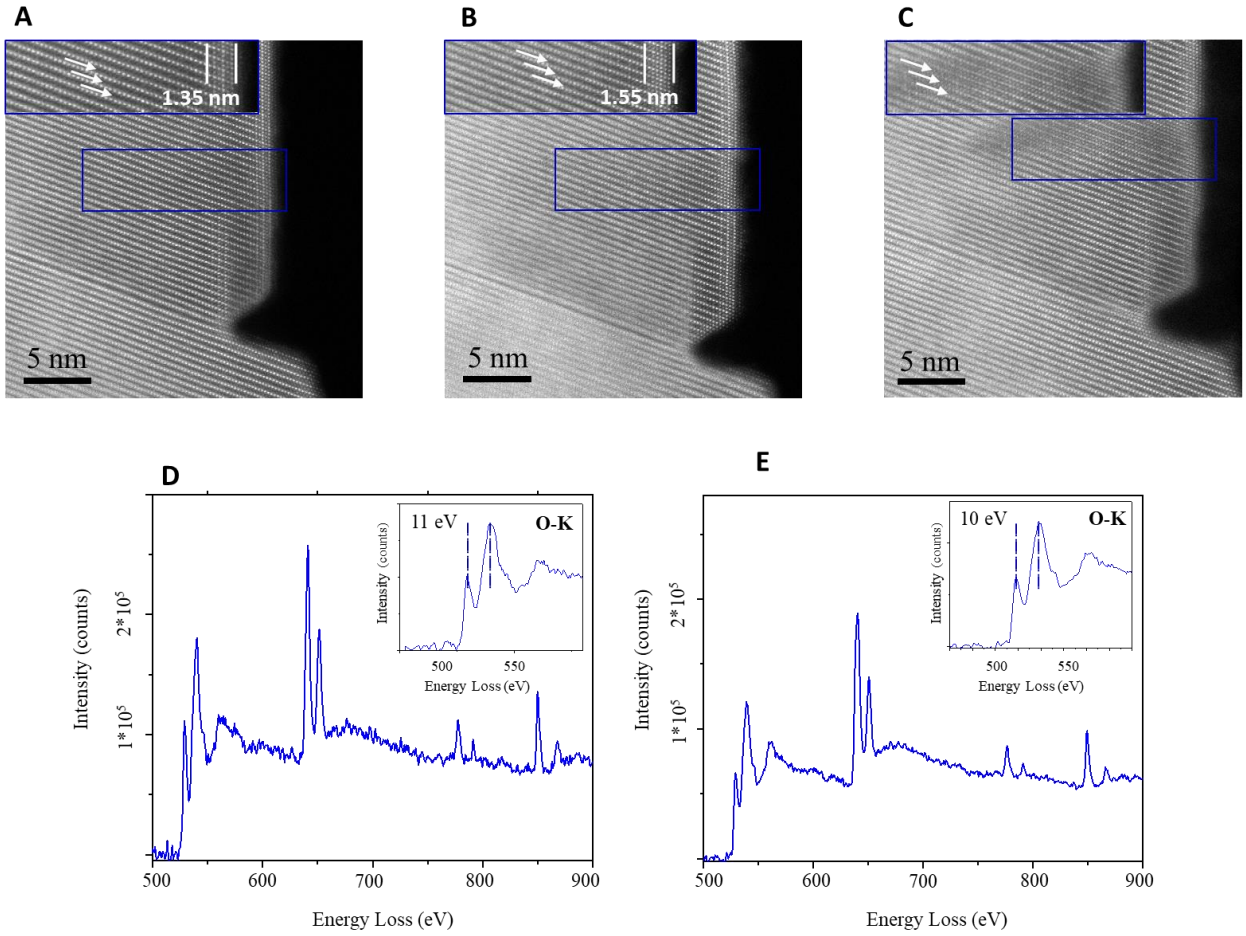

Figure 8. (A) Atomic resolution HAADF image from a pristine NMC cathode with the digitally magnified area of interest shown as inset. (B) Atomic resolution HAADF image from the same area after obtaining the EELS map with the area of interest digitally magnified as the inset. (C) Atomic resolution HAADF image obtained after collecting another EELS map from the same area with 5 times longer pixel dwell times. (D) a sum spectrum from the top 0.5 nm layer of the cathode

surface obtained in the first EELS map acquisition. (E) a sum spectrum from the top 0.5 nm layer of the cathode surface obtained in the second EELS map acquisition.

2.2. *In-situ* Heating TEM

Gatan double tilt heating stage, which is a furnace-based heating holder was utilized for *in-situ* heating experiments. Samples were subjected to high temperatures ranging from 25 to 450 °C with a heating rate of 10 °C/min, before collecting data we kept the samples at the desired temperature for 15 minutes to ensure holder stability and temperature uniformity. Cathode particles were analyzed after electrochemical / chemical delithiation. Electrochemical delithiation was carried out using coin cells. Subsequent to cycling the cells were disassembled, and the cathode laminates were submerged into dimethylcarbonate for 1 hour then rinsed with fresh dimethylcarbonate and dried under vacuum overnight. The laminates then were scratched, and the obtained powder was dispersed in methanol, sonicated and drop casted onto lacy carbon grid and loaded into the microscope with minimum exposure to air. For chemical delithiation, 1 g of $LiCoO_2$ was dispersed in 25 ml of 0.15 M $K_2S_2O_8$ aqueous solution and magnetically stirred at 60 °C for 24 and 72 hours to obtain partially and fully de-lithiated specimens, respectively. Then the solution was vacuum filtered using filter membranes with 100 nm pore size and washed 3 times with DI water and dried in a vacuum furnace for another 72 hours. Following this process, the Li content was measured using inductively coupled plasma optical emission spectroscopy (ICP-OES) by Thermo iCAP 7600. These measurements have shown that the molar ratio of Li/Co is 0.7 and 0.45 for partially and fully de-lithiated samples, respectively.

2.3. Graphene-encapsulation of Individual $LiCoO_2$ Cathode Particles

For achieving graphene-coating on individual particles, surface charge modification should be carried out on $LiCoO_2$ sample. To do so, $LiCoO_2$ (1g) was dispersed in methanol (100 ml) and

sonicated. Then aminopropyltrimethoxysilane (1 ml) was added to the solution and stirred for 24 hours. The sample was then vacuum filtered and washed several times with methanol to obtain the positive surface charged $LiCoO_2$. Graphene-coated $LiCoO_2$ particles then can be obtained as a result of attractive electrostatic force between positively charged $LiCoO_2$ and negatively charged graphene oxide nano-sheets. At this step, surface charged $LiCoO_2$ and graphene oxide nano sheets are redispersed in methanol with the concentration of 10mg/ml. Graphene oxide nano sheets are also redisposed in methanol by centrifugation of water-dispersed GO. Then the GO dispersed in methanol is added dropwise to the LCO containing solution. As the self-assembly takes place, graphene-coated $LiCoO_2$ precipitate. Finally, hydrazine (1ml per 100 ml of cathode solution) was added dropwise to the solution to reduce the GO layer to rGO to enhance the conductivity of the coating layer. The sample is then vacuum filtered to obtain the graphene-coated $LiCoO_2$ particles. Noteworthy, the cost of such process is calculated to be approximately \$0.48/gr of $LiCoO_2$ in laboratory scale, from which only 3.3% is for consumed GO material and the rest relates to the cost of surface charge modification and hydrazine treatment that can be reduced in industrial scale.

2.4. Materials Characterizations to Study and Quantify the Graphene Coating on Cathode Samples

Scanning electron microscopy (SEM): SEM was carried out using a Carl–Zeiss electron microscope integrated into a Raith e-LiNE plus electron-beam lithography system. The acceleration voltage was set at 10 kV, and aperture size of 30 µm was used. Secondary electrons were used for topographical imaging of the rGO coating layers.

Raman spectroscopy: Raman is a spectroscopic technique used to measure vibrational, rotational, and other low-frequency modes in a system. It provides a structural fingerprint that can be used to identify molecules. In this method inelastic scattering of monochromatic light, usually from a laser

is being used as the probe. When a laser light with the wavelength of ν_L hits the sample, energy state of electrons in the bonds of the molecule increases to a virtual state then if the energy returns to the same state it is called Rayleigh scattering (99%) and does not indicate the vibrational energy of the sample. In this case the wavelength of emitted photon is the same as the wavelength of the incident photon However, if the molecule goes back to a higher energy or lower energy level (1%), it will emit a photon with a different energy (ν_s). So $\nu_s = \nu_L - \nu_{0>1}$ by knowing the ν_L and measuring the ν_s we can obtain the $\nu_{0>1}$ which is the fingerprint of molecules. Raman can be used for quantifying composition and contamination identification, defect analysis, doping analysis and the Electronic properties of materials. Raman results were obtained from a Renishaw inVia Reflex Raman system equipped with a green 532nm/50mW diode-pumped solid-state laser. Spectroscopy was performed using a 50x objective lens. Dwell time, and laser strength were set to 100 s and 5% to obtain the best signal to noise ratio and avoid the laser-induced damage in the samples.

X-ray photoelectron spectroscopy (XPS): XPS is a surface characterization technique (up to 10 nm) that reveals the chemical composition of the surface of samples as well as the elements that are bonded to each chemical. XPS is generally used for Analysis of surface composition and contamination and valence state and bonding analysis of the material surface. In principle XPS is used to detect the photoelectrons that are ejected from the sample by the X-ray beam. XPS was carried out using a Kratos AXIS-165 XPS system, equipped with a monochromatic Al Kα source (1,486.7 eV). Survey spectra were collected with a pass energy of 80 eV, step size of 1 eV and dwell time of 200 ms. High-resolution regional spectra were collected with a pass energy of 20 eV, step size of 0.1 eV and dwell time of 1000 ms.

2.5. Thermal Analysis Techniques

Thermal analysis was conducted to study the thermal decomposition of Li_xCoO_2 and to evaluate the effectiveness of rGO-coating on the thermal stability of $LiCoO_2$ sample. For these purposes differential scanning calorimetry (DSC) and thermogravimetric analysis (TGA) methods were utilized. In DSC a reference pan and a sample pan are taken under the same temperature program and while the reference pan has a constant and defined heat capacity throughout the specified temperature, the sample will undergo exothermic or endothermic reactions and the amount of heat that is released or absorbed from the sample pan is recorded and plotted. TA Instruments Q2000 systems were utilized to perform the DSC experiments. To capture the heat flow from the exothermic reaction between flammable gases (from the decomposition of electrolyte) and the evolved oxygen (from the charged $LiCoO_2$), the hermetically sealed aluminum containers were utilized. Bare and graphene-coated $LiCoO_2$ samples were cycled twice and then charged to 4.2 V. Then the cells were opened in Argonne filled atmosphere, and the cathode foils were sealed in the aluminum container without drying or removing the electrolyte. DSC experiments were performed in the range of 25-350 °C with the heating rate of 2 °C/min. In TGA the mass of sample is measured when sample is exposed to a thermal program. TGA is great tool for studying the kinetics of thermal decomposition reactions. TA Instruments Q500 systems were utilized to perform the TGA experiments. In these experiments 10 mg of Li_xCoO_2 was placed in open Pt holders and the thermal program were carried out under N_2 flow, with a heating rate of 5 °C/min.

2.6. Li-ion Battery Cell Fabrication and Electrochemical Testing

Coin-type cells composed of $LiCoO_2$/Li half cells, glass fiber separator and 1M $LiPF_6$ in EC/DMC = 1:1 electrolyte were fabricated for electrochemical tests. $LiCoO_2$ laminates with the composition of 80 wt% of active material, 10 wt% of carbon black and 10 wt% of poly(vinylidene fluoride

were mixed with N-methylpyrrolidone and casted on Al foils, then dried at 80 °C in vacuum. Cycling and EIS tests were conducted by a Bio-Logic VMP3 Electrochemical Workstation working with a EC-Lab software. $LiCoO_2$|Li cells were used for cycling and EIS measurement and EIS measurements were performed at a frequency ranging from 100 kHz to 100 mHz after 1^{st} and 20^{th} cycles.

Chapter 3: Oxygen Release Degradation in Li-ion Battery Cathode Materials, Mechanisms and Mitigating Approaches: A Review[100]

(Previously published as Sharifi-asl, S.; Lu, J.; Amine, K.; Shahbazian-yassar, R. Oxygen Release Degradation in Li-Ion Battery Cathode Materials : Mechanisms and Mitigating Approaches. *Adv. Energy Mater.* 2019, 1900551. Reproduced with permission[100]. Copyright 2019, Wiley-VCH)

3.1. Introduction

High energy density Li-ion batteries (LIBs) hold the key for enabling the next generation of sustainable and green energy technologies[5,101–104]. Oxygen-containing cathodes are the main constituents enabling high voltage, high energy density Li-ion batteries. Since graphite is utilized as the negative electrode in most of the commercialized LIBs, electrochemical properties such as energy density and operating voltage of the cells are defined by the choice of cathode materials. For instance, the charge voltage, which is limited by the top of the anion-p bands of the cathode, can be expanded by replacing an oxide ion with polyanions[105]. However, such changes impact the Li-ion intercalation mechanism, electron conductivity and importantly structural stability of the cathode material[106]. Generally, the LIB cathode materials are transition metal oxides or phosphates that are designated as the reservoir of the Li ions in the batteries. Cubic closed packed array of oxygen framework allows for unrestricted shuttling of Li-ions in the layered and spinel phase oxide structures[6]. Also, oxygen atoms coordinate the phosphorous atoms to form $(PO_4)^{-3}$ polyanions, which are the building blocks of the olivine cathodes structure[107]. Structural instability of such oxygen-containing cathodes can lead to release of the cathode lattice oxygen in form of O_2[108]. Extensive oxygen release leads to severe degradation of the cathode performance and jeopardizes the safety of the battery by triggering a thermal runaway event, in which the battery catches fire and rapidly releases a large amount of uncontrolled heat and energy[109]. Thermal runaway events have been observed in several Li-ion battery powered systems ranging from laptop and cell phones to e-cigarettes, headphones, electric vehicles and even airplanes, and have caused serious injuries

to the consumers[68,69]. It was found that the thermal runaway is the outcome of a series of self-progressive exothermic events triggered by an external stimulus such as ambient temperature rise or mechanical impact, or caused by an internal stimulus such as short circuit, overcharge or applied high current rates[70,71]. The occurrence and sequence of these chain of events can vary based on the materials design and the specific conditions that trigger the thermal runaway reaction[72]. The schematic Figure *9A*, schematically illustrates the general mechanisms identified for thermally triggered / overcharge-induced thermal runaway reaction. Prevalently, external causes such as local temperature rise can initialize the undesired reactions that lead to the thermal runaway. If the battery temperature is increased to above 90 °C, the exothermic breakdown of the solid electrolyte interphase (SEI) formed on the graphite anode can further increase the temperature to above 120 °C[109,110]. Meanwhile, the SEI breakdown triggers the side reactions between the unprotected anode and the alkyl carbonate electrolyte, leading to formation of combustible gases such as ethane and methane[109]. At this point the polymer separator will melt down, causing a short circuit between the positive and negative electrodes that rapidly increases the temperature and expands the area of heat dissipation in the battery[105]. Finally, at above 150 °C the oxide cathode material decomposes and releases a large amount of oxygen that can ignite the flammable electrolyte/combustible gases in presence of the accumulated heat and triggers the thermal runaway of the battery[72]. Noteworthy, it has been identified that the thermal runaway reaction can occur without an internal short circuit caused by the separator meltdown. In this case, it is observed that if the temperature of an NMC/graphite battery exceeds 115.2 °C by ambient temperature rise, even without the separator break-down and the resultant short circuit, a chemical crosstalk between the cathode and the anode can release a large amount of heat that increases the temperature to ~800 °C and eventually leads to the ignition of the battery[111]. These observations further stress the significant role of the oxygen

release from the cathode materials in the safety aspects of LIBs[112]. Overcharge-induced failure can be regarded as another scenario for thermal runaway reactions [113,114]. In this scenario, the lithiation of the graphite anode beyond its intercalating capacity leads to deposition of metallic Li on the graphite particles surface[115]. This results in SEI thickening and increased cell resistance, which will lead to Joule heating of the battery components[116]. In addition, the anode/the cathode will become reducing/oxidizing agents by continuous insertion/extraction of electrons and can trigger exothermic side reactions with the unstable electrolyte[117]. Subsequently decomposition of electrolyte will result in combustible gas formation that leads to battery swelling and further increase in the battery resistance[118]. As the temperature increases gradually, the anode SEI decomposition can lead to exothermic reaction of lithiated graphite with the electrolyte that further increases the temperature. Subsequently the overcharged cathode that is highly susceptible to thermal decomposition, will break down and release oxygen [113,114]. This is due to the fact that charging the cathodes beyond the energy of oxygen 2p band structure can generate peroxo-like oxygen species that can form O-O bonds and evolve as O_2 gas (Figure *9B*)[5,66]. Similarly, local heating of the overcharged cathodes can trigger the migration of transition metal cations by breaking TM-O bonds. This leads to O-O bond formation between the undercoordinated oxygen atoms and results in the parasitic oxygen release that is explained in length throughout the article with regards to specific cathode systems (Figure *9C*) [62,63,119–121].

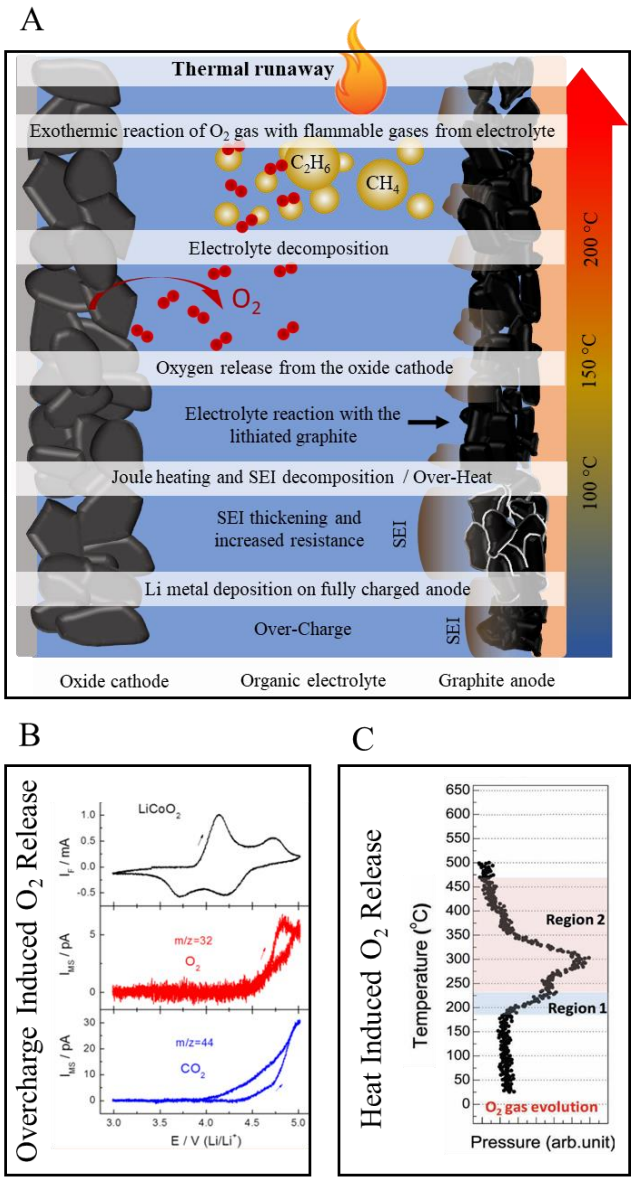

Figure 9. (A) Schematic illustration of the chain of events in a thermal runaway reaction. (B) Mass spectroscopy results demonstrating two possible routes for oxygen evolution from cathodes demonstrating O_2 release from $LiCoO_2$ when charged over 4.4 V, which is beyond the energy level of the O-2p bands in layered oxide cathodes: Reproduced with permission.[66] Copyright 2014, American Chemical Society. (C) Oxygen release during thermal decomposition of charged NMC cathodes as a result of hybridization of undercoordinated oxygen atoms accompanied with spinel and rock-salt phase transformations: Reproduced with permission[62]. Copyright 2012, Wiley-VCH.

Employing a range of characterization techniques at the bulk-scale such as *in-situ* calorimetry[112,122], in–operando high energy synchrotron X-ray tomography and radiography[123,124], it was discovered that the onset temperature and the extent of the thermal runaway reaction is highly dependent on the type and composition of the positive electrode materials[112]. Therefore, the cathodes oxygen release phenomenon have been closely investigated by various means such as thermal analysis[73], time resolved x-ray diffraction (TR-XRD)[125], Raman spectroscopy[85,126–128], *in-situ* differential electrochemical mass spectroscopy (DEMS)[66,129,130], x-ray absorption spectroscopy (XAS)[62,131–135], *in-situ* transmission electron microscopy (TEM)[98,99,136–138] and computational modeling [139,140]. The methods that have been employed for studying the LIBs thermal runaway and cathodes degradation reaction are schematically depicted in the Figure *10*.

Despite the numerous challenges associated with studying the cathode materials such as the structural complexity of the cathode materials[141,142], particle to particle variation caused by gradient state of charge in the electrodes[98,143], the interplay of several degradation mechanisms[67,144] and the sensitivity to various experimental conditions such as the atmosphere[145,146] and electron probe[14,147,148], great progress in understanding and improving their structural stability have been achieved in the past few years. However, the oxygen release from cathode materials still remains as one of the key degradation issues of oxygen-containing cathodes. Thus, herein we have reviewed and summarized the oxygen release degradation mechanisms of the widely used cathode materials such as (1) layered $LiMO_2$ (M = Fe, Mn, Co) cathodes; (2) spinel LiM_2O_4 (M=Ni, Mn) cathodes; (3) olivine $LiMPO_4$ (M = Fe, Mn, Co) cathodes; and (4) Li-rich NMC cathodes. It is concluded that the O_2 evolution is a complex mechanism that is influenced by many parameters such as state of charge (SOC), morphology and size of the particles, chemical composition and atomic arrangements of the cathodes. Additionally, proposed solutions and approaches utilized to

improve the cathodes degradation and alleviate the oxygen release reaction are categorized and reviewed in the following sections.

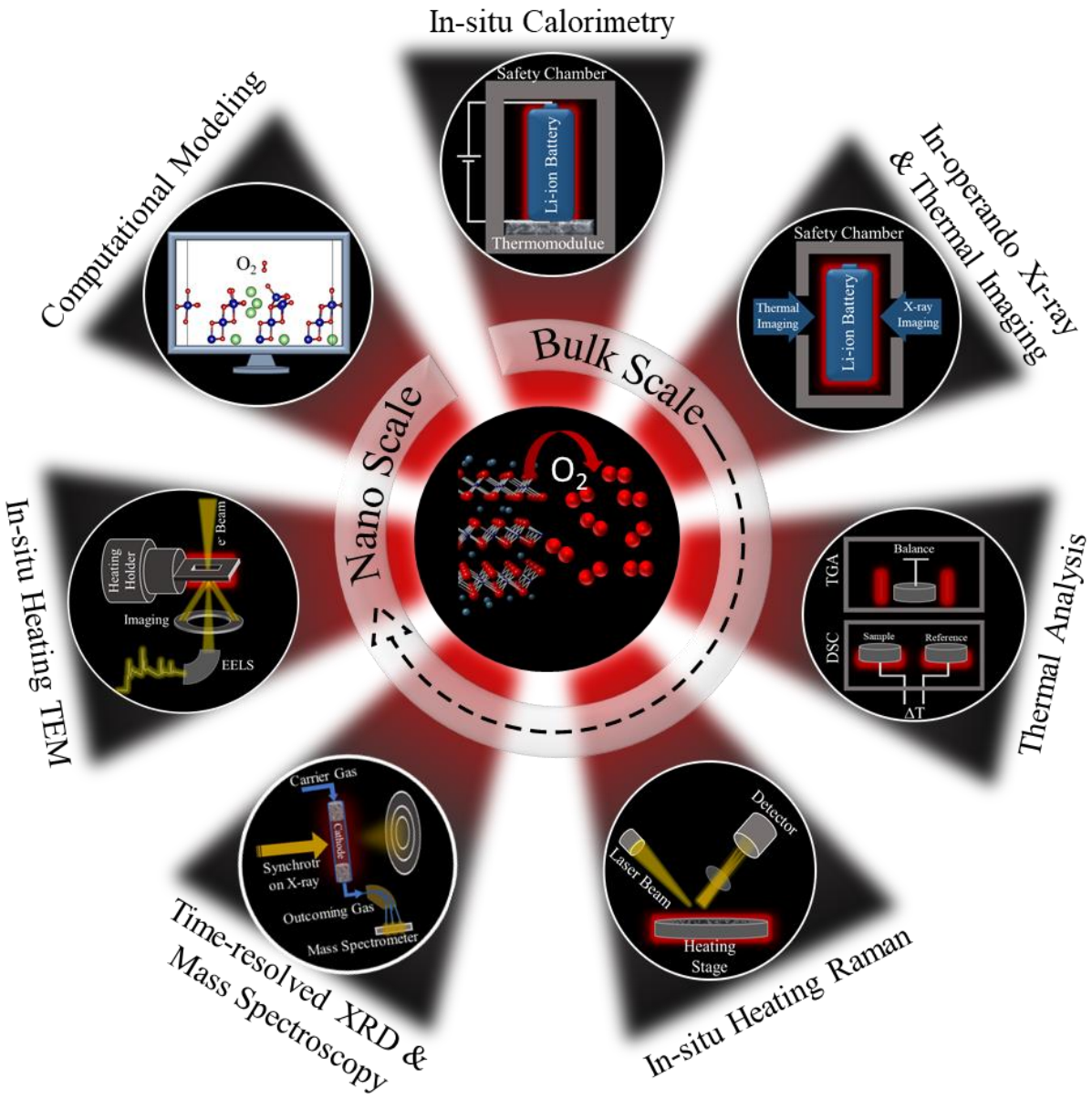

Figure 10. Schematic illustration of the methods used to study the oxygen-release induced degradation of cathode materials ranging from bulk to nanoscale

3.2. Mechanisms of Cathodes Degradations

3.2.1. Layered Oxide Cathodes

$LiMO_2$ (M = Co & Ni). Layered oxide cathode materials that enabled the commercialization of Li-ion batteries are composed of cubic close packed (CCP) oxygen arrays with metal ions occupying octahedral sites, which form consecutive LiO_2 and MO_2 layers[149,150]. Isostructural $LiCoO_2$ and $LiNiO_2$ share the crystal structure of α-$NaFeO_2$ with $R\bar{3}m$ space group where the Li/M ratio is 1 or less in these structures. $LiCoO_2$ was proposed by Goodenough before the discovery of Li-ion batteries in 1980's[7]. The reversible shuttling of Li-ions throughout the electrochemical cycling in between the MO_2 layers is the advantageous characteristic of the layered oxide cathodes. However, since there are several phases viable as a function of Li/M ratio, electrochemical delithiation higher than a certain extent can result in irreversible phase transitions, which leads to rapid capacity fading of the $LiMO_2$-based batteries. The charge voltage of the layered oxide cathodes is manually limited by the energy of the top of O-2p bands. This is because charging beyond this limit (ca. 4.6 V) will result in peroxide $(O_2)^{2-}$ formation and release of O_2 and/or insertion of protons into the cathodes structure[5], which has been quantified experimentally[66] (*Figure 11A*). Additionally, high extent of delithiation (high cut-off voltage charging) can promote the glide of partial dislocations, and provides a path for transition metal migration to the Li octahedral sites that leads to formation of the spinel phase[13,19]. Spinel phase formation and oxygen release has been observed primarily at the surface of the cycled particles (*Figure 11B*)[63,119–121]. This is explained by the electrochemically induced Li deficiency at the surface and inhomogeneous Li distribution throughout the cathode particles[45,63]. In addition to cycling induced oxygen release, thermal treatment of the layered oxide cathode results in the structural decomposition of the $LiMO_2$ cathodes[151]. At pristine state, $LiCoO_2$ is known to be stable up to 900 °C, however partial

delithiation results in the formation of under-coordinated oxygen atoms, that can form O-O bonds and release at around 200 °C[73]. The oxygen release reaction results in the formation of the electrochemically inactive phases with less oxygen in their stoichiometry[152]. The following reaction is suggested to explain the oxygen evolution mechanism from Li_xCoO_2.

$$Li_xCoO_2 \rightarrow \frac{1-x}{3}Co_3O_4 + xLiCoO_2 + \frac{1-x}{3}O_2 \quad (9)$$

Additionally, it is suggested that the activation energy of oxygen release is a function of the SOC and the extent of delithiation, so further delithiation reduces the activation energy and further destabilizes the structure[151]. Also, it is shown that increasing the surface area destabilizes the Li_xCoO_2 structure and increases the extent of oxygen release (*Figure 11C*)[152,153]. Recently, utilizing *in-situ* heating TEM, the effect of particle surface fraction on the thermal instability of $LiCoO_2$ was explained[1] (*Figure 11D*). The results based on scanning transmission electron microscopy and electron energy loss spectroscopy (STEM/EELS), together with ab-initio molecular dynamic simulation (AIMD) revealed that oxygen release reaction is dominant at the surface of Li_xCoO_2 particles, in specific facet terminations. Also, a two-step phase transition that results in the sequential formation of spinel and rock-salt phases at the surface of Li_xCoO_2 particles was identified. Therefore, based on the experimental observations the following decomposition reaction for Li_xCoO_2 was proposed.

$$Li_xCoO_2 \text{ (layered)} \longrightarrow Li_xCoO_2 \text{ (layered)} + Li_xCo_{3-x}O_4 \text{ (spinel)} + \varepsilon O_2 \longrightarrow Li_xCoO_2 \text{ (layered)} + Li_xCo_{3-x}O_4 \text{ (spinel)} + Li_xCo_{1-x}O \text{ (rock-salt)} + \delta O_2 \quad (10)$$

where, ε and δ values depend on the surface facet termination and particle morphology. It has been identified that such phase transitions generate a stress field at the surface of cathode particles, which can affect the oxygen evolution kinetics. In particular, by including elastic energy density

to the free energy functional describing the oxygen release, an alteration of oxygen release at the rock-salt/gas-phase interface can be observed[139].

Moreover, owing to thermodynamic instability of unpaired e_{2g} electrons in high valence Ni ions and Jahn-Teller distortion phenomenon, Li_xNiO_2 is even more structurally unstable compared to Li_xCoO_2[73]. Meaning that at the same SOC, a relatively lower temperature is required to trigger the oxygen release reaction in Li_xNiO_2[154]. Interestingly, thermal decomposition of Ni based cathodes has been shown to proceed to the extent that pure Ni nano-particles form on the surface of the cathodes at elevated temperatures[98]. These observations, carried out by *in-situ* heating TEM technique, further reveal the higher extent of oxygen release in the thermal decomposition reaction of Ni based layered oxide cathodes.

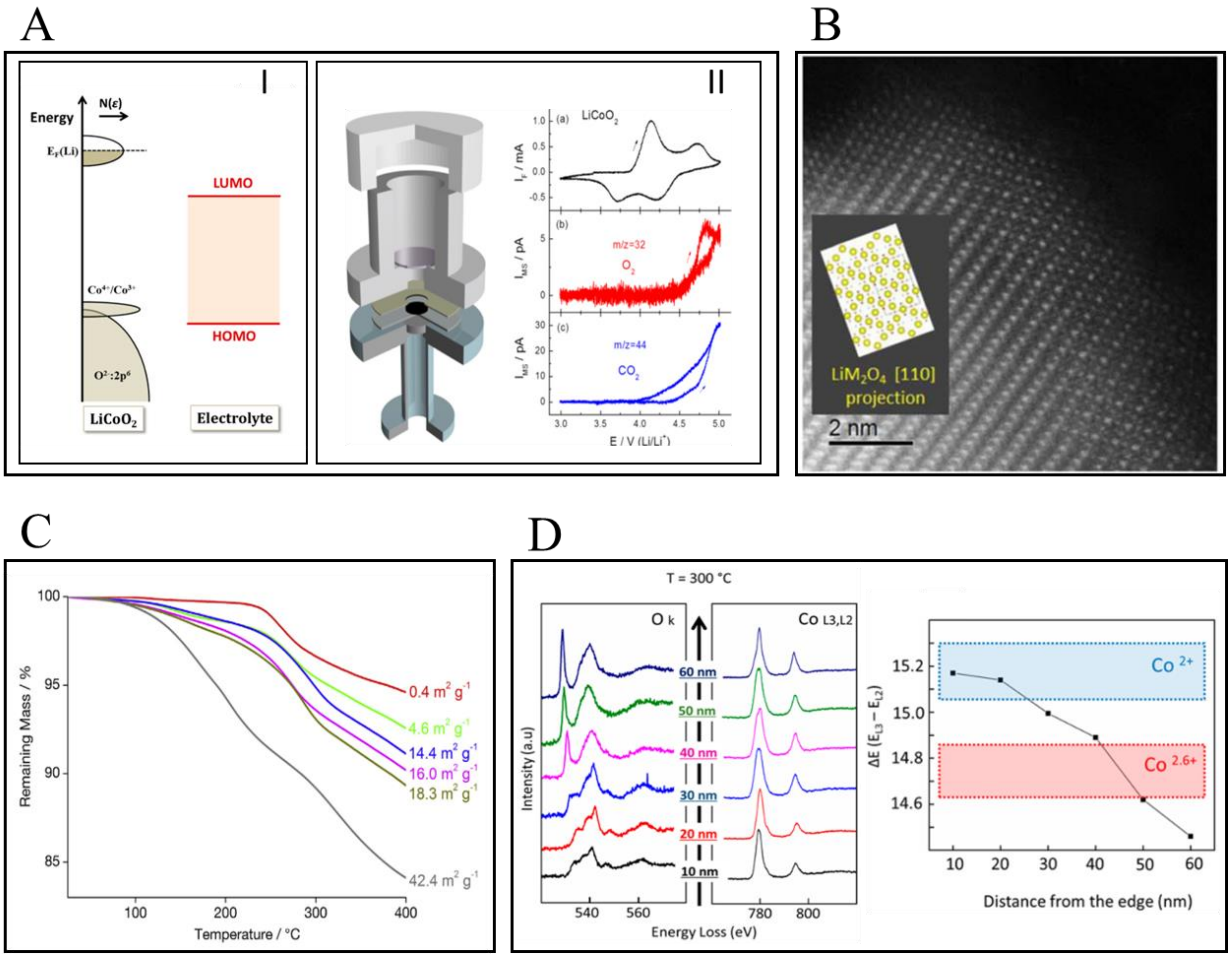

Figure 11. General depiction of the O_2 release mechanisms for $LiCoO_2$ cathodes (A) (I) Schematic energy diagram of $LiCoO_2$ and Li, with respect to the highest occupied molecular orbital (HOMO) and lowest unoccupied molecular orbitals (LUMO) of a carbonate-based electrolyte: Reproduced with permission[5]. Copyright 2013, American Chemical Society , (II) experimental illustration of oxygen release at overcharge condition captured by DEMS experiment: Reproduced with permission[66]. Copyright 2014, American Chemical Society. (B) Surface degradation and phase transition of $LiCoO_2$ upon cycling: Reproduced with permission[63]. Copyright 2017, Electrochemical Society. (C) Thermal analysis results demonstrating the effect of active material surface area on the thermal decomposition extent of Li_xCoO_2: Reproduced with permission[152]. Copyright 2014, Elsevier. (D) *In-situ* EELS results showing the role of the surface area on the thermal instability of Li_xCoO_2: Reproduced with permission[1]. Copyright 2017, American Chemical Society.

$LiNi_{1-x-y}Co_yAl_xO_2$ (NCA) and $LiNi_{1/3}Co_{1/3}Mn_{1/3}O_2$ (NMC). To improve the structural and thermal stability of high capacity layered oxide cathode materials, alloying approach has been regarded as a promising solution. To this end, $Li(Ni_xMn_yCo_z)O_2$ (NMC) and $Li(Ni_{0.8}Co_{0.15}Al_{0.05})O_2$ (NCA) cathodes were successfully synthesized and commercialized[155]. The NCA and NMC cathodes are considered as solid solutions of $LiNiO_2$, $LiCoO_2$ and $LiMnO_2$ that retain the layered $R\bar{3}m$ structure[9]. These materials have superior properties such as better Li-stoichiometry (decreased cation mixing in Li layer), improved electrochemical performance and higher thermal stability compared to $LiNiO_2$ and $LiCoO_2$[75–77]. Therefore, they are dominating the market of high capacity and large scale Li-ion batteries, such as electric vehicles[9,78,79]. The redox active centers in NMC and NCA cathodes are Ni and Co ions and the oxidation of transition metals proceeds by oxidation of Ni^{2+} (NMC) and Ni^{3+} (NCA) to Ni^{4+}, followed by oxidation of Co^{3+} to Co^{4+}. Mn and Al do not participate in the redox reaction and act as structural stabilizers[74].

Here, we categorized the identified structural degradation mechanisms of the NMC/NCA cathodes in three categories as follow; (1) cationic migration and phase transformation[12,49–51]; (2) oxygen release reaction[56]; (4) Li redistribution and extraction[55]; (4) inter/intragranular cracking and fragmentation[57–59]. A representative figure from each degradation mechanism is shown in *Figure 12*. It should be emphasized that although these phenomena are casted into distinct groups, their occurrence are highly corelative and often happen as a chain of events[156,157]. Migration of transition metals (*Figure 12A*) from their octahedral sites into the alternating Li octahedral sites upon excessive Li-deintercalation (increased formation of Li vacancies) and/or temperature rise, is regarded as an initial step in the structural degradation of the NMC/NCA cathodes[49,60]. Such atomic migration triggers the phase transition of the layered ($R\bar{3}m$) structure to the $LiMn_2O_4$-type spinel phase ($Fd\bar{3}m$) and results in oxygen release reaction (*Figure 12B*)[12,61,62]. TEM investigation

on the charged NMC cathodes has shown that Ni is the first cation that migrates to the Li layer and thus has a large contribution on the structural instability of NMC cathodes[51]. *In-situ* heating STEM/EELS experiments also demonstrated that upon increasing the Ni content, oxygen release and structural degradation are facilitated and occur in lower temperatures[136]. Similarly, in-situ X-ray absorption near edge spectroscopy (XANES) analysis on NCA and NMC cathodes have concluded that Ni is the first cation that undergoes the valence reduction in charged NCA and NMC cathodes[62]. It is also suggested that the migration pathways of Ni and Co to the adjacent Li octahedral sites are different. For instance, although Co ions pass through the nearest neighbor tetrahedral sites to migrate into the octahedral Li sites, the migration of Ni ions into the Li layers does not involve the occupation of the adjacent tetrahedral positions and occurs directly from the transition metal slabs to the Li sites, since Ni ions are not stable in the tetrahedral sites[51,62,158,159]. Although both routes lead to the $LiMn_2O_4$-type spinel phase formation, continued migration of Ni ions into Li octahedral sites will lead to the formation of the MO-type rock-salt ($Fm\bar{3}m$) phase. However, Co atoms prefer to migrate to the Li tetrahedral sites and form Co_3O_4 spinel phase that has a higher oxygen stoichiometry compared to the MO type rock-salt phase[160]. Additionally, employing extended X-ray absorption fine structure (EXAFS) analysis on heated NMC cathode, it was concluded that while local coordination of Ni corresponds to $LiMn_2O_4$-type spinel, local coordination of Co transforms to Co_3O_4 spinel type that is a more stable structure. As such, while $LiMn_2O_4$-type spinel structure around Ni cations transfers to rock salt NiO at 350 °C, transition from spinel Co_3O_4 to rock-salt CoO was not observed up to 500 °C. Furthermore, the formation of pure Ni nano particles at the surface of NCA cathodes during *in-situ* heating TEM experiments denotes to a higher structural stability around Co sites compared to Ni sites[98]. These explain the underlying reasons for increased oxygen release extent by increased Ni content in the cathode

composition. Based on the EXAFS analysis Mn cations' environment is thermally stable up to about 400 °C, which is due to the stability of Mn^{4+} in the octahedral sites that contributes to the stability of NMC structure. AIMD simulation on the single oxygen atoms in NMC structures with various local coordination structure units (LCSU), elucidated that the oxygen atoms that have more Ni in their LCSU are highly unstable, and oxygen atoms in such LCSUs are more prone to break bonds with the transition metals and release as O_2[140]. However, the higher number of Mn atoms in LCSU increases the bonding stability of O-TM drastically. These observations were in accordance with the previously reviewed experimental data suggesting the local instability sequence of Ni >> Co >> Mn in NMC structures[51].

In addition to the chemical composition, particle size and morphology are important factors in determining the thermal stability of NMC and NCA cathodes[62,161,162]. Employing analytical electron microscopy investigations, it has been suggested that subsequent to electrochemical cycling Li deficiency at the surface layer is responsible for O1 phase formation in the outmost surface regions that causes the surface instability of the cathode particles[163]. Also, the presence of the undercoordinated atoms at the surface, and direct contact of cathode surface with the electrolyte are among the reasons for surface instability of cathode materials[164]. Additionally, recent reports clarified that the surface phase transition is facet dependent. Meaning that, due to the higher surface energy and higher concentration of under-coordinated oxygen atoms of some facet terminations, the oxygen release and the phase transitions are more favorable to occur in specific facets[93,94,165].

Redistribution of Li within the cathode particles has also been observed in the early stages of the thermal decomposition in NMC samples[55], which eventually leads to Li extraction in form of Li-based surface protrusions upon increased duration of high temperature exposure. The Li-based protrusions are in the shape of lumps or whiskers that resemble the morphology of Li-

dendrites that grow on Li metal anodes[55]. Cracking and fragmentation of cathode materials are identified as other degradation mechanisms that occur due to the generated strain during the phase transitions and oxygen release reaction[164]. This degradation results in the rapid capacity fade and failure of the battery due to the lost contact and inactivity of the detached particles. The cracking of the cathode particles has been observed in both intragranular regions (inside the single crystal primary grains and particles) and in the intergranular spaces (in the grain boundaries and in between the primary particles), as demonstrated in the *Figure 12C* and *D* respectively. High cut-off voltage cycling leads to formation of high density of intragranular cracking. It was proposed that, large strain associated with high extent of delithiation/lithiation cannot be accommodated by highly packed primary particles, therefore inhomogeneous mechanical stress applied on each primary grain is released by formation of the dislocations. To reduce the accumulated strain in the dislocation cores, Li and O release from the area (*Figure 12C*). Therefore, the dislocation cores gradually evolve into premature cracks by further electrochemical cycling. In this condition some of the lattice spacing in (003) direction abruptly increase from 0.48 to about 0.8 nm. Finally, the premature cracks turn into complete cracks that lead to fragmentation and dissociation of the cathode grains[57,59]. Moreover, the intergranular cracking is known be the result of inhomogeneous lattice contraction and expansion in repeated cycling at high cut-off voltages (4.7 V)[58]. Such contraction and expansion of the primary particles will lead to the cracking and disintegration of primary grains and loss of contact of the active materials. It was also suggested that the phase transformation and oxygen release reaction as a result of high temperature exposure could lead to the accumulation of tension stress in the grain boundaries resulting in intergranular cracking (*Figure 12D*)[67,164].

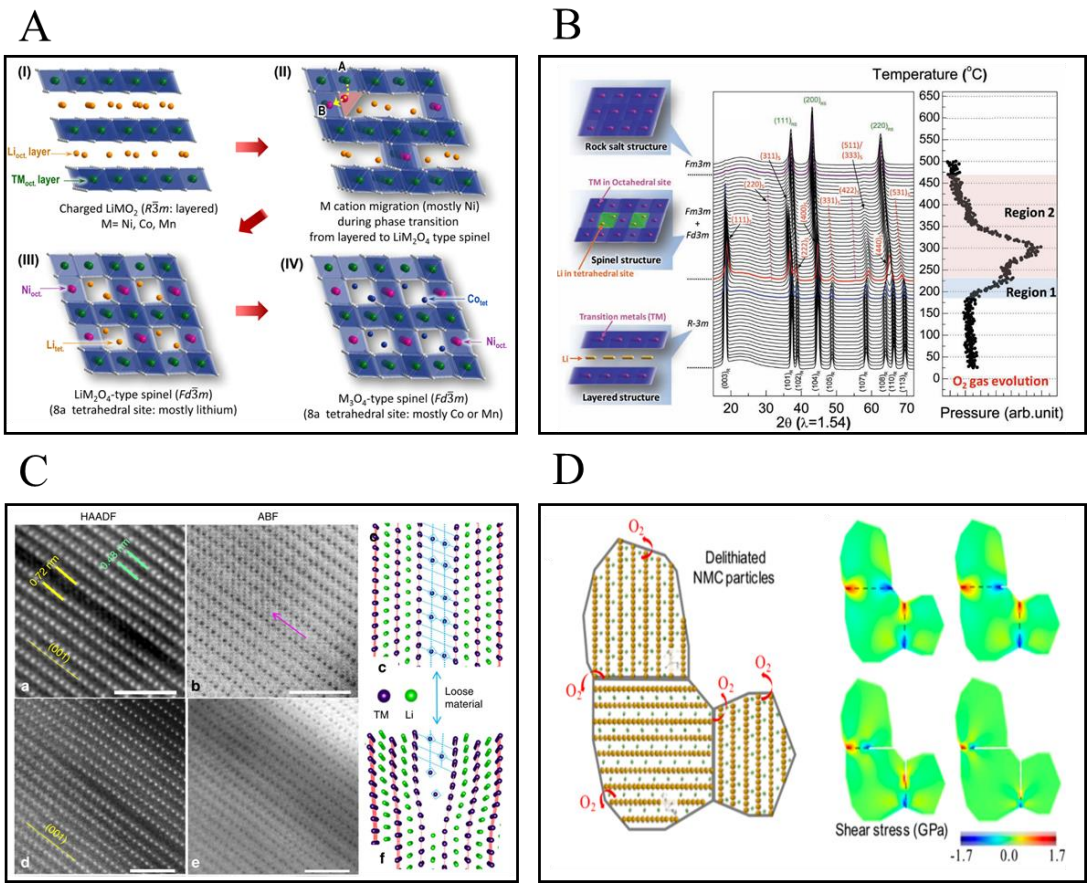

Figure 12. Demonstration of NMC/NCA structural degradations and oxygen release mechanisms. (A) Schematic illustration of cationic migration and structural reconstruction: Reproduced with permission[161]. Copyright 2014, American Chemical Society. (B) Time resolved X-ray diffraction/mass spectroscopy (TRXRD-MS) results correlating the structural reconstruction to the oxygen release phenomenon: Reproduced with permission[62]. Copyright 2012, Wiley-VCH. (C) Atomic resolution image of intragranular crack formation in overcharged NMC structure: Reproduced with permission[57]. Copyright 2017, Springer Nature. (D) Finite element modeling of sheer stress in the grain boundaries of NMC cathodes leading to the intergranular cracking of cathode particles: Reproduced with permission[67]. Copyright 2018, American Chemical Society.

3.2.2. Spinel Structured Cathodes

Reversible Li intercalation in the spinel phase $A(B_2)X_4$ compounds was discovered by Thackeray and Goodenough[166]. In these compounds, A and B refer to the cations in the tetrahedral (8a) and octahedral (16d) sites in a cubic ($Fd\bar{3}m$) structure respectively, and X anions that form a cubic

close packed structure occupy 32e sites. In this structure, only 1/8 and 1/2 of interstitial tetrahedral and octahedral sites are occupied by A and B cations, which enables unrestricted shuttling of Li ions through the vacancies[167,168]. Spinel phase cathodes are one of the main candidates for the next generation of large scale energy storage systems, due to the relatively high energy density (607 W h Kg^{-1}), high ionic and electronic conductivity (10^{-6} and 10^{-4} S cm^{-1} respectively), cost effectiveness (~10 \$ kg^{-1}) and non-toxicity[169]. The main challenge limiting the widespread use of these cathode materials is the rapid capacity fading, particularly at elevated temperatures[170–172]. Mn dissolution, activated by Jahn-Teller distortion of Mn ions at the surface of charged LMO particles, and subsequent deposition on the negative electrode surface, is known as the origin of this problem (*Figure 13A*)[170]. The Mn dissolution is also associated with the parasitic oxygen release reaction[173]. Upon charging, LMO structure is destabilized and structural distortion leads to the Mn_3O_4 phase formation. This phase transition is associated with the oxygen release and formation of soluble Mn^{2+} ions (*Figure 13B*)[173]. Slight increase in the temperature rapidly increases the rate of Mn dissolution and correlative oxygen release. Under such conditions, structural transformation of spinel $LiMn_2O_4$ to the distorted structure and finally to the layered Li_2MnO_3 like (C2m) structure will occur, as identified by atomic resolution STEM imaging (*Figure 13C*)[174]. Nonetheless, spinel cathodes has a higher thermal stability compared to the layered oxide cathodes, and the release of oxygen has a higher onset temperature of ~ 375 °C in de-lithiated $Li_xMn_2O_4$ cathodes[169].

Another member of the spinel cathodes family is $LiNi_xMn_{2-x}O_2$ (LNMO), which has a higher operating voltage (4.7 V vs Li/Li^+) and alleviated Mn dissolution issue. However, unlike $LiMn_2O_4$ that is thermally stable up to 375 °C, oxygen release can occur below 300 °C in charged LNMO cathodes[175]. This is due to the presence of highly unstable Ni ions in this structure. Depending on

the synthesis annealing temperature, Mn^{4+} and Ni^{2+} distribution in the LNMO crystal structure can have short-range order, or the Ni and Mn cations can be randomly distributed (long range order). Such structural variations affect the thermal stability of spinel LNMO cathodes. The LNMO cathodes with long range order have demonstrated a superior thermal stability compared to the short range ordered structures (*Figure 13D*)[175].

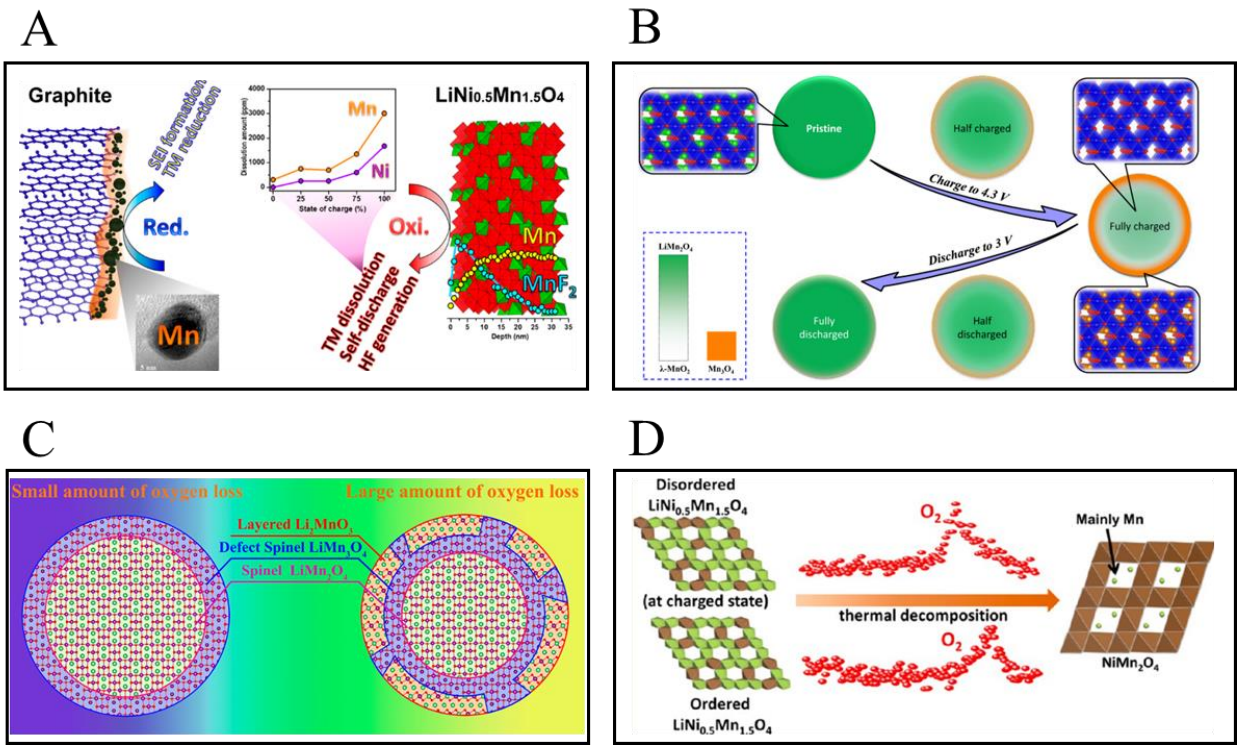

Figure 13. Schematic demonstration of the oxygen release and correlated structural degradations in the spinel phase cathodes. (A) Schematic demonstration of the mechanism of Mn dissolution from LMO cathodes: Reproduced with permission[170]. Copyright 2013, American Chemical Society. (B) Partially reversible formation of Mn_3O_4 phase at the surface of LMO cathodes accompanied by oxygen release reaction: Reproduced with permission[173]. Copyright 2014, American Chemical Society. (C) Schematic demonstration of the effect of cut-off voltage/thermal decomposition temperature on the extent of oxygen release and sequence of phase transition in the spinel LMO cathode: Reproduced with permission [174]. Copyright 2017, American Chemical Society. (D) Higher O_2 release onset temperature of the ordered LNMO spinel cathodes that demonstrates the superior thermal stability of ordered structure compared to the disordered structure: Reproduced with permission[175]. Copyright 2014, American Chemical Society.

3.2.3. Olivine Structured Cathodes

Olivine structured cathode materials with the composition of $LiMPO_4$ (M=Ni, Co, Mn, Fe) were developed as safe alternatives for the layered oxide cathodes[176,177]. It is believed that the tetrahedral $(PO_4)^{3-}$ anions have a very strong covalent P-O bonds that do not allow for oxygen release upon exposure to high temperatures[178]. $LiFePO_4$ is known as a very safe and thermally stable cathode material[179] that has been commercialized for EV applications due to high capacity (~170 $mAhg^{-1}$), flat potential profile through the charge discharge process (caused by first order reaction during the redox process), very high thermal stability (600-700 °C)[178], earth crust abundant constituent and low toxicity of the raw materials. However, because of the sluggish kinetics of Li ion transfer, poor electrical conductivity and low operating voltage, scientific efforts have been stirred towards other phosphate cathodes such as $LiCoPO_4$ and $LiMnPO_4$[180–182]. Despite the structural similarities, these cathodes show a very different thermal stability characteristic. As such, thermal analysis and *in-situ* XRD results demonstrate that while $LiFePO_4$ is thermally stable at a wide range of Li fraction, Li_xCoPO_4 and Li_xMnPO_4 decompose and release oxygen when exposed to elevated temperatures[178,183]. Therefore, it is noted that the constituent transition metals play an important role in defining the thermal stability of the olivine cathode materials. Through high-throughput ab-initio molecular dynamics and first principle calculations[177,184], it has been concluded that the ligand field theory (LFT) is governing the thermal stability of the olivine structured cathode materials. This means that the half-filled high spin electronic configuration that consists of five parallel spin electrons is a highly stable configuration for transition metals in olivine structures. Therefore, when $LiFePO_4$ is in its delithiated state ($FePO_4$), Fe ions with a valence state of 3^+ have a stable half-filled high spin configuration that stabilizes the structure. Nevertheless, Co and Mn phosphates have six and four electrons in their valence orbitals at charged state, respectively. This

is an unstable configuration and results in their valence reduction at high temperatures[184]. In fact, high-throughput density functional theory (DFT) calculations have shown that thermal decomposition onset temperature of some specific olivine cathodes can be lower compared to their layered oxide counterparts[177]. Their findings suggest that there is a trade-off between the intercalation voltage and thermal stability of these class of cathodes. Therefore, a high voltage Li-ion intercalation reaction in $LiMnPO_4$ and $LiCoPO_4$ results in a very unstable delithiated structures.

3.2.4. Li-Rich Cathodes

Li-rich NMC cathodes that are discovered by partial cationic substitution of transition metals with extra Li ions in layered oxide cathodes, are considered as the next milestone in the advancement of the positive electrodes in the Li-ion batteries[185]. Li-rich cathodes that can achieve capacities greater than 250 $mAhg^{-1}$ when cycled between 2-4.8 V (Figure *14A*)[81,186,187] have a complex crystal structure denoted in three opposing ways: (1) a solid solution with the original ($R\bar{3}m$) layered structure, where some of the extra Li ions are occupying the transition metal sites[188]; (2) a nano-composite of the C2/m Li_2MnO_3 and the $R\bar{3}m$ $LiMO_2$ with the general formula of xLi_2MnO_3-$(1-x)LiMO_2$[87,189], known as Li-Mn rich (LMR) cathodes; (3) a single phase solid solution C2/m Li_2MnO_3 phase with random Li/TM mixture (Figure *14B*)[88]. Despite the favorable high capacity, the industrial utilization of the so-called Li-rich cathodes is not realized due to poor capacity retention, voltage fade and low Columbic efficiency[90,190–192]. In general, the two-step plateau that is observed in the voltage profile of Li-rich cathodes has been explained by the participation of oxygen species in the electrochemical reaction known as the anionic redox reaction[193]. The anionic redox reaction eventually results in the release of lattice oxygen and transition metal migration, which leads to the structural evolution, cracking, capacity and voltage fade issues[194–197].

Employing DFT calculations, it has been understood that due to formation of Li-O-Li bonds that only exist in the Li-rich cathodes, density of states (DOS) increases near the Fermi level of oxygen ions (Figure *14C*) and results in evolution of labile electrons. Since there is a large energy gap between O 2p orbitals and Li 2s orbitals, these labile electrons are unhybridized, so their energy level is not dependent on the cationic redox reaction[82]. Therefore, anionic redox can occur simultaneously or subsequent to the cationic redox reaction depending on the electronic band structure of the metal cations. Anyhow, labile oxygen electrons can hybridize with other oxygens, forming O-O dimers[198]. The oxygen dimerization that has a low kinetic barrier results in the formation and release of molecular O_2 and irreversible transition metal migration into Li vacancies[199]. The formation of O-O dimers occurs only when oxygen atoms rotate to overlap their orbitals, which requires broken metal-oxygen bonds[84,86,193]. As such, it is suggested that the degree of cation-anion covalent bonding is a key parameter in stabilizing the structure and retaining the reversibility of the anionic redox reaction. Hence, Li-rich cathodes containing 4d transition metals such as Li_2RuO_3 have been proposed for stabilized oxygen redox reaction[188,200]. These structures show a superior structural stability and less gas release compared to 3d-tranistion metal Li-rich NMC cathodes, but at the expense of significantly higher material cost. It is also suggested that the substitution of inactive ions such as Mn^{4+} with electrochemically active ions (e.g. Ru^{+}), to fully compensate for the Li^{+} charge transfer, alleviates the anionic charge compensation and stabilizes the structure[135]. On the other hand, another research based on Raman spectroscopy claimed that the O-O vibration that is presents in peroxo-like $(O_2)^{n-}$ species were not observed in the charged Li-rich cathodes indicating that O-O dimers were not formed during the cycling[85]. Instead, based on resonance inelastic X-ray spectroscopy (RIXS) analysis it was concluded that, upon charging the Li-rich cathodes to over 4.5V, electron holes are formed on the oxygen atoms that are locally

coordinated with Mn^{4+}/Li^{+} ions. Electron hole formation over these O atoms destabilize their ionic bonds with the local Mn^{4+}/Li^{+}, which results in the oxygen release and structural degradation of the cathodes. Moreover, utilizing atomic resolution imaging, it has been shown that due to the loss of excess Li ions upon electrochemical cycling of Li-rich cathodes, monoclinic (C2/m) structure transforms to hexagonal ($R\bar{3}m$) phase, which then evolves into the spinel ($Fd\bar{3}m$) structure (Figure *14D*)[92]. Such monoclinic to spinel phase transition accounts for the voltage decay that is normally observed in Li-rich cathodes and accompanies the oxygen release reaction. This phase transition can also lead to cracking and fragmentation of the cathode particles that further deteriorates the capacity[156,201].

Thermal decomposition of the Li-rich cathodes is studied and compared with their conventional layered oxide counterparts. Thermal decomposition of the Li-rich cathodes occurs at around 190° C for the half charged $Li[(Ni_{0.5}Mn_{0.5})_xCo_y(Li_{1/3}Mn_{2/3})_{1/3}]O_2$ ($x + y = 2/3$, $y = 1/12$ and $1/6$) electrodes[202]. However, by charging the cathode to the second plateau where anionic redox reaction is activated, the onset temperature for the exothermic reaction between the cathode and the electrolyte decreases to around 130° C. This is significantly lower than the thermal decomposition temperature of conventional layered oxide cathodes[203]. This is due to the presence of readily oxidized Li-O-Li bonds in Li-rich cathodes, which facilitates the thermal decomposition/oxygen release and decreases the onset temperature of the decomposition of charged Li-rich cathodes. Despite the lower onset temperature of thermal decomposition, the amount of released oxygen is relatively smaller for Li-rich cathodes compared to their conventional layered counterparts[204,205]. This is attributed to the dissimilar phase transition route of the Li-rich and conventional layered oxide cathodes upon thermal decomposition. Although, the $LiNi_{0.8}Mn_{0.1}Co_{0.1}O_2$ sample transforms from the layered phase to the spinel and then to the

rock-salt phase, the Li-rich structure only transform to the spinel phase and then the spinel phase remains stable throughout the thermal treatment process. This difference is due to higher tendency of Ni ions in forming the rock-salt structure as opposed to highly stable Mn ions. Additionally, it has been demonstrated that the sequence and onset of such phase transitions is also dependent on the utilized electrolyte[206].

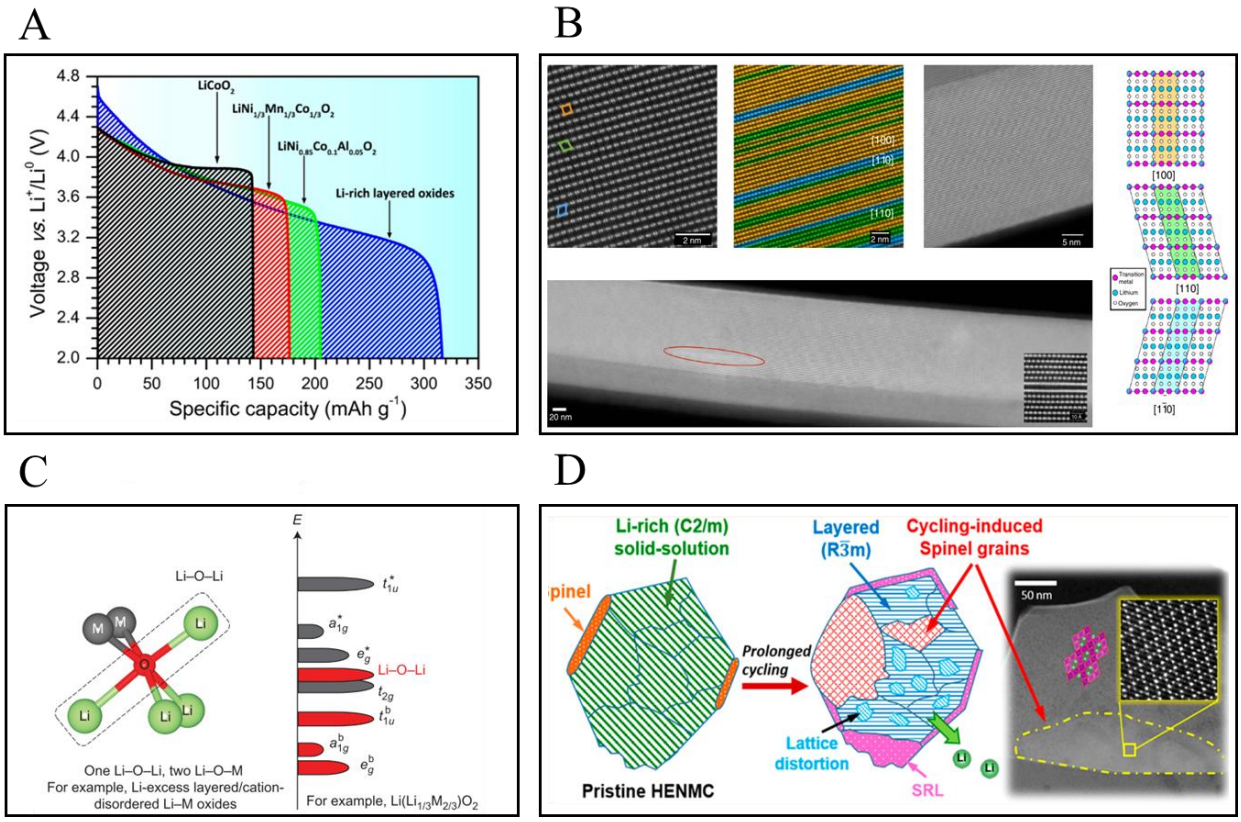

Figure 14. Depiction of the differences in the capacity, redox reaction and degradation mechanism of Li-rich cathode materials compared to conventional layered oxide cathodes. (A) Comparison of voltage profile and electrochemical capacity of the layered oxide cathodes: Reproduced with permission [81]. Copyright 2017, American Chemical Society. (B) Atomic resolution image showing a single phase monoclinic (C2/m) structure of a Li-rich cathode particle: Reproduced with permission[88]. Copyright 2015, Springer Nature. (C) Schematic of local atomic coordination and electron band structure of Li-excess cathodes, that enables the anionic redox reaction: Reproduced with permission[82]. Copyright 2016, Springer Nature. (D) schematic demonstration of the identified

phase transition sequence and structural degradation of Li-rich cathodes: Reproduced with permission[92]. Copyright 2018, American Chemical Society.

3.3. Strategies to Improve the Structural stability of the Cathodes

3.3.1. Chemical Composition Modification

Oxygen release reaction and structural instability of the cathode materials are heavily dependent on the chemical composition of the cathode materials. DFT modeling have demonstrated that the energy of oxygen vacancy formation is a function of the type of transition metal species that are locally bonded with each oxygen atom[140]. As such, modification of the chemical composition of the cathodes have been considered as a promising solution for improving the thermal and structural stability of the cathode materials. In this review, research efforts focused on chemical composition modification as an approach to improve the structural stability of the cathode materials have been summarized in 3 categories; (1) doping; (2) chemical gradient compositions; (3) core shell structures (Figure *15*).

A. Doping. Doping and cationic substitution of transition metals is one of the most widely explored approaches in improving the structural stability of the cathode materials. As such, the effect of the monovalent cations such as K and Na[207–214], divalent ion dopants such as Mg and Zn[215–222], trivalent Fe, Al and Au dopants[196,223–240], and tetravalent cations such as Ti and Ru[241–248] have been studied on the structural stability of various cathode materials. It has been demonstrated that dopants with various valence groups can affect the structure and the properties of the cathode materials in different ways. For instance, it is realized that monovalent and divalent dopants occupy the Li sites in the cathodes structures[249]. Therefore, due to the electrochemical inactivity of the mono and divalent dopant elements throughout the cycling, they remain in the Li slabs acting as pillars that uphold the structural integrity. This phenomenon is known as the “pillar effect”.

Also, the presence of the dopants in Li sites reduces the chances of Li trivacancy formation, hindering the transition metal migration and oxygen release in the delithiated cathodes[250,251]. In addition, it is suggested that dopant ions larger than Li^+ increase the lattice spacings and allow for faster Li-ion diffusion with lower activation energy, thus enable high rate cycling and alleviate structural degradation. Moreover, doping the Li sites with divalent ions such as Mg increases the average charge on the Li sites that decreases the charge on the metal sites, alleviating the lattice distortion and improving the structural stability[252]. Substituting 10% of Co cations with Al is shown to be promising in stabilizing the structure resulting in ~100 °C delay in the thermal decomposition of NMC cathodes [232,253]. Such observation is explained by higher stability of Al ions in the intermediate tetrahedral sites that increases the energy barrier for migration of transition metals and promotes the structural stability[237,238]. Similarly, addition of Fe^{3+} to the spinel LMNO cathodes have shown to improve the thermal stability by alleviating the oxygen release reaction. This is linked to the preferred migration of Fe cations from octahedral sites to Li tetrahedral sites, which stabilizes the Fe_3O_4 type spinel and hinders the oxygen release reaction upon high temperature exposure[196]. In general, trivalent and tetravalent dopants that occupy the TM sites increase the lattice spacings, reduce the bandgap, and increase the electrical conductivity of the cathodes. In addition, through DFT calculations, it was demonstrated that Sb^{3+} doping alters the density of states[236,254]. In this case, the charge around O atoms become more negative in presence of the Sb dopants, which can stabilize the lattice oxygen during electrochemical extraction of Li ions (Figure *15A*)[236].

In addition to cationic substitution, doping of oxygen sites with anions such as F, Cl and S has been carried out in the recent years. Fluorine doping of oxygen sites in Li-rich layered oxide cathodes was shown to improve the structural stability and delay the oxygen release reaction for

~20°C[255,256]. However, a recent DFT study has shown that anionic doping could have conflicting effects on various properties of the cathodes[257]. It has been demonstrated that while F can mitigate Ni migration and improve the cycling stability, it will promote Li/Ni cationic mixing in the synthesis process. On the other hand, while Cl and S alleviate the Li/Ni mixing issue, they adversely affect the structural stability of the cathodes when doped into O sites[257]. Moreover, simultaneous doping of cationic and anionic sites, known as co-doping, is another strategy to improve the structural stability of the oxide cathodes that has been utilized in some of the recent works and should be further explored[258–260].

B. Chemical Concentration Gradient. Another novel approach in designing durable cathode structures without compromising their capacity is the synthesis of chemical concentration gradient cathodes. In these structures, while the core of particles is rich in high capacity elements such as Ni, the structural stability is achieved by increasing the content of the electrochemically stable elements such as Mn at the surface (Figure *15B*)[261]. Thus, the stable Mn-rich surface protects the high capacity Ni-rich core from structural degradation and oxygen release, while maintaining the overall energy density of the material [262–270].

C. Core-shell Composition. Since many unwanted side reactions as well as oxygen release initiate at the cathodes surface, modification of chemical composition of the surface regions without affecting the bulk composition has also been pursued to improve the structural integrity of the cathodes. In this context, incorporation of stabilizing elements such as Al, Zr and Mn in a thin outer layer of cathode particles was suggested to improve the structural stability of $LiCoO_2$ samples[271–276]. Such core-shell structures are generally obtained by coating the cathode particles with a metal containing composition, followed by a thermal treatment that allows for diffusion of coating element into the cathode structure[277]. Additionally, synthesis of dual phase core-shell

cathodes is another approach in improving the structural stability of the cathode materials[278]. For instance, by forming a layer of spinel $LiMn_2O_4$ on a layered Ni rich cathode materials, capacity fading and oxygen release could be mitigated[279]. Moreover, formation of an oxygen-lithium deficient shell was shown to stabilize the structure of Li-rich cathodes. It was illustrated that by uniform distribution of oxygen vacancies at the surface of Li rich NMC cathodes, higher cycling stability and reduction in the release of oxygen at high voltages can be realized (Figure *15C*)[280].

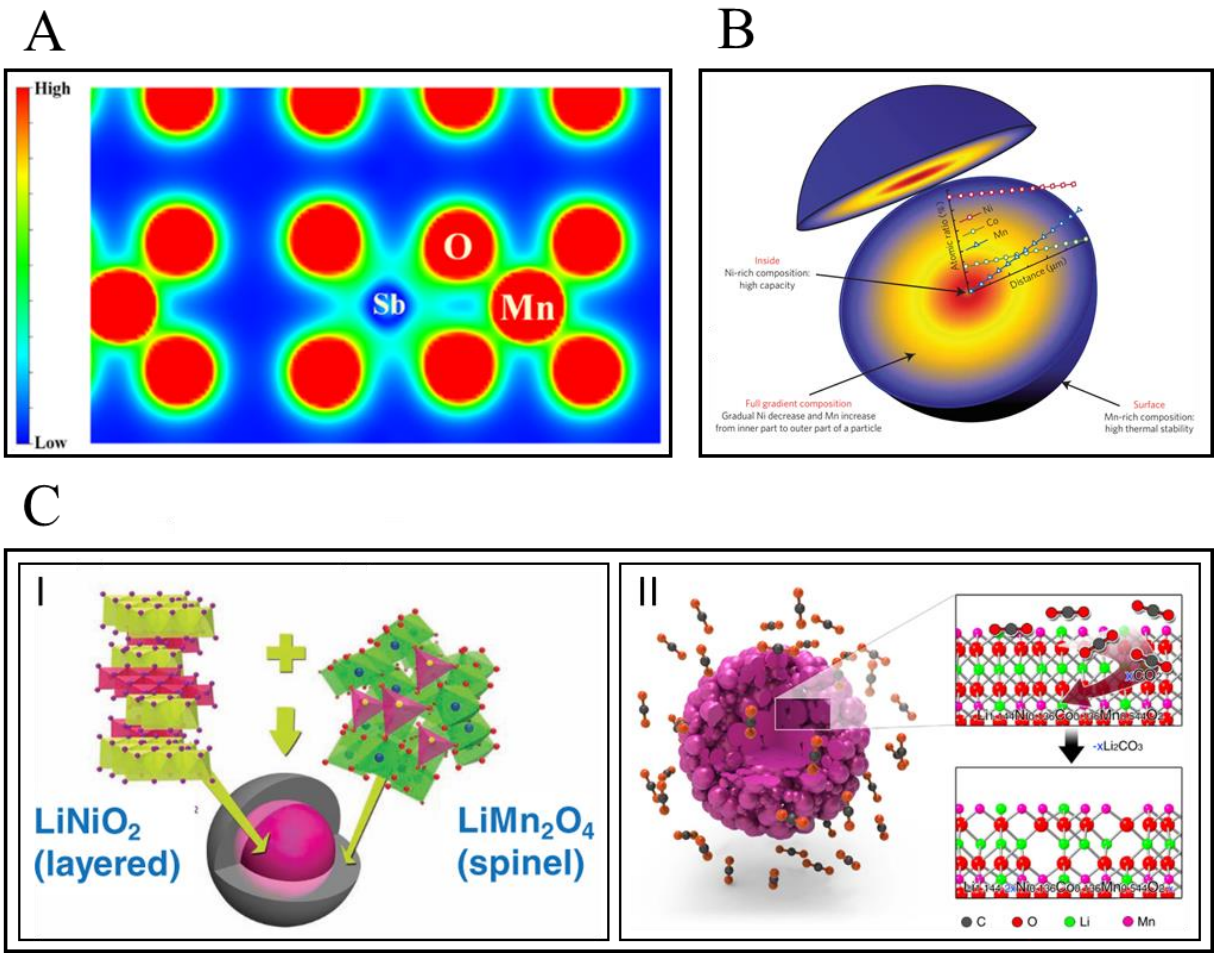

Figure 15. Schematic representation of the chemical composition modification approaches used to improve the structural stability of the cathode materials. (A) Atomic structure of a cationic doped layered oxide cathode: Reproduced with permission[236]. Copyright 2018, American Chemical Society. (B) Schematic illustration of a chemical concentration gradient cathode: Reproduced with permission[261]. Copyright 2012, Springer Nature. (C) Schematic figures representing core-shell

cathode structures: Reproduced with permission [279]. Copyright 2011, Wiley-VCH. Reproduced with permission [280]. Copyright 2016, Springer Nature.

3.3.2. Coating Strategies

Prominent progress in stabilizing the structure of the cathodes and improving their thermal stability were achieved by coating approaches. Since the first breakthrough in improvement of the thermal stability of cathodes, achieved by Cho *el al.*[281], several research groups have investigated the surface coating for hindering the oxygen release reaction and improving the structural stability of cathode materials. Herein, we have categorized the surface coating approaches based on the utilized coating material and will review the mechanisms by which the structural stability is improved in different articles.

A. Phosphate Coating. Aluminum phosphate is the first coating material that was successfully utilized to prevent the thermal runaway reaction in $LiCoO_2$[281]. In this report, it was shown that by charging a pouch cell containing $LiCoO_2$ and liquid electrolyte to 12 V, the cell will experience the thermal runaway reaction and eventually catch fire. However, no indication of thermal runaway and catastrophic failure was detected by exposing the $AlPO_4$ coated $LiCoO_2$ electrode to the same condition. Later on, thickness optimization and identification of the mechanism of retarding the thermal runaway reaction was carried out[282–284]. Utilizing XPS and STEM characterization techniques, it was explained that during annealing, $AlPO_4$ coating on the surface breaks into Li_3PO_4 and $LiCo_{1-x}Al_xO_2$ phases. Formation of Li_3PO_4 that is a lithium conducting phase, reduces the potential at the surface and thus higher structural stability can be achieved in over-charging conditions[284]. Moreover, it was also suggested that the decomposition of $AlPO_4$ and penetration of the Al into the surface of $LiCoO_2$ is contributing to higher structural stability of the coated cathodes (Figure *16A*)[285]. Recently, ALD deposition of $AlPO_4$ layer that allows for a controlled deposition of the coating layer was achieved[286]. Subsequent to the utilization of aluminum phosphate coatings,

the effect of other metal phosphate coatings such as $FePO_4$[287], Li_3PO_4[288–291], $LiMnPO_4$[292], $PrPO_4$[293] and $LiMgPO_4$[294] on the structural stability of the cathodes were explored. Similar to $AlPO_4$, coating of $LiMgPO_4$ was demonstrated to decompose during the calcination process. The decomposition allows for doping the inactive Mg^{2+} into the Li sites at the surface of particles that activates the "pillar effect" during the electrochemical cycling. The remaining phosphate phase inhibits the parasitic oxygen release and other side reactions at the surface of the Li-rich cathode particles leading to improved voltage stability and capacity retention of the battery.

B. Oxide Coating. Parallel to the advancements in utilizing phosphate coatings, researchers explored the effect of oxide coatings on the O_2 release and structural stability of cathode materials. In this approach, magnetron sputtering and atomic layer deposition are the heavily used techniques for deposition of the oxide coatings. In the early investigations, it was observed that the metal oxide coatings such as Al_2O_3 and MgO delay the thermal decomposition reaction and reduce the magnitude of the parasitic exothermic reaction of cathode/electrolyte[295]. Later on, it was demonstrated that a thin coating layer of alumina can greatly enhance the electrochemical and thermal stability of $LiCoO_2$[296,297]. To understand the mechanism of structural stabilization achieved by such oxide coatings, researchers have utilized DFT and ab-initio molecular dynamics calculations to show how the thermal decomposition and oxygen evolution reaction are inhibited by the oxide coatings[298], and also how Li-ions transfer through such coatings[299,300]. It was observed that during electrochemical cycling, Al_2O_3 coating layer is gradually lithiated. Ultimately, the alumina coating transforms to the thermodynamically favorable composition of $Li_{3.4}Al_2O_3$[299]. After reaching to this stable composition, $Li_{3.4}Al_2O_3$ conducts the Li-ions to the cathode structure. Interestingly, first principle calculations also demonstrated that the oxygen release from the cathode can only be suppressed by the lithiated phase of Al_2O_3, which forms naturally when the

alumina coated cathode particles are cycled (Figure *16B*)[298]. Moreover, employing advanced characterization tools such as STEM-EELS, researchers could demonstrate that Al_2O_3 coating can suppress the reduction of transition metal cations at the surface of the cathode particles, which denotes to the suppression of the oxygen release from the cathode surface[301–303]. It was also demonstrated that, upon alumina coating of $LiCoO_2$, a portion of Al from the coating layer diffuses to the surface layer of the cathode. The Al doped $LiCoO_2$ structure is a more stable surface and hinders the oxygen release[304]. Moreover, the contribution of many other metal oxide coatings such as TiO_2[305–307], ZnO[308–311], MgO[295,312] and many more[313–322] are studied on the structural stability of cathode materials. For instance, Cheng *et al.*[323] have compared the performance of Al_2O_3 versus TiO_2 coating on $LiCoO_2$ and have suggested that Al_2O_3 coated cathode has a superior electrochemical performance. They attributed these observations to the difference in the band gap of the coating materials and showed that smaller band gap of TiO_2 results in its participation in the redox reaction and triggering unwanted side reactions. Accordingly, it was suggested that for $LiCoO_2$, the band gap of the coating material should be larger than 3.9 eV. Therefore, MgO coating with 7.8 eV band gap would make a good protective coating for $LiCoO_2$[324].

C. Other Coating Strategies. Aside from phosphate and oxide coatings, the effect of the other coating materials such as polymers[325–327], fluoride coatings[328–332] and two dimensional materials [333] on the structural stability of the cathodes have been explored. Fluoride coatings deposited through ALD technique have been shown to enhance the cycling and structural stability of oxide cathodes under high rate and high voltage cycling conditions. For instance AlF_3 is suggested to prevent the formation of LiF at the surface of the cathodes, thus preventing the impedance rise and Co dissolution[330]. Moreover, $LiAlF_4$ that is shown to be a highly stable compound with high electrical and ionic conductivity was suggested to significantly improve the surface stability of the

Ni-rich NMC cathodes[329]. Polymer coating is another strategy for improving the structural stability of oxide cathodes. Conductive polymer coatings are either applied directly to the surface of cathode particles[334], or employed as a double layer on the oxide and sulphate coating layers[335,336]. Similar to many coating approaches, conductive polymer coatings are suggested to provide a stable interface layer preventing electrolyte side reactions and metal dissolution. Owing to the recent progress in the synthesis of 2D materials and comprehensive understanding of their properties, encapsulation of cathode particles by two-dimensional materials such as graphene and its derivatives are being pursued by researchers. Ultra-thin layers of reduced graphene oxide was firstly used as highly conductive pathways for improving the conductivity of $LiFePO_4$ electrodes[337–339]. Recently, conformal wrapping of reduced graphene oxide (rGO) layers around cathode particles was enabled by employing silane coupling agents[340]. Using such methodologies, facile and scalable coating of highly conductive and chemically inert rGO layers have been achieved that led to improved ion conduction kinetics throughout the electrodes (Figure *16C*). Also structural stabilization of cathodes due to excellent chemical stability of the rGO coating layers is realized by utilizing by graphene-encapsulation of cathode particles[340–342].

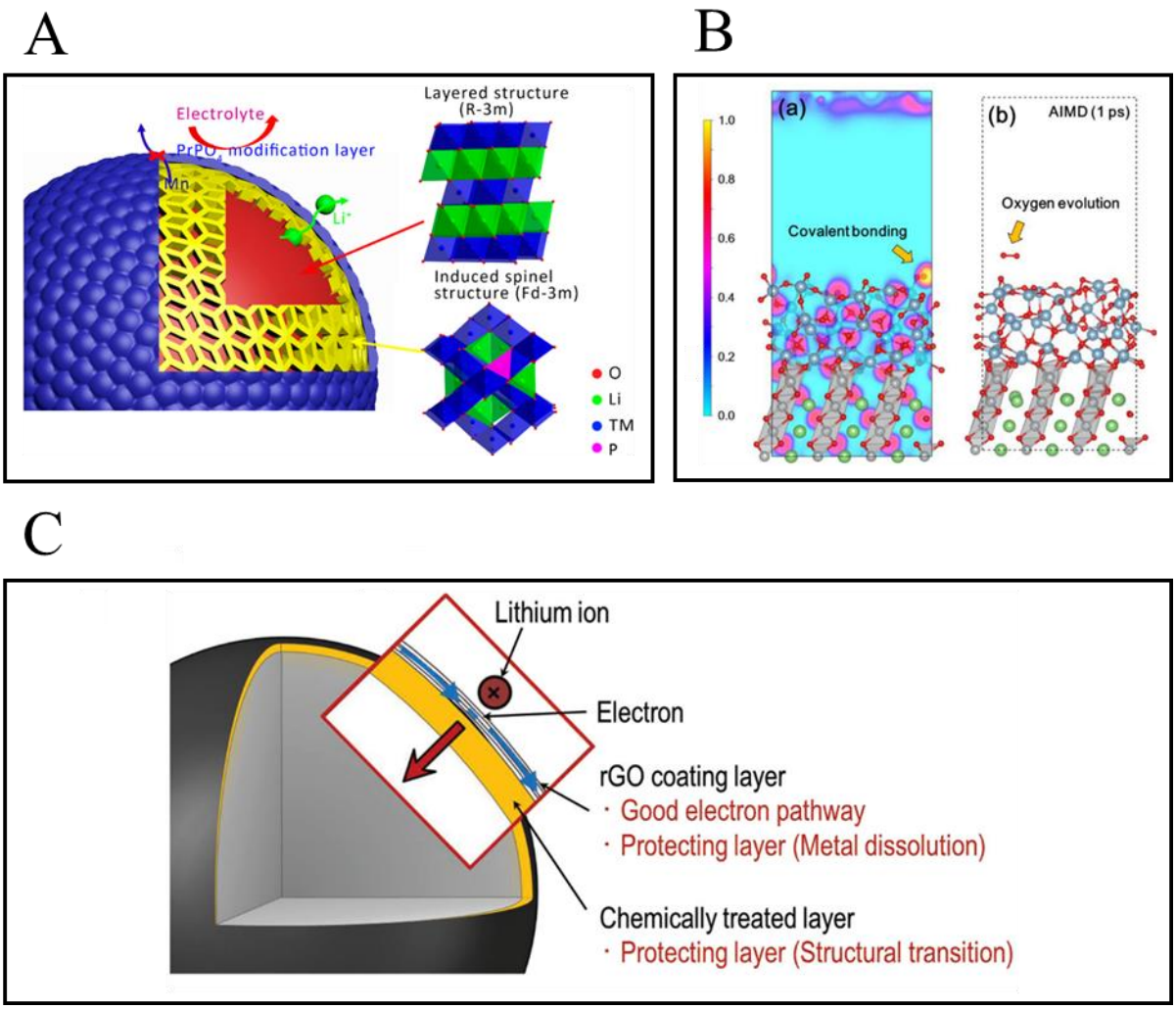

Figure 16. Schematic illustration of coating strategies utilized to improve the structural stability of cathodes. (A) Schematic representation of phosphate coating on layered oxide cathode particles: Reproduced with permission [293]. Copyright 2017, American Chemical Society. (B) Representative AIMD modeling results on the effect of alumina coatings on oxygen release and structural stability of layered oxide cathodes: Reproduced with permission [298]. Copyright 2015, American Chemical Society. (C) Schematic representation of the rGO coating and its effects on the physical properties of the cathode materials: Reproduced with permission [342]. Copyright 2014, Wiley-VCH.

3.4. Summary and Future Prospective

The oxygen release reaction and the correlated structural degradation mechanisms of the cathode materials are not only detrimental to the service life of the Li-ion batteries but also cause the catastrophic failure and thermal runaway events. Herein, we reviewed the recent progress in

understanding and mitigating the parasitic oxygen evolution and the correlated structural degradation of the major cathode materials. In summary, oxygen release is a complex, multimodal reaction that occurs under diverse abusive conditions and is influenced by many parameters such SOC, size and morphology, chemical composition, and atomic arrangements of the cathodes. O_2 release phenomenon is identified at the surface of the cathode particles as characterized by the valence state reduction and structural reconstruction, as well as the bulk of the cathode particles, identified by defect formation and inter/intragranular cracking. The efforts to suppress such detrimental reactions can be categorized in two main approaches: (1) surface coating and (2) chemical composition modification. Coating approaches have shown to be highly effective in suppressing the oxygen release and mitigating the thermal runaway of LIBs. However, it is still not clear that if surface engineering approaches can hinder the bulk-originated oxygen release mechanisms and control the cracking and disintegration of cathode materials. In addition, due to inhomogeneous expansion and contraction in the cathode/coating interface during the electrochemical cycling, the coated and core-shell cathodes are highly prone to delamination and mechanical failure during repeated cycling. On the other hand, chemical composition modification approaches can effectively suppress the oxygen evolution reaction both at the bulk and the surface level. However, doping and alloying of cathode materials are associated with challenges such as uniformity of the dopant dispersion and electrochemical properties deterioration by the introduction of the inactive dopant ions.

Chapter 4: Facet-Dependent Thermal Instability in $LiCoO_2$

(Previously published as Sharifi-Asl, S.; Soto, F. A.; Nie, A.; Yuan, Y.; Asayesh-Ardakani, H.; Foroozan, T.; Yurkiv, V.; Song, B.; Mashayek, F.; Klie, R. F.; et al. Facet-Dependent Thermal Instability in LiCoO2. Nano Lett. 2017, 17 (4), 2165–2171. Reproduced with permission[1]. Copyright 2017, American Chemical Society)

4.1. Introduction

Temperature rise is an inevitable phenomenon in Li-ion batteries which can be caused by mechanical stress, overcharge or simply by high-temperature environments[70,71,103,109,112,343–346]. In such conditions, oxygen release from the oxide cathode materials, including Li_xCoO_2, is known to be one of the major reasons of the thermal runway in which the decomposed oxygen reacts with the flammable electrolyte exothermically and causes Li-ion battery failure[99,151,161,175,347–351]. To be able to control and/or hinder these processes, one needs to understand the underlying mechanisms associated with the oxygen release in oxide cathode materials. As such, a significant and growing body of literature is devoted to understanding the thermal instability of oxide cathode materials using X-ray diffraction (XRD)[206], optical and photoelectron spectroscopy[352], transmission electron spectroscopy[98,136,353], thermogravimetric analysis and differential scanning calorimetry[354].

$LiCoO_2$ is one of the most heavily used cathode materials with high energy density (180 mAh/g) and high voltage limit (4.3 V), which is extensively used in consumer electronics and even in large-scale systems such as the Boeing 787 Dreamliner airplanes recently[5,121,149,296,355–359]. However, due to the safety concerns its usage in transportation systems was discontinued, and now its application is mostly limited to consumer electronics[68,73]. A well-accepted reaction based on XRD results suggests that Li_xCoO_2 ($x<1$), when exposed to high temperatures, decomposes based on the empirical global reaction[73]:

$$Li_xCoO_2 \rightarrow \frac{1-x}{3}Co_3O_4 + xLiCoO_2 + \frac{1-x}{3}O_2 \quad (9)$$

Certainly, this global reaction does not allow the detailed understanding of thermal degradation mechanism occurring in Li_xCoO_2. For instance, Geder *et al.*[152] recently reported that the oxygen release amount varies as a function of particle size in Li_xCoO_2 (x<1) particles and they concluded that the decomposition mechanism could be different at the surface compared to the bulk. They also hypothesized that $Li_xCo_{2-x}O_2$ rock salt structure is formed in samples with higher surface area based on their XRD observations. This example shows how our understanding of the thermal degradation of cathode materials yet needs to be improved, and some aspects remain to be addressed. In this work, we utilized *in-situ* high-temperature aberration-corrected scanning transmission electron microscopy (STEM) to investigate the microstructure evolution on the surface of $LiCoO_2$ at different states of charge (Figure *17*). Using a broad range of techniques such as selected area diffraction pattern, TEM dark field imaging, high angle angular dark field (HAADF) and EELS, we monitored the phase transitions and local chemical changes associated with oxygen release in $Li_{0.7}CoO_2$ and $Li_{0.45}CoO_2$ particles. Also, the local decomposition reactions at the surface and interior regions of particles are investigated, which allows gaining information about valence change of Co in Li_xCoO_2 (x<1) under high temperatures. Finally, *ab-initio* molecular dynamics (AIMD) simulations were performed to gain further insights on the local oxygen release in $Li_{0.45}CoO_2$ particles.

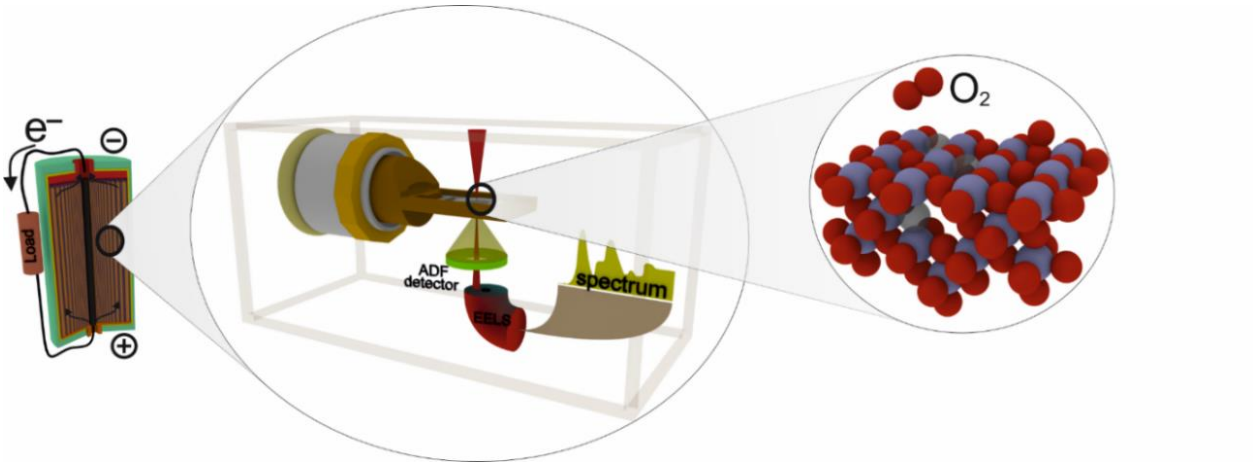

Figure 17. (designed by Dr. Yurkiv) Schematic illustration of the work-flow used in the present study. Note that all structural details and scaling are exaggerated merely for illustration purposes.

4.2. Experimental

Sample preparation. In the present study, commercially available $LiCoO_2$ (Sigma-Aldrich) samples were used. To de-convolute the effect of binder and electrolyte from the investigated physico-chemical behavior of the cathode, we applied a chemical de-lithiation method to remove Li^+ from $LiCoO_2$ structure. Chemical de-lithiation has been reported previously [360]. In short, 1 g of $LiCoO_2$ was dispersed in 25 ml of 0.15 M $K_2S_2O_8$ aqueous solution and magnetically stirred at 60 °C for 24 and 72 hours to obtain partially and fully de-lithiated specimens, respectively. Then the solution was vacuum filtered using filter membranes with 100 nm pore size and washed 3 times with DI water and dried in a vacuum furnace for another 72 hours. Following this process, the Li content was measured using inductively coupled plasma optical emission spectroscopy (ICP-OES) by Thermo iCAP 7600. These measurements have shown that the molar ratio of Li/Co is 0.7 and 0.45 for partially and fully de-lithiated samples, respectively.

Sample characterization. Specimens with different Li contents were drop casted onto lacy carbon grids and loaded on Gatan double tilt heating stage for *in-situ* heating investigations. After loading to the microscope, the sample was subjected to high temperatures ranging from 25 °C to 450 °C

with a heating rate of 10 °C·min^{-1}, before collecting data we kept the samples at the desired temperature for 15 minutes to ensure holder stability and temperature uniformity. Also, to ensure that the actual temperature of the particles is the same as the reading temperature, we collected our data only from particles very close to the copper grid mesh. Morphological TEM images and selected area diffraction patterns were collected by JEOL JEM-3010 TEM, and atomic resolution HAADF imaging and electron energy loss spectroscopy were performed using JEOL JEM-ARM200CF STEM equipped with a cold field emission gun with 0.78 Å spatial resolution and a Gatan Enfina EELS system. A 22 mrad probe convergence angle was used to perform STEM imaging. HAADF detector with 90 mrad inner-detector angle was utilized to obtain Z-contrast atomic resolution images. Spectroscopy was done with 0.1 eV/channel dispersion and with a 2 mm detector aperture. At each temperature, three spectra were obtained from each spot and measurements were repeated to generate the error bars with a standard deviation of the mean. Full-width half maximum of zero loss peak was measured 0.6 eV which determines the energy resolution of the obtained spectra. Some HAADF images have been filtered using a HRTEM filter.

AIMD simulations (done by Dr. Soto and Prof Balbuena at Texas A&M University). Slab surface models were constructed from the layered crystal structure reported by Takahashi *et al*. [361] to study the stability of $LiCoO_2$. Three lithiated and de-lithiated surface models were considered (Supplementary Information, Figure *28*): [012] $LiCoO_2$; [014] $LiCoO_2$; [001] $LiCoO_2$. Partially de-lithiated models were $Li_{0.45}CoO_2$. All the surface models were O-terminated when Li atoms were removed from the surface sites to create the de-lithiated structures and the vacuum space normal to the surface was set to guarantee a separation between the periodic images. The bottom-most atoms were fixed to their lattice site, and the atoms in the top layers were allowed to relax.

Here, ab-initio molecular dynamics (AIMD) simulations were employed to study the evolution of the systems at 400 ^{o}C. Within AIMD, the forces acting on the atoms are obtained through electronic structure calculations. These electronic structure calculations are performed using the plane-wave projector-augmented wave method [362,363] with a kinetic energy cutoff of 400 eV, and the k-point mesh is set to gamma point using the Vienna ab-initio Simulation Package (VASP)[364–367]. In this work, the exchange-correlation contribution to the total energy is implemented through the use of the GGA-PBE approximation to the exchange and correlation functional [368].

Spin-polarized calculations were performed for all investigated surface slabs. The DFT+U method introduced by Dudarev *et al*. [369] is applied to take into account the on-site Coulomb interaction of 3d electrons with the U value set to 4.91 eV for lithiated surfaces and 4.5 eV for de-lithiated surfaces [150,370]. Tritium masses were used for hydrogen to set the time step at 1.0 femtoseconds, and the temperature was maintained using the Nosé-Hoover thermostat [371] with configurations belonging to the canonical (N, V, T) ensemble. To study the stability of the structures we evaluated the Li-Co radial distribution function (RDF) for each surface slab.

4.3. EELS Calibration for Co Valence State Analysis

The EELS results from $LiCoO_2$ contain two main features in 530 and 780 eV. The edge that appears in 530 eV is known as the oxygen K-edge, which consists of a pre-edge peak corresponding to the transition of O 1s state to O 2p states hybridized with Co 3d states and can be used to quantify the valence of transition metals[136]. The main peak also corresponds to the transition of electrons from O 1s to O 2p hybridized with Co 4sp states. Cobalt L3, L2 edges are also a result of the transition from 2p 3/2 and 2p 1/2 electrons to 3d orbitals, which can also be very useful for determining the Co oxidation state[372,373] (Figure *18A*).

To carry out EELS calibration and quantify the valence state alteration of Co during *in-situ* heating experiments, we used CoO, Co_3O_4 and $LiCoO_2$ samples, which correspond to Co^{2+}, $Co^{2.6+}$ and Co^{3+} respectively. Then performed EELS on the samples and analyzed the data based on three methods. The energy difference between O k edge pre-edge peak and main peak, Co L3/L2 integrated intensity ratio and energy difference between Co L3, L2 edges were extracted from the obtained spectra plotted as a function of Co valence state. Figure *18* presents EELS obtained from different cobalt oxides. Apparently, by changing cobalt valence from 2.6 to 2, O k edge pre-peak shifts to higher energies and intensity of this peak reduces, which is due to larger number of unoccupied 3d orbital in Co_3O_4 compared to CoO[372]. Likewise, Co L3, L2 edges undergo similar changes over different valence states. A dramatic increase in the L3/L2 intensity ratio can be observed by changing from Co_3O_4 to CoO, and also the energy difference between L3, L2 peaks (ΔE) increases slightly. To analyze the data based on these variations, we utilized Gaussian peak fitting method, which yields the least error compared to other methods in our case. After peak fitting, intensity ratio and energy difference of Co L3, L2 edges as well as energy difference of O k edge pre-peak and main peak (O k edge ΔE) was plotted for comparison (*Figure 18B-D*). Obviously ΔE for oxygen k edges and cobalt L3/L2 intensity ratio are a good indication of valence change from 2.6 to 3, but it is not sensitive to changes from 3 to 2.6. However, the energy difference of Co L3, L2 edges shows a more linear trend over the change of valence state from 3+ to 2+, and it changes from 14.2 to about 14.7 for the transition from 3+ to 2.6+ and then reaches to 15.2 for Co^{2+}. Therefore, we have chosen this method to quantify our obtained spectra from *in-situ* experiments. However, O k-edges will be shown in all figures for a better visualization of changes.

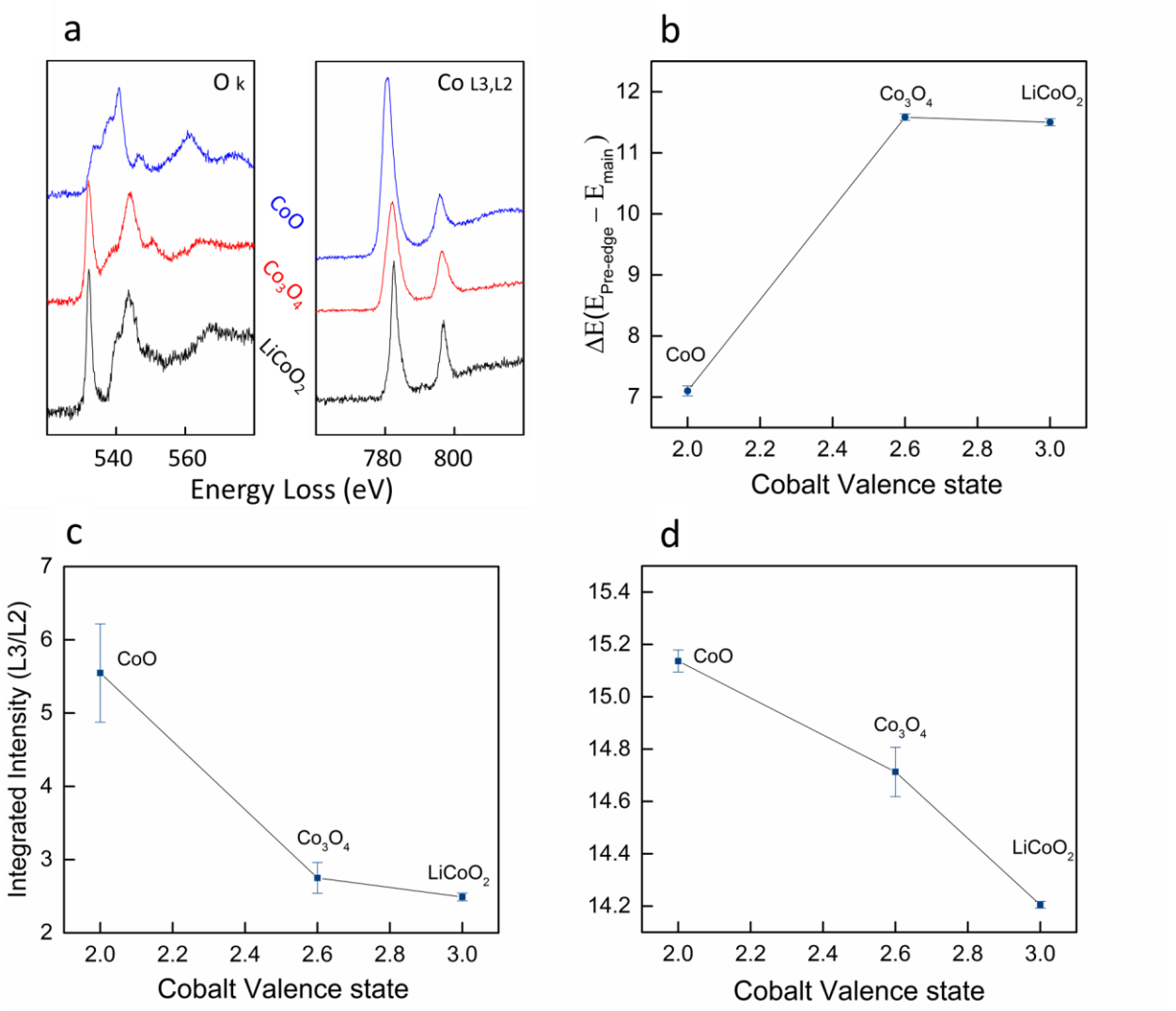

Figure 18. (a) O k edge and Co L3, L2 edges obtained from CoO, Co_3O_4, and $LiCoO_2$. (b) Oxygen K edge ΔE (E pre-edge peak –E main). (c) Co L3/L2 integrated intensity ratio. (d) Co L edge ΔE (L3-L2) as a function of Co valence state. It can be seen that Co L edge ΔE has a linear correlation with Co valence state. From each sample, 3 spectra were obtained and measurements were repeated to generate the error bars with a standard deviation of the mean.

4.4. *In-situ* heating TEM/STEM Study on Li_XCoO_2

Figure *19*A shows a HAADF atomic resolution image from pristine $LiCoO_2$, which can be indexed as $[12\bar{1}]$ zone axis of the layered phase based on the fast Fourier transform (FFT) pattern (inset in Figure *19A*). An atomic model from the same zone axis is super-imposed, which confirms the ($R\bar{3}m$) structure of the $LiCoO_2$ sample. High-temperature behavior including morphological TEM images, selected area diffraction patterns (SADPs) and EELS results from a pristine sample in 25 and 450 °C are presented in *Figure 19B-19D*. SADPs are identical in both conditions and can be indexed as [001] zone axis of layered ($R\bar{3}m$) structure and no change can be observed in the morphological images.

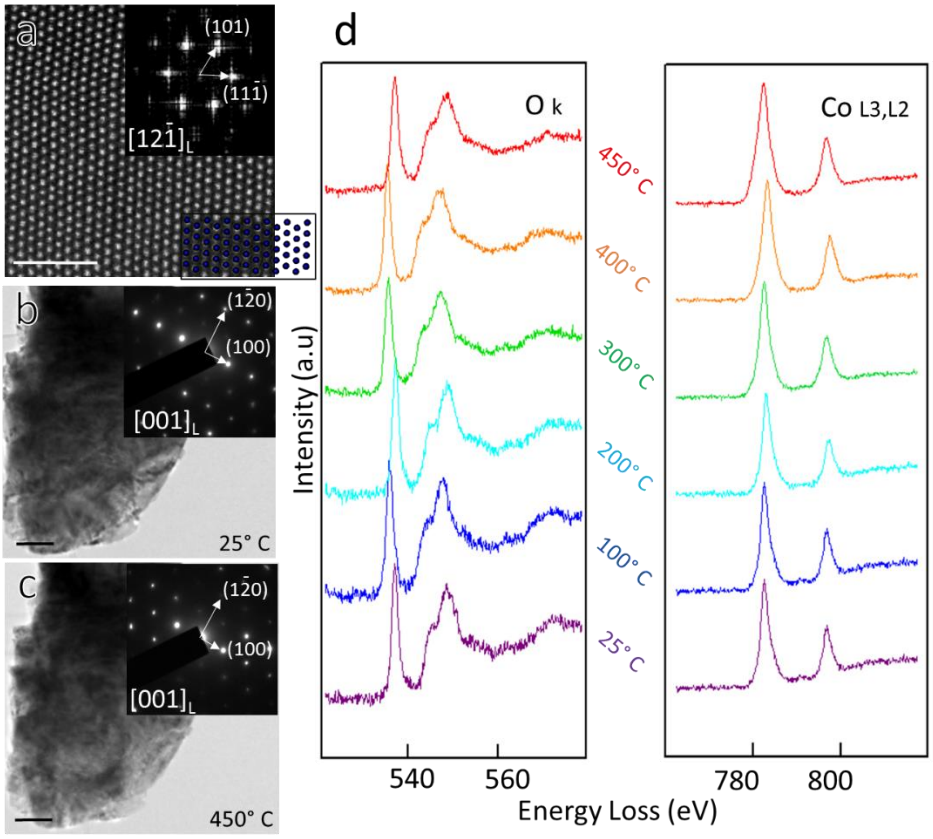

Figure 19. (a) Atomic resolution HAADF image from pristine $LiCoO_2$ layered ($R\bar{3}m$) structure. FFT image (inset) is indexed as $[12\bar{1}]$ zone axis (scale bar is 2 nm). (b, c) Morphological TEM

images and SADPs (inset panels) from pristine $LiCoO_2$ at 25 and 450 °C temperatures (scale bars are 200 nm). (d) EELS results from pristine $LiCoO_2$ at 25-450 °C. To maximize the energy resolution of the spectra, a dispersion of 0.1 eV was used that results in a small energy window (124 eV). Therefore, regions of interest containing O k-edge and Co L3, L2 edges were recorded separately.

However, Li_xCoO_2 (x = 0.7 and 0.45) does not show the same stability at high temperatures. Figure *20* shows *in-situ* heating TEM results obtained from a $Li_{0.45}CoO_2$ particle at [001] zone axis of the layered structure. *Figure 20A, B* correspond to SADPs recorded from the core and the surface of a $Li_{0.45}CoO_2$ particle at 25 °C. Both $SADP_s$ indicate the existence of the layered structure before temperature rise. However, by increasing the temperature to 200 °C, spinel phase forms on the surface as indicated by the diffraction pattern. Figure *20D* illustrates the co-existence of both layered and spinel $LiCoO_2$ in the [001] and [111] zone axis, respectively. This means that the spinel phase nucleated on the original layered structure due to increasing the temperature. However, In the diffraction pattern collected form the core, diffraction from the spinel phase (marked by red circles) becomes faint and almost invisible (Figure *20C*), which means that the proportion of the spinel phase decreases in the core. To visualize this phenomenon, dark field TEM imaging was performed using $(0\bar{2}2)$ lattice plane of the spinel phase, and it shows that a newly formed spinel structure is mostly present on the surface. By further increasing the temperature (Figure *20D*), the surface area of $Li_{0.45}CoO_2$ particle undergoes another phase transition and the diffraction from the rock-salt structure ($fm\bar{3}m$) can be observed (Figure *20E*). This SADP can be indexed as $[1\bar{1}1]$ zone axis of rock salt structure. However, at 450 °C diffraction from spinel + layered structure can be recorded at the core of the particles, meaning that the spinel phase which initially nucleated at surface propagates toward the core by increasing the temperature and eventually the surface transfers to rock salt structure. To correlate the identified phase transitions

with the oxygen evolution mechanism and to further investigate thermal degradation, EELS was performed on the surface of a $Li_{0.45}CoO_2$ particle as a function of temperature (Figure *20H*). As expected, both oxygen K-edge and Co L3, L2 edges undergo noticeable changes by increasing the temperature. A shift in O K-edge pre-peak is evident, which indicates the reduction of transition metal atoms around the O sites[374]. Simultaneously, by analyzing Co L-edges, it can be seen that both ΔE (energy difference between L3, L2 white lines) and the L3/L2 intensity ratio increase by increasing the temperature, also representing the reduction of Co atoms at elevated temperatures. As discussed above, performing EELS on standard cobalt oxide samples, we realized that the energy difference (ΔE) of cobalt L-edges is the best indicator for cobalt valence analysis. Thereby, the Co valence state at the surface of the particle can be plotted as a function of temperature (Figure *20I*). From this figure, it can be concluded that oxygen release which simultaneously occurs with the phase transitions, starts at temperatures as low as 100 °C for the $Li_{0.45}CoO_2$ sample. The oxygen release and reduction process continue up to 300 °C where Co^{2+} forms on the surface which we believe corresponds to the formation of the rock-salt structure. It should be noted that the slight decrease in (ΔE) value to the extent of 0.1 eV, by increasing the temperature beyond 300 °C, does not indicate a significant change in Co valence state. As can be seen fromFigure *18*, the change in the Co valence from 2.6+ to 2+ (using the standard cobalt oxide samples) results in a much larger change in △E (from 14.7 to about 15.1 eV), and variation of 0.1 eV in EELS results obtained from a microscope not equipped with a monochromator is reasonable. Also, to further investigate the effect of Li content on the thermal instability of $Li_{0.45}CoO_2$ we performed the same set of TEM experiments on $Li_{0.7}CoO_2$ samples and the results are shown in Supplementary Information (). As expected, the degree of de-lithiation affects the instability of cathode particles slightly. As such, from the analyzed EELS results (Figure *20H*) it can be seen that there is a delay for cobalt valence

change in $Li_{0.7}CoO_2$ sample compared to $Li_{0.45}CoO_2$, which corresponds to the effect of Li content on the thermal instability of the sample.

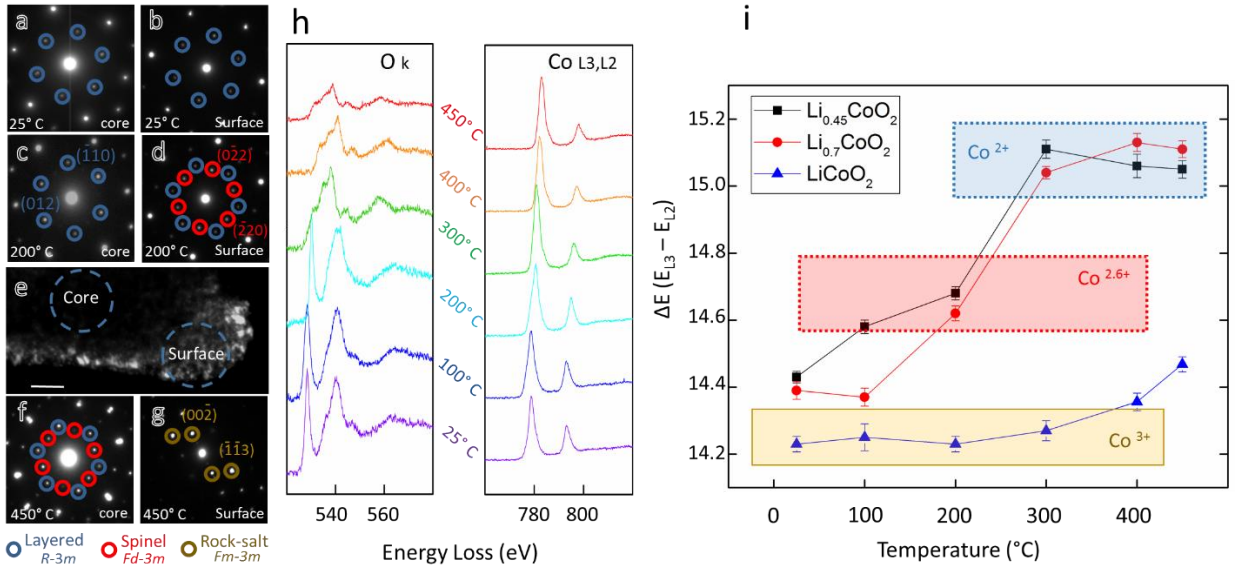

Figure 20. Diffraction patterns collected at 25 °C from (a) core and (b) surface of a $Li_{0.45}CoO_2$ particle. Blue spots correspond to the original layered structure ($R\bar{3}m$) with the [001] zone axis. Diffraction patterns collected at 200 °C from (c) core and (d) surface of a $Li_{0.45}CoO_2$ particle, red spots correspond to the [111] zone axis of the spinel phase ($fd\bar{3}m$). (e) Dark-field TEM image obtained from ($0\bar{2}2$) lattice plane of spinel phase at 200 °C (scale bar is 50 nm). Diffraction patterns collected at 450 °C from (f) the core and (g) the surface of a $Li_{0.45}CoO_2$ particle. (h) EELS results obtained from the surface of $Li_{0.45}CoO_2$ as a function of temperature. (i) Energy difference of Co L3, L2 edges (ΔE) is plotted against temperature.

To confirm the TEM results and sequence of phase transitions associated with the oxygen evolution in macro scale, we performed thermogravimetric analysis (TGA) and differential scanning colorimetry (DSC) experiments on $Li_{0.45}CoO_2$ samples. Thermogravimetric analysis (TGA) and differential scanning calorimetry (DSC) was performed on $Li_{0.45}CoO_2$ sample and results are shown in Figure *21*. It can be seen that by reaching to 100 °C, negative heat flow corresponding to layered to spinel phase transitions shows up on the DSC curve. Simultaneously,

mass loss to the extent of 4% can be observed on TGA curve which is due to oxygen evolution from the sample. Another endothermic phase transition can be recorded at about 250 °C which is corresponding to rock salt phase formation. Along with this phase transition, about 8% mass loss due to more intense oxygen evolution can be observed (Figure *21*a). Although the thermal decomposition reaction of the layered oxide cathodes is considered as an exothermic reaction[1–3], it should be noted that most of the DSC results are obtained from cathode materials that are charged in Li-ion cells. In these experiments the cells are either unwashed, so the samples either contain electrolyte residue and Li-salts or were mixed with added electrolyte. Moreover, it is shown that the thermal decomposition reaction is highly dependent on the added Li salt[5]. Additionally, it has been experimentally shown that the outcoming gases from such thermal decomposition reactions are CO_2 rather than pure O_2 which denotes to an additional reaction between O_2 and other compounds in the sample[6]. In the discussed thermal analysis experiments, chemically delithiated and washed Li_xCoO_2 samples were used, which did not contain any electrolyte, Li salt residue, or carbon black. According to the weight loss observed in the TGA results the sample was decomposed in endothermic reactions (Figure 21a). However, authors suggest that dedicated thermal analysis/mass spectroscopy experiments to be carried out to clarify the thermodynamic nature of thermal decompaction reaction of the layered oxide cathodes and verify the correctness of the DSC results.

Also, to deconvolute the mass loss due to absorbed/adsorbed water from the oxygen release, we compared TGA results from air/water exposed $LiCoO_2$. Results indicated less than 0.1 wt% mass loss in water exposed sample which is negligible compared to more than 12 wt% mass loss in $Li_{0.45}CoO_2$ caused by oxygen release (Figure *21*b).

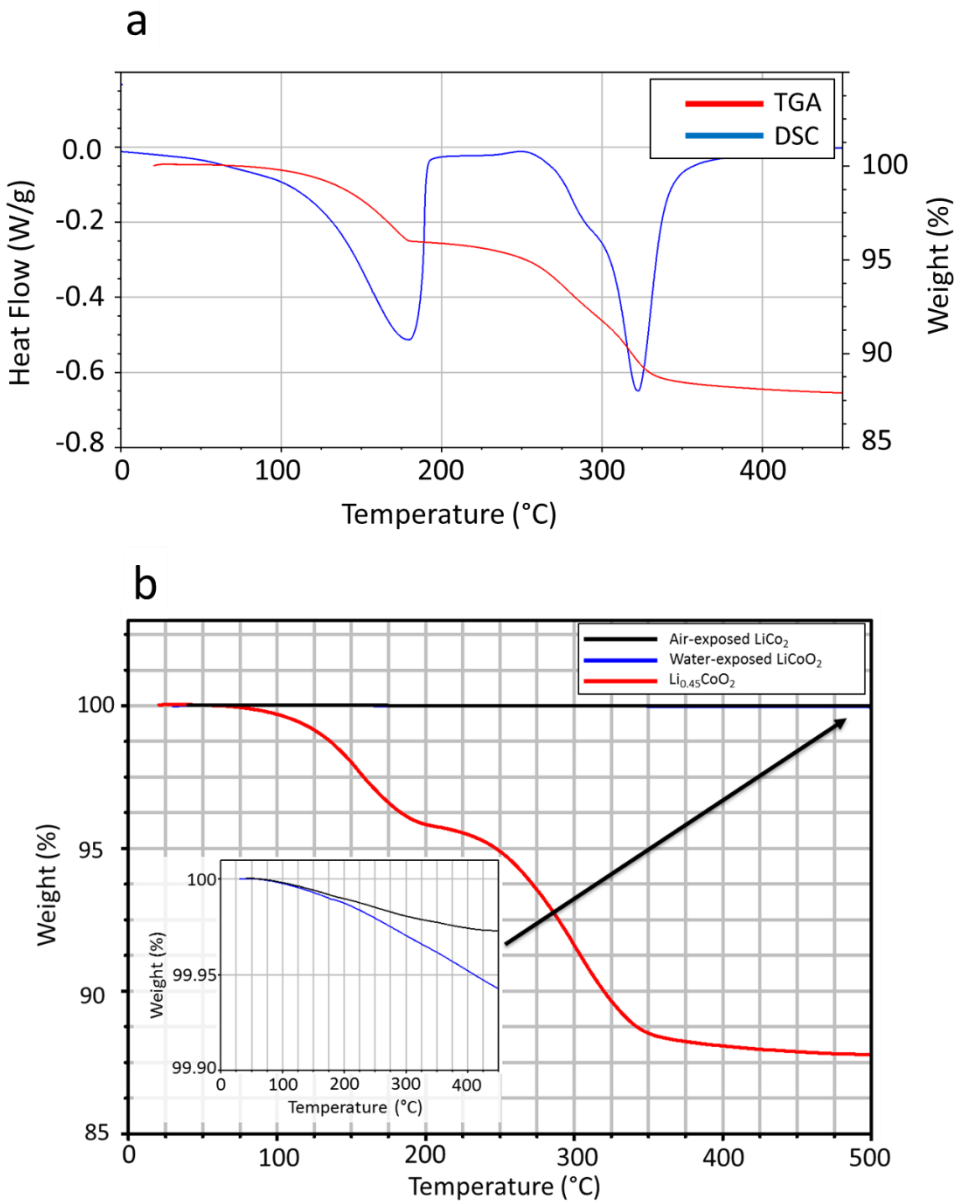

Figure 21. (a) Overlaid TGA/DSC result obtained from $Li_{0.45}CoO_2$. (b) TGA results obtained from air-exposed and water exposed $LiCoO_2$ and $Li_{0.45}CoO_2$.

To gain further understanding of phase transitions associated with $Li_{0.45}CoO_2$ samples, we performed atomic resolution STEM imaging, as well as EELS line scanning on $Li_{0.45}$ CoO_2 particles that has been heated to 300 °C., Figure *22A-F* present HAADF images from a $Li_{0.45}CoO_2$ sample before and after a heating cycle from 25 to 300 °C. As can be seen from Figure *22A* and *B* and, after de-lithiation there is no change in morphology, and atomic structure and $Li_{0.45}CoO_2$ sample preserve its layered structure. However, after heating to 300 °C, morphological and structural alterations are noticeable. Formation of dark contrast regions on the surface of the $Li_{0.45}CoO_2$ particle can be observed (Figure *22C*), which is an indication of oxygen release from the structure [379]. Effect of elevated temperature on the formation and growth of these dark contrast regions are described below. Moreover, rock salt and spinel phase formation can clearly be observed from atomic resolution HAADF images in different regions of the particle. Figure *22D* corresponds to the filtered HAADF image, showing the formation of rock salt structure at the surface of the sample. FFT (inset) can be indexed as a [111] zone axis of the rock salt ($Fm\bar{3}m$) structure. However, by moving towards the core of the sample, the formed spinel phase can be observed. Figure *22E* corresponds to the [112] zone axis of spinel $LiCoO_2$ ($Fd\bar{3}m$). Based on these atomic resolution observations, areas within ca. 20 nm distance from the surface have transferred to spinel structure ($Fd\bar{3}m$). By moving to the core of the particle (Figure *22F*), we can find areas where layered, and spinel structures co-exist in one image. To have a better demonstration of co-existence of both phases, the image is shown in the format of a reconstructed color-coded image. Accordingly, red marked spots correspond to the $(11\bar{1})$ and $(02\bar{2})$ lattice plane of spinel phase ($Fd\bar{3}m$), and green marked spots correspond to the (100) and (010) lattice planes of layered phase ($R\bar{3}m$). To correlate the observed phase transitions with oxygen release from the sample, we performed EELS line scan perpendicular to the surface of the sample while keeping the

temperature constant at 300 °C. As it can be seen in Figure *22G*, both oxygen K-edge, and Co L3, L2 edges undergo major changes moving across the sample, meaning that the oxidation state of cobalt totally changes across the particle. Analyzing the Co L-edges, it can be seen that the energy difference (ΔE) of cobalt L-edges is changing from about 15.18 eV (Co^{2+}) to about 14.44 eV ($Co^{2.8+}$) by moving 60 nm towards the core of the particle (Figure *22H*). The results indicate that cobalt's valence is increasing gradually from the surface to core, meaning that oxygen is mostly released from the surface where rock salt and spinel structures are formed. Based on our EELS analysis performed at 450 °C (shown in Supplementary Information, Figure 25), this reaction front propagates about 60 nm toward the core, meaning that oxygen evolution and surface degradation is continuing from the surface. To summarize, based on the atomic resolution imaging and diffraction pattern observations, we observe that the spinel structure forms around $Li_{0.45}CoO_2$ particles at elevated temperatures. The oxygen then leaves the structure from the surface of this newly formed spinel type $LiCoO_2$, forming $Li_xCo_{1-x}O$ rock salt structure with less oxygen content compared to spinel and layered $LiCoO_2$. The rock salt structure forms a very thin layer around this oxygen deficient spinel structure.

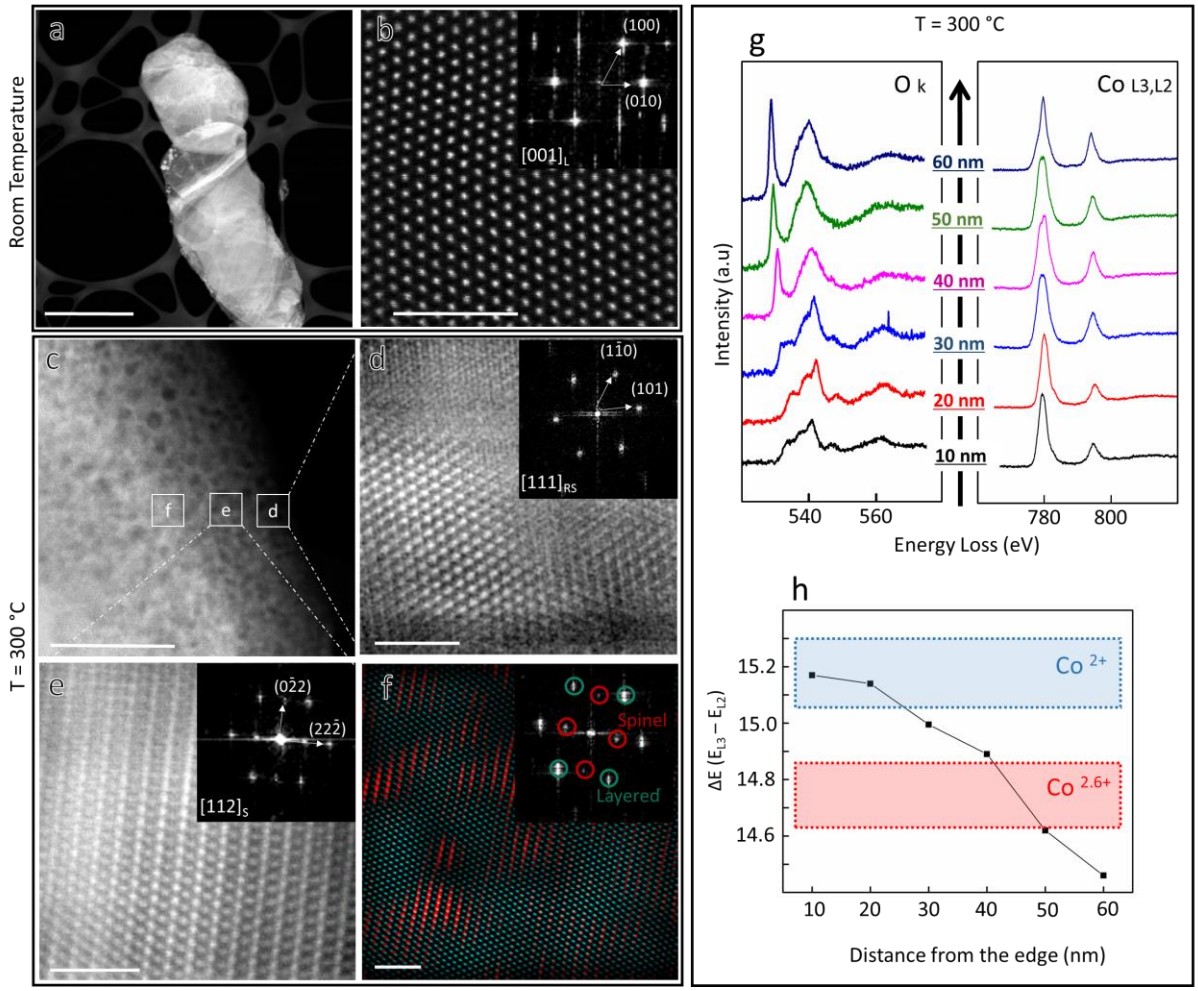

Figure 22. (a) HAADF low-mag image from a $Li_{0.45}CoO_2$ particle (scale bar is 1 µm). (b) HAADF atomic resolution image from the same particle showing that the layered structure is well preserved after de-lithiation (scale bar is 1 nm in all atomic resolution images). Inset FFT corresponds to the [001] zone axis of the layered ($R\bar{3}m$) phase. (c) HAADF low-mag image from a $Li_{0.45}CoO_2$ particle heated to 300 °C (scale bar is 50 nm). Void formation and thermal degradation resulting from oxygen release can be observed. (d) Filtered HAADF atomic resolution image corresponding to [111] zone axis of rock salt structure captured from the surface of the sample (as marked in Figure 3c) with FFT inset. (e) Filtered HAADF atomic resolution image of the marked area in panel c. The corresponding FFT image (inset) can be indexed as the [112] zone axis of the spinel structure. (f) Reconstructed color coded image obtained from the marked area in panel c. (g) EELS results from a line scan performed perpendicular to the surface of the sample at 300 °C. Results are shown as a function of distance (10, 20, 30, 40, 50, 60 nm) from the edge of $LiCoO_2$ particle. (h) Energy difference of Co L3, L2 edges (ΔE) as a function of position.

According to our STEM observations, dark-contrast areas (voids) form on Li_xCoO_2 particles by increasing the temperature. These voids can be observed at about 200 °C, and by increasing the temperature their frequency and size grow. Formation of these voids can be attributed to oxygen release and migration of Co species to the adjacent areas for nucleation and growth of the spinel phase, and as the oxygen release is noted to happen on the side facets, void concentration is higher around the surface of particles. As can be seen in Figure *23*, even at 400 °C, there is not a significant number of voids in the core of the particle compared to the high concentration of voids along the surface of the sample, distinguished by the white line in 400 °C. This observation also emphasizes the inhomogeneous and surface-controlled oxygen release from Li_xCoO_2 particles. To evaluate the effect of temperature on the growth of the so-called voids we performed EELS mapping on the indicated void that first appeared at 200 °C and was grown by reaching to 400 °C. We obtained the EELS maps from the zero loss peak (ZLP) section of our spectra to be able to measure the relative thickness and diameter spontaneously as a function of temperature. ZLP spectrum images, shown as inset figures in HAADF images at 200 and 400 °C show that, rather than void formation (with throughout holes in the core), we are dealing with local thickness reduction in our samples. So, by obtaining HAADF images (where a number of atomic columns that interact with the beam controls the signal intensity), we observe dark contrast in our images. ZLP thickness measurements show that at 200 °C, the relative thickness of the core of the void is 0.43 compared to 0.53 for adjacent areas. This thickness reduces to 0.37 at 400 °C but does not reach to zero, meaning that we have a reduction in thickness in the observed dark contrast spot for ~18 % and ~ 30% at 200 and 400 °C respectively. The diameter of this thinned area also increases from about 2 nm to more than 5 nm under heating from 200 to 400 °C.

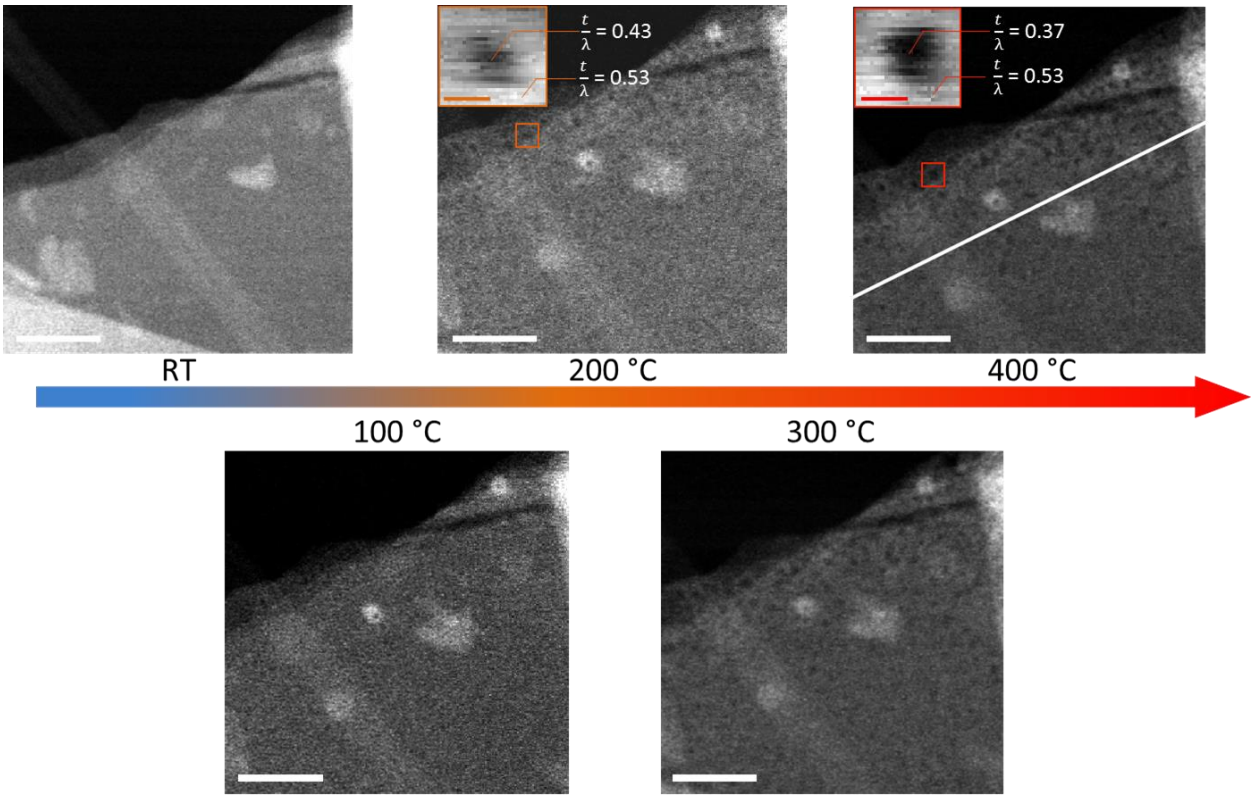

Figure 23. STEM images show a $Li_{0.45}CoO_2$ particle that is heated gradually to 400 °C (scale bars are 100 nm for HAADF images and 5 nm for inset ZLP spectrum images). At 100 °C, particle surface is smooth, while by increasing the temperature, dark contrast spots form mostly around the surface of the particle. ZLP spectrum images show that at 200 °C, the relative thickness of the core of the void is 0.43 compared to 0.53 for adjacent areas. The relative thickness reduces to 0.37 at 400 °C. The diameter of this thinned area also increases from about 2 nm to more than 5 nm under heating from 200 to 400 °C. Looking at the particle at 400 °C, there is a distinct difference in the concentration of the dark contrast spots between the surface and the core, which confirms our main conclusion that the oxygen release is facet-dependent and inhomogeneous.

Overall, *in-situ* TEM results suggest that the local thermal degradation is occurring at the surface of $Li_{0.45}CoO_2$ samples. Overall, *in-situ* TEM results suggest that the local thermal degradation is occurring at the surface of $Li_{0.45}CoO_2$ samples. Based on our STEM/EELS observations thermal decomposition of Li_xCoO_2 is an inhomogeneous reaction that occurs locally at the surface of each particle. Therefore, suggesting a chemical reaction equation, may bury some

of the details of this phenomena, but to convey our observation, in brief, we propose the following two-step decomposition reaction:

$$Li_xCoO_2\ (\text{layered}) \xrightarrow{\geq 100\ ^\circ C} Li_xCoO_2\ (\text{layered}) + Li_xCo_{3-x}O_4\ (\text{spinel}) + \varepsilon O_2 \xrightarrow{\geq 250\ ^\circ C} Li_xCoO_2\ (\text{layered}) + Li_xCo_{3-x}O_4\ (\text{spinel}) + Li_xCo_{1-x}O\ (\text{rock-salt}) + \delta O_2 \quad (10)$$

where ε and δ values depend on the surface fraction and particle morphology.

4.5. Ab-initio Molecular Dynamics (done by Prof. Balbuena and Dr. Soto at Texas A&M University)

To understand the underlying reasons that cause the so-called inhomogeneous oxygen release, we performed AIMD simulations on $Li_{0.45}CoO_2$ samples at elevated temperatures (Figure *24*). Indeed, surface phenomena may affect the electrochemical performance of the cathode[380,381]. Using calorimetric techniques, Maram *et al.*[380]. determined surface energies of $LiCoO_2$ in the [001], [104] and [012] planes, which agree very well with DFT calculated values by Ceder *et al.*[37]. It was demonstrated that the missing Co-O bonds in the [104] and [012] planes result in a significantly lower surface energy due to the Co ions becoming arranged in square pyramidal (intermediate spin) and pseudotetrahedral (high spin) configurations. Thus, the [104] surface energies are much lower than those of the [001] planes, and although the majority of the $LiCoO_2$ surface is presumably composed of [001] planes, experimental evidence suggests that the edges are dominated by the [104] and [012] planes[381]. Three low-energy facets of the layered structure of $LiCoO_2$ were considered. Each facet was simulated at pristine and de-lithiated conditions to resemble the experimental conditions, at 300 and 400 °C. The results show that oxygen evolution behavior depends on the structure of the exposed facets. For instance, the [001] facet is more stable

in both pristine and de-lithiated conditions at 300 and 400 °C than the higher Miller index facets (i.e. [012] and [104]), and there is no oxygen evolution from the structure at time spans of about 2000 fs (Figure *24A*). Whereas, the release of O_2 species can be observed at the [012] and [104] facets at 300 and 400 °C in time spans starting from 400-900 fs (Figure *24A* and *B*). The reason behind such structure-dependence is that O_2 evolution from the [012] and [104] facets proceeds due to the presence of under-coordinated O atoms in these $Li_{0.45}CoO_2$ structures (see Supplementary Information, *Figure 28-Figure* 30). Those atoms that are usually coordinated to one Co and one Li atom, under de-lithiation become coordinated to only one Co. Under these conditions, two neighbor O under-coordinated atoms can become bonded and eventually evolve as O_2. The O-O distance oscillates during the detachment until it finally stabilizes. The changes in the Co-O coordination are clearly observed from radial distribution functions (see Supplementary Information, Figure *31*). This can fully explain the surface degradation phenomena that were observed in the TEM experiments. Noticeably, all the TEM experiments were performed on LCO particles in [001] zone axis which is the stable surface, and degradation which start from the higher Miller indices such as [012] and [104] side facets appear on the surface of particles. Accordingly. Figure *24D* is designed to summarize the experimental and simulation results. An in-depth discussion on the AIMD experimental methods are presented in the Chapter 4.7.

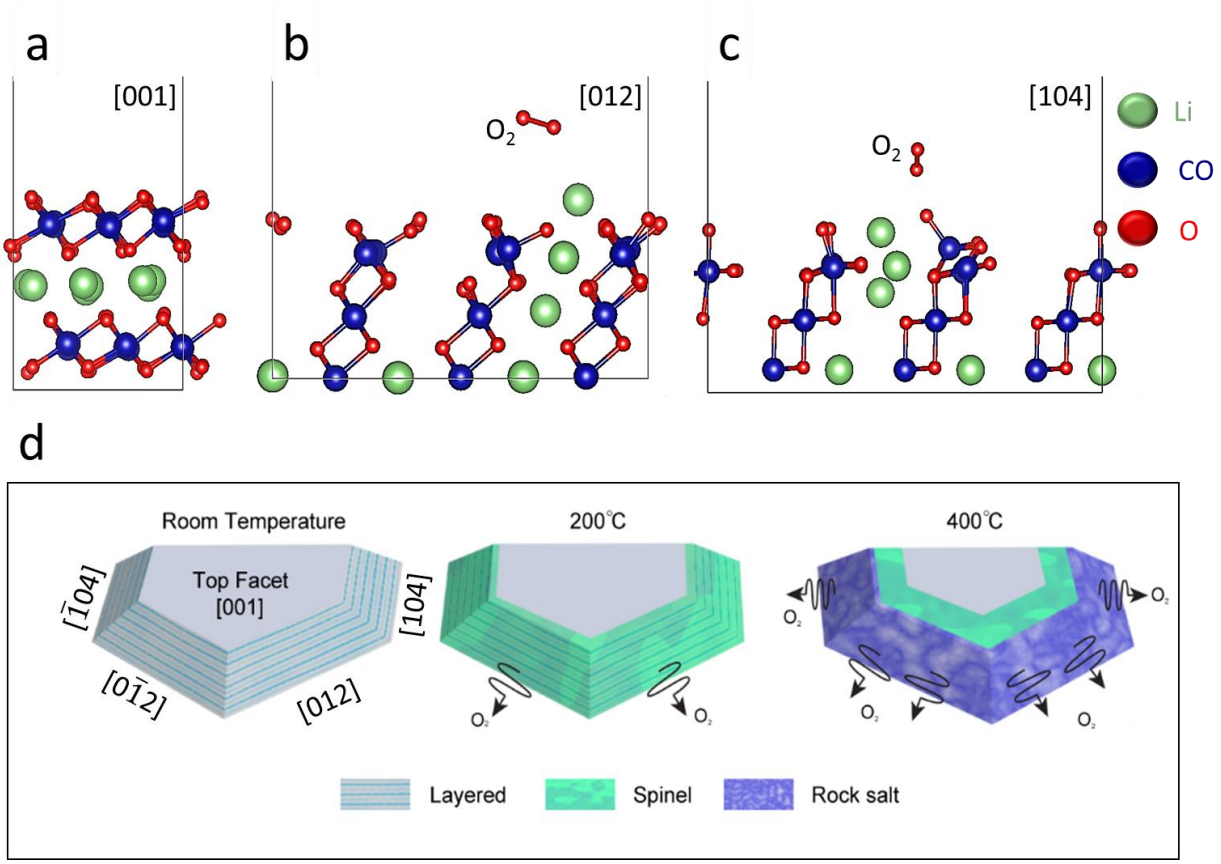

Figure 24. Snapshots of the $LiCoO_2$ surface slabs taken at various times when subjected to a temperature of 400°C. (a) The [001] $Li_{0.45}CoO_2$ surface slab after 2000 fs. (b) Side view of the [012] $Li_{0.45}CoO_2$ surface slab after 400 fs where the evolution of an O_2 species is observed. (c) Configuration of the [104] $Li_{0.45}CoO_2$ surface slab, after 800 fs of simulation time, where the evolution of an O_2 species is observed. Green, blue, and red spheres denote Li, Co, and O atoms, respectively. (d) Schematic illustration of Li_xCoO2 degradation mechanism. Evidently, low energy [001] facet is stable at elevated temperatures, while oxygen evolves from side facets and causes phase transitions to occur at the surface of the particle.

4.6. Summary and Conclusion

In summary, our *in-situ* TEM results of the thermal degradation of Li_xCoO_2 suggest that layered ($R\bar{3}m$) Li_xCoO_2 ($x < 1$) transfers to spinel ($Fd\bar{3}m$) and rock salt structure when exposed to high temperatures. Based on our dark field TEM imaging and atomic resolution observations, these phase transitions start from the facets of the crystals and propagate towards the core. Utilizing the

EELS technique, we revealed the correlation between the observed phase transitions and oxygen loss from the facets of particles. We found that the cobalt valence state substantially changes moving from the interior to the surface, which means that oxygen release is just occurring at the surface while the core remains intact. AIMD simulations explain the underlying mechanisms of the surface degradation of de-lithiated Li_xCoO_2, showing that oxygen release and thermal decomposition behavior depend on the structure of the exposed facets. Accordingly, the [001] facet is more stable while release of oxygen species can be observed in very short time spans from the [012] and [104] facets. These findings explain the local phase transitions and oxygen release that occurs from the surface of $LiCoO_2$ particles. Tailoring the morphology of $LiCoO_2$ is shown to be achievable[37]. Therefore, we believe that the optimization of stable $LiCoO_2$ facets can eventually improve the overall safety of the Li-ion battery systems.

4.7. Supplementary Information

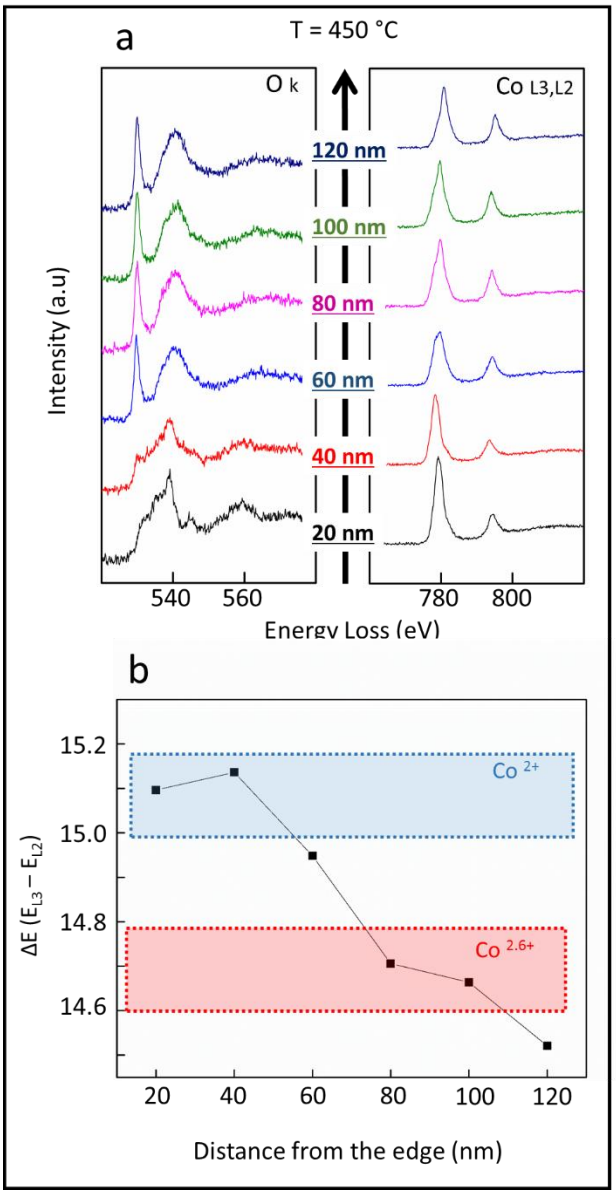

Figure 25. EELS results from a line scan performed perpendicular to the surface of the sample at 450 °C. Results are shown as a function of distance (20, 40, 60, 80, 100, 120 nm) from the edge of the $LiCoO_2$ particle. Apparently, both oxygen K-edge and Co L3, L2 edges have major changes by moving from the edge to the core of the sample.

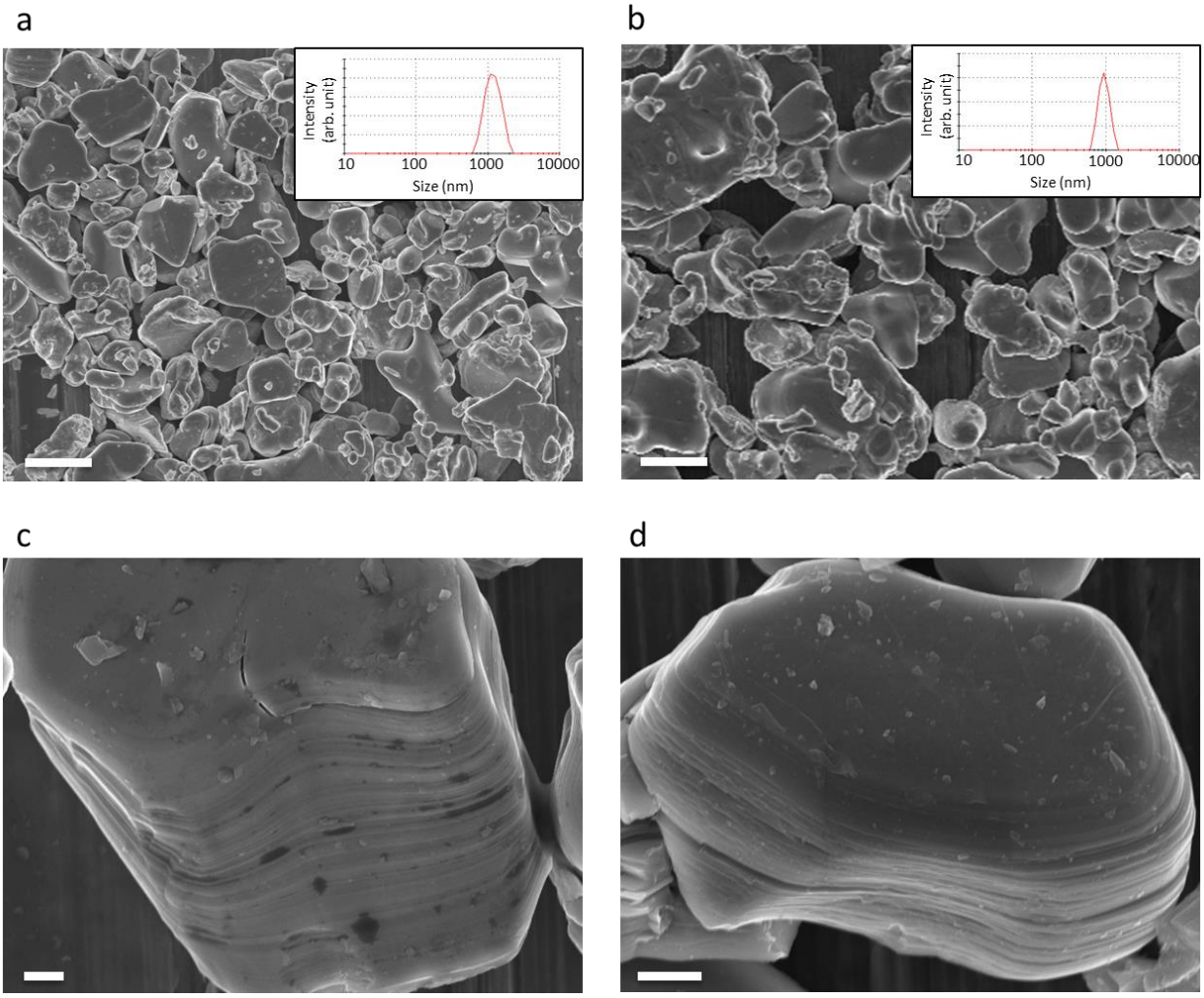

Figure 26. (a) SEM image of the pristine $LiCoO_2$ with dynamic light scattering (DLS) measurement inset (scale bar 10µm). (b) SEM image of $Li_{0.45}CoO_2$ sample with DLS measurement inset. Particle size distribution and morphology are not affected (scale bar 10µm). (c) High magnification image of a pristine $LiCoO_2$ particle showing the layered structure (scale bar 1µm). (d) high magnification image from a $Li_{0.45}CoO_2$ particle showing the preserved layered structure (scale bar 1µm).

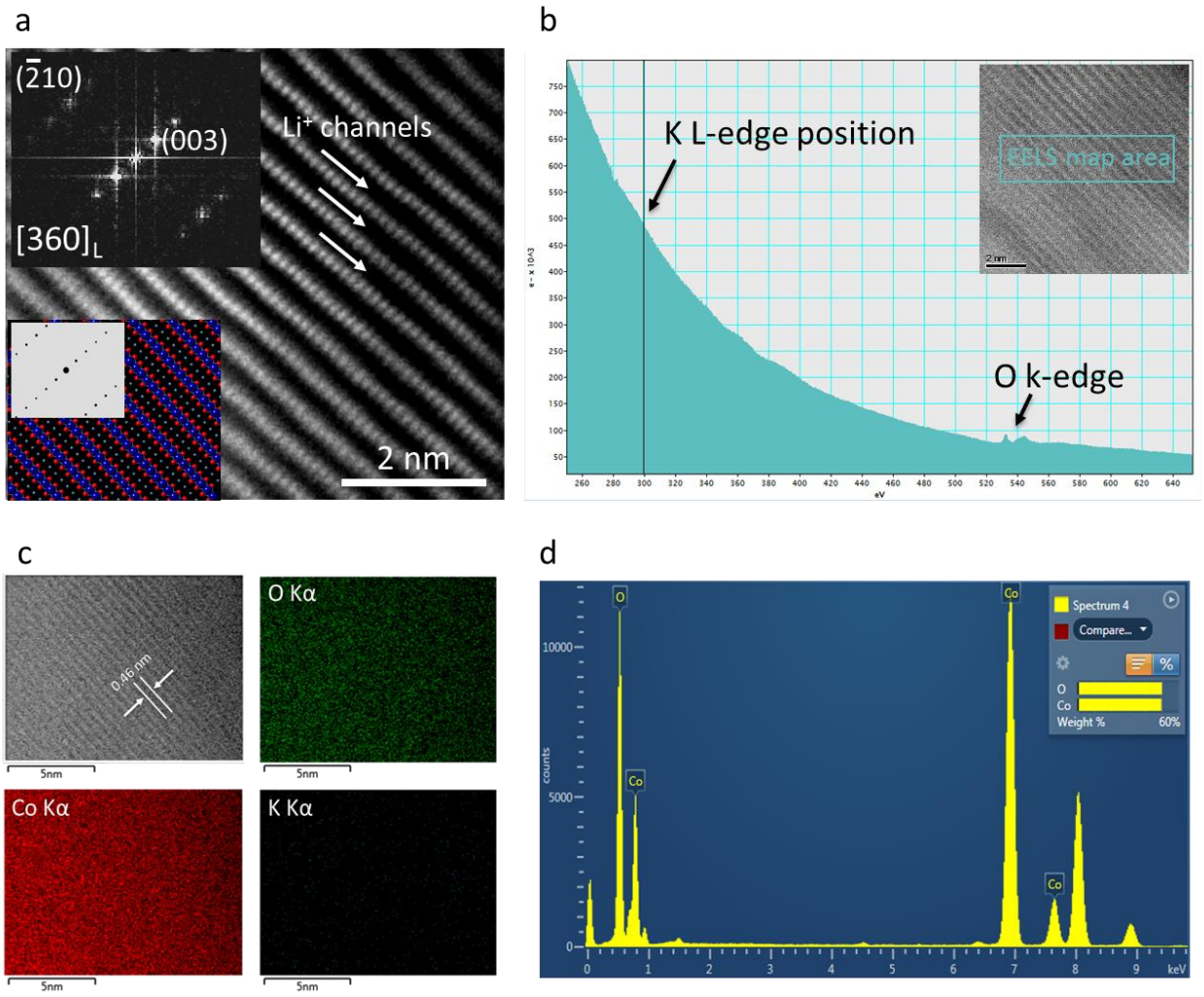

Figure 27. (a) Atomic resolution HAADF image from [360] zone axis (side view). Obviously, Li+ transport channels are not occupied with a heavy ion such as potassium, and the sample is completely retaining its original layered structure. (b) EELS map sum spectrum from the area indicated in the inset figure. As Can be seen, potassium L-edge (295 eV) is not showing up in the spectrum, and only oxygen K-edge can be identified. (c) High-resolution EDS map results and (d) EDS map sum spectrum, from the $Li_{0.45}CoO_2$ sample to evaluate K ion exchange. As can be seen, no potassium is detected in the EDS spectrum (no peak at 3.312 KeV for potassium K_α).

Ab initio* molecular dynamics methods *(Done by Professor Balbuena's group at Texas A&M University)

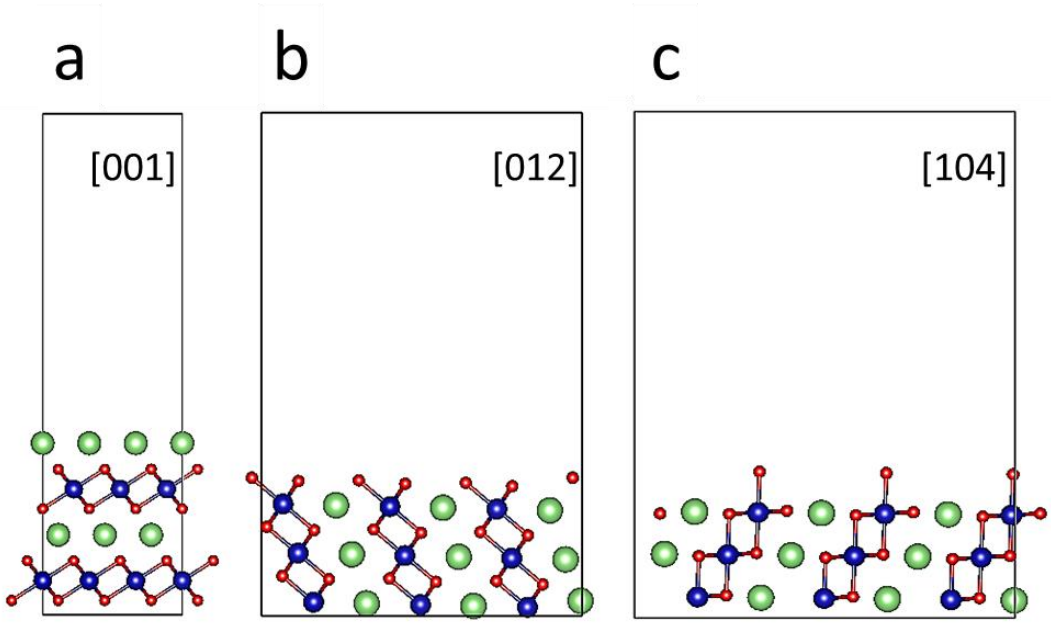

Figure 28. Side views of (a) [001] $Li_{0.45}CoO_2$ surface slab, (b) [012] $Li_{0.45}CoO_2$ surface slab and (c) [104] $Li_{0.45}CoO_2$ surface slab. A vacuum space normal to the surface is added to avoid interactions with a periodic image in this direction. Green, blue, and red spheres denote Li, Co, and O atoms, respectively.

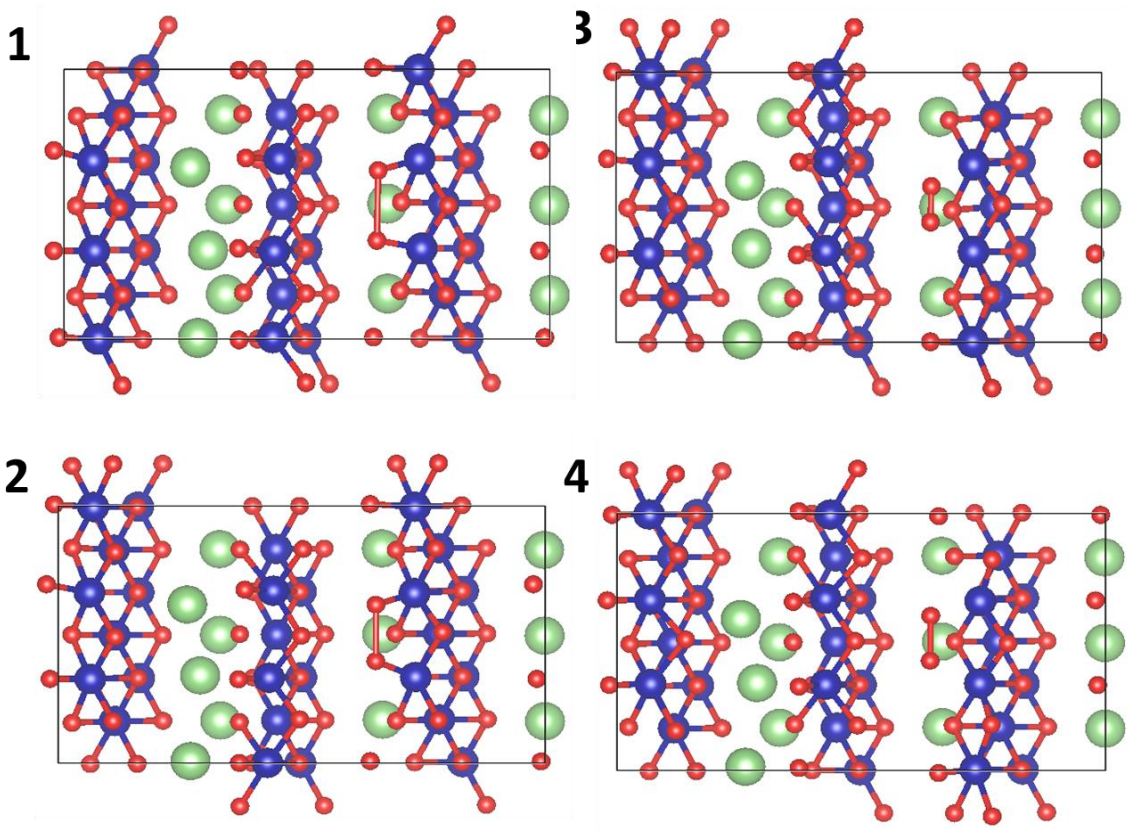

Figure 29. Steps for O_2 formation on the [012] facet. Images 1, 2, 3, 4, show snapshots of side views of the [012] facet at various simulation times. At **1**, two undercoordinated O atoms are initially 2.38 Å apart, but immediately they associate becoming 2.18 Å apart after 20 fs (a line is shown connecting these two atoms). At **2**, after 40 fs, the O-O distance is reduced to 1.85 Å. At **3**, after 60 fs, the O-O distance reduces to 1.11 Å, and both O atoms are dissociated from the Co atoms (evolving as O_2), At **4**, after 80 fs, the O-O distance is 1.49 Å and the O_2 (with an elongated bond distance with respect to gas phase) remains dissociated from the Co atoms. Green, blue, and red spheres denote Li, Co, and O atoms, respectively.

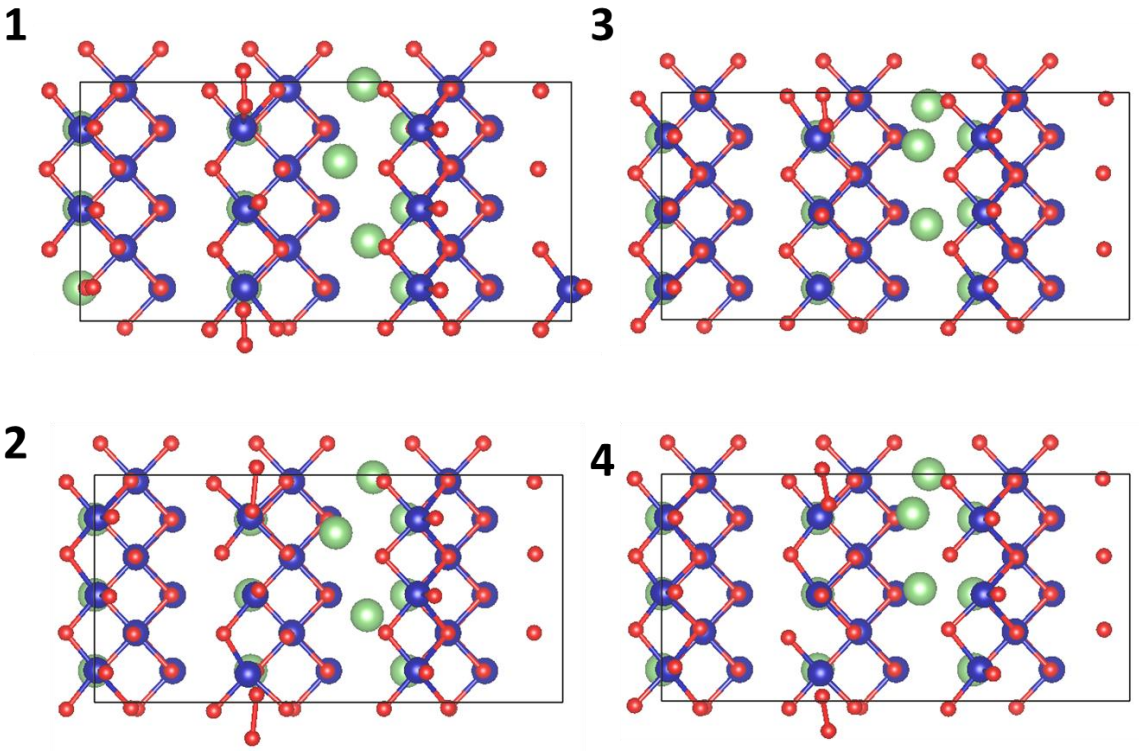

Figure 30. Steps for O_2 formation on the [104] facet. Images 1, 2, 3, 4, show snapshots of side views of the [104] facet at various simulation times. At **1**, after 275 fs two undercoordinated O atoms associate and form a bond with distance 1.32 Å (a line is shown connecting these two atoms). At **2**, after 275 fs, 1 O atom is still bonded to the Co atom (1.95 Å), and the O-O bond elongates to 1.65 Å. At **3**, at 325 fs, the O-O distance reduces to 1.15 Å, and both O atoms are dissociated from Co atoms and evolve as O_2 (Co-O distance > 1.95 Å) At **4**, the O-O distance elongates to 1.4 Å and O_2 moves farther away from the surface. Green, blue, and red spheres denote Li, Co, and O atoms, respectively.

Slab surface models were constructed from the layered crystal structure reported by Takahashi *et al*. [361] to study the stability of $LiCoO_2$. Three pristine ($LiCoO_2$) and de-lithiated ($Li_{0.45}CoO_2$) surface models were considered (Figure *28*): [012] Li_xCoO_2; [014] Li_xCoO_2; [001] Li_xCoO_2 (x = 1, 0.45). All the surface models were O-terminated when Li atoms were removed from the surface sites to create the $Li_{045}CoO_2$ structures, and the vacuum space normal to the surface was set to

guarantee a separation between the periodic images. The bottom-most atoms were fixed to their lattice site, and the atoms in the top layers were allowed to relax.

Here, ab-initio molecular dynamics (AIMD) simulations were employed to study the evolution of the systems at 400 ^{o}C. Within AIMD, the forces acting on the atoms are obtained through electronic structure calculations. These electronic structure calculations are performed using the plane-wave projector-augmented wave method [362,363] with a kinetic energy cutoff of 400 eV, and the k-point mesh is set to gamma point using the Vienna Ab-Initio Simulation Package (VASP)[364–367]. In this work, the exchange-correlation contribution to the total energy is implemented through the use of the GGA-PBE approximation to the exchange and correlation functional [368].

Spin-polarized calculations were performed for all investigated surface slabs. The DFT+U method introduced by Dudarev *et al*. [369] is applied to take into account the on-site Coulomb interaction of 3d electrons with the U value set to 4.91 eV for pristine ($LiCoO_2$) surfaces and 4.5 eV for de-lithiated ($Li_{0.45}CoO_2$) surfaces [150,370]. Tritium masses were used for hydrogen to set the time step at 1.0 femtoseconds, and the temperature was maintained using the Nosé-Hoover thermostat [371] with configurations belonging to the canonical (N, V, T) ensemble. To study the stability of the structures, we evaluated the Li-Co radial distribution function (RDF) for each surface slab.

Discussion

Using AIMD simulations, instabilities of the [012] and [104] facets are revealed for the $Li_{0.45}CoO_2$ models. At 400 ^{o}C no oxygen species desorbs from the [001] surface for the $LiCoO_2$ models. Similarly, at 300 ^{o}C and when the temperature was increased to 400 ^{o}C, no oxygen species desorbs from the $Li_{0.45}CoO_2$ [001] surfaces as well. On the other hand, Li loss ($Li_{0.45}\,CoO_2$) destabilizes the higher Miller index facets [012] and [104]. When the [012] $Li_{0.45}CoO_2$ surface slab is subjected

to 300 °C, an O_2 species forms and desorbs into the vacuum and the O-O distance evaluated at 900 fs is 1.33 Å, which is slightly longer than the gas phase bond length, 1.21 Å. The Bader charge analysis shows a total charge of -0.012 |e|; therefore, it is an almost neutral molecule. RDF plots depicting the Co-O interactions (Figure *31*) are used to characterize the stability of the facets. The Co-O RDF for the [012] model at 300 °C shows a broadening of the 1st peak when compared to the initial model, with a maximum at 1.875 Å. This broadening is a consequence of the O atoms becoming separated from the crystal surface.

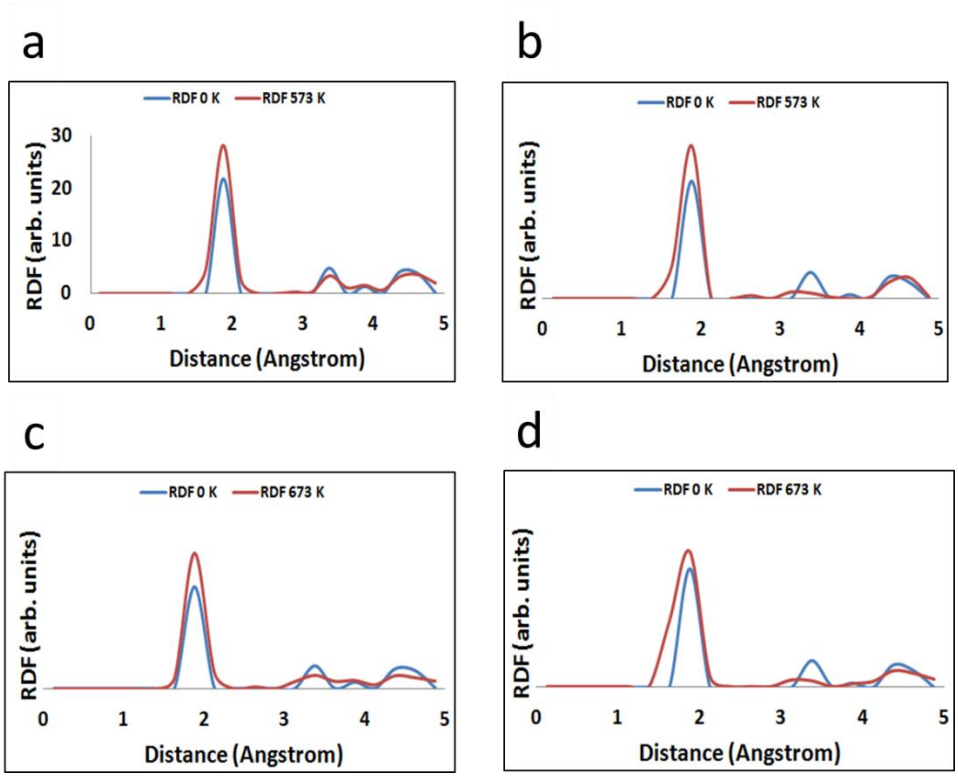

Figure 31. Co-O RDF plots (a)for [012] $Li_{0.45}CoO_2$ at 300 °C , (b) for [104] $Li_{0.45}CoO_2$ at 300 °C (c) for [012] $Li_{0.45}CoO_2$ at 400 °C and (d) for [104] $Li_{0.45}CoO_2$ at 400 °C .

The [104] facet of $Li_{0.45}CoO_2$ shows a similar behavior at 300 °C, where an O_2 species forms and desorbs into the vacuum. The O-O bond length evaluated at 650 fs is approximately 1.44 Å. The Bader charge analysis for this molecule is -0.06 |e|; therefore, it is also a neutral intermediate that

is a precursor to an O_2 molecule. The Co-O RDF plot for this system also shows a broadened first peak with a maximum at approximately 1.875 Å. However, the 2nd peak is flattened, and the 3rd peak is invariant, reflecting variations in the location of the O atoms that are in the process of forming the O_2 molecule. For these models the average Bader charge of the constituent elements is as follows: +0.65 |e| and +0.63 |e| for Li in the [012] and [104] facets respectively; +1.01 |e| and +1.16 |e| for Co in the [012] and [104] facets respectively; and -0.65|e| and -0.72 |e| for O in the [012] and [104] facets, respectively.

We also ran the surface models at 400 °C to detect if additional reactions may be present. Two O_2 species with slightly different O-O bond length elongations appear as precursors of O_2 evolution at the $Li_{0.45}CoO_2$ [012] surface. At 400 fs one of the species has already desorbed from the [012] surface with a 1.46 Å O-O bond bearing a -0.231 |e| total Bader charge. Meanwhile, an O_2 molecule with a 1.35 Å bond distance and a -0.034 |e| Bader charge remains closer to the surface. The formation of this O_2 species causes a distortion in the facet as can be seen from the RDF plot where the 2nd and third peaks are flattened while the 1st peak is broadened. The average Bader charge remained similar to the values obtained at 300 °C: +0.66 |e| for Li, +1.08 |e| for Co and -0.69 |e| for O atoms. Similarly, an O_2 species is also generated from the [104] facet of the $Li_{0.45}CoO_2$ surface slab. The O-O bond distance is approximately 1.46 Å and bears a -0.026 |e| Bader charge, denoting a precursor to a neutral molecule with a slightly elongated bond distance. The average Bader charges in the crystal at 400 °C are: +0.61 |e| for Li, +1.13 |e| for Co, and -0.71 |e| for O atoms. The evolution of the O_2 species causes a local distortion at the surface, substantially moving a Co atom from its lattice site, which results in the broadening of the 1st maxima and complete flattening of the 2nd peak. On average, the Bader charge of the top Co atoms is +1.29 |e| while that of the bottom Co atoms is +0.81 |e|.

Chapter 5: Anti-oxygen Leaking $LiCoO_2$

(Previously published as Sharifi-asl, S.; Soto, F. A.; Foroozan, T.; Asadi, M.; Yuan, Y.; Deivanayagam, R.; Rojaee, R.; Song, B.; Bi, X.; Amine, K.; et al. Anti-Oxygen Leaking LiCoO 2. *Adv. Funct. Mater.* 2019, 1901110. Reproduced with permission[2]. Copyright 2012, Wiley-VCH.)

5.1. Introduction

From the early adoption of Li-ion battery systems in portable electronics, thermal runaway incidents have always been a major concern[343,382]. However, despite the great progress in improving the electrochemical properties of Li-ion batteries, their safety aspects have not advanced significantly, as many still confront thermal runaway incidents in the Li-ion battery containing devices[68,109]. Integration of the Li-ion batteries into the electric vehicle and large-scale transportation systems further stresses the importance of the Li-ion battery thermal stability and safety issues[383–385]. Thus, efforts are underway to better understand the thermal runaway events. In general, thermal runaway is the outcome of a chain of reactions that take root from a slight temperature rise caused by overcharge, fast cycling or high ambient temperature[112,386]. Under these circumstances, cell temperature rises and causes the decomposition of the organic electrolyte, releasing flammable gases. Subsequently, oxide-based cathodes such as $LiCoO_2$ will decompose and lose their lattice oxygen. The released oxygen can ignite the flammable gases, which are heated beyond their flash point, leading to the thermal runaway[103,123,387].

Considering the importance of the layered oxide cathode materials in the commercialization of the lithium-ion batteries, various experimental studies using *in-situ* X-ray diffraction/absorption spectroscopy[62,98,161,206,349], thermal analysis[73,151,152,347,348,354], *in-situ* transmission electron microscopy (TEM)[99,136,175] and computational efforts [140,158] were carried out to characterize and understand the oxygen-release phenomenon and the thermal degradation

mechanisms in these materials. Overall, it is understood that the extraction of Li-ions from the cathode unit cell results in the formation of under-coordinated oxygen atoms, which destabilizes the structure[140]. At elevated temperatures these under-coordinated oxygens break the bonds with the transition metals and form O_2 molecules leaving the host structure. As a result, the layered structure will rearrange to form the spinel and the rocksalt phases that contain less oxygen in their unit cell[136]. It has been shown that the extent of oxygen-release is dependent on the surface fraction of the particles[152].

In addition to safety aspects, there has been a strong thrust in improving the cycling stability and Li-intercalation kinetics of $LiCoO_2$. In this context, synthesis of high surface area structures such as nanorod arrays[388] or porous nanosheet 3D structures[388] of $LiCoO_2$ have been carried out to achieve fast intercalation kinetics and flexible Li-ion batteries. However, since many degradation mechanisms including the parasitic oxygen release reaction, are surface and sub-surface originated[1,389–391], various approaches such as coating[281,296,297,305,316,392], surface passivation[328,393], synthesis of core-shell structures[278–280] and chemical gradient compositions[261] have been pursued for improving the cyclability and stability of cathode materials. For instance, it has been shown that coating the $LiCoO_2$ cathodes with Al, F based material that forms a Li-Co-Al-F-O solid solution beneath the surface can improve the structural stability of LCO when operating at 4.6 V. Similarly, $AlPO_4$ coating on $LiCoO_2$ has shown to effectively prevent the oxygen release reaction and inhibit the over-charge induced thermal runaway reaction[13]. However, large thickness of surface coatings that can potentially increase the charge transfer resistance, the presence of porosities that can allow for O_2 release, decomposition and instability of the coating material[285], uniformity issue associated with deposition techniques and high cost of deposition methods, slow down the inclusion of this approaches into the industry.

In order to improve the thermal stability of the cathodes and simultaneously maintain the electrochemical properties, the surface coating of cathodes should meet a number of requirements; (1) it should be impermeable to the oxygen gas but allow for the Li-ion transfer, (2) have high electronic conductivity, (3) remain stable in contact with the electrolyte, and (4) be scalable and cost effective[394]. In this regard, atomically-thin graphene and its derivatives such as reduced graphene oxide (rGO) appear to be good candidates since it has been shown that graphene and rGO are impermeable to various gases specially oxygen[395–400]. Reduced graphene-oxide has shown a great potential in the gas barrier applications[401]. Also, the rGO membranes are leak-tight against various gasses such as He, N_2 and O_2[402] since the transfer of gas molecules through the rGO layers cannot happen in out-of-plane direction and can only occur through the gaps between the individual rGO sheets and through the interlayer spacings. Therefore, by reduction of GO to rGO and reduction of interlayer distance from 10 Å to 4 Å, the diffusivity of molecules can be effectively decreased[403]. In another study, the layer by layer deposition of few layer rGO through electrostatic bond formation (similar to our case) is shown to decrease the oxygen transfer rate (OTR) of poly(ethylene terephthalate) substrates by 95%[404]. In another work, rGO/polyimide films prepared by *in-situ* polymerization showed to decrease the OTR by 93% compared to pure PI films[405]. Therefore, our goal was set to utilize the gas barrier properties of rGO to inhibit the release of O_2 in the thermal decomposition reaction of $LiCoO_2$. A conformal thin coating of rGO that does not compromise the ionic transport was achieved and O_2 release phenomenon was characterized under high voltage and high temperature conditions. Reduced graphene oxide also benefits from a number of other properties such as superior electronic and ionic conductivity[406–408], high mechanical flexibility[409] and stability in long electrochemical cycling[410]. Herein, we demonstrate coating of individual $LiCoO_2$ cathode particles with reduced graphene oxide to suppress the

oxygen-release from the layered oxide cathodes under high temperature and harsh electrochemical cycling. Using a broad range of electrochemical measurements and materials characterization techniques, such as high voltage cycling, DEMS measurements, *in-situ* heating TEM and thermal analysis, we demonstrated that rGO-coating can successfully mitigate the oxygen release and improve the structural stability of $LiCoO_2$.

5.2. Experimental

Sample preparation. In the present study, commercially available $LiCoO_2$ (Sigma-Aldrich) sample was used as the baseline sample. Graphene coating was carried out using commercially available aqueous dispersed monolayer graphene-oxide (Graphenea). The method of graphene coating is described in previous publications. In brief, for achieving graphene-coating on individual particles, surface charge modification should be carried out on $LiCoO_2$ sample. To do so, $LiCoO_2$ (1g) was dispersed in methanol (100 ml) and sonicated. Then aminopropyltrimethoxysilane (1 ml) was added to the solution and stirred for 24 hours. The sample was then vacuum filtered and washed several times with methanol to obtain the positive surface charged $LiCoO_2$. Graphene-coated $LiCoO_2$ particles then can be obtained as a result of attractive electrostatic force between positively charged $LiCoO_2$ and negatively charged graphene oxide nano-sheets. At this step, surface charged $LiCoO_2$ and graphene oxide nano sheets are redispersed in methanol with the concentration of 10mg/ml and water dispersed graphene-oxide nano-sheets are added dropwise to the solution. As the self-assembly takes place, graphene-coated $LiCoO_2$ precipitate. Finally, hydrazine (1ml per 100 ml of cathode solution) was added dropwise to the solution to reduce the GO layer to rGO to enhance the conductivity of the coating layer. The sample is then vacuum filtered to obtain the graphene-coated $LiCoO_2$ particles. Noteworthy, the cost of such process is calculated to be approximately \$0.48/gr of $LiCoO_2$ in laboratory scale, from which only 3.3% is for consumed GO

material and the rest relates to the cost of surface charge modification and hydrazine treatment that can be reduced in industrial scale.

SEM imaging. SEM was carried out using a Carl–Zeiss electron microscope integrated into a Raith e-LiNE plus electron-beam lithography system. The acceleration voltage was set at 10 kV, and aperture size of 30 µm was used.

Raman spectroscopy. Raman results were obtained from a Renishaw inVia Reflex Raman system equipped with a green 532nm/50mW diode-pumped solid-state laser. Spectroscopy was performed using a 50x objective lens. Dwell time, and laser strength were set to 100 s and 5% to obtain the best signal to noise ratio and avoid the laser-induced damage in the samples.

XPS. X-ray photoelectron spectroscopy was carried out using a Kratos AXIS-165 XPS system, equipped with a monochromatic Al Kα source (1,486.7 eV). Survey spectra were collected with a pass energy of 80 eV, step size of 1 eV and dwell time of 200 ms. High-resolution regional spectra were collected with a pass energy of 20 eV, step size of 0.1 eV and dwell time of 1000 ms.

Electrochemical Cycling. Coin-type cells composed of $LiCoO_2$/Li half cells, glass fiber separator and 1M $LiPF_6$ in EC/DMC = 1:1 electrolyte were fabricated for electrochemical tests. $LiCoO_2$ laminates with the composition of 80 wt% of active material, 10 wt% of carbon black and 10 wt% of poly(vinylidene fluoride were mixed with N-methylpyrrolidone and casted on Al foils, then dried at 80 °C in vacuum.

DEMS. The DEMS experimental setup was consisted of an MTI potentiostat, a mass spectrometer (Hiden Analytical) and a Swagelok type cell with the air outlet on the cathode side. The cell was composed of $LiCoO_2$ and Graphene coated- $LiCoO_2$ samples coated on aluminum mesh as the cathode, 0.5 mm stainless steel spacer, 0.25 mm thick lithium chip, a 0.26 mm thick glassy fiber

separator, and 1M $LiPF_6$ in EC:DMC electrolyte (30 μL). To measure the evolution of oxygen during charging experiment, the cell and DEMS capillary was purged with Argon to remove any impurities before the experiment.

In-situ heating STEM/EELS characterization: After electrochemical cycling, the coin cells were disassembled, and the cathode laminates were submerged into dimethylcarbonate for 1 hour then rinsed with fresh dimethylcarbonate and dried under vacuum overnight. The laminates then were scratched, and the obtained powder was dispersed in methanol, sonicated and drop casted onto lacy carbon grid and loaded into the microscope with minimum exposure to air. Gatan double tilt heating stage was utilized for *in-situ* heating experiments. Samples were subjected to high temperatures ranging from 25 to 450 °C with a heating rate of 10 $°C \cdot min^{-1}$, before collecting data we kept the samples at the desired temperature for 15 minutes to ensure holder stability and temperature uniformity. STEM/EELS investigations were performed using JEOL JEM-ARM200CF STEM equipped with a cold field emission gun with 0.78 Å spatial resolution and a Gatan Enfina EELS system. A 22 mrad probe convergence angle was used to perform STEM imaging. HAADF detector with 90 mrad inner-detector angle was utilized to obtain Z-contrast atomic-resolution images. Spectroscopy was done with 0.1 eV/channel dispersion and with a 2 mm detector aperture. Full-width half maximum of zero loss peak was measured 0.6 eV which determines the energy resolution of the obtained spectra.

DSC. TA Instruments Q2000 DSC systems were utilized to perform the thermal analysis experiments. To capture the heat flow from the exothermic reaction between flammable gases (from the decomposition of electrolyte) and the evolved oxygen (from the charged $LiCoO_2$), the hermetically sealed aluminum containers were utilized. Bare and graphene-coated $LiCoO_2$ samples were cycled twice and then charged to 4.2 V. Then the cells were opened in Argonne filled

atmosphere, and the cathode foils were sealed in the aluminum container without drying or removing the electrolyte. DSC experiments were performed in the range of 25-350 °C with the heating rate of 2 °C/min.

5.3. Graphene-coating of Individual $LiCoO_2$ Particles

Figure 32A is a schematic representation of the coating procedure. *Figure 32B* shows the SEM images from several individual $LiCoO_2$ particles coated with graphene layers. *Figure 32C* presents high magnification SEM images from the indicated areas to better illustrate the graphene-coating of individual $LiCoO_2$ particles. The presence of the ultra-thin graphene can be identified from the graphene wrinkles at the surface of the particles.

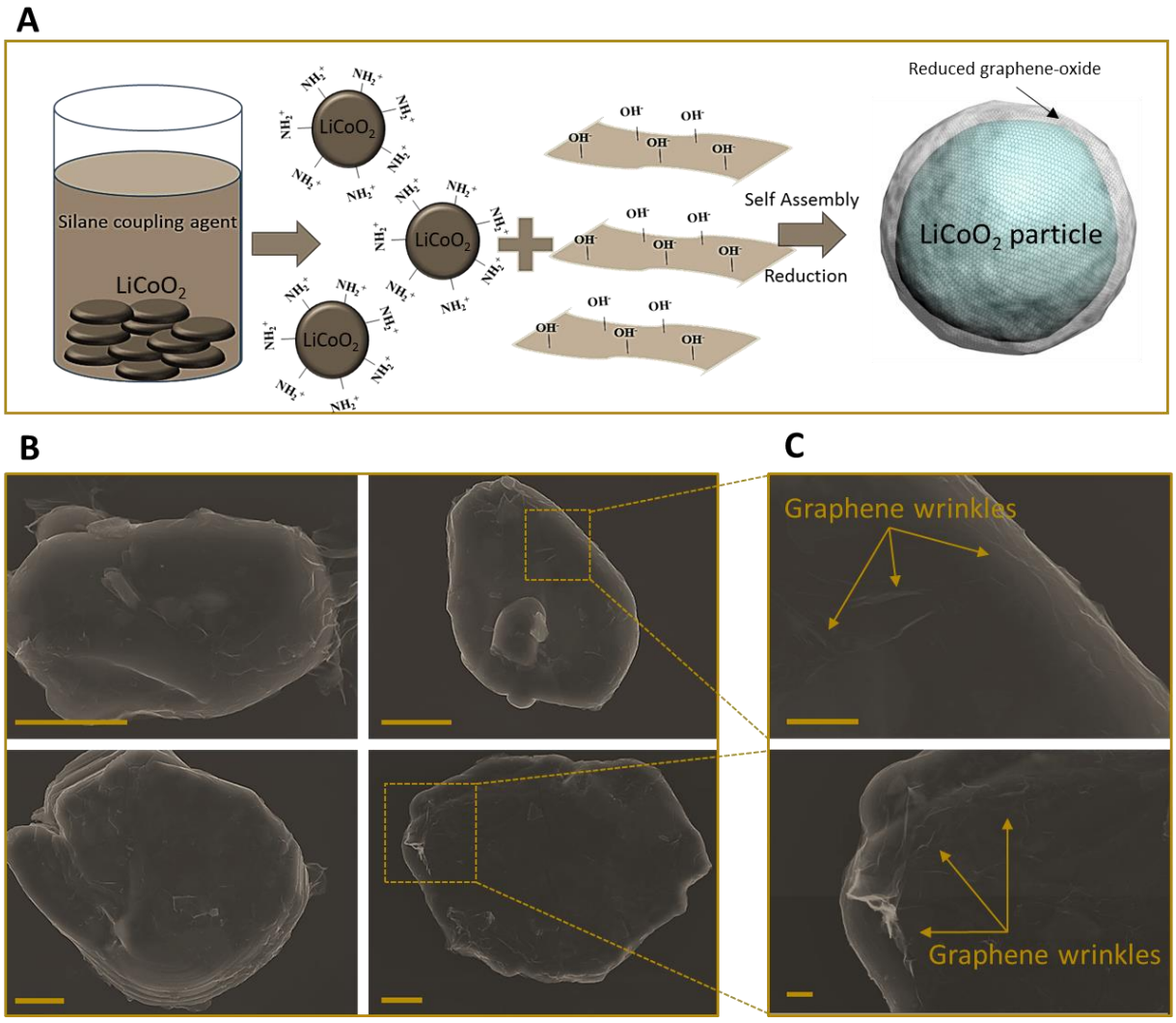

Figure 32. Illustration of graphene-coating method and the confirmation of graphene coverage on the surface of cathode particles. (A) Schematic illustration of the coating process. The surface of $LiCoO_2$ particles is charged positively to facilitate the self-assembly with negatively charged graphene oxide nano-flakes. The resulting material will be individual graphene-coated $LiCoO_2$ particles. (B) SEM images from several individual $LiCoO_2$ particles after graphene-coating (scale bars are 2 μm). (C) High-magnification SEM images from the areas indicated in Panel B. Graphene wrinkles can be clearly observed on the surface of $LiCoO_2$ particles (Scale bars are 500 nm).

5.4. Graphene-coating Characterization (SEM, Raman, XPS and HRTEM)

Further characterization of the graphene-coating $LiCoO_2$ sample was carried out utilizing high-resolution transmission electron microscopy (HRTEM), electron diffraction analysis, Raman

and XPS spectroscopy. From the HRTEM image shown in Figure *33A*, a ~2nm layer of rGO consist of 3-5 layers can be seen on the surface of the $LiCoO_2$ particle. Additional TEM images to confirm the uniformity of coating thickness are demonstrated in Supporting Information Figure *39*. Intensity profile (inset) from the rGO coating illustrates the presence of 4 rGO layers, each ~0.41 nm thick. It should be noted that thickness of the mono layer GO and rGO is reported to be 1.1 ± 0.1 and 0.5 ± 0.2 nm respectively[411,412]. Therefore, it can be concluded that reduction of initial GO layers is achieved by the hydrazine treatment. Also, electron diffraction pattern (shown at the bottom right inset) suggests that the original layered ($R3\bar{m}$) structure of $LiCoO_2$ is maintained after the graphene-coating process. *Figure 33B*, presents the Raman results from the bare and the graphene-coating sample and illustrates the presence of reduced graphene oxide peaks without affecting the bonding properties of $LiCoO_2$ particles. Raman results were obtained which shows Raman active E_g and A_{1g} modes generated from oxygen vibrations in $R\bar{3}m$ $LiCoO_2$ at 482 and 596 cm^{-1} respectively[31]. Reduced graphene oxide D peak and G peak generated from sp^2 carbon lattice can be observed at 1345 and 1595 cm^{-1} respectively with $(I_D/I_G)= 1.71$[406]. X-ray photoelectron spectroscopy (XPS) is also performed on graphene-coated $LiCoO_2$ samples to confirm the reduction of GO layers to rGO through the hydrazine treatment. As can be seen from Figure *33C*, the proportion of oxide groups in the C1s peak is small and shows that GO is successfully reduced to rGO.

The Li-ion diffusion mechanism through the rGO coating is shown to be highly dependent on the defect sites. It is demonstrated that only divacancies and higher order defects have achievable diffusion barrier for Li transfer[18,19]. In addition, the grain boundaries have been found as low energy sites for Li adsorption and diffusion[20]. So it can be concluded that an ultrathin rGO layer

with plenty of defects, low range structural order and oxygen functional groups can enable Li-ion conduction when coated on electrode materials[21].

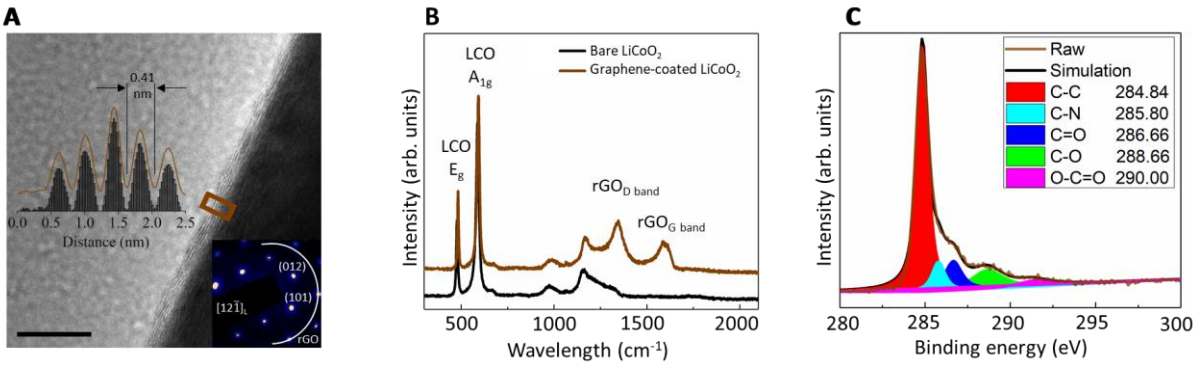

Figure 33. Characterization of graphene-coated $LiCoO_2$ samples. (A) High-resolution TEM image of a graphene-coated $LiCoO_2$ particle and the corresponding diffraction pattern shown in the inset. Diffraction pattern shows that $LiCoO_2$ has retained its original layered structure after the graphene-coating process. The intensity profile is shown in the inset from the red-colored rectangular shows that the rGO coating consists of 3-5 layers of rGO each about 0.41 nm thick and the overall coating thickness is below 2 nm (scale bar is 10 nm). (B) Raman spectrum from the bare and the graphene-coated $LiCoO_2$ sample. Raman active Eg and A1g modes generated from oxygen vibrations in R3$\bar{m}$ $LiCoO_2$ can be observed at 482 and 596 cm^{-1} respectively. Reduced graphene oxide D peak and G peak generated from sp_2 carbon lattice can be observed at 1345 and 1595 cm^{-1}, respectively with (I_D/I_G)=1.71. (C) High resolution XPS scan from C 1s, minimal fraction of carbon bonding with O and N confirms the reduction of GO coting to rGO.

5.5. Electrochemical Cycling and Impedance Spectroscopy

The electrochemical performance of the graphene-coated $LiCoO_2$ under high voltage cycling condition (voltage window of 3.3 - 4.8 V at 0.5 C rate) was evaluated and compared with the bare sample. Figure 34*A* and *Figure 34B* show the first four charge/discharge curves of the samples. Both samples show the first charge capacity of about 250 $mAhg^{-1}$ that is typically observed in $LiCoO_2$ samples[63]. The hexagonal to monoclinic phase transition in the capacity range of ~135 $mAhg^{-1}$ is evidenced by the change of the plateaus at 4.2 V in both samples. Also, two plateaus

corresponding to the formation of H1-3 and O1 phases can be clearly observed at > 4.5 V in the curve of bare $LiCoO_2$. O1 is the hexagonal form of rhombohedral O_3 Li_xCoO_2 and H1-3 is considered as the transition structure with a hybrid rhombohedral/ hexagonal phase[43,417]. The origin of these phase transformations are suggested to be the glide of partial dislocations formed as a result of excessive extraction of Li ions, which eventually provide a path for cation mixing and formation of spinel phase[13,19,57]. By running the derivative (dQ/dV), two plateaus observed in at >4.5 V in the voltage profile of the bare sample will transform into two sharp peaks corresponding to the inflection point within each plateau (Figure 34D). In the second cycle, the second plateau is disappeared which correspond to irreversibility of the ascribed phase transition[29], and the intensity of the first peak has decreased leading to gradual disappearance in the next cycles, as evident from the voltage profile. However, the graphene coated sample is showing a very different behavior. As can be seen from Figure 34B, there is only one plateau at >4.5V in the voltage profile of the graphene coated sample for the initial charge. The derivate (dQ/dV)curve shown in Figure 34E shows that there is only one peak at the 4.5-4.8 voltage window that can be due to suppressed O1 phase formation, as a result of lower delithiation extent in the coated sample, or higher structural stability achieved by the coating. The second possibility is that both plateaus are merged to each other due to lower kinetics of delithiation in the first cycle from the graphene coated cathode particles. This is suggested because of the higher voltage plateau at the initial stages of charging that occurs at over 4.1 V and decreases to lower values for the next cycles.

Also, it is suggested that partial reduction and dissolution of Co at the surface of particles due to direct contact of the cathode surface with the electrolyte is another degradation mechanism, which results in capacity loss and failure of the $LiCoO_2$ cathode[45,52]. However, the coating of cathode particles will put a barrier in the contact of cathode particles and the electrolyte and possibly

hinders the Co dissolution. Nevertheless, the cationic migration leading to partial phase transition that occurs throughout the particles thickness will occur in the graphene-coated sample regardless of the surface condition. Hence, we observed capacity/voltage fade in smaller extents compared to the bare sample. Noteworthy, a higher over-potential in the voltage profile of the graphene-coated sample at the first cycle can be observed. Most probably, this corresponds to the required energy for the Li-ion pathway formation in the coating rGO layers at the first cycle. To confirm that the graphene-coating is effectively suppressing the oxygen-release from the cathode structure, we performed *in-situ* differential electrochemical mass spectrometry (DEMS) experiment on the bare and the graphene-coated $LiCoO_2$ samples (*Figure 34C*). The DEMS experimental setup was consisted of an MTI potentiostat, a mass spectrometer (Hiden Analytical) and a Swagelok type cell with the air outlet on the cathode side. The cell was composed of $LiCoO_2$ and Graphene coated-$LiCoO_2$ samples coated on aluminum mesh as the cathode, 0.5 mm stainless steel spacer, 0.25 mm thick lithium chip, a 0.26 mm thick glassy fiber separator, and 1M $LiPF_6$ in EC:DMC electrolyte (30 μL). To measure the evolution of oxygen during charging experiment, the cell and DEMS capillary was purged with Argon to remove any impurities before the experiment and the experiment was conducted during the linear sweep voltammetry measurement in the potential window of 3-5.0 V. The results from the cell containing the bare $LiCoO_2$ cathode shows the evolution of O_2 at ~ 4.7 V[418] while the results from the graphene-coated $LiCoO_2$ cathode exhibited almost no O_2 evolution throughout the experiment. These results confirm that the graphene-coating completely suppresses the evolution of oxygen during high voltage charging.

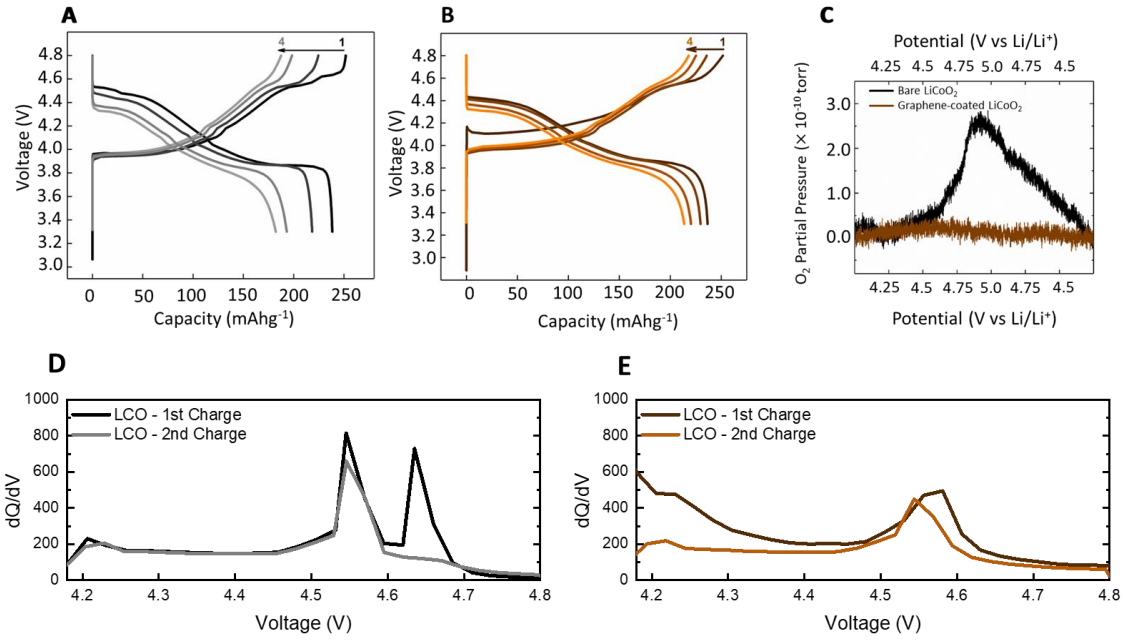

Figure 34. high-voltage cycling stability evaluation of graphene-coated $LiCoO_2$ samples. (A) Voltage profile of bare $LiCoO_2$ cycled at 3.3-4.8 V. (B) Voltage profile of the graphene-coated $LiCoO_2$ cycled at 3.3-4.8 V. (C) Differential electrochemical mass spectroscopy (DEMS) results from the bare and the graphene-coated $LiCoO_2$ during cyclic voltammetry (CV) experiment in the potential window of 4-5.2 V vs Li/Li^+.(D) dQ/dV profile for the intial two charge cycles of bare $LiCoO_2$. (E) dQ/dV profile for the intial two charge cycles of the graphene coated $LiCoO_2$.

Additionally, electrochemical cycling experiments in lower cut-off voltage were performed to evaluate the effect of graphene-coating on the cycling stability of $LiCoO_2$ cathodes under equilibrium conditions, where the organic electrolytes are stable and various degradation mechanisms that activate as a result of excessive Li-removal from the cathodes (e.g. slab sliding, cationic migration and structural transformation to H1-3 and O1 phases) do not occur[6,13,19]. As can be seen from *Figure 35A*, the bare and the graphene-coated $LiCoO_2$ cathodes have been cycled for 200 cycles in the voltage limit of 3.0 - 4.2 V with the current rate of C/10 for the initial formation cycle, followed by 1C current rate for the rest of the experiment. Cycling results demonstrate superior capacity retention for the graphene-coated sample. While the capacity retention of the

bare $LiCoO_2$ is ~55% after 200 cycles[277], the graphene-coated sample has retained about 85.9% of its initial capacity. This enhancement can be attributed to the prevention of direct contact between the electrolyte and the cathode surface, which protects the cathodes against detrimental interface reactions such as HF attack and Co dissolution[419–422]. Furthermore, the electrochemical impedance spectroscopy (EIS) analysis was performed to evaluate the effect of graphene-coating on the electrode resistance. The EIS spectra were acquired after the 1st charge (*Figure 35B*) and the 20th charge (*Figure 35C*) from the bare and the graphene-coated samples. The EIS spectra from charged $LiCoO_2$ exhibits an initial intercept, two semicircles and a 45° inclined line at various frequency regions. The first intercept of the Nyquist plot, R_s represents the internal resistance related to the electrolyte resistance and cell connections. The first semi-circle (high frequency) represents the resistance from the surface film (R_{SF}). This surface film can be either the solid electrolyte interface (SEI) or the rGO coating or a combination of both. Formation of a SEI on the surface of bare-$LiCoO_2$ as a surface film during the first charge has been well-documented in the literature[421,423,424]. Prior reports have shown that the SEI is predominantly composed of Li_2CO_3 and LiOR[424], where R-groups correspond to the organic species from the electrolyte. Although this surface film is known to protect the electrode from further side reactions, it is not stable and can decompose rapidly at high voltage or high temperature[423]. The decomposition and reformation of such surface film can result in electrolyte consumption, cathode surface phase transition and increase in the resistance[421,424]. The second semicircle at middle frequency describes the lithium-intercalation process, which is also known as charge transfer at electrode/electrolyte interface (R_{CT}). Here the very low frequency regime is attributed to the diffusion-controlled behavior and is shown as an inclined line with ca. 45º angle (Warburg phase)[420]. Since Nyquist plot is considering R_{real} and $R_{imaginary}$ for X- and Y-axis respectively, it does not have enough resolution to resolve the

two different time-constants at some frequency levels. This is the main reason that in both graphene coated $LiCoO_2$ and bare $LiCoO_2$ samples, R_{SF} gets coupled to R_{CT} and forms a larger semi-circle. However, we can distinguish the different resistive behaviors upon running the Zsim for modeling the electrical circuit of the batteries. Zsim takes into account the precise frequencies assigned for each specific resistance and models the equivalent circuit[420]. The equivalent electrical circuit model for all EIS spectra is shown as inset in the *Figure 35C*. Table *1* summarizes the resistance values for the components of each spectrum based on the fitted model. The EIS spectra obtained after 1st charge demonstrates a large resistance in the graphene-coated $LiCoO_2$. This behavior is correlated to two reasons; (1) limited Li-ion pathways in the out of plane direction of pristine rGO coating layer[425], (2) improved electronic conductivity of rGO coating due to electrochemical reduction during repeated cycling[426,427]. After 20 cycles and full charge to 4.2 V, the EIS spectra from the graphene-coated sample shows a remarkable decrease in both R_{SF} and R_{CT}. Specifically, R_{SF} and R_{CT} have reduced from 231.6 Ω and 64.1 Ω at first charge to 15.3 Ω and 9.5 Ω after 20th charge. The reduction of the surface film resistance can be attributed to the cumulative reduction of rGO during electrochemical cycling [428–430], which results in improved conductivity of the solid electrolyte interface after initial cycles. In addition, the reduction of R_{CT} can be attributed to the formation of Li-ion transfer pathways in the rGO layers during the initial cycles, where repeated Li transfer causes defect formation and further lowers the measured resistance[425]. In contrast, the EIS results from the bare $LiCoO_2$ after the 1st and the 20th charge show that there is an increase both in R_{SF} (from 17.3 Ω to 21.1 Ω) and R_{CT} (from 6.1 Ω to 14.0 Ω) during cycling. The increase in R_{SF} can be explained by the instability and degradation of the surface film due to the cathode surface degradation and Co dissolution, and increase in R_{CT} can be attributed to the surface phase transitions. Overall, based on the EIS results it can be concluded that the graphene-coating process

does not increase the cell resistance and alleviates the surface degradation of cathode particles by providing a protective coating on the cathode particles surface, thus decreasing the charge transfer and solid/surface film resistance. To further evaluate the technological implication of this research, structural and morphological studies of rGO-coated cathode subsequent to prolonged electrochemical cycling in full cells should be carried out in future.

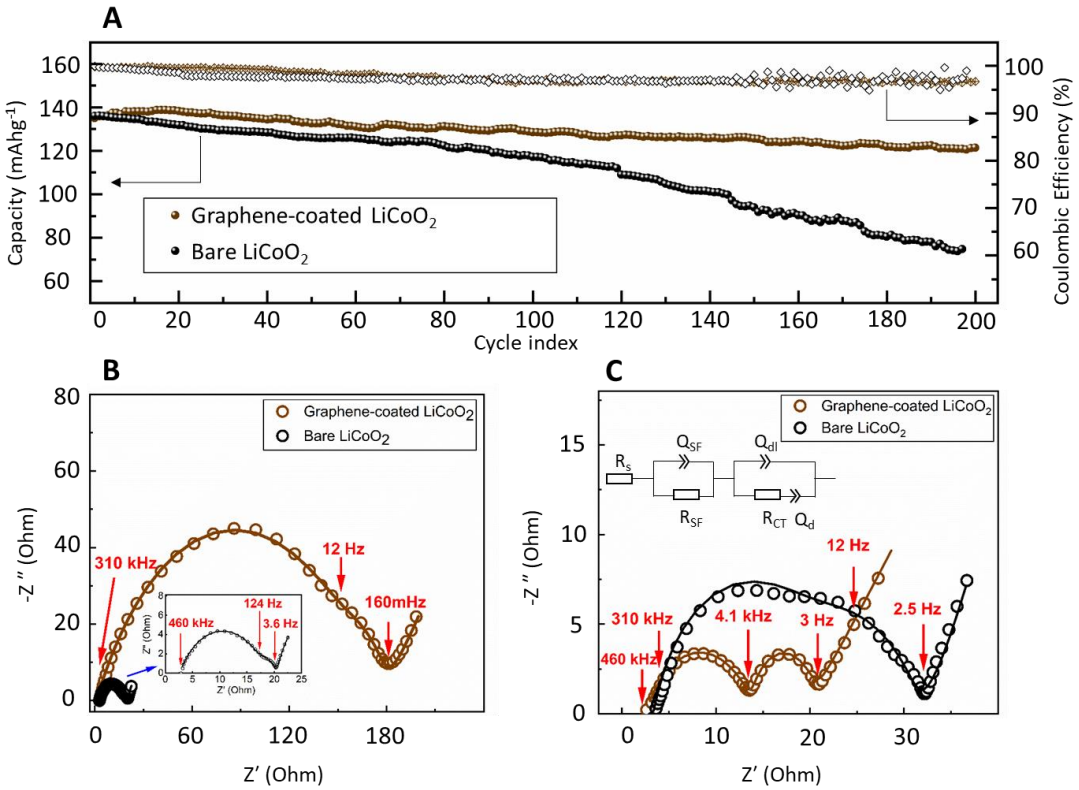

Figure 35. Electrochemical cycling and impedance spectroscopy results. (A) Half-cell cycling test performed on the bare and the graphene-coated $LiCoO_2$. (B) Electrochemical impedance spectra from bare and graphene-coated samples after first full charge, and (C) electrochemical impedance spectra after 20 cycles and full charge. The equivalent circuit is shown in inset (C).

Table 1. Resistance parameters fitted from EIS spectra

Cycle	bare LCO			GLCO		
	Rs (Ω)	RSF (Ω)	RCT (Ω)	Rs (Ω)	RSF (Ω)	RCT (Ω)
1st	2.85	17.3	6.1	1.45	231.6	64.1
20th	3.29	21.1	14.0	2.57	15.3	9.5

5.6. *In-situ* Heating STEM/EELS Analysis and Thermal Analysis

To test the structural stability of the samples under thermal abusive conditions, we performed *in-situ* heating TEM experiments on the bare and the graphene-coated Li_xCoO_2 samples. It is known that the pristine $LiCoO_2$ is thermally stable and oxygen-release occurs after de-lithiation due to the formation of under-coordinated oxygen atoms[1]. Therefore, the bare and the graphene-coated samples were cycled three times and charged to 4.2 V to obtain $Li_{0.5}CoO_2$[431]. *Figure 36A* demonstrates SEM images from the graphene-coated $Li_{0.5}CoO_2$ particles after electrochemical cycling, and evidently, the rGO layer is well maintained on the surface of the particles. Charged cathode particles were extracted and loaded into the Gatan heating holder to perform the *in-situ* heating STEM/EELS experiments. In these experiments, samples were heated to 300 °C incrementally at 50 °C steps. Based on our previous report[1], $Li_{0.5}CoO_2$ is thermally unstable and starts to release oxygen when heated to above 100 °C. This oxygen-release, which results in the reduction of cobalt, can be quantified by analyzing the Co L edges in the EELS signal. To quantify the Co valence state based on the EELS results, we have performed EELS calibration experiments which are explained in our previous work[1]. Specifically, by measuring the cobalt L3, L2 edges ΔE value as a function of temperature and acquisition position, we can quantify the cobalt valence state at each point in our samples and effectively compare the bare and the graphene-coated Li_xCoO_2 structural stability at high temperatures. *Figure 36B* shows a HAADF image from the surface of the graphene-coated $Li_{0.5}CoO_2$ particle, where a thin layer of graphene can be observed. It should be noted that, oxygen-release and reduction of cobalt start from the surface areas of Li_xCoO_2[1]. Hence, by performing TEM experiments on the Li_xCoO_2 particles, the oxygen-release

is initially detected at the surface which by increasing the temperature propagates towards the core areas. Therefore, to understand the role of the graphene-coating on the oxygen-release, we performed the *in-situ* heating EELS experiments as a function of temperature and beam position. *Figure 36C* illustrates the EELS results obtained from the outmost ~5 nm of the surface of particles. As can be seen from the analyzed results based on cobalt L3, L2 edges *ΔE* value in *Figure 36D*, Co valence change at the surface of the particle is effectively delayed by the presence of graphene layer. The reduction of Co from 3+ to 2.6+ that occurs at ~ 100 °C in bare $Li_{0.5}CoO_2$, is postponed to higher than 200 °C for the graphene-coated sample. Also, further reduction of Co species to 2+ which is observed between 200-300 °C does not occur in the graphene-coated sample up to 300 °C. It should be noted that lower signal to noise ratio in the spectra from the graphene-coated samples is due to shorter acquisition time to avoid electron beam damage to the graphene layer. Furthermore, we performed EELS line scanning at each temperature to track the extent of oxygen-release from the cathode particles. To compare the degradation extent in both samples, we considered the valence of 2.6+ as the degradation threshold and measured the degradation extent accordingly as a function of length in the bare and graphene-coated samples at each temperature. Accordingly, by reaching to 100 °C, reduction of cobalt and oxygen-release occurs in a layer of 10 nm at the surface of the bare $Li_{0.5}CoO_2$ particles. However, the graphene-coated sample shows higher thermal stability, and the reduction of cobalt can be seen in < 5nm from the surface of the sample after increasing the temperature to higher than 150 °C. When the temperature reaches 300 °C, the thickness of this damaged layer reaches to 50 nm in the bare $Li_{0.5}CoO_2$, while it is only about 10 nm for the graphene-coated sample. These observations can be explained in two ways: (1) graphene-coating does not allow the formation and release of O_2 molecules since oxygen species bond with carbon atoms from the rGO layer, and breaking such bonds has a high barrier

energy. (2) If O_2 is formed, graphene layer inhibits the release of O_2, which results in a O_2 rich atmosphere underneath the rGO layer that hinders the further O_2 release from the surface of the cathodes. This hypothesis is supported by the recent work from Karki *et al.*[432], where inhibiting the O_2 release from the layered oxide cathodes was achieved in O_2-rich atmosphere. Their environmental controlled *in-situ* heating STEM/EELS results suggest that in O_2 atmosphere oxygen release and reduction of transition metals in the layered oxide cathode framework is significantly delayed and thus the structure is more stabilized. Although, applying O_2 gas to a Li-ion battery for mitigating the thermal runway is not a sensible approach, their study supports our hypothesis and confirms the discussed mechanism.

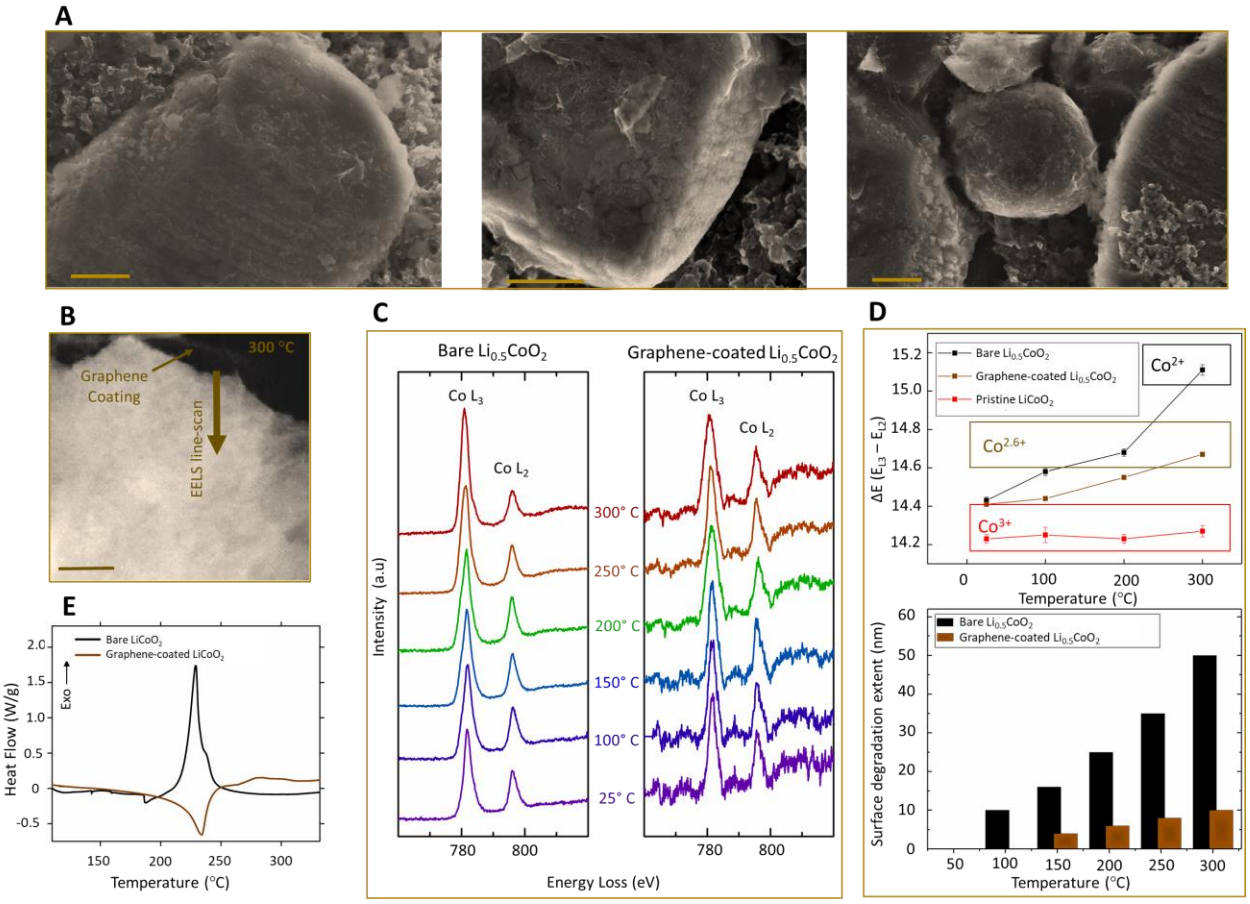

Figure 36. Thermal stability evaluation of graphene-coated Li_xCoO_2 sample. (A) SEM images from de-lithiated (charged) $Li_{0.5}CoO_2$ sample (scale bars are 1 µm). (B) Low magnification STEM

image at 300 °C showing the presence of graphene coating (scale bar is 100 nm). (C) EELS analysis results from *in-situ* heating experiments. Reduction of cobalt at high temperatures is delayed by the presence of graphene coating. (D) EELS line scan analysis results demonstrate the thickness of the layer with reduced cobalt species and released oxygen. At 100 °C, no valence change could be observed at the surface of the sample. At 200 °C, the thickness of the degraded layer is measured to be less than 10 nm compared to the bare sample. (E) DSC results from the bare and graphene-coated $Li_{0.5}CoO_2$.

In addition, the oxygen-release and thermal decomposition is accompanied by structural degradation and phase transformations from original layered structure to spinel and rocksalt phases. Through dark filed TEM imaging and atomic resolution STEM analysis, it has been identified that such phase transformations result in evolution of distinct spinel/rocksalt grains on the subsurface and shell of the layered cathode particles respectively[1]. Therefore, visualization of the effect of graphene-coating on the structural stability of the $Li_{0.5}CoO_2$ particles is also possible. Supplemental Movie 1, taken in the ronchigram mode from a graphene-coated $Li_{0.5}CoO_2$ illustrates the effect of graphene-coating on the structural stability of the cathode. In the Ronchigram mode, Kikuchi patterns that are the indication of crystal structure and its zone axis with respect to the electron beam will also show up. Here we demonstrate an interesting case, which is a particle with a discontinuity in the graphene coating. Due to the discontinuity in the coating layer of the shown individual particle, the effect of graphene-coating on the structural stability can be comprehended from this movie. Snapshots of this movie are shown in *Figure 37*. In the area with the presence of the graphene coating strong contrast from the Kikuchi pattern confirms that the layered crystal structure is maintained at 300 °C (*Figure 37B*). However, by looking at the area where graphene layers have been discontinued, this pattern cannot be observed which implies that the original layered structure is collapsed and disordered-spinel and rocksalt phases in small distinct grains are formed on the bare side of $Li_{0.5}CoO_2$ particle surface (*Figure*

37C). The evidence of phase transformation from layered structure to spinel and rocksalt phases can be found here[1]. It should be noted that acquisition of diffraction patterns that requires high dose exposure of the electron beam on the sample and the graphene layer, can generate knock-on damage in the graphene layer and diminishes its effectiveness in suppressing the O_2 release. Therefore, ronchigram movie is presented to illustrate the effect of graphene-coating on the structural stability of the $Li_{0.5}CoO_2$ cathode. To further investigate the significance of oxygen evolution in the partially-coated $LiCoO_2$ particles, we performed EELS line scans on areas indicated in *Figure 37A* at 300 °C. The line scans are obtained perpendicular to the surface of the sample on the top 60 nm distance from the surface with 10 nm step size (*Figure 37D*). Results are analyzed based on the energy difference between Co L_3 and L_2 edges. By plotting the results from each point as a function of ΔE, it can be observed that Co species in areas with graphene-coverage are reduced from 3+ to 2+ only in the top 10 nm layer and the Co species in underneath areas maintain their valence state (*Figure 37E*). In contrast, the reduction of Co species in the non-coated areas grew for 50 nm underneath of the surface. It should be noted that these numbers represent the lateral distance of the analyzed points from the surface of the specific particle and do not correspond to the thickness or the cross section of particles.

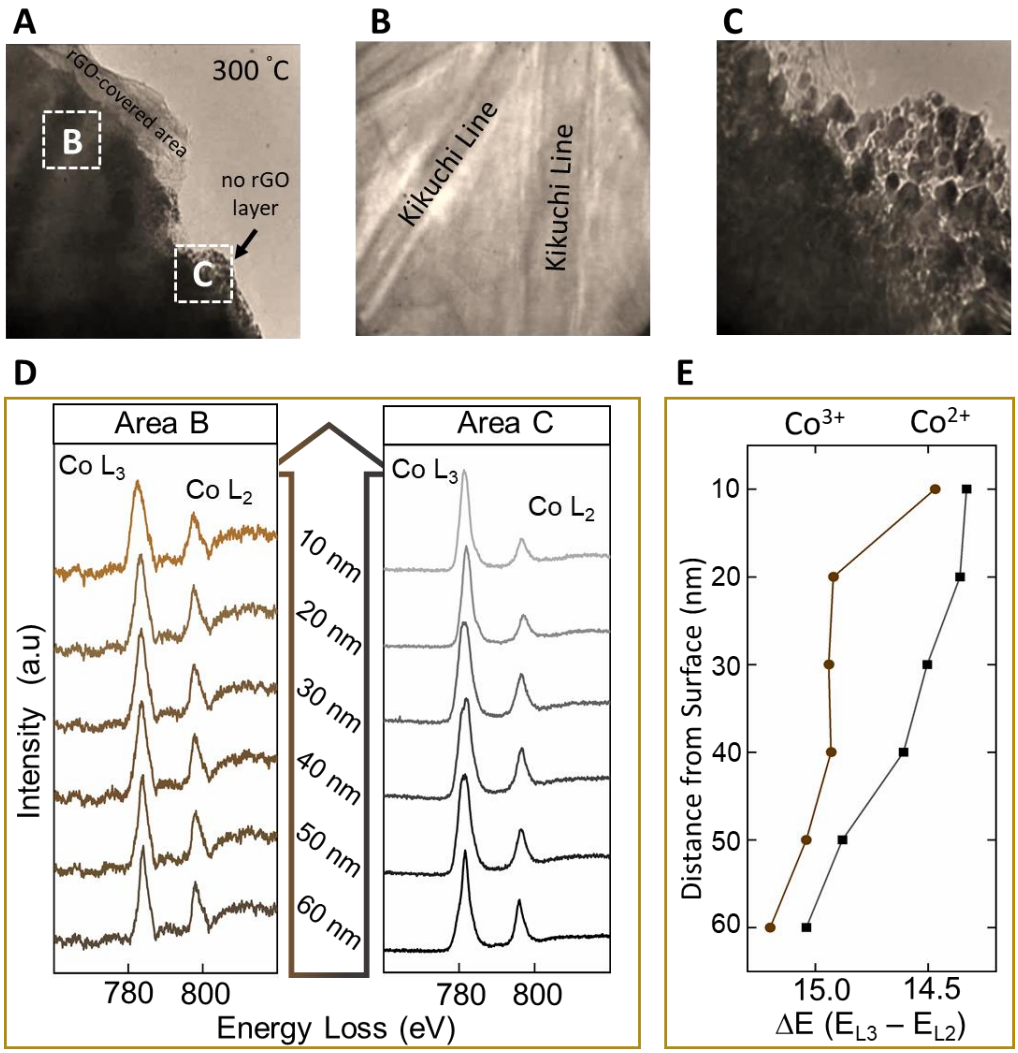

Figure 37. Snapshot from TEM movie of a partially coated Li_xCoO_2 at 300 ˚C with corresponding EELS results. (A) Snapshot from the lower magnification showing an area with partial graphene coating. (B) Snapshot from the graphene-covered area shows the Kikuchi pattern confirming the preserved layered structure in this area. (C) Snapshot of the area without graphene-coverage shows the typical Li_xCoO_2 structural degradation at elevated temperatures. (D) EELS line scan results obtained at 300 °C from the areas indicated in the panel A. (E) Energy difference of Co L_3 and L_2 edges (ΔE) as a function of distance from the surface.

In addition, bulk scale characterization of the thermal stability of the cathode sample has been carried out by DSC experiments. TA Instruments Q2000 DSC systems were utilized to perform the thermal analysis experiments. To capture the heat flow from the exothermic reaction

between flammable gases (from the decomposition of electrolyte) and the evolved oxygen (from the charged $LiCoO_2$), the hermetically sealed aluminum containers were utilized. Bare and graphene-coated $LiCoO_2$ samples were cycled twice and then charged to 4.2 V. Then the cells were opened in Argonne filled atmosphere, and the cathode foils were sealed in the aluminum container without drying or removing the electrolyte. DSC experiments were performed in the range of 25-350 °C with the heating rate of 2 °C/min. *Figure 36E* corresponds to the DSC results from the bare and graphene-coated cathode that have been charged to 4.2 V after two charge/discharge cycles. The sharp exothermic peak, which can be seen around 210 °C in the DSC curve from the bare $Li_{0.5}CoO_2$ is the result of highly exothermic reaction between the flammable gases evolving from the electrolyte and the released oxygen from the cathode. It should be noted that, the DSC results were performed in the hermetically sealed containers to keep the released flammable gases and oxygen inside to complete the reaction. Interestingly, the results from the graphene-coated $Li_{0.5}CoO_2$ shows a significant reduction in the extent of this exothermic reaction and almost no exothermic event can be recorded from this sample, which means that oxygen evolution is extensively hindered due to the graphene-coating process. The reason for observing a slight endothermic peak is that, a small amount of O_2 release is still taking place on the graphene-coated surfaces (as demonstrated in *Figure 36*D). However, the graphene layer does not allow for the interaction of the released oxygen with the decomposed electrolyte and acts as an impermeable membrane. The released oxygen remains under the graphene layer and form an oxygen rich environment on the cathode surface, which mitigates the further release of oxygen[433]. The experiments were performed on more samples to ensure the reproducibility.

5.7. Computational Modeling of rGO/LCO structure (*Done by Professor Balbuena's group at Texas A&M University*)

To explain the experimental observations and to understand how the graphene coating could prevent/delay the release of oxygen from the cathodes surface, comprehensive computational modeling, utilizing density functional theory (DFT) and *ab-initio* molecular dynamics (AIMD) were carried out. Using such complementary modeling techniques, we studied the effect of graphene coating on the activation/barrier energy of the O_2 release reaction as well the dynamics of the rGO/LCO surface interactions at the atomic scale. The details of the DFT model configuration are discussed in the Supporting Information. Before proceeding to compute the reaction energies and activation barriers for O_2 formation in presence of rGO coating, we carried out cNEB calculations to obtain activation energies for O_2 formation in the bare (012) and (104) facets of $Li_{0.5}CoO_2$. Here, the reaction energy is defined as the energy of the product minus the energy of the reactant. Meanwhile, the activation energy is defined as the energy difference between the ground state energy and the transition state. It is important to note that zero-point energies are not included for the calculation of these electronic energies. Based on our previous study, side facets are more prone to oxygen release compared to the top (001) facet[1]. Therefore, side facets such as (012) and (104) that are prone to oxygen release are chosen for the modeling in this research. Optimized structures are used as the initial state structures for cNEB calculations. For final state structures, one $O_{cathode}$ atom was removed from the Co-$O_{cathode}$ bond and located near an adjacent $O_{cathode}$ atom to recombine as an O_2 molecule with an O-O bond length of 1.25 Å. Our results indicate that the motion of a surface $O_{cathode}$ atom to recombine as an O_2 molecule with a nearest-neighbor O atom occurs by a jump of approximately 2.82 Å. The reaction energies at the (012) and (104) facets are -1.61 eV and -1.72 eV, respectively. These energies are highly exergonic indicating that both facets are expected to undergo O_2 formation under non-equilibrium conditions.

The cNEB calculations show that the O_2 formation at the bare (012) and (104) facets need to overcome the activation energies of $E_{activation}$ = 0.14 eV and 0.23 eV, respectively (Figure *38A*). The Arrhenius equation $\kappa = \nu * e^{\frac{Eactivation}{kT}}$ with a prefactor of $\nu = 10^{13}\,s^{-1}$ yields that the time to see an O_2 formation event at 400 °C at the (012) and (104) facets are very close and have an average of 3.20 picoseconds. This evolution time is in the same order of magnitude of events observed in AIMD simulations that will be discussed later on.

Next, we calculated the O_2 formation energy barrier at the facets in the presence of a rGO coating material. As discussed in the Supporting Information, the undercoordinated $O_{cathode}$ atoms form chemical bonds with C atoms from the graphene layer. Following the procedure described in the previous section, which is inducing O_2 formation through breaking the Co-$O_{cathode}$ bonds at the rGO-coated facet, we observed that the $O_{cathode}$ atom is rejoining the C atom from rGO layer. In other words, the simulations show that no O_2 formation can be observed in presence of a fully covered rGO coating. This is because complete coordination of oxygen atoms by bonding with the C atoms from the rGO layer. As another condition, we assume that the rGO material is not covering the complete surface and there are uncovered domains in the rGO coating layer such as defect sites. We considered that the first O atoms are bonded to the C atom from the graphene layer and the second O atoms are in the defective area and are undercoordinated. Our calculation demonstrates that formation of an O_2 molecule at the (104) facet under the described circumstances yields a reaction energy of $E_{reaction}$ = -0.88 eV and an activation energy barrier of $E_{activation}$ = 2.77 eV. According to the Arrhenius equation, such reaction will take more than 16600 hours to happen at 400 °C, which is kinetically unfeasible. So it can be concluded that, while the bare surfaces are expected to undergo O_2 evolution within the first few picoseconds, the rGO coating material forms a stable interface with the side facets due to its chemisorption via C-$O_{cathode}$ bond formation,

leading to higher reaction energies and activation barriers of the O_2 formation at non-equilibrium conditions. Figure *38A* and Figure *38B* demonstrate O_2 formation Energy profile based on DFT calculation for the bare and the rGO coated (104) slabs together with the snapshots of the initial state (IS), transition state (TS) and final state (FS).

Moreover, AIMD simulations were performed to better understand the interaction of the rGO-coating layer with the Li_xCoO_2 species at the elevated temperature. Figure *38C* shows the AIMD results from the bare (012) facet of $Li_{0.5}CoO_2$ before and after temperature elevation, where rapid release of O_2 molecule can be observed after 400 fs. It should be noted that it is very well known that the DFT PBE exchange-correlation functional overestimates O_2 atomization energies[434], which may lead to the extremely rapid release of O_2. Hence, we applied PBE+vdW+U (U-J correction of 4.75 eV only applied to the Co atoms), and we also tested alternative approaches using the revised PBE (revPBE)+vdW+U and plain PBE methods to maximize the accuracy of our results. We checked the evolution of the bare and rGO-coated (012) $Li_{0.5}CoO_2$ by AIMD simulations starting from the revPBE+vdW+U (see the Supporting Information for further clarification). Results from rGO interaction with the $Li_{0.5}CoO_2$ side slab (Figure *38D*) indicate that, at 400 °C, the rGO layer moves closer to the $Li_{0.5}CoO_2$ surface slab and C atoms from the rGO layer form bonds with the under-coordinated O atoms found at the surface. The C-O bond formation takes place within the first 500 fs of the simulation time. Therefore, the formation of the C-O bonds prevents the formation of O_2 molecules. After 4 ps of the simulation time, our simulations of the rGO/$Li_{0.5}CoO_2$ (012) interface indicates some O_2 evolution, which is a significant delay compared to the O_2 formation in the span of 500 fs in the bare sample[1]. This is in accordance with the experimental results that show a reduction of Co species at the surface of the graphene-coated $Li_{0.5}CoO_2$ with a delay and to lower extent compared to the bare sample. Overall,

by studying the dynamics of the rGO/Li_xCoO_2 interfaces at 400 °C we conclude that the graphene-coating improves the structural stability of the facets by two mechanisms; (1) graphene-coating does not allow the formation and release of O2 molecules since oxygen species bond with carbon atoms from the rGO layer. (2) If O2 is formed in the defective sites of rGO coating, graphene layer inhibits the release of O2, which results in a O2 rich atmosphere underneath the rGO layer that hinders the further O2 release from the surface of the cathodes[432]. Noteworthy, authors acknowledge that the trajectory times in AIMD modeling are in the span of pico-seconds and may not capture all the possible reaction in a certain system. Therefore, we performed both DFT and AIMD modeling to compensate such fundamental shortcomings of each modeling approach and obtain the most reliable and accurate understanding.

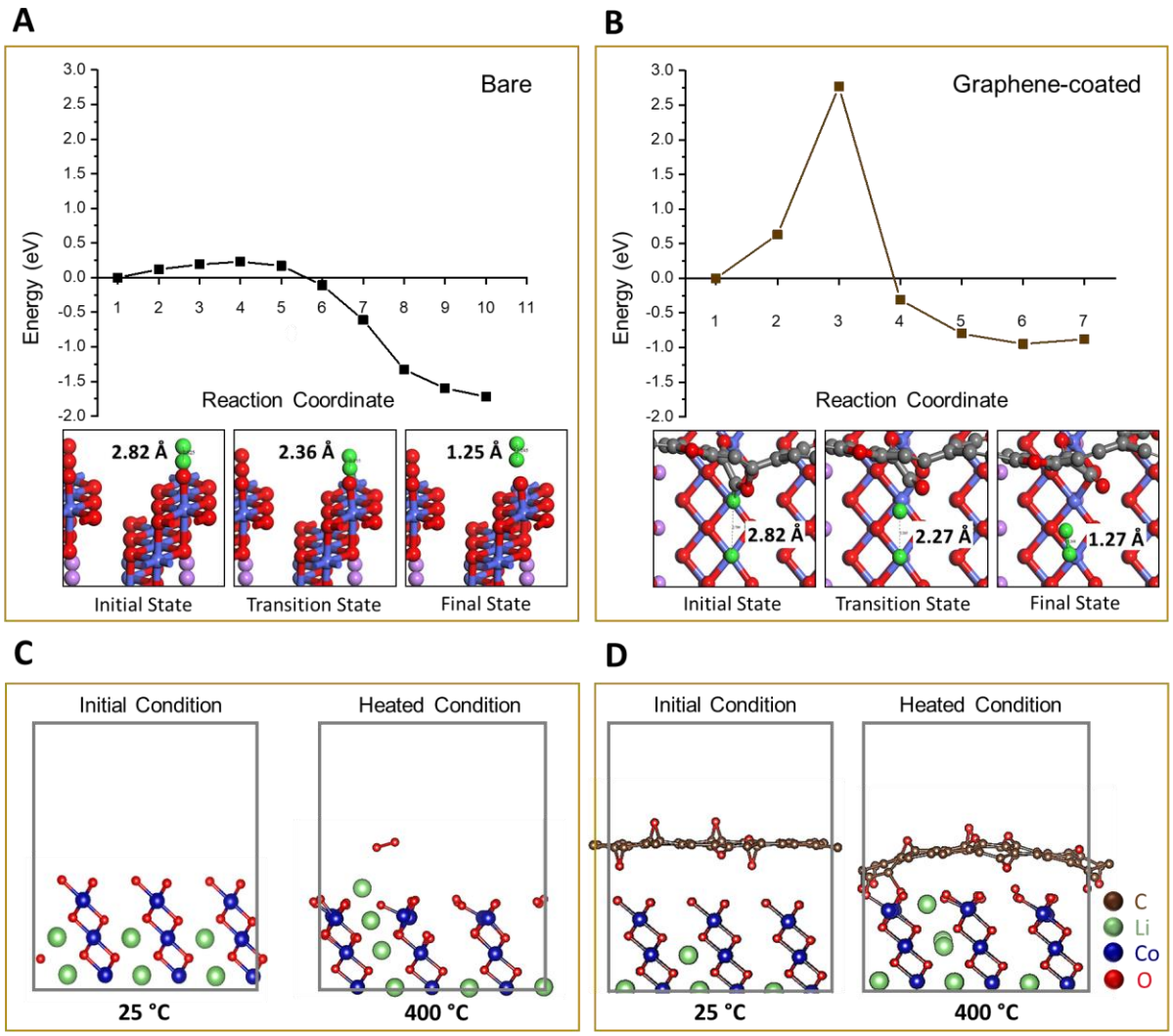

Figure 38. O_2 formation energy profile based on DFT calculations and AIMD modeling results. (A) Energy profile for O_2 formation for the bare $Li_{0.5}CoO_2$. (B) Energy profile for O_2 formation for the rGO coated $Li_{0.5}CoO_2$. Snapshots of the initial state (IS), transition state (TS) and final state (FS) structures are also shown. Green spheres represent $O_{cathode}$ atoms forming the O_2 molecule. (C) AIMD results from the bare $Li_{0.5}CoO_2$ (012) slab at 25 °C and 400 °C after 400 fs. (D) AIMD results from the rGO coated $Li_{0.5}CoO_2$ (012) slab at 25 °C and 400 °C after 4,320 fs.

5.8. Summary and Conclusion

In summary, this work proposes graphene-coating of $LiCoO_2$ to suppress the oxygen-release from oxide-based cathodes. Our electrochemical cycling and *in-situ* DEMS results show that graphene-coating impedes the degradation of $LiCoO_2$ under high cut-off voltage cycling. *In-*

situ TEM/EELS technique and thermal analysis show that the reduction of Co species and oxygen-release is effectively suppressed with the presence of graphene layer. The mitigation of oxygen release by graphene-coating has been explained in two ways: (1) bonding between the oxygen atoms from the cathode surface with carbon atoms from the rGO coating increases the energy barrier for O_2 formation and (2) the impermeable graphene layer hinders the release of any formed O_2, thus results in a O_2 rich atmosphere underneath the rGO layer that hinders the further O_2 formation from the surface of the cathodes. Overall, we believe these results pave the roadmap for the design of thermally-stable oxide cathodes enabled by two-dimensional materials. Such realization is critical for *safe,* high voltage cathodes. Another advantage of our approach is its economic viability since our graphene-coating technique is simple, effective, and scalable for large-scale applications.

5.9. Supplementary Information

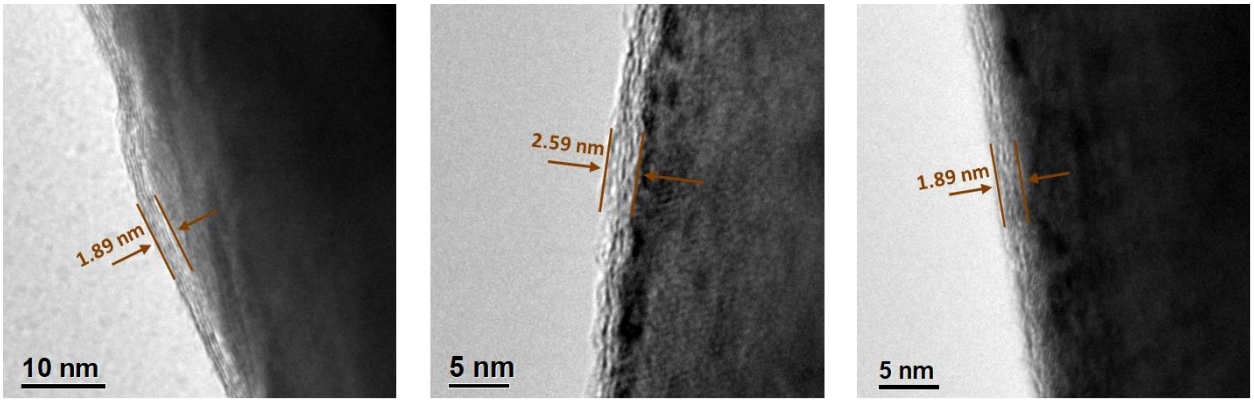

Figure 39. Additional TEM images from various rGO-coated LCO particles that demonstrate the uniformity of the coating and acceptable homogeneity of coating thickness among various particles.

DFT Simulations Details. RPBE and Co Oxidation State. (Done by Professor Balbuena's group at Texas A&M University)

Our DFT model consists of a rGO ribbon having the top atoms saturated with H atoms while at the bottom C sites are able to interact with the oxide surface. The final stable structures obtained after geometry optimization are shown in *Figure 40*. The rGO coating material chemisorbs at LCO facets. The simulations show that the rGO coating material chemisorbs to the particles surface with C atoms bonding to under-coordinated $O_{cathode}$ atoms (where $O_{cathode}$ atoms are under-coordinated atoms interacting with the rGO coating material). To avoid an excessive computational cost, we reduced the height of the rGO coating material and only considered a fragment from the rGO coating material connected to the (104) facet for our cNEB calculations. Optimization of the rGO-coated (104) slab shows that the interface bonding occurs via C-$O_{cathode}$ bonds with a C-$O_{cathode}$ bond length of approximately 1.66 Å. The optimized configuration shows that the $O_{cathode}$ atoms

interact with the Co atoms at approximately 2.11 Å, which results in an elongation of the bonding compared to the initial Co-$O_{cathode}$ bond length of approximately 1.66 Å.

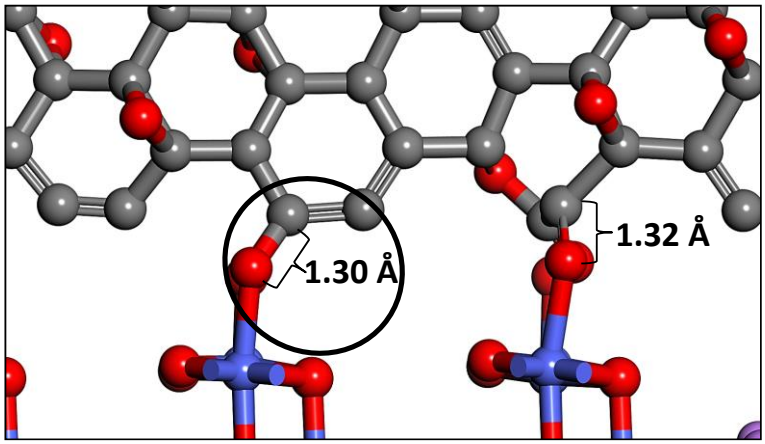

Figure 40. The front view of the optimized rGO-coated (104) slab. Selected C-$O_{cathode}$ bonds are circled in black. Color code: Red, blue and gray spheres represent O, Co and C atoms; respectively.

The DFT PBE exchange-correlation functional overestimates O_2 atomization energies[434]. We checked the atomization energy with the RPBE functional by Hammer *et al.*[435] using the following equation:

$$E_a = 2*E_O - E_{O2}. \quad (1)$$

Here, E_a, E_O, and E_{O2} represent the atomization energy, energy of a single O and energy of an oxygen molecule. An O atom was placed in the middle of a 15 Å cube to perform a single point energy calculation. The O_2 molecule was placed inside of a simulation box with the following dimensions: a = 8.480 Å, b = 14.945 Å and c = 16.750 Å. The dimensions of the box are similar to the ones used in the AIMD simulations. According to the values in Table *2*, the error in calculating the atomization energy of O_2 is 0.95 eV and 0.56 eV for PBE and RPBE, respectively. Compared to the experimental value, the error is smaller for the RPBE functionals. Thus, the use of RPBE substantially weakens the $O_{cathode}$-$O_{cathode}$ bond.

Table 2. Calculated O_2 atomization energy with DFT PBE and RPBE functionals.

Theory level	Atomization Energy (eV)
PBE	6.07
RPBE	5.68

Furthermore, we followed a similar procedure presented by Aykol *et al.*[436] to determine the effect of +U on the magnetic moment of the outermost Co atoms of the (104) $Li_{0.4}CoO_2$ slab. Aykol *et al.*[436] reported a sharp metal-insulator transition (MIT) and magnetic moment transition for the $LiCoO_2$ cell. Here, we show in *Figure 41* a magnetic moment versus U plot where a slight change in the magnetic moment values is noticeable at U = 2.5 eV. Thus, we followed a procedure as reported by Aurbach, Majors, and co-workers[437] to calculate the oxidation state of the outermost Co atoms in the coated (104) $Li_{0.4}CoO_2$ slab at U = 2.5 eV. We assign the oxidation state by calculating the number of unpaired electrons based on the local magnetic moment using the spin-only formula:

$$\mu = \sqrt{n(n+2)} \qquad (2)$$

Where μ is the local magnetic moment (in Bohr Magneton units) and n is the number of unpaired electrons. From *Figure 41*, the magnetic moments calculated with the RPBE functional and a U = 2.5 eV correction lead to zero unpaired electrons, that when taking into consideration the $3d_74s_1$ configuration for the valence electrons of Co provided by the projector-augmented-wave (PAW) potentials[362,363], results in a majority of Co atoms at the low-spin (LS) Co^{2+} oxidation state.

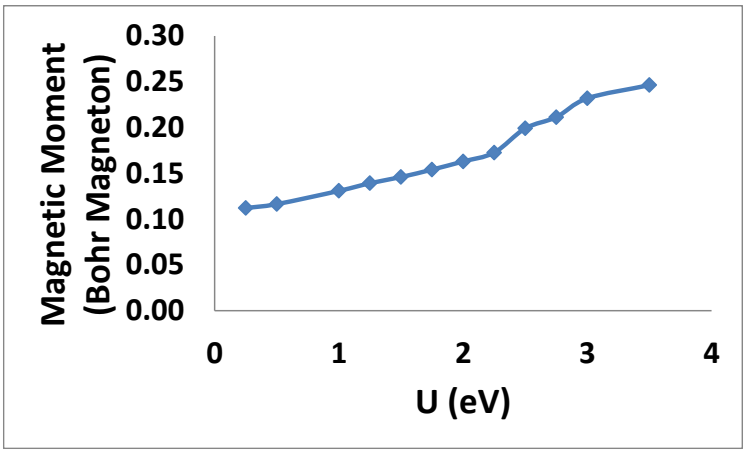

Figure 41. The magnetic moment for outermost Co atoms in the (104) $Li_{0.44}CoO_2$ slab as a function of U.

AIMD simulations. Ab-initio molecular dynamics (AIMD) simulations of the rGO/Li_xCoO_2 interfaces at 400 °C are carried out to investigate the case where rGO layer has a distance with the LCO facets and thus is not forming direct C-O bonding to the surface. The results show that the graphene-coating improves the structural stability of the facets by (1) preventing and delaying O_2 formation and (2) trapping the formed O_2. Our previous observation showed that in the bare Li_xCoO_2 particles, the under-coordinated $O_{cathode}$ atoms rapidly join to form O_2 molecules in (012) and (104) facets. Regarding the observed formation of O_2 in the AIMD simulations, it is extremely well known that the DFT PBE exchange-correlation functional overestimates O_2 atomization energies[434] which may lead to the following interpretation: the rapid release of O_2 is due to the large overestimate of the O_2 formation energy. To confirm that this is not the case in our models, we ran AIMD simulations of the thermally unstable Li_xCoO_2 facets and rGO-coated Li_xCoO_2 using two different combinations of functionals and van der Waals (vdW) corrections: 1) plain PBE, and 2) the revised PBE (revPBE)+vdW+U. Moreover, we want to highlight that the atomization energy of O_2 is only one of the important components leading to O_2 release. In this case, the dynamics of the surface and the interaction of the coating layer with the surface are additional very important aspects of $O_{cathode}$-$O_{cathode}$ recombination and O_2 evolution. Therefore, to illustrate the significance

of rGO the coating on the O_2 formation in comparison with the PBE functionals, rGO layer was displaced in this model to be further away from the cathode surface to avoid the C-O bond formation (*Figure 42*).

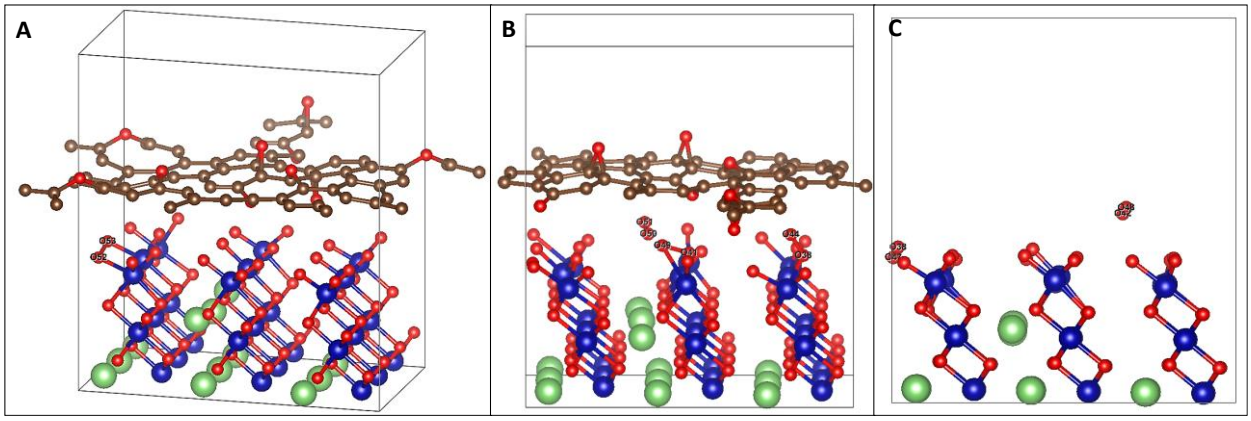

Figure 42. (A) Snapshot of the structure of the coated (012) $Li_{0.4}CoO_2$ slab layer at 879 fs of simulation time using the PBE functional without +U and vdW corrections. (B) Snapshot of the structure of the coated (012) $Li_{0.4}CoO_2$ slab at 159 fs of simulation time using the revPBE+vdW+U functional. (C) Snapshot of the structure of the bare (012) $Li_{0.5}CoO_2$ slab at 667 fs of simulation time using the revPBE+vdW+U functional. Color code: Green, blue, red, and brown spheres represent Li, Co, O, and C atoms, respectively.

Panel A in Figure S5 shows the configuration of the system after 879 fs of simulation time using the PBE functional. Here, two under-coordinated $O_{cathode}$ atoms (labeled O53 and O52 in *Figure 42*) move closer at a distance of 1.53 Å, yet no desorption takes place at this time. The second test with the revPBE+vdW+U functional results in a rapid O_2 formation and release (see panel B in *Figure 42*). The release of O_2 (atoms labeled O51 and O50 in Figure S5) takes place within 160 fs of simulation time. This confirms that even by using revised PBE (revPBE)+vdW+U that reduces the overestimation of O_2 atomization energy, O_2 formation and release occurs in a shorter duration of time. Moreover, as seen in panel B of *Figure 42*), other O_2 molecules are already formed at the cathode's surface (one O_2 formed by the atoms labeled O41 and O49 and the other O_2 formed by atoms labeled O38 and O44). The evolved O_2 has an elongated bond length of 1.28 Å. Panel C in

Figure 42 shows that in the absence of a barrier, the evolved O_2 moves farther away from the surface. Incidentally, these simulations show that O_2 molecules can be formed underneath the rGO layer. The O_2 formed at the surface and evolved O_2 are found to be in the triplet state (ground state). This was done by checking the magnetic moment of the O atoms at the end of the AIMD simulation run. To be clear, the singlet oxygen (excited state) is associated with a magnetic moment equal to zero.

Regarding the role of the barrier with the revPBE functional, the snapshots that are shown in *Figure 43* indicate that O_2 formation is delayed in the rGO-coated (012) $Li_{0.5}CoO_2$ slab. These results are in accordance with the experiments and with the PBE+vdW+U/AIMD simulations. Specifically, panel C in *Figure 43* shows that the O_2 formation in the bare sample starts within the first 60 fs and a second O_2 molecule forms at approximately 200 fs. On the other hand, panel D in *Figure 43* shows that the first O_2 molecule forms at approximately 100 fs while a second O_2 molecule forms after 400 fs of simulation time. More importantly, the O_2 molecules stay close to the surface when the surface is coated.

It should be noted that, DFT functionals contain errors in the O_2 atomization energy that question the accuracy of the interpreted AIMD results. Currently, this error for revPBE+U+vdW functionals is about 0.5 eV which is a considerable error for an oxygen-related redox event such as superoxide/peroxide formation and oxygen release in the thermal degradation event of oxide cathodes. Therefore, achieving high accuracy in the utilized DFT functionals is a highly important goal that should be followed to carry out reliable AIMD simulation of oxygen-related redox events in future.

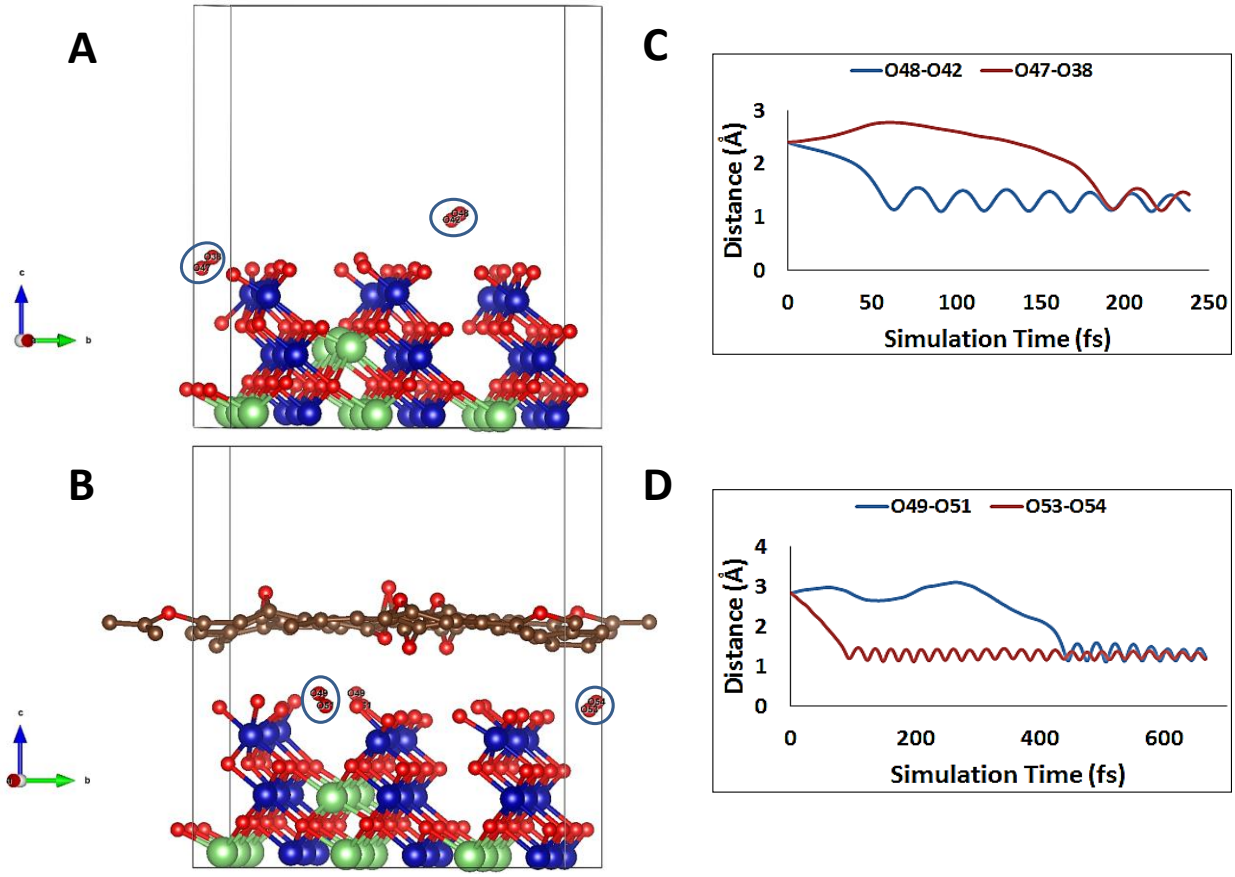

Figure 43. RevPBE/AIMD simulation results of the bare (012) $Li_{0.5}CoO_2$ slab (panels A and C) and graphene-coated (012) $Li_{0.5}CoO_2$ slab (panels B and D). (A) Snapshot of the structure of the bare (012) $Li_{0.5}CoO_2$ slab layer at 667 fs. (B) Snapshot of the structure of the graphene-coated (012) $Li_{0.5}CoO_2$ slab at 239 fs. Red spheres circled in red represent the evolved O_2 molecule. (C) Time evolution of O-O distances for two O_2 molecules for the bare (012) $Li_{0.5}CoO_2$ slab. (D) Time evolution of O-O distances for two O_2 molecules for the graphene-coated (012) $Li_{0.5}CoO_2$ slab. Color code: Green, blue, red, and brown spheres represent Li, Co, O, and C atoms, respectively.

Chapter 6: Revealing the Atomic Structure of Grain Boundaries in Li-rich Cathode Materials

(Previously published as Sharifi-asl, S.; Yurkiv, V.; Gutierrez, A.; Cheng, M.; Croy, J.; Balasubramanian, M.; Mashayek, F.; Shahbazian-Yassar, R. Revealing Grain Boundary Induced Degradation Mechanisms in Li-Rich Cathode Materials. Nano Letters. 2020, 20 (2), Reproduced with permission[3]. Copyright 2017, American Chemical Society)

6.1. Introduction

Layered, $LiTMO_2$-type cathode-oxides are the dominant positive electrodes in commercial Li-ion battery (LIB) technologies. Such materials have been aggressively developed and are now nearing the point of intrinsic limitation, thereby hindering further advancements[11]. Li-rich, LMR-NMC cathodes, that can deliver capacities between 250 – 300 $mAhg^{-1}$, are considered promising options for the next generation of LIBs[438,439]. However, the practical application of Li-rich materials has been challenging due to several phenomena that are unique to these oxides; namely, voltage fade, hysteresis, and impedance at low states of charge (SOC)[440–445]. The mechanisms behind these phenomena are unique to these oxides because of the complexity of their local structures and recent works have made progress with respect to understanding in this regard[442,446,447]. However, as with all cathode-oxides, macroscopic phenomena can also play a critical role in performance. For example, cracking and disintegration of secondary macro-particles, which are agglomerates of primary cathode grains, have been correlated with severe capacity degradation[448]. It has been demonstrated that the lithiation/de-lithiation process induces contraction/expansion of the crystal structure, which leads to large strain in the primary particles and promotes the disintegration and cracking of secondary particles[449]. In addition, surface degradation such as layered-to-spinel-to-disordered rock-salt transformations, as well as transition metal migration/dissolution, have been observed in virtually all conventional, layered oxides[57,161,450–452].

In LMR-NMC cathodes, it has been shown that even a small concentration of local defects can greatly influence the macroscopic electrochemical properties of cathode electrodes[453,454]. However, to what extend the atomic-scale structure can affect properties such as particle cracking/disintegration, in complex LMR-NMC-based particles, is not well-understood. Recent work, using operando X-ray tomography, has reported that charging LMR-NMCs induces a high extent of defects, consistent with previous findings, which is not observed in conventional cathodes such as $Li(Ni_xCo_yAl_{1-x-y})O_2$ (NCA)[197]. In that work the authors hypothesize that the lower Young's modulus of the Li-rich materials[197] is the underlying cause for defect formation/activity, although an atomic-scale analysis that explains such results is still lacking. Furthermore, though the pristine structure of LMR-NMCs has been the subject of extensive study and debate[87,88,189,197,455–460], the atomic arrangement of the phase boundaries in these structures, and how those boundaries change during cycling, have not been thoroughly investigated.

Herein, we have used aberration corrected-scanning transmission electron microscopy (AC-STEM) to investigate the atomic structure and chemistry of a Li-rich, layered-layered-spinel material before and after electrochemical cycling. Our findings directly indicate that the primary cathode particles are composed of distinct, randomly oriented nano-grains of hexagonal $LiTMO_2$ and monoclinic Li_2TMO_3 structures (TM=Co, Ni, and Mn). Hence, high concentrations of phase/grain boundaries were detected in the structure of these cathodes. Based on the geometrical phase analysis (GPA) such phase boundaries are highly strained, which can cause cracking and disintegration of particles during repeated electrochemical cycling. In addition, chemical analysis, through electron dispersive spectroscopy (EDS) and electron energy loss spectroscopy (EELS), suggests a uniform composition across the boundaries in the pristine samples. However, Mn depletion and Ni enrichment were detected in the boundaries of cycled samples. Additionally,

crack initiation was observed in the phase boundaries after extended cycling, which implies that grain/phase boundaries play a detrimental role in the structural stability of the Li-rich cathode materials. Finally, density function theory (DFT) investigations were conducted in order to better understand the underlying reasons for composition variation of the grain boundaries.

6.2. Experimental

Synthesis of cathode particles - A co-precipitation process was used to synthesize Ni-Mn-Co (NMC) carbonates precursors using 4L continuously-stirred-tank-reactor (CSTR). An initial volume of 3L DI water was used. The CSTR was sealed and N_2 was flowed to remove air and avoid oxidation of the product. Stock solutions of ammonium hydroxide (0.05 M NH_4OH), sodium carbonate (2M Na_2CO_3) and NMC sulfate (2M NMC-SO_4) were pumped into the tank to allow for a 6 hr residence time. The reaction was stopped after 24 hr (4 residence times) and the product was filtered, washed then dried overnight at 110°C. The NMC-carbonate was then mixed with the appropriate amount of lithium carbonate and fired at 900°C (2°C/min) for 20 hours. The "parent" LMR-NMC material for this work is based on the following composition: $0.25Li_2MnO_3 \bullet 0.75LiMO_2$ or $Li_{1.25}Mn_{0.53}Ni_{0.28}Co_{0.19}O_x$, where the Li/TM = 1.25. In order to integrate a spinel-type component into the composite material used in this work, less lithium was used to achieve a Li/TM < 1.25. The composition achieved for the baseline cathode in this work was $Li_{1.18}Mn_{0.53}Ni_{0.28}Co_{0.19}O_x$, where the Li/TM = 1.18, suggesting a spinel component of ~ 6%.

Electrochemical characterization – Slurries containing the baseline cathode material, polyvinylidene fluoride (PVDF) and C45 carbon (84:8:8) were cast on aluminum foil and dried overnight. The electrodes were calendared to 80% of the original thickness before use in cells. The active material loading was 8 mg/cm^2. Celgard polypropylene and graphite-based electrodes were

used as the separator and anode, respectively, for coin cell testing. The electrolyte was 1.2 M LiPF6 dissolved in ethylene carbonate / ethyl methyl carbonate (EC:EMC - 3:7 by weight).

The cycling protocol used consists of an activation cycle between 4.5 – 2.0 V (vs. graphite) at C/10 followed by continuous cycling between 4.4 – 2.5 V (C/2). Further details of the cycling protocol can be found elsewhere[461]. The capacity delivered during the 1st cycle activation between 4.5 – 2.0 V was ~ 215 mAh/g (not shown). In the current work, the capacity dropped to ~ 190 mAh/g upon limiting the voltage window to 4.4 – 2.5 V (~ C/2) in subsequent cycles.

Scanning electron microscope imaging – The morphologies of the material were investigated by scanning electron microscopy (SEM) and energy dispersive X-ray spectroscopy using a Hitachi S-4700-II microscope in the Electron Microscopy Center, Argonne National Laboratory.

X-ray Diffraction – High-energy synchrotron X-ray diffraction measurements were carried out on the LMR-NMC cathode powder at 11-BM at the Advanced Photon Source at Argonne National Lab (λ = 0.414561 Å).

Transmission electron microscopy. Cathode samples were scratched from the Al current collector, sonicated in IPA and drop casted onto lacy carbon grids, dried and loaded on double tilt TEM holder. Scanning transmission electron microscopy and electron energy loss spectroscopy were performed using JEOL JEM-ARM200CF STEM equipped with a cold field emission gun with 0.78 Å spatial resolution and a Gatan Quantom EELS detector. A 22 mrad probe convergence angle was used to perform STEM imaging. HAADF detector with 90 mrad inner-detector angle was utilized to obtain Z-contrast atomic resolution images. LAADF detector with 45 mrad inner-detector angle was utilized to obtain defect-sensitive images. The color-coded images were restructured from the atomic resolution images using Gatan Microscopy Suit (GMS3) software, in which diffraction spot from each grain were masked to generate reconstructed atomic image by

inverted FFT function. Then images from various phase were combined to form the color-coded reconstructed images. EELS was carried out with 0.5 eV/channel dispersion on a 2048 channel EELS detector using a 5 mm detector aperture. Full-width half maximum of zero loss peak was measured 0.6 eV which determines the energy resolution of the obtained spectra. EELS map acquisitions were carried out by 5 Å pixel size and 0.2 s dwell time on a 7×7 nm area. Electron dispersive spectroscopy (EDS) was carried out using an Oxford X-max 100TLE windowless SDD X-ray detector.

Density Functional Theory calculations: DFT calculations[462] were performed using the Vienna Ab Initio Simulations Package (VASP)[367] code employing the generalized-gradient approximation (GGA)[463] using the PBE (Perdew, Burke, and Ernzerhof)[464] functional to account for the exchange-correlation effects. In addition, to account for the Coulombic repulsion between localized electrons in transition metals (Ni, Mn and Co), the DFT+U schema is used. The Hubbard parameters (U–J) for Ni, Mn and Co are set as 6.7, 4.2 and 5.96, respectively.[465] For systems with an even number of electrons non spin-polarized calculations, and for systems with an odd number of electrons unrestricted spin-polarized calculations, are performed. The migration paths and barriers are determined using the linear nudged-elastic-band method as implemented in VASP code.

For all calculations, a cutoff energy of 500 eV is used. The further increase of cutoff energy to 550 eV led to the change of the total energy of less than 0.02 eV. All structural optimizations are carried out until the forces, acting on atoms, are below 0.01 eV/Å. The criteria for energy change is set to 0.1 eV.

The $LiNi_xMn_xCo_xO_2$ (NMC) computational slab is created from the $LiCoO_2$ (LCO) unit cell, by repeating it three times through **a** and **b** vectors (Figure S3) and randomly substituting Co atoms by the appropriate amount of Ni and Mn atoms. The final NMC slab has 108 atoms and the

lattice constants $a = b = 8.45$ Å and $c = 14.05$ Å ($\alpha = \beta = 90^0$, $\gamma = 120^0$). For all the calculations a k-point mesh of 4 × 4 × 2 is used. In order to ensure that the slab size is chosen properly and represents the properties of the macroscopic crystal structure, the Li diffusion energetics is calculated for two different slab sizes. The first slab is 108 atoms as described above and the second one is 192 atoms configuration. In the case of 192 atoms, the Li diffusion barrier has changed less than 1 % comparing to the slab with 108 atoms. Thus, in order to perform computationally effective calculations, the slab with 108 atoms is used.

6.3. Li-rich Cathode Characterization (*Done by Dr. Croy's Group at Argonne National Laboratory*)

The morphology and structure of Li- and Mn-rich, layered-layered, xLi_2MnO_3•$(1-x)LiTMO_2$ (TM=Ni, Mn, Co) (LMR-NMC) specimens were characterized by scanning electron microscopy (SEM) and X-ray diffraction (XRD). The SEM imaging, which was done using a Hitachi S-4700-II microscope in the Electron Microscopy Center at Argonne National Laboratory, demonstrated the spherically shaped secondary particles (Figure *44A*) in the range of ~ 15 micron in size (Figure *44B*). Each secondary particle is made up of smaller nanometer sized primary particles (Figure *44C*). High-energy synchrotron X-ray diffraction measurements were carried out on the LMR-NMC cathode powder at 11-BM at the Advanced Photon Source at Argonne National Lab (λ = 0.414561 Å) that confirmed the presence of both R-3m and C2/m as shown in Figure *44D*. The LMR-NMC cathode was cycled against graphite anode in a full-cell configuration. Figure *44E* is a representative example of the cycle life performance of LMR-NMC cathodes, when tested against graphite anodes. The capacity delivered during the 1st cycle activation between 4.6 – 2.0 V was ~ 215 mAh/g (not shown). In the current work, the capacity dropped to ~ 190 mAh/g upon limiting the voltage window to 4.4 – 2.5 V (~ C/2) in subsequent cycles. The electrochemical

cycling results demonstrated that the capacity fades quickly, reaching the end of life (~ 150 mAh/g which is 80% of capacity delivered during 2nd cycle) near the 35th cycle (Figure *44E*). It is known that one of the main capacity degradation mechanisms is the dissolution of manganese from the cathode and subsequent deposition on the anode, which exacerbates the trapping of lithium on the anode and causing the capacity fade[466]. However, since such degradation mechanisms have been also observed in the conventional layered NMC cathodes, the current work is intended to investigate the additional degradation mechanism that account for faster capacity degradation observed in LMR-NMC cathode structures.

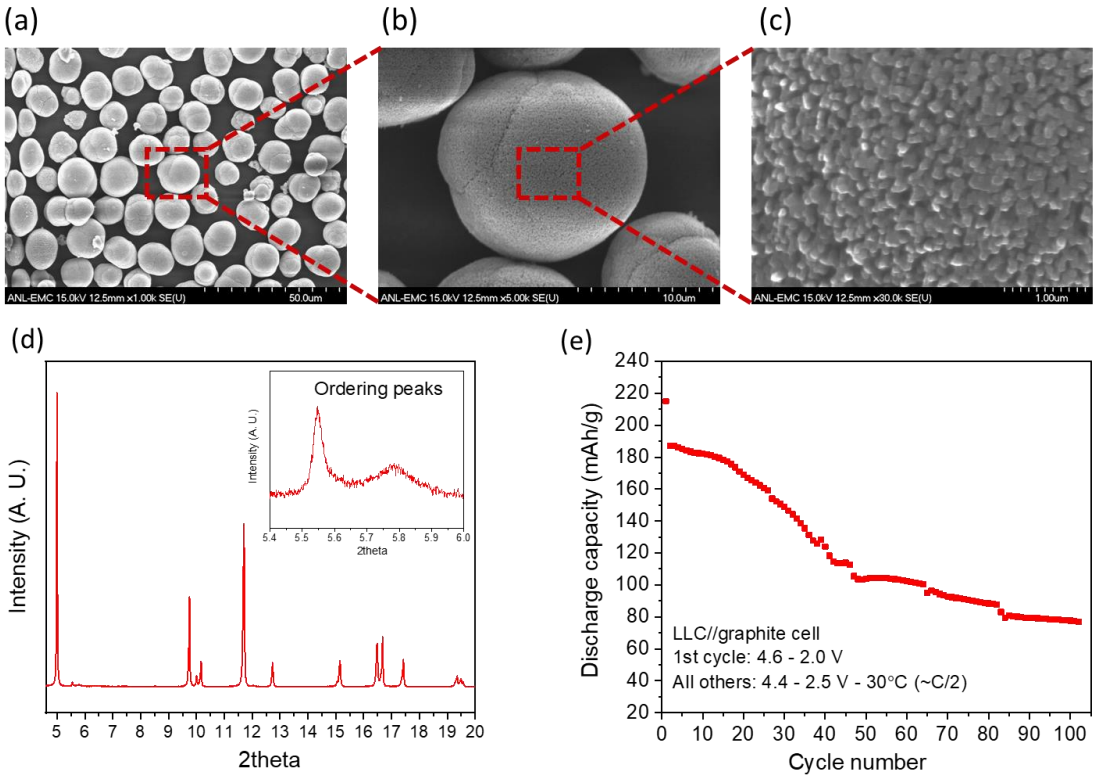

Figure 44. (a-c) Low to high-magnification SEM images (d) high-energy X-ray diffraction (e) representative cycle life for unoptimized *LMR-NMC*//graphite cells. The cycling protocol details are shown in the figure.

6.4. STEM Atomic Resolution Imaging and Strain Analysis of the Grain/Phase Boundaries in Primary Particles

Figure 45A and *B* demonstrates low-magnification HAADF images from the primary LMR-NMC particles. The uniform contrast denotes to the even thickness of the particles, which enables STEM imaging from the surface as well as core areas of each sample. *Figure 45C* and *D* demonstrates atomic resolution HAADF images from the surface of the pristine and the cycled sample (after 100 cycles). Clearly, the migration of transition metals to Li-octahedral sites has been promoted during the cycling, causing the thickening of the surface reconstruction spinel/rock-salt layer from < 1nm to ca. 3 nm from the pristine sample to the cycled sample. However, surface reconstruction has been observed in many studies on the conventional layered oxide cathodes[63,119–121]. Therefore, such relatively small fraction of change in the surface cannot fully explain the rapid capacity degradation observed in Li-rich cathodes (Figure *44*). Therefore, further analysis was carried by atomic investigation of the bulk structure of the pristine and cycled samples.

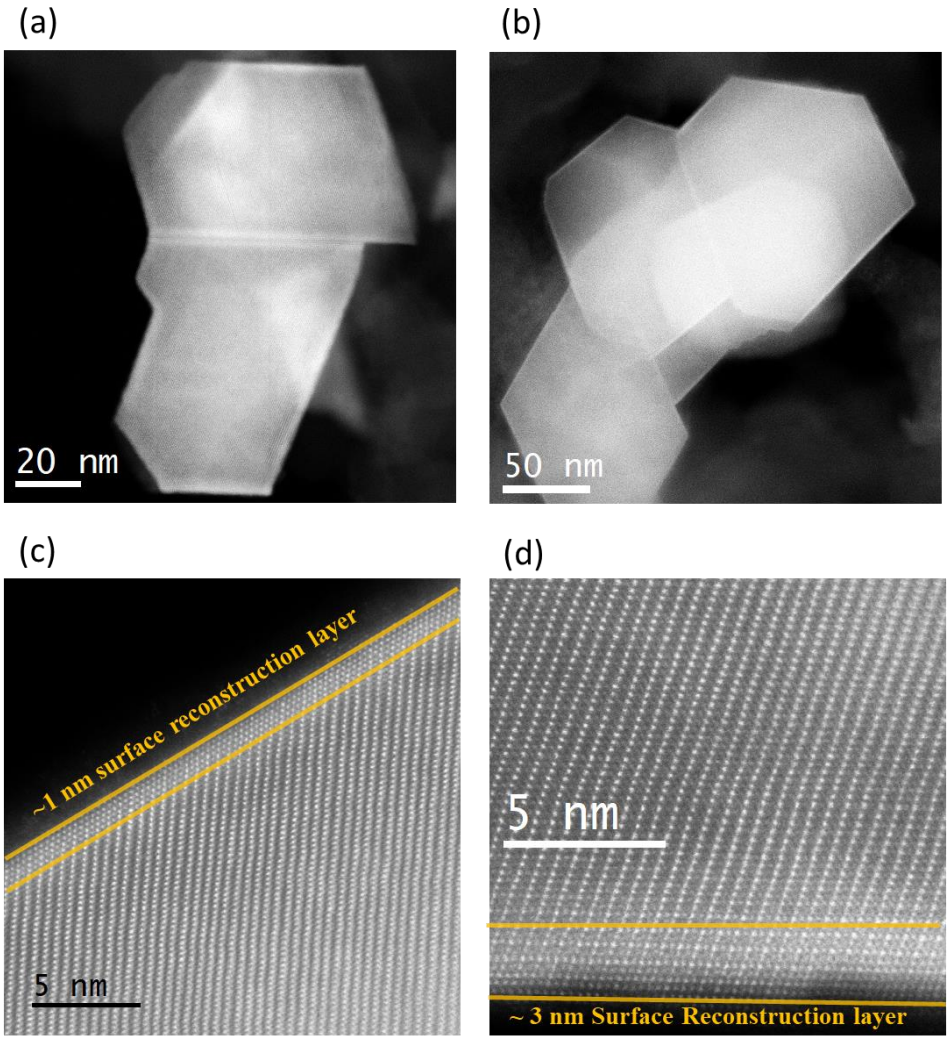

Figure 45. (a, b) Low magnification HAADF images, demonstrating the morphology of primary cathode grains. Atomic resolution HAADF images from the edge of (c) a pristine cathode particle and (d) a cycled cathode particle, showing a 1 nm and 3 nm thick SRL layer on the surface.

By examining the pristine cathode samples, it was realized that the primary particles are composed of layered-structured grains with varied orientations with respect to each other (*Figure 46*A, B). The corresponding fast Fourier transformed (FFT) images are shown in *Figure 46*C, D. Based on the FFT analysis, it can be concluded that the two intersecting grains correspond to [010] and [$\bar{3}$10] projections of the monoclinic Li_2MO_3 phase and the [100] projection of the hexagonal $LiMO_2$ phase, respectively. In addition to FFT analysis, the interlayer distances of the layered structures in *Figure 46*C are quantified through line profile measurements and the results are

demonstrated in *Figure 46*E. The yellow and red profiles correspond to the monoclinic and the hexagonal phases, respectively. It can be observed that the interlayer distances of the monoclinic-labeled structure are ca. 0.2 Å larger, which is in accordance with the atomic models. Although such projections from the monoclinic and hexagonal phases have a very close atomic configuration and interlayer distances, such small variations can be quantified through sub-angstrom AC-STEM imaging. In addition, chemical composition analysis using EDS and EELS was carried out as a complimentary technique to verify the co-existence of monoclinic Li_2MO_3 and hexagonal $LiMO_2$ phases. *Figure 46*F demonstrates an EDS line scan collected across a grain boundary between Li_2MO_3 and $LiMO_2$ grains. In spite of a very small variation in the transition metal signals, a considerable reduction in O signal intensity can be observed by moving from the Li_2MO_3 grain to the $LiMO_2$ grain.

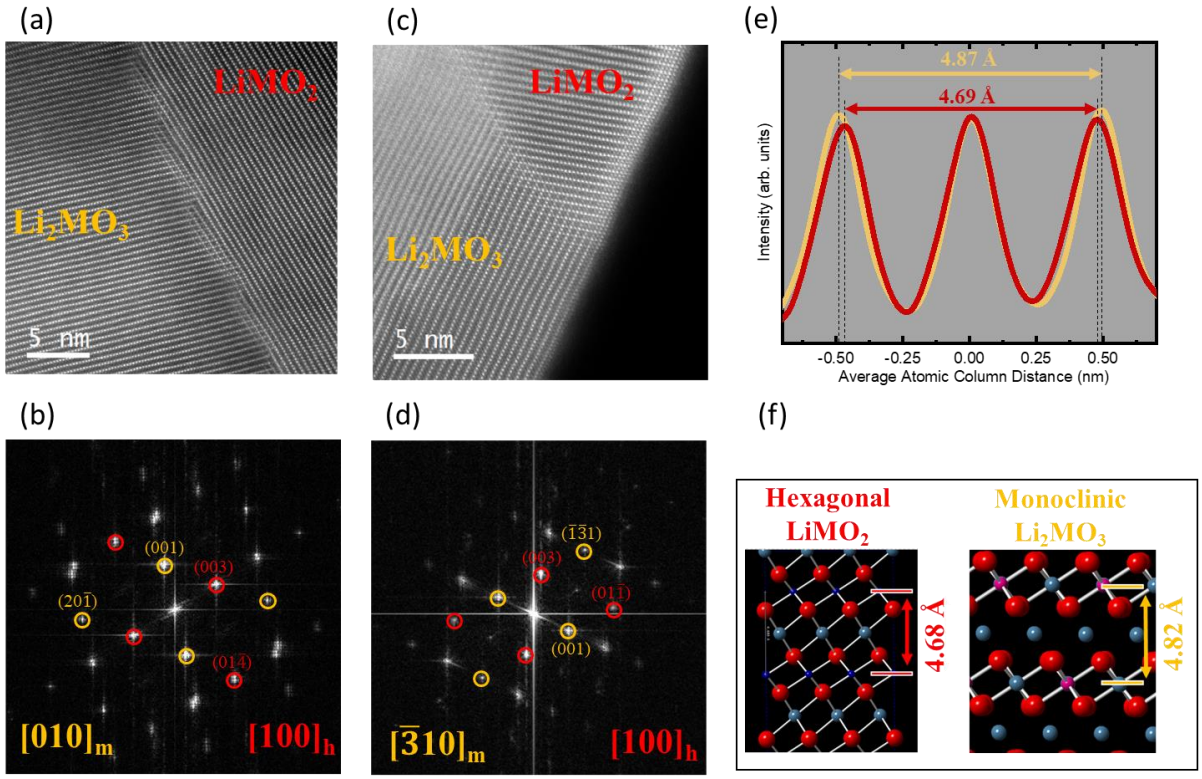

Figure 46. (a-d) Atomic resolution HAADF images and the corresponding FFT patterns from the core of an LMR-NMC particle showing a boundary between two layered phases. FFT analysis reveals that the observed layered phases shown in panels (a) and (c) correspond to the [010] and [$\bar{3}$10] projections of the monoclinic Li_2MO_3 phase and the [100] projection of the hexagonal $LiMO_2$ phase respectively. (e) Line profile analysis from the interlayer distances observed in (a). Yellow and red profiles correspond to the monoclinic and the hexagonal phase respectively. The plot illustrates a 0.2 Å increase in the interlayer distance in the monoclinic-labeled phase compared to the hexagonal phase, which is in accordance with the atomic models shown above. (f) The EDS line scan taken across a $LiMO_2/Li_2MnO_3$ grain boundary.

Further investigation of the grain boundaries in the pristine cathode particles were carried out by defect-sensitive LAADF and atomic resolution imaging. Large inner collection angle of the HAADF detector eliminates the diffraction contrast and only detects only the electron that are scattered by the thermal diffuse scattering mechanism which is highly dependent on the Z number of atomic columns[29]. However, by reducing the detector inner angle, the Z-dependence of the contrast decreases and the image contrast will be influenced by the coherent diffraction contrast

formed by Braggs reflections[30]. Therefore, the contrast in an LAADF image is similar to the dark-field TEM images. The reason for observing defects in LAADF images is suggested to be "de-channeling" effect of electrons from crystalline defects and strained areas[29,31].*Figure 47*A demonstrates a low-magnification LAADF image from a pristine particle. The high contrast lines, indicated with red arrows, correspond to defects in the structure. Considering the 50 nm width of the image, the presence of four line-defects demonstrates a high concentration of defects in this particle. Atomic resolution imaging reveals that the bright elongated lines in the LAADF correspond to an increased interlayer distance in the layered structure of the sample (*Figure 47*B). As shown in the *Figure 47*C, the interlayer distance has increased from 4.87 Å in the adjacent area to 5.73 Å in the defect line. Based on the FFT pattern analysis shown in *Figure 47*D, it is concluded that the increased interlayer distance corresponds to a grain boundary between [010] and $[\bar{3}10]$ projections of the monoclinic structure. *Figure 47*E demonstrates the color-coded reconstructed image based on the FFT pattern, illustrating the presence of various projections of the monoclinic phase in this area. Moreover, GPA was carried out on the atomic resolution image in Figure 2b, which demonstrates a large strain in the grain boundary (*Figure 47*F). The observed strain is generated as a result of the increased interlayer distance in the grain boundary, which can possibly lead to cracking, impedance rise, and capacity fade of the battery during electrochemical cycling.

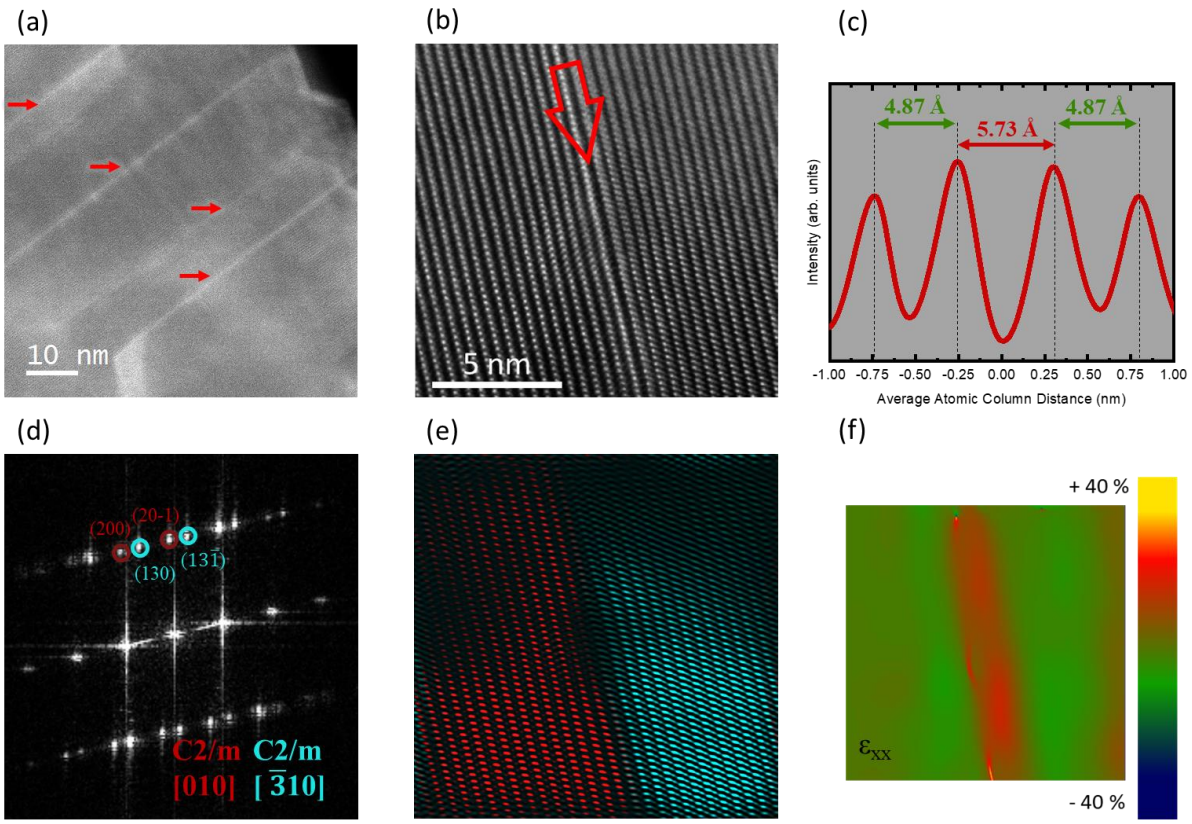

Figure 47. (a) low magnification LAADF image from a pristine cathode particle showing a high concentration of elongated defects as indicated by red arrows. (b) Atomic resolution HAADF image from a line defect indicated in (a). Based on the (c) line profile measurement and (d) FFT analysis, the defect is an elongated interlayer distance where [010] and [$\bar{3}$10] projections of monoclinic Li_2MO_3 phases are forming a grain boundary. (e) Reconstructed color-coded image from the indicated diffraction spots in (d) illustrating the separation of two grains. (f) GPA results showing a large strain in the grain boundary as a result of increased interlayer distance.

A different configuration of grain boundaries is shown in *Figure 48*A, where dissimilar projections of the monoclinic structure are facing each other. Although there is a one-to-one correspondence between the atomic layers of [010] and [$\bar{3}$10] phases, a distinct spinel-type grain boundary is formed that is a result of transition metal migration to the Li-octahedral sites. Such transition metal migration has occurred in 1-2 unit-cells that are adjacent to the grain boundary. *Figure 48*B demonstrates the corresponding FFT pattern, which is analyzed as a three-phase

structure consisting of [010] and [$\bar{3}$10] projections of the monoclinic Li_2MO_3 structure, plus the spinel-type interface. A color-coded reconstructed image is shown as an inset in *Figure 48*A for illustration of grain configurations. As can be seen from the GPA shown in *Figure 48*C, such spinel-type grain boundaries are also highly strained and may also act as crack and failure initiation points in the cycled material. In addition, chemical analysis has been carried out on the spinel-type grain boundary area by EDS, shown in *Figure 48*D. The results demonstrate that the distribution of Mn, Ni and Co is uniform in both surrounding monoclinic grains as well as across the boundary, confirming, within detection accuracy, a uniform composition in the monoclinic Li_2MO_3 phases.

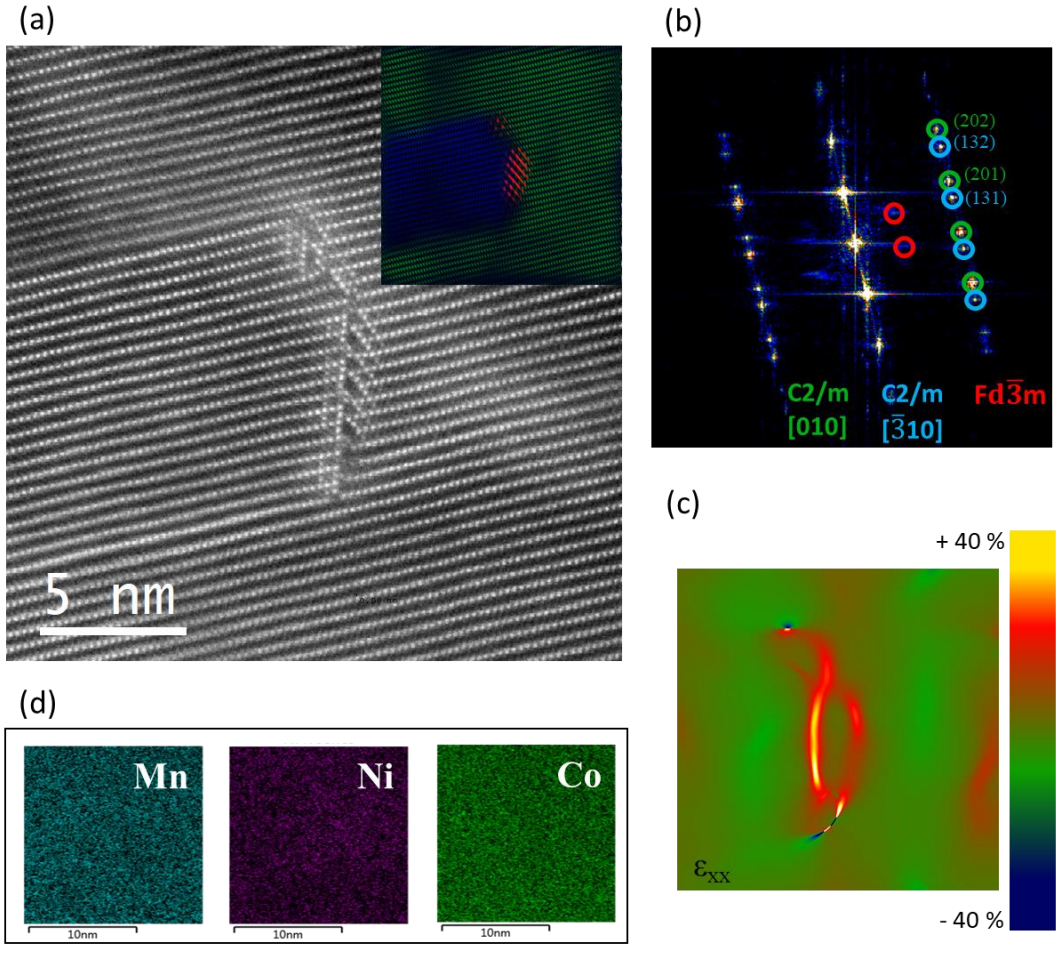

Figure 48. (a) The atomic resolution HAADF image from a pristine cathode particle, showing a spinel-type grain boundary. (b) The corresponding FFT image demonstrating the presence of the

[010] and [$\bar{3}$10] projections of the monoclinic Li_2MO_3 phase and formation of the spinel-type structure at the grain boundary as a result of migration of transition metals to the Li-octahedral sites. A color-coded reconstruction image based on the diffraction spots indicated in (b) is shown as inset in (a) for illustration of the triple phase boundary. (c) GPA, showing a large strain in the spinel-type grain boundary. (d) EDS maps of Mn, Ni and Co from the grain boundary confirming a uniform composition at the grain boundary.

6.5. Post Cycling TEM Analysis of the Cathodes and Grain Boundaries

To understand the role of the identified grain/phase boundaries on electrochemical degradation structural stability of the particles, AC-STEM experiments were carried out on the cycled cathode particles. *Figure 49*A demonstrates an LAADF image from a cycled cathode particle with bright contrast features that correspond to the identified grain/phase boundaries. *Figure 49*B is an atomic resolution image from the indicated area in the low-magnification image. The analysis of the FFT pattern (*Figure 49*C), demonstrates a spinel-type grain boundary with the same grain configuration as was observed in the pristine particle shown in *Figure 48*. The phase transition at the surface regions of the particle can be observed, which is an expected phenomenon in the cycled layered oxide cathodes[12,157]. Additionally, it can be observed that a nano-crack has initiated on the grain boundary, which might develop into a more significant crack and initiate disintegration of the cathode upon further cycling. The analyzed FFT pattern demonstrates that the spinel-type boundary is located between the [010] and [$\bar{3}$10] projections of the monoclinic Li_2MO_3 phase, similar to the atomic configuration observed in the pristine sample. The color-coded reconstructed image, *Figure 49*D, illustrates the configuration of the identified grains and the spinel-type grain boundary. Aside from the layered to spinel/rock-salt phase transformation that can be observed in the surface areas of both grains, and transition metal migration to Li sites, stacking fault disorder can be detected in the cycled sample. *Figure 49*E shows an atomic resolution image from the [010]

grain located on the right side of the *Figure 49*B, demonstrating a disorder in the stacking of the layers. The stacking faults, induced by slab sliding during electrochemical cycling, denotes the electrochemical activity present in the Li-rich domains. Figure 4f demonstrates EDS map results from the indicated spinel-type boundary, which shows localized depletion of Mn and enrichment of Ni at the boundary. The localized chemical inhomogeneity in the interface is only observed after electrochemical cycling of the particles. The depletion of Mn may be attributed to a preferred dissolution of Mn from high energy grain-boundaries that subsequently promotes the diffusion of Ni into the Mn/Li vacancies, as discussed below. The increased dissolution of Mn and increased Ni migration to the grain boundary can also be the result of cracking of particle surface and exposing new surfaces to the electrolyte, which promotes the metal dissolution. The promoted metal dissolution can, in turn, negatively affect cell performance through Mn deposition and Li consumption at the graphite anode as well as impedance rise at the now disordered cathode surface[467,468]. In addition, crack formation, exposure of fresh particle surfaces, and eventual disintegration of the active materials serve to exacerbate these problems.

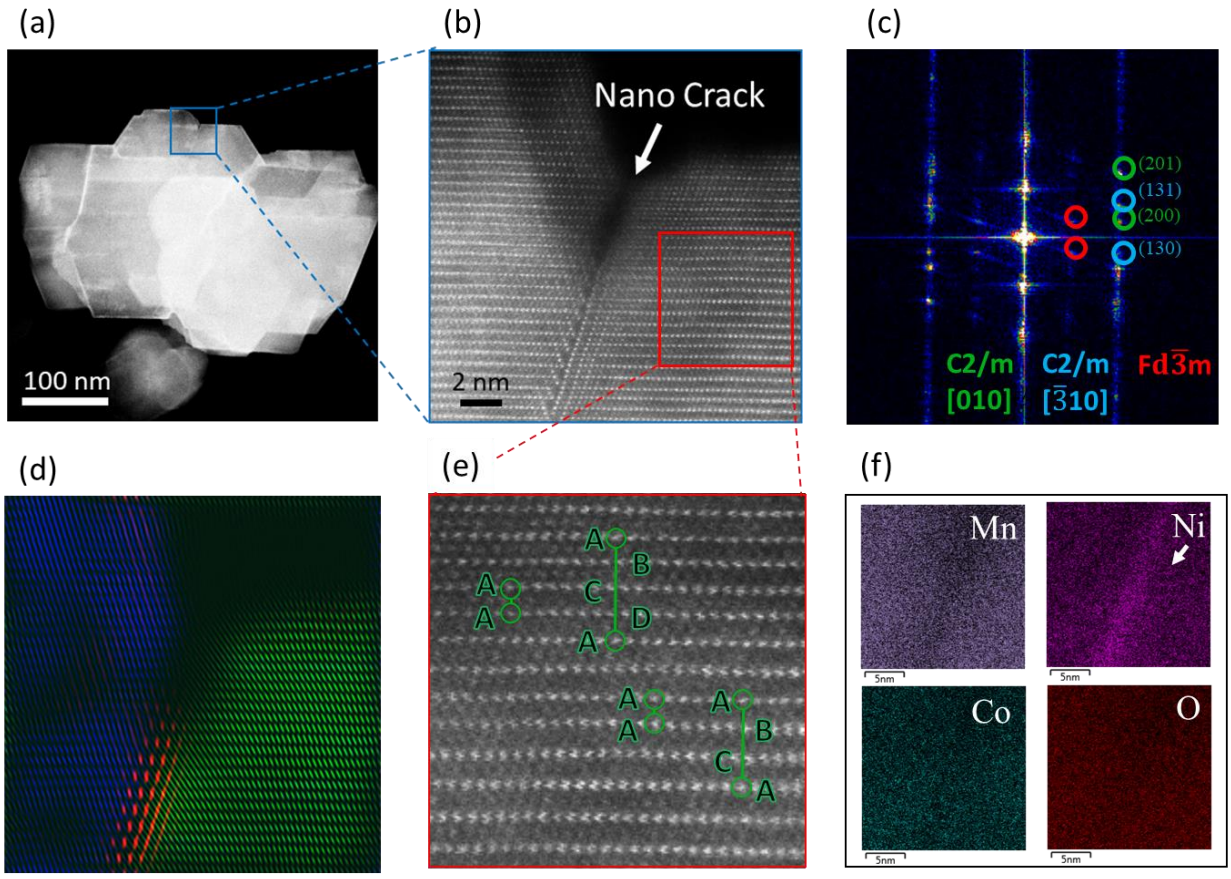

Figure 49. (a) Low-magnification LAADF image showing a cycled cathode particle. Various bright contrast feature can be observed in the particle which can be attributed to previously shown grain/phase boundaries. (b) Atomic resolution HAADF image from the indicated area in (a), which shows a spinel-type grain boundary that forms a nano-crack at the particle surface. (c) The corresponding FFT pattern that is indexed as a three-phase structure consisting [010] and [$\bar{3}$10] projections of the Li_2MO_3 structure together with the spinel-type boundary, similar to the atomic configuration of the pristine sample. (d) Color-coded reconstructed image, based on the indicated diffraction spots in (c), illustrating the three-phase structure of the imaged area. (e) Atomic resolution image from the [010] projection on the right side of (b), showing a disorder in the stacking of the layers. (f) EDS maps obtained from the spinel-type grain boundary showing the depletion of Mn and enrichment of Ni in the grain boundary subsequent to the electrochemical cycling.

The increased Ni concentration at the grain boundary has also been confirmed by EELS. *Figure 50*A demonstrates an atomic resolution HAADF image from a grain boundary detected at the core of a cycled cathode particle. An EELS map was acquired from the grain boundary and the

signal from an equal number of pixels in the spinel-type grain boundary, and the adjacent layered areas, were summed and compared as shown in *Figure 50*B. It can be clearly observed that the grain boundary shows a less intense Mn signal. However, the Ni concentration has increased while, interestingly the Co content has remained almost the same, consistent with EDS results on a different particle (*Figure 50*B). It should be noted that while the intensity of Ni L_3-edge at 851 eV has substantially increased at the grain boundary, the L_2 edge at 870 eV has a very similar intensity in both spectra. This increase in the relative intensity of Ni L_3/L_2 edges denotes to the reduction of valence state and change in the Ni bonding at the interface[136]. The increased Ni concentration in the spinel-type boundaries could also be explained by the preferred migration of Ni cations into the Li layers that forms these structures. Preferred migration of Ni ions into Li vacancies has been observed in conventional NMC cathodes via electron microscopy and X-ray spectroscopy [51,157,467]. Moreover, segregation of Ni and Co has been observed at specific facet terminations in the Li-rich cathode materials[157]. However, it is interesting that here we observe such phenomena at complex, bulk interfaces within these materials.

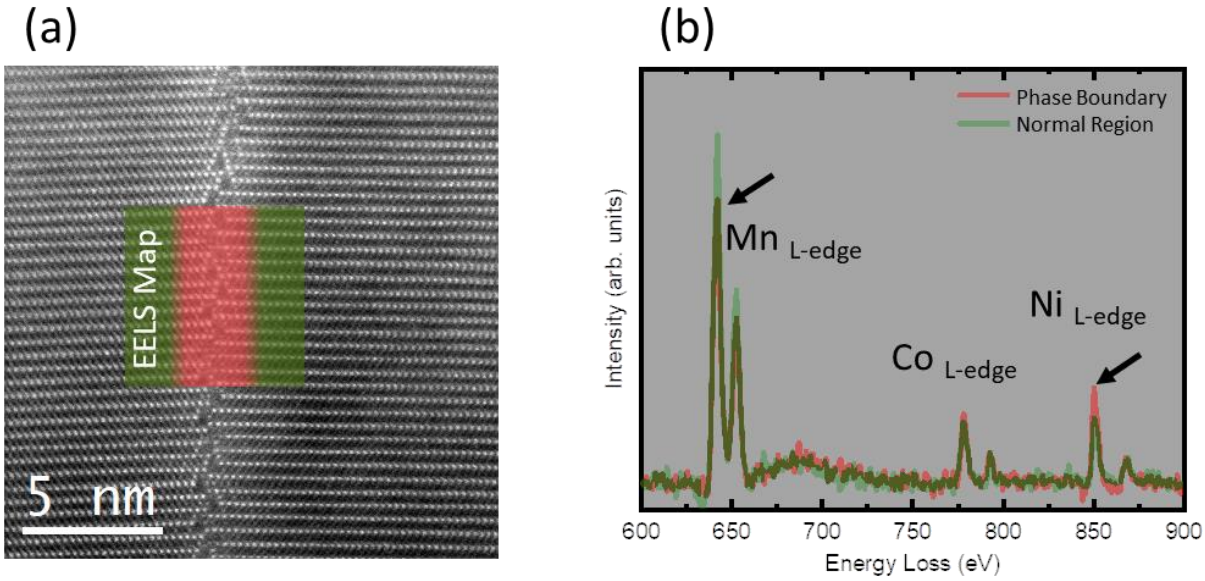

Figure 50. (a) HAADF atomic resolution image from a grain boundary in bulk structure of a cycled LMR-NMC sample. (b) EELS spectra showing the Co and Ni L-edges from the specified area in (a). increased Ni concentration can be observed at the grain boundary area.

The role of grain boundaries in O_2 release has also been studied in the cycled sample. As ca be seen from the Figure *51*, there is not a significant alteration in the fine structure of the oxygen and other transition metals obtained from the grain boundary versus the adjacent layered grain. So, it can be concluded that there is not any considerable oxygen loss from the detected grain boundaries and the chemical composition alteration occurs without a significant loss of oxygen.

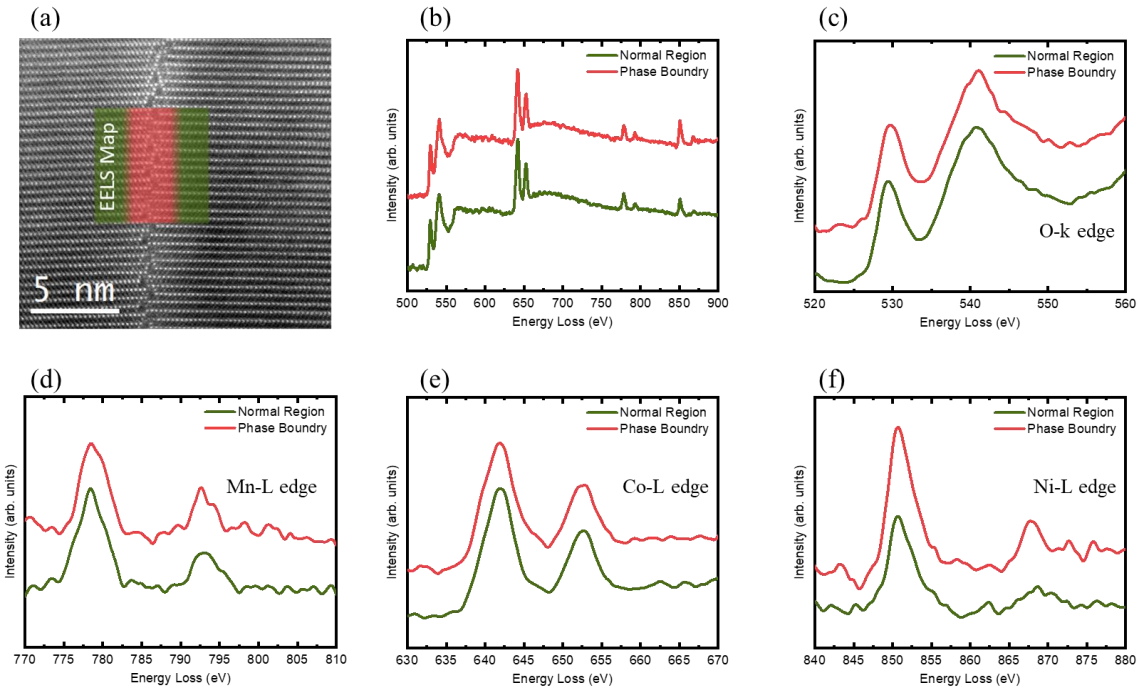

Figure 51. (a) HAADF atomic resolution image from a grain boundary in bulk structure of a cycled LMR-NMC sample. (b) The EELS spectra from the grain boundary and adjacent area. (c) Oxygen K-edge, (d) Mn L-edge, (e) Co L-edge and (f) Ni-L edge from the grain boundary and adjacent areas as shown in the panel (a).

6.6. DFT Calculations. (Done by Prof. Yurkiv and Prof. Mashayek at UIC**)**

To understand the atomic interactions that promote preferred Ni migration to the grain boundaries we have performed complementary DFT calculations. We have studied the favorable pathways for Li/M (M = Ni, Mn and Co) exchange in the cathode structure. Several configurations varying Ni, Mn and Co position within the simulated slab were considered (*Figure 54*). Among many possible calculated structures, a structure with Ni segregation in the grain boundary revealed to be the most stable. In addition, all three transition metal atoms diffusion into Li vacancy are calculated and compared (*Figure 55* and *Figure 56*). It was found that diffusion of Ni ions into the Li vacancies is the most favorable process compared to Mn and Co (*Figure 52*). These results explain the experimentally observed Ni accumulation in the grain boundaries.

Additional calculations have been carried out to uncover the details of Ni migration to the grain boundaries and Li vacancies. *Figure 52A* demonstrates the DFT calculations regarding the Ni migration to Li vacancies. Two possible pathways for Ni migration are identified that are regarded as Path I and Path II and are illustrated in *Figure 52A*. The Path 1 depicts the "direct" exchange of Ni/Li vacancy and the Path II corresponds to the "side" exchange. Both pathways start with the same atomic configuration (namely; S1 and S2), where the indicated Ni atom diffuses to the Li vacancy of the nearest neighbor. This process is energetically favorable by 3.1 eV as shown in *Figure 52B* and *C*, where the energies of all diffusion pathways are shown. The Li atom diffusion into the metal vacancy in S2 configuration could occur from two nearest neighbors. Path I describe the Li atom diffusion from the nearest neighbor on the right and Path II shows the Li atom diffusion from the nearest neighbor on the left. As such, P.I-S1 and P.II-S1 configurations are formed leading to the creation of Li vacancy. Subsequently, the Ni atom from the nearest neighbor to the Li vacancy could diffuse into this Li vacancy creating next metal vacancy. This process progresses along the bulk structure of NMC, which could potentially create defects or even cracks in the electrode. *Figure 52B* and *C* show the energetics and the activation barriers for Li and Ni atoms diffusion corresponding to Path I and Path II shown in *Figure 52A*. The second diffusion process S2 to P.1-S1 in Path I and S2 to P.II-S1 in Path II describes Li atom diffusion into the metal vacancy from the right and left nearest Li neighbor, correspondingly. The Li atom diffusion in Path II is more energetically favorable (Δh = –0.97 eV) with the smaller activation barrier (E^{act} = 0.3 eV) than the respective Li atom diffusion of Path I (Δh = –0.38 eV and E^{act} = 0.7 eV). Due to the creation of Li vacancy Ni atom can diffuse into the respective side in both the paths. The processes P.I-S1 to P.I-S2 in Path I and P.II-S1 to P.II-S2 in Path II describe this Ni atom diffusion. As can be observed in both the paths this process is energetically unfavorable by Δh = +1.03 eV

(E^{act} = 2.24 eV) in Path I and by Δh = +1.79 eV (E^{act} = 2.25 eV) in Path II. However, the consequent Li atom diffusion into the metal vacancy is significantly energetically favorable by Δh = –4.92 eV in Path I and Δh = –2.27 eV (E^{act} = 1.31 eV) in Path II. The large difference between the enthalpies in Path I and Path II is because in Path I a Li atom is inserted into the metal vacancy, since there is no further Li atom in the slab. The corresponding insertion in Path II is shown by P.II-S5 structure, where the enthalpy difference is Δh = –6.64 eV.

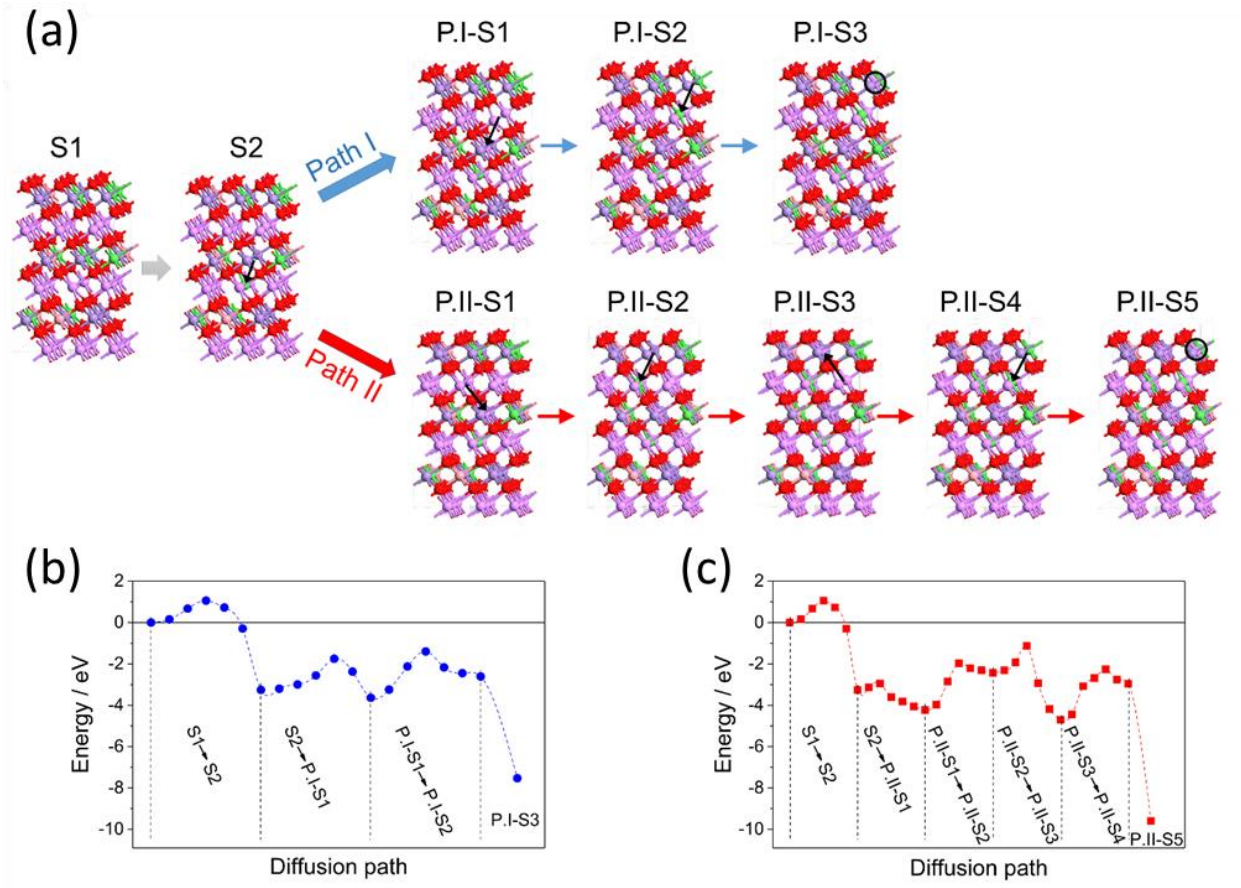

Figure 52. Two paths (Path I and Path II) of Li/Ni exchange. Path I (upper panel) depicts the "direct" (shortest distance) Li/Ni exchange. Path II (lower panel) shows the 'side" Li/Ni exchange. First two slabs on the left are the same for both the paths. (d) and (e) the energetics and the migration barriers of Li and Ni atoms for Path I and Path II as obtained in the present DFT calculations.

6.7. Conclusion and Summary

Aberration corrected-scanning transmission electron microscopy was performed on the bulk structure of Li-rich cathode materials having integrated spinel-type domains. The complex atomic structure of grain/phase boundaries that can form in the LMR-NMC cathode materials was identified. The presented atomic study, which was enabled by synthesis of thin, electron transparent cathode particles, demonstrated the presence of a layered-layered, hexagonal-monoclinic structure with various possible grain/phase boundary structures, such as spinel interfaces. These structures were found to have a dependence on the configuration of the adjacent grains, where stacking of two layered grains perpendicular to their layered structure formed grain boundaries with increased interlayer distances, whereas staking of grains parallel to their layered structures resulted in a spinel-type grain boundary. It was demonstrated that such grain boundaries, that are also highly strained, would promote initiation of crack formation. Subsequently, fracture and disintegration of the active materials may ensue resulting in loss of performance. Additionally, preferred Mn dissolution and Ni-enrichment was observed in the grain boundaries of cycled samples, implying an important role of such boundaries in performance degradation mechanisms. (*Figure 53*). The underlying reason for atomic migration of Ni into spinel-type grain boundaries was investigated using DFT calculations. Among the various calculated structures, a configuration with Ni migration into Li vacancies was revealed to be the most energetically favorable structure, correlating well with the experimental observations. This work reveals the complex role between composition, synthesis, and structure-property relationships of advanced cathode designs and reiterates the important role that local atomic structures can play in defining macroscopic electrode properties as well as the need to further understand these materials across various length scales.

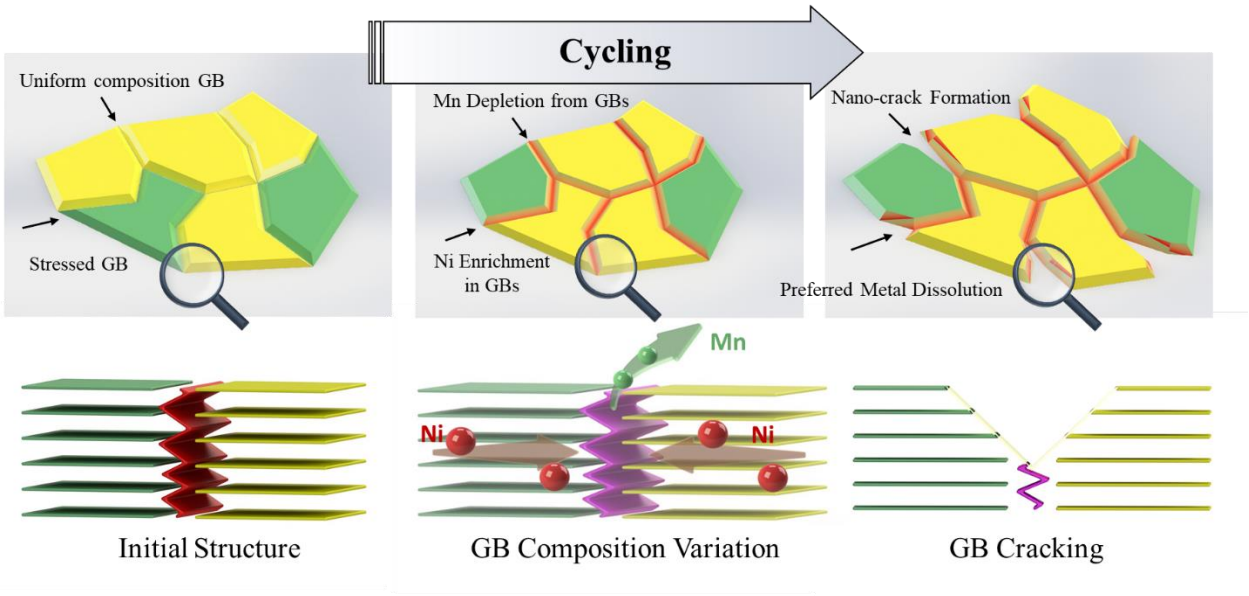

Figure 53. Schematic illustration of the proposed grain boundary-induced degradation mechanisms in Li-rich cathodes. During cycling, the grain boundaries are depleted of Mn and enriched in Ni, possibly aiding in crack initiation at the already strained grain boundaries.

6.8. Supplementary Information

Figure *54* shows the creation of NMC slab used in the present DFT calculations. We start with the LCO unit cell, followed up by the creation of 3x3x1 slab. In the last step Ni and Mn atoms are introduced by random substitution of Co atoms. *Figure 55* shows the for Mn diffusion into Li vacancy side. *Figure 56* shows DFT results for Co atom diffusion into Li vacancy side.

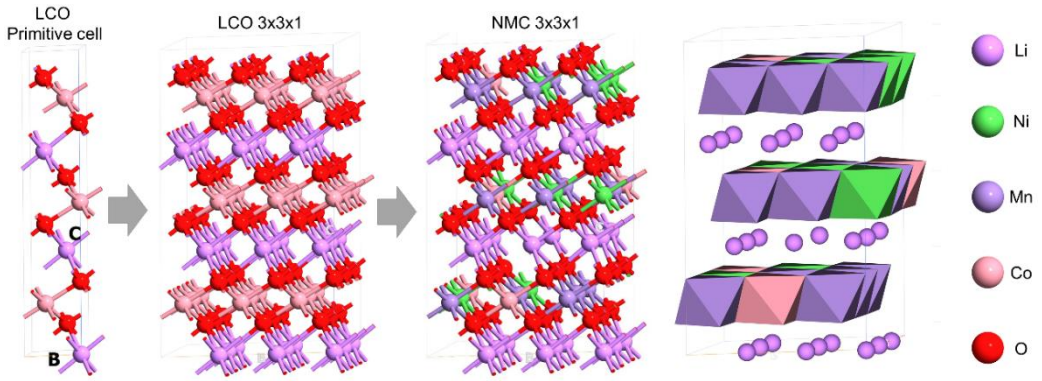

Figure 54. Left picture – crystal structure of LCO rhombohedral ($R\bar{3}m$) primitive cell; middle picture 3x3x1 LCO slab and right picture 3x3x1 NMC slab used for DFT calculations in this work.

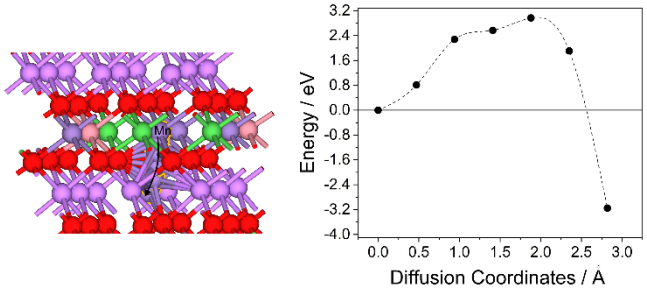

Figure 55. The structure (left) and the barrier (right) of Mn atom diffusion into Li vacancy.

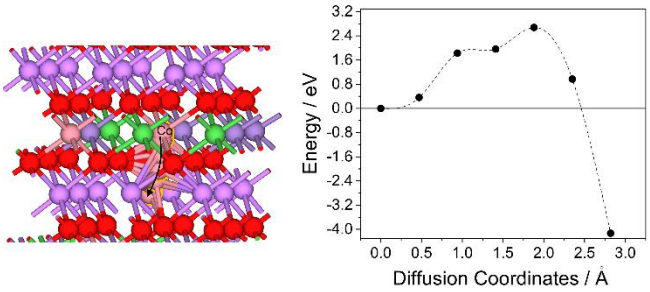

Figure 56. The structure (left) and the barrier (right) of Co atom diffusion into Li vacancy.

We compare our DFT obtained structures with the TEM images. *Figure 57* shows the comparison between the structures obtained from Path I and Path II (*Figure 52*) and the experimentally obtained TEM image (right picture). As can be seen in the upper picture comparison, there are three Ni atoms occupying Li sides. These Ni atoms are located between the metallic layers of NMC structure. In the lower part of the atomic resolution image, which corresponds to the NMC structure obtained in Path I, with two aligned Ni atoms in Li sides.

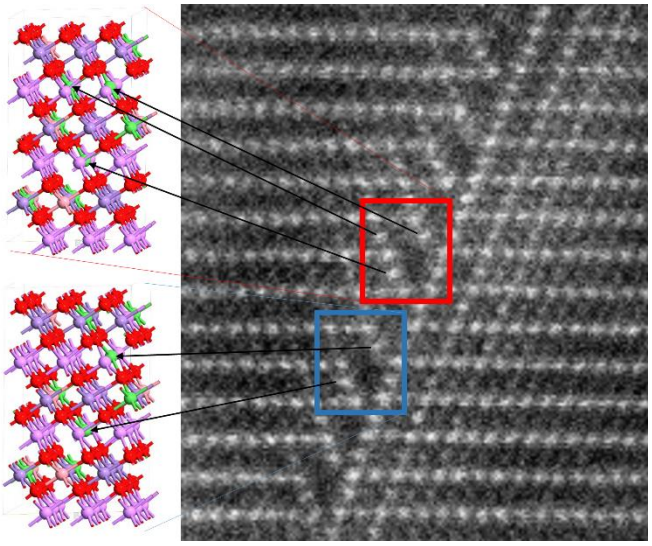

Figure 57. Comparison between the DFT calculated structures (left) and the TEM image recorded (right). Upper-left picture depicts the result of Path II, where three Ni atoms occupy Li side, whereas lower-left picture shows the result of Path I with two Ni atoms into Li side (*Figure 50C*).

Chapter 7: Conclusion and Future Work

7.1. Conclusion

The presented PhD thesis sheds light on the degradation phenomena of layered oxide cathode materials. Five topics that were directly focused on the degradation behavior of the cathode materials were covered in this PhD research including (1) literature review on oxygen release originated degradation of cathode materials, (2) in-situ heating TEM study of the thermal decomposition of Li_xCoO_2, (3) mitigation of thermal decomposition and oxygen release from Li_xCoO_2 by graphene-coating of individual particles, (4) Atomic study of the grain boundaries in the composite Li-rich layered oxide cathodes and their contribution to rapid degradation of Li-rich cathodes.

In Chapter 3, a comprehensive literature review has been carried out on the oxygen release originated degradation mechanisms of various classes of the cathodes. In this review article we summarized the recent progress in understanding the mechanisms of the oxygen release phenomena and corelative structural degradations observed in four major groups of cathode materials: layered, spinel, olivine and Li-rich cathodes. The methodology of studying the oxygen release originated degradation mechanisms, the state-of-the-art understanding of such phenomena and the proposed solutions to mitigate the parasitic oxygen release reactions, were the topics that were covered in this comprehensive review.

Next, by identifying the missing pieces of information in understanding the thermal decomposition reaction of Li_xCoO_2, a rigorous study by the combination of thermal analysis, advanced *in-situ* TEM technique and computational modeling, was carried out in this research. The results presented in Chapter 4 show that Li_xCoO_2 cathode crystals undergo surface originated thermal decomposition in which oxygen loss initiates on the surface and propagates to core of the

particle in a kinetically controlled reaction. Ab initio molecular dynamics simulations (AIMD) results carried out by Dr. Balbuena's group demonstrated that the reason for such heterogenous thermal decomposition reaction is that the oxygen release is highly dependent on the Li_xCoO_2 facet orientation. While the [001] facets are stable at 300 °C, oxygen release is observed from the [012] and [104] facets, where under-coordinated oxygen atoms from the delithiated structures are able to combine and eventually evolve as O_2. The novel understanding that emerges from the present study provides in-depth insights into the thermal runaway mechanism of Li-ion batteries and can assist the design and fabrication of cathode crystals with the most thermally stable facets.

By understanding the role of surface structure in the thermal decomposition of Li_xCoO_2, we proposed a novel surface engineering technique to mitigate the parasitic oxygen release reaction. In Chapter 5, we show that atomically thin layer of reduced graphene oxide can suppress the oxygen-release from Li_xCoO_2 particles and improve their structural stability significantly. We performed electrochemical cycling, differential electrochemical mass spectroscopy (carried out by Dr. Salehi-Khojin's group), differential scanning calorimetry (DSC), and *in-situ* heating transmission electron microscopy to characterize the effectiveness of the graphene-coating on the abusive tolerance of Li_xCoO_2. Electrochemical cycling mass spectroscopy results suggest that oxygen-release is hindered at high cut-off voltage cycling when the cathode is coated with reduced graphene oxide (rGO). Thermal analysis, *in-situ* heating transmission electron microscopy and electron energy loss spectroscopy (TEM/EELS) results show that the reduction of Co species from the graphene-coated samples is significantly delayed compared with the case of bare cathode. Finally, density functional theory (DFT) and *ab-initio* molecular dynamics (AIMD) calculations (done by Dr. Balbuena's group) show that the rGO layers could suppress O_2 formation more effectively due to the strong $C\text{-}O_{cathode}$ bond formation at the interface of rGO/LCO where low

coordination oxygens exist. This systematic investigation uncovers a reliable approach for hindering the oxygen release reaction and mitigating the thermal instability of battery cathodes.

Chapter 6 presented our research on identification of composite structure of Li-rich cathodes, the atomic structure of the grain boundaries in these nanocomposites and contribution of the grain boundaries on rapid degradation process of these cathodes. Aberration corrected scanning transmission electron microscopy (AC-STEM) was utilized to study the core atomic structure of Li- and Mn-rich, layered-layered, $xLi_2MnO_3 \bullet (1-x)LiTMO_2$ (TM=Ni, Mn, Co) (LMR-NMC) materials prior and subsequent to electrochemical cycling. The results demonstrated that the Li-rich cathode particles are nanocomposites composed of hexagonal $LiMO_2$ and monoclinic Li_2MO_3 phases with various possible grain/phase boundary structures, such as spinel interfaces. These structures were found to have a dependence on the configuration of the adjacent grains, where stacking of two layered grains perpendicular to their layered structure formed grain boundaries with increased interlayer distances, whereas staking of grains parallel to their layered structures resulted in a spinel-type grain boundary. It was demonstrated that such grain boundaries, that are also highly strained, would promote initiation of crack formation. Subsequently, fracture and disintegration of the active materials may ensue resulting in loss of performance. Additionally, preferred Mn dissolution and Ni-enrichment was observed in the grain boundaries of cycled samples, implying an important role of such boundaries in performance degradation mechanisms. This work reveals the complex role between composition, synthesis, and structure-property relationships of advanced cathode designs and reiterates the important role that local atomic structures can play in defining macroscopic electrode properties as well as the need to further understand these materials across various length scales.

7.2. Future Work

7.2.1. Investigating the effect of the spinel and the rock-salt surface reconstruction layers on the electrochemical properties and structural stability of the layered oxide cathode materials

The electrochemical performance of the layered oxide cathode materials is highly correlated to their surface structure[49–51]. Surface originated phase transitions, namely reconstruction of the layered to disordered rock-salt and spinel-like structures is considered as one of the primary issues that is observed in almost all the layered oxide cathode either at pristine or cycled state[12,157,469]. As discussed in the Introduction and demonstrated in Figure 3, the layered, spinel and the disordered rock-salt phases share the common oxygen fcc framework and the formation of such phase reconstruction layers occurs by migration of transition metal to the Li-octahedral sites. Spinel phase formation is due to the migration of ¼ of transition metals to Li octahedral sites forming a cubic symmetry, however in the disordered rock-salt structure, both cations are intermixed in the slabs and do not exhibit a long-range order (Figure 3B)[13,14].

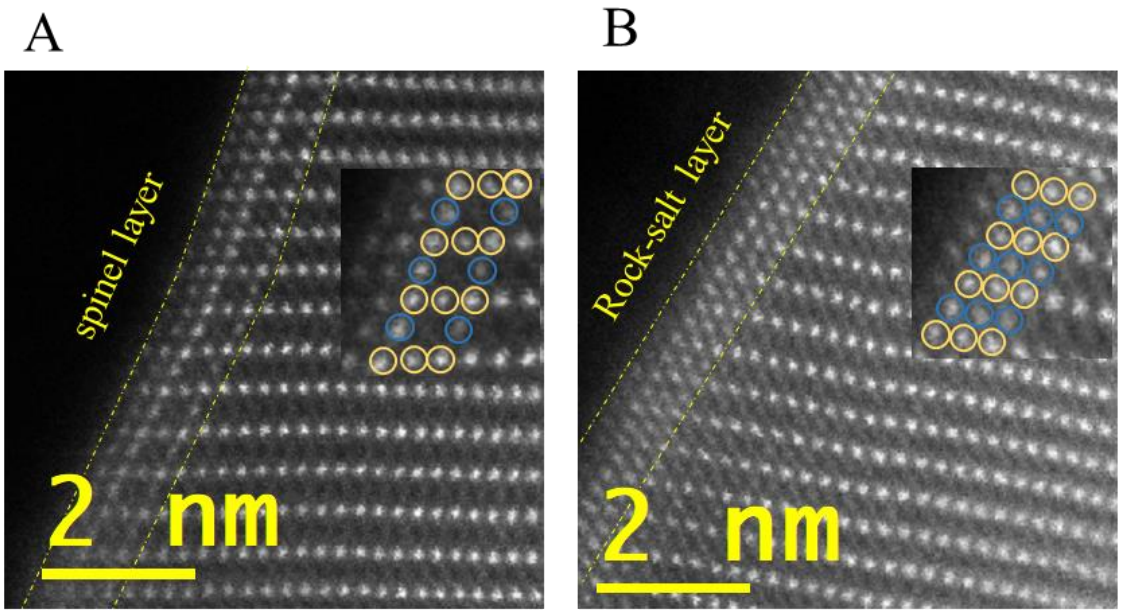

Figure 58. atomic resolution HAADF images from the surface structure of pristine NMC Samples with (A) spinel-like surface reconstruction layer and (B) rock-salt surface reconstruction layer. In the digitally magnified inset images, yellow circles correspond to the transition metal octahedral sites and blue circles correspond to migrated transition metals.

Although the occurrence and the atomic mechanisms of such phase transformations are heavily studied and are widely accepted in the literature, there are still many ambiguities about their role in the battery performance and degradation. For instance, it is suggested that such surface layers might act as stabilizers on the cathode surface and protect the interface, similar to the anode SEI layer[11]. However, some works suggest that such electrochemically inactive phases limit the Li-ion transfer, cause capacity degradation and can result in voltage polarization of the cell[94]. In addition, it is not totally clear that why the spinel or the rock-salt structures preferably form in various imaged particle. For instance, does chemical composition variation affects the preference of each phase over the other? Does the phase type have any correlation to the local disruption in the chemical composition of the surface? And most importantly, how does rock-salt or spinel phase formation affect the electrochemical properties and structural stability of the cathode samples, if

their formation can be controlled through synthesis procedure. Therefore, a suggested future work to follow up in thesis would be extensive atomic resolution study on the layered oxide cathodes to understand the causative, correlative and affective parameters of spinel or rock-salt surface reconstruction layers. As can be seen from the *Figure 58*, such phases can be detected on the layered oxide cathodes surfaces. Subsequently, chemical analysis through EDS and EELS spectroscopy would be helpful in determining the relationship of the surface phase with chemical composition and oxygen stoichiometry. By understanding such governing parameters, cathodes with either spinel or rock-salt phase can be synthesized. This is a very challenging step as identification of the of the surface layers can only be carried out through atomic resolution STEM imaging, because the very small thickness of the surface layer cannot be characterized with any other method. However, after successful synthesis of the cathodes with either spinel or rock-salt phase structures, various electrochemical tests such as long-term cycling and EIS measurements, together with ex-situ characterization techniques such as XRD, XPS and TEM can be utilized to understand the effect of the surface reconstruction phase. Additionally, *in-situ* synchrotron X-ray absorption and diffraction methods can also be utilized to acquire a more robust understanding. Then, by processing and comparing all the acquired data, a comprehensive understanding on the effect of phase structure of cathodes surface will be acquired. The proposed research flow is schematically illustrated in Figure *59*.

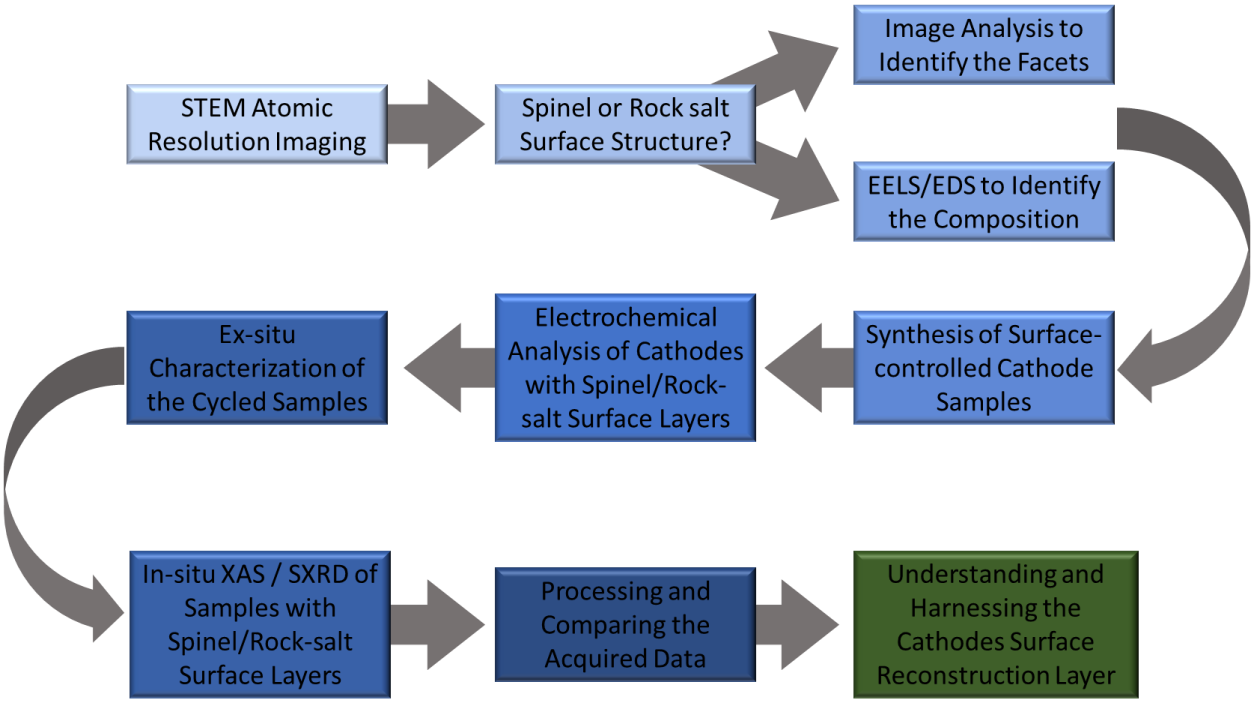

Figure 59. The flow chart for the proposed future step on identifying the effect of spinel and rock-salt reconstruction layers on the electrochemical properties of cathode materials.

7.2.2. Atomic scale analysis of the layered oxide cathodes dopants distribution and correlating the atomic findings to their electrochemical performance.

Effect of dopants on the electrochemical performance and the structural stability of the cathode materials have been widely studied in the recent past. Such studies have been summarized thoroughly in the Section 3.1.1 of the Chapter 3. Although, the extent of the improvements achieved by using different dopant elements are not quite similar, the variations are typically addressed by attributes such as the dopants' site occupancy, dopants effect on the band gap and conductivity of the materials or lattice spacing. However, the distribution of the dopant ions has been mostly taken for granted as most researchers believe that the dopants will distribute homogenously in the crystal structure of the cathodes. Therefore, agglomeration and clustering of the dopant ions that can play a key role in the structural stability and electrochemical properties of

the materials were not thoroughly investigated. Interestingly, our recent study on the distribution of W dopants in the $LiCoO_2$ structure in collaboration with Dr. Croy's team at Argonne National Laboratory (Discussed in the Appendix) demonstrated that the dopant distribution can be inhomogeneous, localized and ordered in the cathode structure. *Figure 60* shows an example of a W-doped $LiCoO_2$ particle. The z-contrast HAADF image demonstrates that the W dopants do not distribute homogeneously in the crystal structure. In fact, it can be observed that the W atoms appear as distinct WO_2 slabs within the $LiCoO_2$ structure. In other words, dopant W ions have been ordered in the structure, forming distinct lines to minimize W-Co bond formation. Through crystal strain analysis, it was understood that the interlayer distance has remained unchanged and the introduction of the dopant rich layers has not induced any strain in the crystal. In addition to Z-contrast imaging, EDS line scan is also performed that is shown as inset in the HAADF image, which demonstrates a sudden decrease in the content of Co and a peak in the content of W over the high-contrast lines in the HAADF image.

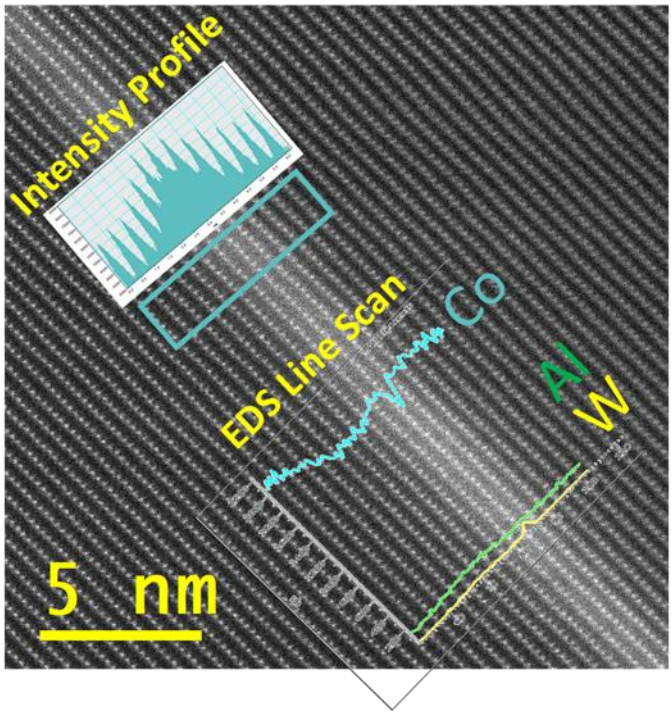

Figure 60. Atomic resolution, z-contrast HAADF image from a W-doped $LiCoO_2$ particle. The bright layers correspond to W-rich slabs that demonstrate the accumulation of W dopants in ordered W layers rather than a random dispersion of the dopant ions.

Accordingly, a future work dedicated to investigation of the atomic dispersion of dopants in the layered oxide cathodes is proposed following this thesis. In this proposed research, various dopants can be added to a layered oxide cathode structure such as $LiCoO_2$. Then, atomic resolution imaging and chemical analysis can be carried out on the doped sample. The capability of z-contrast STEM imaging together with chemical analysis techniques such as EELS and EDS in identification of various atomic species with high spatial resolution can be utilized extensively in this research. Then based on the homogeneity of the dispersion of dopant species, the doping conditions can be modified to improve the dopant dispersion. Electrochemical tests should be carried out at this point to understand the correlation of dopant dispersion with the electrochemical properties of the cathodes. DFT calculations can also be carried out to better understand the underlying reasons governing the dopant dispersion homogeneity in the cathode structure. By carrying out all the

proposed experimental and computational efforts, a comprehensive understanding on the effect of parameters such as doping concentration, the annealing temperature, the chemical composition of the bare cathode and the nature of the dopant ions on the dopant dispersion and electrochemical properties of cathodes can be acquired and reported. Such through investigation can have a great contribution in identifying the suitable dopant and its optimum concentration in each class of cathode materials, which can pave the way for future generation of engineered cathode materials. The work follow of this proposed research is shown in the following in the Figure *61*.

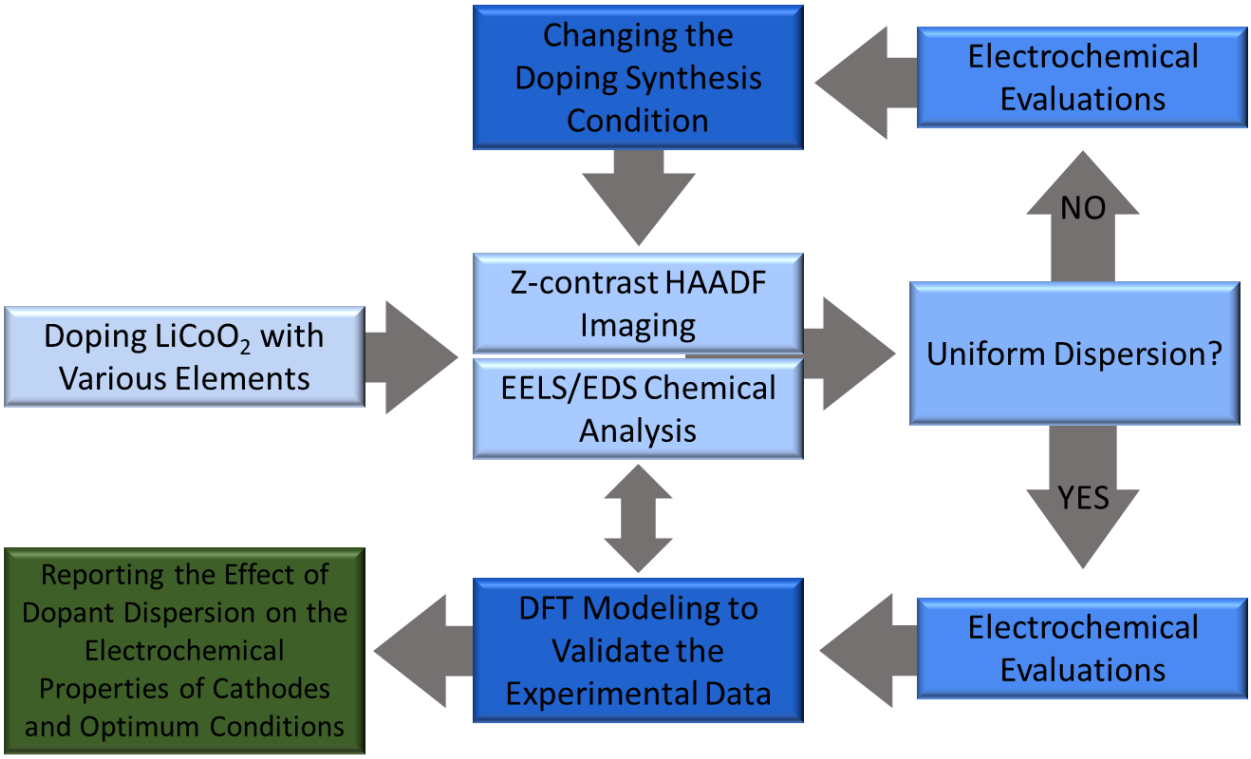

Figure 61. The flow chart for the proposed future step on studying the effect of dopant dispersion in the layered oxide cathodes structure and identifying the optimum doping conditions.

7.2.3. Cell scale study of the effect of graphene-coating on the thermal/structural stability of layered oxide cathodes.

Following the research presented in the Chapter 5 of this thesis, which demonstrated successful mitigation of oxygen release and improved structural properties of $LiCoO_2$ upon graphene-coating

at single particle scale, larger cell scale analysis on our modified electrodes is proposed as a future step. As such, *in-situ* synchrotron XRD experiments as well as *in-situ* calorimetry analysis are considered as the future steps to be carried out. *In-situ* synchrotron XRD (that can be done at ANL through user proposal competitions), is capable of both *in-situ* heating and *in-operando* cycling experiments and the results are representative of the average sample and have a better statistical reliability than TEM experiments. High energy synchrotron X-rays are favorable for *in-operando* cycling tests because 1) they are able to penetrate the coin-cells without major diffraction from the coin-cell casing and materials, and 2) the spectrum acquisition time is much faster compared to in-lab XRD experiments. Also, *in-situ* heating experiments can also be carried out using special SXRD setups to compare the thermal stability of the bare and the coated cathode samples. To evaluate the possibility of such tests, preliminary *in-situ* heating SXRD experiment has been carried out on the bare $LiCoO_2$ sample. As can be seen from the *Figure 62*, upon heating the sample major changes can be observed in the crystal structure. For instance, the d-spacing of the (003) lattice have changed from 4.871 to 4.700 at over 200 °C, which correspond to the phase transitions from hexagonal Li_xCoO_2 to spinel Co_3O_4 phase. Similarly, the (010), (107) and (018) planes of the hexagonal phase transforms to (311), (333) and (440) planes of the spinel Co_3O_4 phase respectively and the (012) and (113) spacings of the hexagonal phase vanish during the phase transition. The temperature of the phase transition and the extent of phase transitions can be analyzed by comparing the results to the coated sample. Also, cathodes that are engineered with other mitigating strategies such as alumina coating or doped cathodes that are more extensively studied and have well-known properties can be studied using the same experimental procedure and compared to the graphene coated samples.

Another cell-scale analysis that can be carried out on the graphene-coated sample is the *in-situ* heating/cycling calorimetry experiments. In these experiments a Li-ion battery coin cell is exposed to non-equilibrium working conditions such as high voltage cycling or high temperatures and the heat flow from the coin cell is recorded using a calorimeter. Therefore, endothermic reactions such as cathode decomposition, electrolyte decomposition and separator meltdown and exothermic reactions such as reactions between the O_2 (released from the cathode) and the decomposed electrolyte can be recorded and compared in the graphene-coated and the bare sample. Therefore, the distinct endothermic and exothermic peaks that are recorded under abusive battery operation can be identified and the extent and onset temperature of such reaction can be compared in the coin-cell with bare cathode versus the cell with coated cathodes.

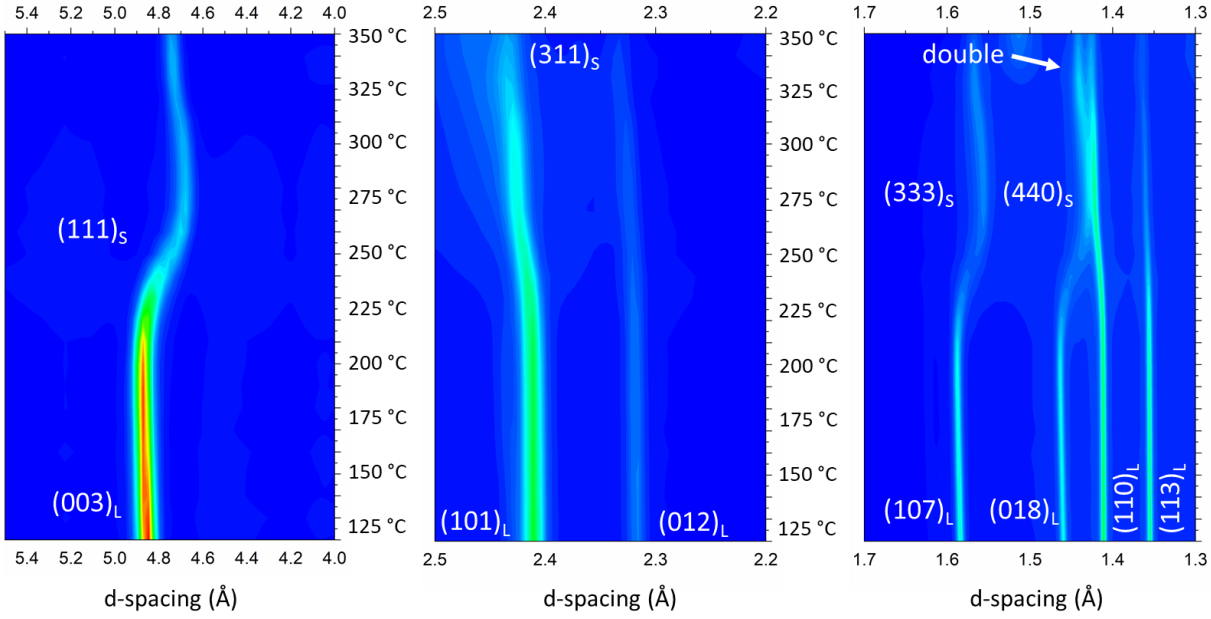

Figure 62. *In-situ* heating synchrotron XRD results from $Li_{0.5}CoO_2$ sample. The phase transformation from layered to spinel/rock-salt phases can be determined using this technique.

References

(1) Sharifi-Asl, S.; Soto, F. A.; Nie, A.; Yuan, Y.; Asayesh-Ardakani, H.; Foroozan, T.; Yurkiv, V.; Song,

B.; Mashayek, F.; Klie, R. F.; et al. Facet-Dependent Thermal Instability in LiCoO2. *Nano Lett.* **2017**, *17* (4), 2165–2171.

(2) Sharifi-asl, S.; Soto, F. A.; Foroozan, T.; Asadi, M.; Yuan, Y.; Deivanayagam, R.; Rojaee, R.; Song, B.; Bi, X.; Amine, K.; et al. Anti-Oxygen Leaking LiCoO 2. *Adv. Funct. Mater.* **2019**, 1901110.

(3) Whittingham, M. S. The Role of Ternary Phases in Cathode Reactions. *J. Electrochem. Soc.* **1976**, *123* (3).

(4) Deng, D. Li-Ion Batteries : Basics , Progress , and Challenges. *Energy Sci. Eng.* **2015**, *3* (5), 385–418.

(5) Goodenough, J. B.; Park, K. S. The Li-Ion Rechargeable Battery: A Perspective. *J. Am. Chem. Soc.* **2013**, *135* (4), 1167–1176.

(6) Whittingham, M. S. Lithium Batteries and Cathode Materials. *Chem. Rev.* **2004**, *104* (10), 4271–4301.

(7) Mizushima, K.; Jones, P. C.; Wiseman, P. J.; Goodenough, J. B. LixCoO2 (0<x⩽1): A New Cathode Material for Batteries of High Energy Density. *Solid State Ionics* **1981**, *4*, 171–174.

(8) Croguennec, L.; Saadoune, I. An Overview of the Li(Ni,M)O2 Systems: Syntheses, Structures and Properties. *Electrochim. Acta* **1999**, *45*, 243–253.

(9) Xu, B.; Qian, D.; Wang, Z.; Meng, Y. S. Recent Progress in Cathode Materials Research for Advanced Lithium Ion Batteries. *Mater. Sci. Eng. R Reports* **2012**, *73* (5–6), 51–65.

(10) Kim, J.; Lee, H.; Cha, H.; Yoon, M.; Park, M. Prospect and Reality of Ni-Rich Cathode for Commercialization. *Adv. Energy Mater.* **2018**, *8*, 1702028.

(11) Radin, M. D.; Hy, S.; Sina, M.; Fang, C.; Liu, H.; Vinckeviciute, J.; Zhang, M.; Whittingham, M. S.; Meng, Y. S. Narrowing the Gap between Theoretical and Practical Capacities in Li-Ion Layered Oxide Cathode Materials. *Adv. Energy Mater.* **2017**, *7*, 1–33.

(12) Lin, F.; Markus, I. M.; Nordlund, D.; Weng, T.-C.; Asta, M. D.; Xin, H. L.; Doeff, M. M. Surface Reconstruction and Chemical Evolution of Stoichiometric Layered Cathode Materials for Lithium-Ion Batteries. *Nat. Commun.* **2014**, *5*, 1–9.

(13) Wang, H.; Jang, Y.; Huang, B.; Sadoway, D. R.; Chiang, Y. TEM Study of Electrochemical Cycling-Induced Damage and Disorder in LiCoO2 Cathodes for Rechargeable Lithium Batteries. *J. Electrochem. Soc.* **1999**, *146* (2), 473–480.

(14) Lu, P.; Yan, P.; Romero, E.; Spoerke, E. D.; Zhang, J. G.; Wang, C. M. Observation of Electron-Beam-Induced Phase Evolution Mimicking the Effect of the Charge-Discharge Cycle in Li-Rich Layered Cathode Materials Used for Li Ion Batteries. *Chem. Mater.* **2015**, *27* (4), 1375–1380.

(15) Zhou, G. Atomic Insight into the Layered/Spinel Phase Transformation in Charged LiNi0.80Co0.15Al0.05O2 Cathode Particles. *J. Phys. Chem. C* **2017**, *121*, 1421–1430.

(16) Yeon, N.; Yim, T.; Ho, J.; Yu, J.; Lee, Z. Microstructural Study on Degradation Mechanism of Layered Electron Microscopy. *J. Power Sources* **2016**, *307*, 641–648.

(17) Ceder, G.; Ven, A. Van Der. Phase Diagrams of Lithium Transition Metal Oxides : Investigations from First Principles. *Electrochim. Acta* **1999**, *45*, 131–150.

(18) Wolverton, C.; Zunger, A. Prediction of Li Intercalation and Battery Voltages in Layered vs . Cubic LiCoO2. *J. Electrochem. Soc.* **1998**, *145* (7), 2424–2431.

(19) Gabrisch, H.; Yazami, R.; Fultz, B. Hexagonal to Cubic Spinel Transformation in Lithiated Cobalt Oxide. *J. Electrochem. Soc.* **2004**, *151* (6), A891.

(20) Division, A. B. Solid-State Synthesis and Characterization of LiCoO 2 and LiNi y Co 1 – y O 2 Solid Solutions. **2000**, *23* (5), 345–348.

(21) Mizushima, K.; Jones, P. C.; Wiseman, P. J.; Goodenough, J. B. LixCoO2 (0<X<-1): A New Cathode Material for Batteries of High Energy Density. *Mater. Res. Bull.* **1980**, *15* (6), 783–789.

(22) Wu, N.; Zhang, Y.; Guo, Y.; Liu, S.; Liu, H.; Wu, H. Flakelike LiCoO2 with Exposed {010} Facets As a Stable Cathode Material for Highly Reversible Lithium Storage. *ACS Appl. Mater. Interfaces* **2016**, *8* (4), 2723–2731.

(23) Yan, H.; Huang, X.; Lu, Z.; Huang, H.; Xue, R.; Chen, L. Microwave Synthesis of LiCoO2 Cathode Materials. *J. Power Sources* **1997**, *68*, 530–532.

(24) Balaji, S.; Mutharasu, D.; Subramanian, N. S.; Ramanathan, K. A Review on Microwave Synthesis of Electrode Materials for Lithium-Ion Batteries. *Ionics (Kiel).* **2009**, *15* (6), 765–777.

(25) Hu, G.; Liao, G.; Peng, Z.; Xiao, J.; Zhang, X.; Yu, X. Structure and Electrochemical Properties of LiCoO2 Synthesized by Microwave Heating. *J. Cent. South Univ. Technol.* **2004**, *11* (3), 261–264.

(26) Kang, S. G.; Kang, S. Y.; Ryu, K. S.; Chang, S. H. Electrochemical and Structural Properties of HT-LiCoO and LT- 2 LiCoO Prepared by the Citrate Sol-Gel Method. *Solid State Ionics* **1999**, *120*, 155–161.

(27) Peng, Z. S.; Wan, C. R.; Jiang, C. Y. Synthesis by Sol–Gel Process and Characterization of LiCoO 2 Cathode Materials. *J. Power Sources* **1998**, *72*, 215–220.

(28) Sun, Y.-K.; Oh, I.-H.; Hong, S.-A. Synthesis of Ultrafine LiCo02 Powders by the Sol-Gel Method. *J. Mater. Sci.* **1996**, *31*, 3617–3621.

(29) In-Hwan, O.; Hong, S.-A. Low-Temperature Preparation of Ultrafine LiCoO 2 Powders by the Sol – Gel Method. *J. Mater. Sci.* **1997**, *32*, 3177–3182.

(30) Sun, Y. Synthesis of LiCo Ni O Powders by a Sol – Gel Method. **1997**, *7* (8), 1481–1485.

(31) Fu, J.; Bai, Y.; Liu, C.; Yu, H.; Mo, Y. Physical Characteristic Study of LiCoO2 Prepared by Molten Salt Synthesis Method in 550-800 ??C. *Mater. Chem. Phys.* **2009**, *115* (1), 105–109.

(32) Tan, K. S.; Reddy, M. V.; Rao, G. V. S.; Chowdari, B. V. R. High-Performance LiCoO2 by Molten Salt (LiNO3:LiCl) Synthesis for Li-Ion Batteries. *J. Power Sources* **2005**, *147* (1–2), 241–248.

(33) Chen, J.; Wang, S.; Whittingham, M. S. Hydrothermal Synthesis of Cathode Materials. *J. Power Sources* **2007**, *174* (2), 442–448.

(34) Tabuchi, M.; Ado, K.; Kobayashi, H.; Sakaebe, H.; Kageyama, H.; Masquelier, C.; Yonemura, M.; Hirano, A.; Kanno, R. Preparation of LiCoO<inf>2</Inf> and LiCo(1-x)Fe(x)O<inf>2</Inf> Using Hydrothermal Reactions. *J. Mater. Chem.* **1999**, *9* (1), 199–204.

(35) Song, S. W.; Han, K. S.; Sasagawa, I.; Watanabe, T.; Yoshimura, M. Effect of LiOH Concentration Change on Simultaneous Preparation of LiCoO2 Film and Powder by Hydrothermal Method. *Solid*

State Ionics **2000**, *135* (1–4), 277–281.

(36) Burukhin, A.; Brylev, O.; Hany, P.; Churagulov, B. R. Hydrothermal Synthesis of LiCoO2 for Lithium Rechargeable Batteries. *Solid State Ionics* **2002**, *151* (1–4), 259–263.

(37) Kramer, D.; Ceder, G. Tailoring the Morphology of LiCoO2: A First Principles Study. *Chem. Mater.* **2009**, *21* (16), 3799–3809.

(38) Chen, H.; Wu, L.; Zhang, L.; Zhu, Y.; Grey, C. P. LiCoO2 Concaved Cuboctahedrons from Symmetry-Controlled Topological Reactions. *J. Am. Chem. Soc.* **2011**, *133* (2), 262–270.

(39) Saadoune, I.; Delmas, C. The Insulator – Metal Transition upon Lithium Deintercalation From. *J. Mater. Chem.* **1999**, 1135–1140.

(40) Marianetti, C. A.; Kotliar, G.; Ceder, G. ARTICLES A First-Order Mott Transition in Li x CoO 2. *Nat. Mater.* **2004**, *3* (September), 627–631.

(41) Ven, A. Van der; Ceder, G.; Asta, M.; Tepesch, P. D. First-Principles Theory of Ionic Diffusion with Nondilute Carriers. *Phys. Rev. B* **2001**, *64*, 1–17.

(42) Dompablo, M. E. A. De; Ven, A. Van Der; Ceder, G. First-Principles Calculations of Lithium Ordering and Phase Stability on Li x NiO 2. *Phys. Rev. B* **2002**, *66* (August), 1–9.

(43) Xia, H.; Meng, Y. S.; Lu, L.; Ceder, G.; Alliance, S. Electrochemical Behavior and Li Diffusion Study of LiCoO 2 Thin Film Electrodes Prepared by PLD. In *Advanced Materials for Micro- and Nano-Systems (AMMNS)*; 2007; p http://en.scientificcommons.org/20613936.

(44) Xu, B.; Meng, S. Factors Affecting Li Mobility in Spinel LiMn 2 O 4 — A First-Principles Study by GGA and GGA + U Methods. *J. Power Sources* **2010**, *195* (15), 4971–4976.

(45) Kikkawa, J.; Terada, S.; Gunji, A.; Nagai, T.; Kurashima, K.; Kimoto, K. Chemical States of Overcharged LiCoO 2 Particle Surfaces and Interiors Observed Using Electron Energy-Loss Spectroscopy. *J. Phys. Chem. C* **2015**, *119* (28), 15823–15830.

(46) Zhao, J.; Wang, L.; He, X.; Wan, C.; Jiang, C. Kinetic Investigation of LiCoO 2 by Electrochemical Impedance Spectroscopy (EIS). *Int. J. Electrochem. Sci.* **2010**, *5*, 478–488.

(47) Jung, S.-K.; Gwon, H.; Hong, J.; Park, K.-Y.; Seo, D.-H.; Kim, H.; Hyun, J.; Yang, W.; Kang, K. Understanding the Degradation Mechanisms of LiNi0.5Co0.2Mn0.3O2 Cathode Material in Lithium Ion Batteries. *Adv. Energy Mater.* **2014**, *4*, 1300787.

(48) Hausbrand, R.; Cherkashinin, G.; Ehrenberg, H.; Gröting, M.; Albe, K.; Hess, C.; Jaegermann, W. Fundamental Degradation Mechanisms of Layered Oxide Li-Ion Battery Cathode Materials: Methodology, Insights and Novel Approaches. *Mater. Sci. Eng. B Solid-State Mater. Adv. Technol.* **2015**, *192* (C), 3–25.

(49) Zhao, J.; Zhang, W.; Huq, A.; Misture, S. T.; Zhang, B.; Guo, S.; Wu, L.; Zhu, Y.; Chen, Z.; Amine, K.; et al. In Situ Probing and Synthetic Control of Cationic Ordering in Ni-Rich Layered Oxide Cathodes. *Adv. Energy Mater.* **2017**, *7* (3), 1–13.

(50) Reale, P.; Privitera, D.; Panero, S.; Scrosati, B. An Investigation on the Effect of Li+/Ni2+cation Mixing on Electrochemical Performances and Analysis of the Electron Conductivity Properties of LiCo0.33Mn0.33Ni0.33O2. *Solid State Ionics* **2007**, *178* (23–24), 1390–1397.

(51) Yan, P.; Zheng, J.; Zhang, J. G.; Wang, C. Atomic Resolution Structural and Chemical Imaging Revealing the Sequential Migration of Ni, Co, and Mn upon the Battery Cycling of Layered Cathode. *Nano Lett.* **2017**, *17*, 3946–3951.

(52) Tarascon, J. M.; Klein, L. C. Cobalt Dissolution in LiCoO2-Based Non-Aqueous Rechargeable Batteries. *Solid State Ionics* **1996**, *83*, 167–173.

(53) Wandt, J.; Freiberg, A.; Thomas, R.; Gorlin, Y.; Siebel, A.; Jung, R.; Gasteiger, H. A.; Tromp, M. Transition Metal Dissolution and Deposition in Li- Ion Batteries Investigated by Operando X-Ray Absorption Spectroscopy †. *J. Mater. Chem. A* **2016**, 18300–18305.

(54) Evertz, M.; Horsthemke, F.; Kasnatscheew, J.; Markus, B.; Winter, M.; Nowak, S. (NCM 111) in Lithium Ion Full Cells by Using the Total Re Fl Ection X-Ray Fl Uorescence Technique. *J. Power Sources* **2016**, *329*, 364–371.

(55) Wei, C.; Zhang, Y.; Zhang, Y.; Mud, L.; Liu, J.; Wang, C.; Yang, Y.; Doeff, M.; Pianetta, P.; Nordlund, D.; et al. Thermally Driven Mesoscale Chemomechanical Interplay in Li0.5Ni0.6Mn0.2Co0.2O2 Cathode Materials. *J. Mater. Chem. A* **2018**, *6*, 23055–23061.

(56) Wandt, J.; Freiberg, A. T. S.; Ogrodnik, A.; Gasteiger, H. A. Singlet Oxygen Evolution from Layered Transition Metal Oxide Cathode Materials and Its Implications for Lithium-Ion Batteries. *Mater. Today* **2018**.

(57) Yan, P.; Zheng, J.; Gu, M.; Xiao, J.; Zhang, J. G.; Wang, C. M. Intragranular Cracking as a Critical Barrier for High-Voltage Usage of Layer-Structured Cathode for Lithium-Ion Batteries. *Nat. Commun.* **2017**, *8*, 1–9.

(58) Lim, J. M.; Hwang, T.; Kim, D.; Park, M. S.; Cho, K.; Cho, M. Intrinsic Origins of Crack Generation in Ni-Rich LiNi0.8Co0.1Mn0.1O2Layered Oxide Cathode Material. *Sci. Rep.* **2017**, *7*, 2–11.

(59) Yan, P.; Zheng, J.; Chen, T.; Luo, L.; Jiang, Y.; Wang, K.; Sui, M.; Zhang, J.-G.; Zhang, S.; Wang, C. Coupling of Electrochemically Triggered Thermal and Mechanical Effects to Aggravate Failure in a Layered Cathode. *Nat. Commun.* **2018**, No. 100, 1–8.

(60) Wen, Y.; Xiao, D.; Liu, X.; Gu, L. Microstructure Dynamics of Rechargeable Battery Materials Studied by Advanced Transmission Electron Microscopy. *NPG Asia Mater.* **2017**, *9* (3), e360-12.

(61) Lin, C.; Tang, A.; Mu, H.; Wang, W.; Wang, C. Aging Mechanisms of Electrode Materials in Lithium-Ion Batteries for Electric Vehicles. *J. Chem.* **2015**, *2015*, 1–11.

(62) Nam, K.-W.; Bak, S.-M.; Hu, E.; Yu, X.; Zhou, Y.; Wang, X.; Wu, L.; Zhu, Y.; Chung, K.-Y.; Yang, X.-Q. Combining In Situ Synchrotron X-Ray Diffraction and Absorption Techniques with Transmission Electron Microscopy to Study the Origin of Thermal Instability in Overcharged Cathode Materials for Lithium-Ion Batteries. *Adv. Funct. Mater.* **2013**, *23* (8), 1047–1063.

(63) Yano, A.; Shikano, M.; Ueda, A.; Sakaebe, H.; Ogumi, Z. LiCoO 2 Degradation Behavior in the High-Voltage Phase Transition Region and Improved Reversibility with Surface Coating. *J. Electrochem. Soc.* **2017**, *164*, 6116–6122.

(64) Aurbach, D.; Markovsky, B.; Salitra, G.; Markevich, E.; Talyossef, Y.; Koltypin, M.; Nazar, L.; Ellis, B.; Kovacheva, D. Review on Electrode – Electrolyte Solution Interactions , Related to Cathode Materials for Li-Ion Batteries. *J. Power Sources* **2007**, *165*, 491–499.

(65) Xu, K. Electrolytes and Interphases in Li-Ion Batteries and Beyond. *Chem. Rev.* **2014**, No. 114, 11503−11618.

(66) Wang, H.; Rus, E.; Sakuraba, T.; Kikuchi, J.; Kiya, Y.; Abruna, H. D.; Abruña, H. D.; Abruna, H. D.; Abruña, H. D. CO2 and O2 Evolution at High Voltage Cathode Materials of Li-Ion Batteries: A Differential Electrochemical Mass Spectrometry Study. *Anal. Chem.* **2014**, *86* (13), 6197–6201.

(67) Mu, L.; Lin, R.; Xu, R.; Han, L.; Xia, S.; Sokaras, D.; Steiner, J. D.; Weng, T.; Nordlund, D.; Doeff, M. M.; et al. Oxygen Release Induced Chemomechanical Breakdown of Layered Cathode Materials. *Nano Lett.* **2018**, *18*, 3241–2149.

(68) Williard, N.; He, W.; Hendricks, C.; Pecht, M. Lessons Learned from the 787 Dreamliner Issue on Lithium-Ion Battery Reliability. *Energies* **2013**, *6* (9), 4682–4695.

(69) Liu, X.; Ren, D.; Hsu, H.; Feng, X.; Xu, G. L.; Zhuang, M.; Gao, H.; Lu, L.; Han, X.; Chu, Z.; et al. Thermal Runaway of Lithium-Ion Batteries without Internal Short Circuit. *Joule* **2018**, *2*, 1–18.

(70) Spotnitz, R.; Franklin, J. Abuse Behavior of High-Power, Lithium-Ion Cells. *J. Power Sources* **2003**, *113* (1), 81–100.

(71) Saito, Y.; Takano, K.; Negishi, A. Thermal Behaviors of Lithium-Ion Cells during Overcharge. *J. Power Sources* **2001**, *97* (January), 693–696.

(72) Liu, K.; Liu, Y.; Lin, D.; Pei, A.; Cui, Y. Materials for Lithium-Ion Battery Safety. *Sci. Adv.* **2018**, No. June.

(73) Dahn, J. R.; Fuller, E. W.; Obrovac, M.; von Sacken, U. Thermal Stability of LixCoO2, LixNiO2 and λ-MnO2 and Consequences for the Safety of Li-Ion Cells. *Solid State Ionics* **1994**, *69* (3–4), 265–270.

(74) Li, W.; Liu, X.; Celio, H.; Smith, P.; Dolocan, A.; Chi, M.; Manthiram, A. Mn versus Al in Layered Oxide Cathodes in Lithium-Ion Batteries: A Comprehensive Evaluation on Long-Term Cyclability. *Adv. Energy Mater.* **2018**, *8*, 1703154.

(75) Belharouak, I.; Lu, W.; Liu, J.; Vissers, D.; Amine, K. Thermal Behavior of Delithiated Li(Ni0.8Co0.15Al0.05)O2 and Li1.1(Ni1/3Co1/3Mn1/3)0.9O2 Powders. *J. Power Sources* **2007**, *174* (2), 905–909.

(76) Belharouak, I.; Lu, W.; Vissers, D.; Amine, K. Safety Characteristics of Li(Ni0.8Co0.15Al 0.05)O2 and Li(Ni1/3Co1/3Mn 1/3)O2. *Electrochem. commun.* **2006**, *8* (2), 329–335.

(77) Wang, Y.; Jiang, J.; Dahn, J. R. The Reactivity of Delithiated Li(Ni1/3Co1/3Mn1/3)O2, Li(Ni0.8Co0.15Al0.05)O2 or LiCoO2 with Non-Aqueous Electrolyte. *Electrochem. commun.* **2007**, *9* (10), 2534–2540.

(78) Vinodkumar Etacheri, Rotem Marom, Ran Elazari, G. S. and D. A. Challenges in the Development of Advanced Li-Ion Batteries : A Review. *Energy Environ. Sci.* **2011**, No. 4, 3243–3262.

(79) Chikkannanavar, S. B.; Bernardi, D. M.; Liu, L. A Review of Blended Cathode Materials for Use in Li-Ion Batteries. *J. Power Sources* **2014**, *248*, 91–100.

(80) Lu, Z.; Beaulieu, L. Y.; Donaberger, R. A.; Thomas, C. L.; Dahn, J. R. Synthesis , Structure , and Electrochemical Behavior of Li[NixLi1/3-2x/3Mn2/3-x/3]O2. *J. ofThe Electrochem. Soc.* **2002**, *149* (6), 778–791.

(81) Qiu, B.; Zhang, M.; Xia, Y.; Liu, Z.; Meng, Y. S. Understanding and Controlling Anionic Electrochemical Activity in High-Capacity Oxides for Next Generation Li-Ion Batteries. *Chem. Mater.* **2017**, *29* (3), 908–915.

(82) Seo, D.-H.; Lee, J.; Urban, A.; Malik, R.; Kang, S.; Ceder, G. The Structural and Chemical Origin of the Oxygen Redox Activity in Layered and Cation-Disordered Li-Excess Cathode Materials. *Nat. Chem.* **2016**, *8*, 692–697.

(83) Lu, J.; Wu, T.; Amine, K. State-of-the-Art Characterization Techniques for Advanced Lithium-Ion Batteries. *Nat. Energy* **2017**, *2* (3).

(84) Marusczyk, A.; Albina, J.-M.; Hammerschmidt, T.; Drautz, R.; Eckl, T.; Henkelman, G. Oxygen Activity and Peroxide Formation as Charge Compensation Mechanisms in Li_2MnO_3. *J. Mater. Chem. A* **2017**, *5* (29), 15183–15190.

(85) Luo, K.; Roberts, M. R.; Hao, R.; Guerrini, N.; Pickup, D. M.; Liu, Y. S.; Edström, K.; Guo, J.; Chadwick, A. V.; Duda, L. C.; et al. Charge-Compensation in 3d-Transition-Metal-Oxide Intercalation Cathodes through the Generation of Localized Electron Holes on Oxygen. *Nat. Chem.* **2016**, *8* (7), 684–691.

(86) Bhowmick, S.; Sadrzadeh, A.; Yakobson, B. I.; Penev, E. S.; Yakobson, B. I.; Gao, J.; Zhao, J.; Struzhkin, V. V; Mao, H.; Hemley, R. J.; et al. Visualization of O-O Peroxo-like Dimers in High-Capacity Layered Oxides for Li-Ion Batteries. *Science (80-.).* **2015**, *350* (6267), 1516–1521.

(87) Yu, H.; Zhou, H. High-Energy Cathode Materials (Li 2 MnO 3 –LiMO 2) for Lithium-Ion Batteries. *J. Phys. Chem. Lett.* **2013**, *4*, 1268–1280.

(88) Shukla, A. K.; Ramasse, Q. M.; Ophus, C.; Duncan, H.; Hage, F.; Chen, G. Unravelling Structural Ambiguities in Lithium- and Manganese-Rich Transition Metal Oxides. *Nat. Commun.* **2015**, *6*, 1–9.

(89) Yu, H.; Ishikawa, R.; So, Y.-G.; Shibata, N.; Kudo, T.; Zhou, H.; Ikuhara, Y. Direct Atomic-Resolution Observation of Two Phases in the $Li_{1.2}Mn_{0.567}Ni_{0.166}Co_{0.067}O_2$ Cathode Material for Lithium-Ion Batteries. *Angew. Chemie Int. Ed.* **2013**, *52* (23), 5969–5973.

(90) Sathiya, M.; Abakumov, A. M.; Foix, D.; Rousse, G.; Ramesha, K.; Saubanère, M.; Doublet, M. L.; Vezin, H.; Laisa, C. P.; Prakash, a S.; et al. Origin of Voltage Decay in High-Capacity Layered Oxide Electrodes. *Nat. Mater.* **2015**, *14* (2), 230–238.

(91) Ates, M. N.; Jia, Q.; Shah, A.; Busnaina, A. Mitigation of Layered to Spinel Conversion of a Li-Rich Layered Metal Oxide Cathode Material for Li-Ion Batteries. *J. Electrochem. Soc.* **2014**, *161* (3), 290–301.

(92) Liu, H.; Harris, K. J.; Jiang, M.; Wu, Y.; Goward, G. R.; Botton, G. A. Unraveling the Rapid Performance Decay of Layered High-Energy Cathodes: From Nanoscale Degradation to Drastic Bulk Evolution. *ACS Nano* **2018**, *12* (3), 2708–2718.

(93) Dixit, H.; Zhou, W.; Idrobo, J. C.; Nanda, J.; Cooper, V. R. Facet-Dependent Disorder in Pristine High-Voltage Lithium-Manganese-Rich Cathode Material. *ACS Nano* **2014**, *8* (12), 12710–12716.

(94) Kuppan, S.; Shukla, A. K.; Membreno, D.; Nordlund, D.; Chen, G. Revealing Anisotropic Spinel Formation on Pristine Li- and Mn-Rich Layered Oxide Surface and Its Impact on Cathode Performance. *Adv. Energy Mater.* **2017**, *7*, 1602010.

(95) Williams, D. B.; Carter, C. B. *Transmission Electron Microscopy A Textbook for Materials Science*; Springer, 2009.

(96) Jarvis, K.; Wang, C. C.; Varela, M.; Unocic, R. R.; Manthiram, A.; Ferreira, P. J. Surface Reconstruction in Li-Rich Layered Oxides of Li-Ion Batteries. *Chem. Mater.* **2017**, *29* (18), 7668–7674.

(97) Amos, C. D.; Roldan, M. A.; Varela, M.; Goodenough, J. B.; Ferreira, P. J. Revealing the Reconstructed Surface of Li[Mn2]O4. *Nano Lett.* **2016**, *16* (5), 2899–2906.

(98) Hwang, S.; Kim, S. M.; Bak, S. M.; Cho, B. W.; Chung, K. Y.; Lee, J. Y.; Chang, W.; Stach, E. A. Investigating Local Degradation and Thermal Stability of Charged Nickel-Based Cathode Materials through Real-Time Electron Microscopy. *ACS Appl. Mater. Interfaces* **2014**, *6* (17), 15140–15147.

(99) Wu, L.; Nam, K. W.; Wang, X.; Zhou, Y.; Zheng, J. C.; Yang, X. Q.; Zhu, Y. Structural Origin of Overcharge-Induced Thermal Instability of Ni-Containing Layered-Cathodes for High-Energy-Density Lithium Batteries. *Chem. Mater.* **2011**, *23* (17), 3953–3960.

(100) Sharifi-asl, S.; Lu, J.; Amine, K.; Shahbazian-yassar, R. Oxygen Release Degradation in Li-Ion Battery Cathode Materials : Mechanisms and Mitigating Approaches. *Adv. Energy Mater.* **2019**, 1900551.

(101) J.-M. Tarascon & M. Armand. Issues and Challenges Facing Rechargeable Lithium Batteries. *Nature* **2001**, *414* (November), 359–367.

(102) Abraham, K. M. Prospects and Limits of Energy Storage in Batteries. *J. Phys. Chem. Lett.* **2015**, *6* (5), 830–844.

(103) Lu, L.; Han, X.; Li, J.; Hua, J.; Ouyang, M. A Review on the Key Issues for Lithium-Ion Battery Management in Electric Vehicles. *J. Power Sources* **2013**, *226*, 272–288.

(104) Nitta, N.; Wu, F.; Lee, J. T.; Yushin, G. Li-Ion Battery Materials: Present and Future. *Mater. Today* **2015**, *18* (5), 252–264.

(105) Ganesh Venugopal. Characterization of Thermal Cut-off Mechanisms in Prismatic Lithium-Ion Batteries. *J. Power Sources* **2001**, *101*, 231–237.

(106) Zhang, Y. Di; Li, Y.; Xia, X. H.; Wang, X. L.; Gu, C. D.; Tu, J. P. High-Energy Cathode Materials for Li-Ion Batteries: A Review of Recent Developments. *Sci. China Technol. Sci.* **2015**, *58* (11), 1809–1828.

(107) Gong, Z.; Yang, Y. Recent Advances in the Research of Polyanion-Type Cathode Materials for Li-Ion Batteries. *Energy and Environmental Science*. 2011.

(108) Jung, R.; Strobl, P.; Maglia, F.; Stinner, C.; Gasteiger, H. A. Temperature Dependence of Oxygen Release from $LiNi_{0.6}Mn_{0.2}Co_{0.2}O_2$ (NMC622) Cathode Materials for Li-Ion Batteries. *J. Electrochem. Soc.* **2018**, *165* (11), A2869–A2879.

(109) Wang, Q.; Ping, P.; Zhao, X.; Chu, G.; Sun, J.; Chen, C. Thermal Runaway Caused Fire and Explosion of Lithium Ion Battery. *J. Power Sources* **2012**, *208*, 210–224.

(110) Aurbach, D.; Zaban, A.; Ein-Eli, Y.; Weissman, I.; Chusid, O.; Markovsky, B.; Levi, M.; Levi, E.; Schechter, A.; Granot, E. Recent Studies on the Correlation between Surface Chemistry, Morphology, Three-Dimensional Structures and Performance of Li and Li-C Intercalation Anodes

in Several Important Electrolyte Systems. *J. Power Sources* **1997**, *68* (1), 91–98.

(111) Liu, X.; Ren, D.; Hsu, H.; Xuning Feng; Gui-Liang Xu; Minghao Zhuang; Han Gao; Lu, L.; Chu, Z.; Li, J.; et al. Thermal Runaway of Lithium-Ion Batteries without Internal Short Circuit Thermal Runaway of Lithium-Ion Batteries without Internal Short Circuit. *Joule* **2018**, *2* (10), 2047–2064.

(112) Golubkov, A. W.; Fuchs, D.; Wagner, J.; Wiltsche, H.; Stangl, C.; Fauler, G.; Voitic, G.; Thaler, A.; Hacker, V. Thermal-Runaway Experiments on Consumer Li-Ion Batteries with Metal-Oxide and Olivin-Type Cathodes. *RSC Adv.* **2014**, *4* (7), 3633–3642.

(113) Austin, F.; Morales, R.; Coultas-mckenney, C. A.; Hargather, M. J.; Ostanek, J. Overcharge and Thermal Destructive Testing of Lithium Metal Oxide and Lithium Metal Phosphate Batteries Incorporating Optical Diagnostics. *J. Energy Storage* **2017**, *13*, 378–386.

(114) Ouyang, D.; Chen, M.; Liu, J.; Wei, R.; Weng, J.; Wang, J. Investigation of a Commercial Lithium-Ion Battery under Overcharge/over-Discharge Failure Conditions. *RSC Adv.* **2018**, *8*, 33414–33424.

(115) Sharma, N.; Peterson, V. K. Overcharging a Lithium-Ion Battery : Effect on the Li x C 6 Negative Electrode Determined by in Situ Neutron Diffraction. *J. Power Sources* **2013**, *244*, 695–701.

(116) Ren, D.; Feng, X.; Lu, L.; Ouyang, M.; Zheng, S.; Li, J.; He, X. An Electrochemical-Thermal Coupled Overcharge-to-Thermal-Runaway Model for Lithium Ion Battery. *J. Power Sources* **2017**, *364*, 328–340.

(117) Lin, C.; Ren, Y.; Amine, K.; Qin, Y.; Chen, Z. In Situ High-Energy X-Ray Diffraction to Study Overcharge Abuse of 18650-Size Lithium-Ion Battery. *J. Power Sources* **2013**, *230*, 32–37.

(118) Shearing, P. R.; Michiel, M. Di; Hinds, G.; Brett, J. L.; Shearing, P. R. Investigating Lithium-Ion Battery Materials during Overcharge-Induced Thermal Runaway: An Operando and Multi-Scale X-Ray CT Study. *Phys. Chem. Chem. Phys.* **2016**, *18* (45), 30881–31340.

(119) Taguchi, N.; Akita, T.; Sakaebe, H.; Tatsumi, K.; Ogumi, Z. Characterization of the Surface of LiCoO2 Particles Modified by Al and Si Oxide Using Analytical TEM. *J. Electrochem. Soc.* **2013**, *160* (11), A2293–A2298.

(120) Taguchi, N.; Sakaebe, H.; Tatsumi, K.; Akita, T. Degradation Analysis of $LiCoO_2$ Positive Electrode Material of a Li-Ion Battery Using the Li K-Edge Signal Obtained from STEM-EELS Measurements. *e-Journal Surf. Sci. Nanotechnol.* **2015**, *13* (June), 284–288.

(121) Lu, X.; Sun, Y.; Jian, Z.; He, X.; Gu, L.; Hu, Y. S.; Li, H.; Wang, Z.; Chen, W.; Duan, X.; et al. New Insight into the Atomic Structure of Electrochemically Delithiated O3-Li((1)-x)CoO(2) (0 </= x </= 0.5) Nanoparticles. *Nano Lett* **2012**, *12* (12), 6192–6197.

(122) Golubkov, A. W.; Scheikl, S.; Planteu, R.; Voitic, G.; Wiltsche, H.; Stangl, C.; Fauler, G.; Thaler, A.; Hacker, V. Thermal Runaway of Commercial 18650 Li-Ion Batteries with LFP and NCA Cathodes – Impact of State of Charge and Overcharge. *RSC Adv.* **2015**, *5* (70), 57171–57186.

(123) Finegan, D. P.; Scheel, M.; Robinson, J. B.; Tjaden, B.; Hunt, I.; Mason, T. J.; Millichamp, J.; Michiel, M. Di; Offer, G. J.; Hinds, G.; et al. In-Operando High-Speed Tomography of Lithium-Ion Batteries during Thermal Runaway. *Nat. Commun.* **2015**, *6* (888), 23.

(124) Lin, F.; Liu, Y.; Yu, X.; Cheng, L.; Singer, A.; Shpyrko, O. G.; Xin, H. L.; Tamura, N.; Tian, C.; Weng, T.

C.; et al. Synchrotron X-Ray Analytical Techniques for Studying Materials Electrochemistry in Rechargeable Batteries. *Chem. Rev.* **2017**, *117* (21), 13123–13186.

(125) Hu, E.; Bak, S. M.; Liu, J.; Yu, X.; Zhou, Y.; Ehrlich, S. N.; Yang, X. Q.; Nam, K. W. Oxygen-Release-Related Thermal Stability and Decomposition Pathways of LixNi0.5Mn1.5O4 Cathode Materials. *Chem. Mater.* **2014**, *26* (2), 1108–1118.

(126) Membreño, N.; Xiao, P.; Park, K.-S.; Goodenough, J. B.; Henkelman, G.; Stevenson, K. J. In Situ Raman Study of Phase Stability of α-Li3V2(PO4)3upon Thermal and Laser Heating. *J. Phys. Chem. C* **2013**, *117* (23), 11994–12002.

(127) Nishi, T.; Nakai, H.; Kita, A. Visualization of the State-of-Charge Distribution in a LiCoO2 Cathode by In Situ Raman Imaging. *J. Electrochem. Soc.* **2013**, *160* (10), A1785–A1788.

(128) Singh, G.; West, W. C.; Soler, J.; Katiyar, R. S. In Situ Raman Spectroscopy of Layered Solid Solution Li2MnO3–LiMO2 (M = Ni, Mn, Co). *J. Power Sources* **2012**, *218*, 34–38.

(129) Xiong, D. J.; Ellis, L. D.; Li, J.; Li, H.; Hynes, T.; Allen, J. P.; Xia, J.; Hall, D. S.; Hill, I. G.; Dahn, J. R. Measuring Oxygen Release from Delithiated $LiNi_x Mn_y Co_{1-x-y} O_2$ and Its Effects on the Performance of High Voltage Li-Ion Cells. *J. Electrochem. Soc.* **2017**, *164* (13), A3025–A3037.

(130) Jung, R.; Metzger, M.; Maglia, F.; Stinner, C.; Gasteiger, H. A. Oxygen Release and Its Effect on the Cycling Stability of $LiNi_x Mn_y Co_z O_2$ (NMC) Cathode Materials for Li-Ion Batteries. *J. Electrochem. Soc.* **2017**, *164* (7), A1361–A1377.

(131) Yoon, W.-S.; Kim, K.-B.; Kim, M.-G.; Lee, M.-K.; Shin, H.-J.; Lee, J.-M. Oxygen Contribution on Li-Ion Intercalation-Deintercalation in LiAl[Sub y]Co[Sub 1−y]O[Sub 2] Investigated by O K-Edge and Co L-Edge X-Ray Absorption Spectroscopy. *J. Electrochem. Soc.* **2002**, *149* (10), A1305.

(132) Buchholz, D.; Li, J.; Passerini, S.; Aquilanti, G.; Wang, D.; Giorgetti, M. X-Ray Absorption Spectroscopy Investigation of Lithium-Rich, Cobalt-Poor Layered-Oxide Cathode Material with High Capacity. *ChemElectroChem* **2015**, *2* (1), 85–97.

(133) Coleman, V. A.; Knut, R.; Karis, O.; Grennberg, H.; Jansson, U.; Quinlan, R.; Holloway, B. C.; Sanyal, B.; Eriksson, O. Defect Formation in Graphene Nanosheets by Acid Treatment: An x-Ray Absorption Spectroscopy and Density Functional Theory Study. *J. Phys. D. Appl. Phys.* **2008**, *41* (6), 1–4.

(134) Tsai, Y. W.; Hwang, B. J.; Ceder, G.; Sheu, H. S.; Liu, D. G.; Lee, J. F. In-Situ X-Ray Absorption Spectroscopic Study on Variation of Cathode Material during Electrochemical Cycling. *Chem. Mater.* **2005**, *17*, 3191–3199.

(135) Xu, J.; Sun, M.; Qiao, R.; Renfrew, S. E.; Ma, L.; Wu, T.; Hwang, S.; Nordlund, D.; Su, D.; Amine, K.; et al. Elucidating Anionic Oxygen Activity in Lithium-Rich Layered Oxides. *Nat. Commun.* **2018**, *9* (1), 1–10.

(136) Hwang, S.; Kim, S. M. Y.; Bak, S. M.; Kim, S. M. Y.; Cho, B. W.; Chung, K. Y.; Lee, J. Y.; Stach, E. A.; Chang, W. Using Real-Time Electron Microscopy To Explore the Effects of Transition-Metal Composition on the Local Thermal Stability in Charged LixNiyMnzCo1−y−zO2 Cathode Materials. *Chem. Mater.* **2015**, *27*, 3927–3935.

(137) Yuan, Y.; Amine, K.; Lu, J.; Shahbazian-Yassar, R. Understanding Materials Challenges for Rechargeable Ion Batteries with in Situ Transmission Electron Microscopy. *Nat. Commun.* **2017**, *8*

(May), 1–14.

(138) Ghodsi, S. M.; Megaridis, C. M.; Shahbazian-yassar, R. Advances in Graphene-Based Liquid Cell Electron Microscopy : Working Principles , Opportunities , and Challenges. *Small Methods* **2019**, *1900026*, 1–16.

(139) Yurkiv, V.; Sharifi-Asl, S.; Ramasubramanian, A.; Shahbazian-Yassar, R.; Mashayek, F. Oxygen Evolution and Phase Transformation in LCO Cathode: A Phase-Field Modeling Study. *Comput. Mater. Sci.* **2017**, *140*, 299–306.

(140) Zheng, Jiaxin, Tongchao Liu, Zongxiang Hu, Yi Wei, Xiaohe Song, Yang Ren, Weidong Wang, Mumin Rao, Yuan Lin, Zonghai Chen, Jun Lu, Chongmin Wang, Khalil Amine, F. P. Tuning of Thermal Stability in Layered Li(NixMnyCoz)O2. *J. Am. Chem. Soc.* **2016**, *138*, 13326−13334.

(141) Yabuuchi, N.; Kawamoto, Y.; Hara, R.; Ishigaki, T.; Hoshikawa, A.; Yonemura, M.; Kamiyama, T.; Komaba, S. A Comparative Study of LiCoO2 Polymorphs: Structural and Electrochemical Characterization of O2-, O3-, and O4-Type Phases. *Inorg. Chem.* **2013**, *52* (15), 9131–9142.

(142) Ben Yahia, H.; Shikano, M.; Kobayashi, H. Phase Transition Mechanisms in LixCoO2 ($0.25 \leq x \leq 1$) Based on Group-Subgroup Transformations. *Chem. Mater.* **2013**, *25* (18), 3687–3701.

(143) Lin, F.; Nordlund, D.; Markus, I. M.; Weng, T.-C.; Xin, H. L.; Doeff, M. M. Profiling the Nanoscale Gradient in Stoichiometric Layered Cathode Particles for Lithium-Ion Batteries. *Energy Environ. Sci.* **2014**, *7* (9), 3077–3085.

(144) Chenxi Wei; Yijin Liu; Zhang, Y. Thermally Driven Mesoscale Chemomechanical Interplay in Li0.5Ni0.6Mn0.2Co0.2O2 Cathode Materials. *J. Mater. Chem. A* **2018**, 23055–23061.

(145) Oh, P.; Song, B.; Li, W.; Manthiram, A. Overcoming the Chemical Instability on Exposure to Air of Ni-Rich Layered Oxide Cathodes by Coating with Spinel $LiMn_{1.9}Al_{0.1}O_4$. *J. Mater. Chem. A* **2016**, *4* (16), 5839–5841.

(146) Keil, P.; Jossen, A. Calendar Aging of NCA Lithium-Ion Batteries Investigated by Differential Voltage Analysis and Coulomb Tracking. *J. Electrochem. Soc.* **2017**, *164* (1), A6066–A6074.

(147) Lin, F.; Markus, I. M.; Doeff, M. M.; Xin, H. L. Chemical and Structural Stability of Lithium-Ion Battery Electrode Materials under Electron Beam. *Sci. Rep.* **2014**, *4*, 5694.

(148) Phillips, P. J.; Iddir, H.; Abraham, D. P.; Klie, R. F. Direct Observation of the Structural and Electronic Changes of Li2MnO3 during Electron Irradiation. *Appl. Phys. Lett.* **2014**, *105* (11), 113905.

(149) Shao-Horn, Y.; Croguennec, L.; Delmas, C.; Nelson, E. C.; O'Keefe, M. a. Atomic Resolution of Lithium Ions in LiCoO2. *Nat. Mater.* **2003**, *2* (July), 464–467.

(150) Xiong, F.; Yan, H. J.; Chen, Y.; Xu, B.; Le, J. X.; Ouyang, C. Y. The Atomic and Electronic Structure Changes Upon Delithiation of LiCoO 2 : From First Principles Calculations. *Int. J. Electrochem. Sci.* **2012**, *7* (10), 9390–9400.

(151) Furushima, Y.; Yanagisawa, C.; Nakagawa, T.; Aoki, Y.; Muraki, N. Thermal Stability and Kinetics of Delithiated LiCoO2. *J. Power Sources* **2011**, *196* (4), 2260–2263.

(152) Geder, J.; Hoster, H. E.; Jossen, A.; Garche, J.; Yu, D. Y. W. Impact of Active Material Surface Area on Thermal Stability of LiCoO 2 Cathode. *J. Power Sources* **2014**, *257*, 286–292.

(153) Li, W.; Currie, J. C.; Wolstenholme, J. Influence of Morphology on the Stability of LiNiO2. *J. Power Sources* **1997**, *68* (2), 565–569.

(154) Arai, H.; Shigeto Okada; Yoji Sakurai; Yamaki, J. Thermal Behavior of Li1−yNiO2 and the Decomposition Mechanism. *Solid State Ionics* **1998**, *109* (3–4), 295–302.

(155) Ohzuku, T.; Makimura, Y. Layered Lithium Insertion Material of LiCo 1/3 Ni 1/3 Mn 1/3 O 2 for Lithium-Ion Batteries. *Chem. Lett.* **2001**, *30* (7), 642–643.

(156) Zheng, J.; Gu, M.; Xiao, J.; Zuo, P.; Wang, C.; Zhang, J. G. Corrosion/Fragmentation of Layered Composite Cathode and Related Capacity/Voltage Fading during Cycling Process. *Nano Lett.* **2013**, *13* (8), 3824–3830.

(157) Yan, P.; Zheng, J.; Zheng, J.; Wang, Z.; Teng, G.; Kuppan, S.; Xiao, J.; Chen, G.; Pan, F.; Zhang, J. G.; et al. Ni and Co Segregations on Selective Surface Facets and Rational Design of Layered Lithium Transition-Metal Oxide Cathodes. *Adv. Energy Mater.* **2016**, *6*, 1–9.

(158) Wang, L.; Maxisch, T.; Ceder, G. A First-Principles Approach to Studying the Thermal Stability of Oxide Cathode Materials. *Chem. Mater.* **2007**, *19* (3), 543–552.

(159) Yabuuchi, N.; Kim, Y.; Li, H. H.; Shao-horn, Y. Thermal Instability of Cycled Li x Ni 0 . 5 Mn 0 . 5 O 2 Electrodes : An in Situ Synchrotron X-Ray Powder Diffraction Study. *Chem. Mater.* **2008**, No. 5, 4936–4951.

(160) Reed, J.; Ceder, G. Role of Electronic Structure in the Susceptibility of Metastable Transition-Metal Oxide Structures to Transformation. *Chem. Rev.* **2004**, *104*, 4513–4534.

(161) Bak, S. M.; Hu, E.; Zhou, Y.; Yu, X.; Senanayake, S. D.; Cho, S. J.; Kim, K. B.; Chung, K. Y.; Yang, X. Q.; Nam, K. W. Structural Changes and Thermal Stability of Charged LiNixMnyCozO2 Cathode Materials Studied by Combined in Situ Time-Resolved XRD and Mass Spectroscopy. *ACS Appl. Mater. Interfaces* **2014**, *6*, 22594–22601.

(162) Yoon, W. S.; Chung, K. Y.; Balasubramanian, M.; Hanson, J.; McBreen, J.; Yang, X. Q. Time-Resolved XRD Study on the Thermal Decomposition of Nickel-Based Layered Cathode Materials for Li-Ion Batteries. *J. Power Sources* **2006**, *163* (1 SPEC. ISS.), 219–222.

(163) Yuan, Y.; Nie, A.; Odegard, G. M.; Xu, R.; Zhou, D.; Santhanagopalan, S.; He, K.; Asayesh-Ardakani, H.; Meng, D. D.; Klie, R. F.; et al. Asynchronous Crystal Cell Expansion during Lithiation of K(+)-Stabilized α-MnO2. *Nano Lett.* **2015**, *15* (APRIL), 2998–3007.

(164) Zhang, H.; Omenya, F.; Yan, P.; Luo, L.; Whittingham, M. S.; Wang, C.; Zhou, G. Rock-Salt Growth-Induced (003) Cracking in a Layered Positive Electrode for Li-Ion Batteries. *ACS Energy Lett.* **2017**, *2* (11), 2607–2615.

(165) Luo, D.; shi, P.; Fang, S.; Yang, L.; Hirano, S. ichi. Unraveling the Effect of Exposed Facets on Voltage Decay and Capacity Fading of Li-Rich Layered Oxides. *J. Power Sources* **2017**, *364*, 121–129.

(166) Thackeray, M. M.; de Picciotto, L. A.; de Kock, A.; Johnson, P. J.; Nicholas, V. A.; Adendorff, K. T. Spinel Electrodes for Lithium Batteries - A Review. *J. Power Sources* **1987**, *21* (1), 1–8.

(167) Thackeray, M. M. Spinel Electrodes for Lithium Batteries . *J. Am. Ceram. Soc* **1999**, *82*, 3347–3354.

(168) Julien, C. M.; Mauger, A.; Zaghib, K.; Groult, H. Comparative Issues of Cathode Materials for Li-Ion Batteries. *Inorganics* **2014**, *2*, 132–154.

(169) Park, O. K.; Cho, Y.; Lee, S.; Yoo, H.-C.; Song, H.-K.; Cho, J.; Environ, E. Who Will Drive Electric Vehicles, Olivine or Spinel? *Energy Environ. Sci.* **2011**, *4* (5), 1621.

(170) Pieczonka, N. P. W.; Liu, Z.; Lu, P.; Olson, K. L.; Moote, J.; Powell, B. R.; Kim, J.-H. Understanding Transition-Metal Dissolution Behavior in LiNi 0.5 Mn 1.5 O 4 High-Voltage Spinel for Lithium Ion Batteries. *J. Phys. Chem. C* **2013**, *117* (31), 15947–15957.

(171) Aurbach, D.; Markovsky, B.; Talyossef, Y.; Salitra, G.; Kim, H. J.; Choi, S. Studies of Cycling Behavior, Ageing, and Interfacial Reactions of LiNi0.5Mn1.5O4and Carbon Electrodes for Lithium-Ion 5-V Cells. *J. Power Sources* **2006**, *162* (2 SPEC. ISS.), 780–789.

(172) Talyosef, Y.; Markovsky, B.; Salitra, G.; Aurbach, D.; Kim, H. J.; Choi, S. The Study of LiNi0.5Mn1.5O4 5-V Cathodes for Li-Ion Batteries. *J. Power Sources* **2005**, *146* (1–2), 664–669.

(173) Tang, D.; Sun, Y.; Yang, Z.; Ben, L.; Gu, L.; Huang, X. Surface Structure Evolution of LiMn2O4 Cathode Material upon Charge/Discharge. *Chem. Mater.* **2014**, *26* (11), 3535–3543.

(174) Ben, L.; Yu, H.; Chen, B.; Chen, Y.; Gong, Y.; Yang, X.; Gu, L.; Huang, X. Unusual Spinel-to-Layered Transformation in LiMn2O4Cathode Explained by Electrochemical and Thermal Stability Investigation. *ACS Appl. Mater. Interfaces* **2017**, *9* (40), 35463–35475.

(175) Hu, E.; Bak, S. M.; Liu, J.; Yu, X.; Zhou, Y.; Ehrlich, S. N.; Yang, X. Q.; Nam, K. W. Oxygen-Release-Related Thermal Stability and Decomposition Pathways of LixNi0.5Mn1.5O4 Cathode Materials. *Chem. Mater.* **2014**, *26* (2), 1108–1118.

(176) Brand, M.; Gläser, S.; Geder, J.; Menacher, S.; Obpacher, S.; Jossen, A.; Quinger, D. Electrical Safety of Commercial Li-Ion Cells Based on NMC and NCA Technology Compared to LFP Technology. *World Electr. Veh. J.* **2013**, *6*, 572.

(177) Geoffroy, HautierJain, A.; Ong, S. P.; Kang, B.; Moore, C.; Doe, R.; Ceder, G. Phosphates as Lithium-Ion Battery Cathodes : An Evaluation Based on High-Throughput Ab Initio Calculations. *Chem. Mater.* **2011**, 3495–3508.

(178) Chen, G.; Richardson, T. J. Thermal Instability of Olivine-Type LiMnPO4 Cathodes. *J. Power Sources* **2010**, *195* (4), 1221–1224.

(179) Andersson, A. S.; Thomas, J. O.; Kalska, B.; Häggström, L. Thermal Stability of LiFePO 4 -Based Cathodes. *Electrochem. Solid-State Lett* **2000**, *3* (2), 66–68.

(180) Malik, R.; Zhou, F.; Ceder, G. Kinetics of Non-Equilibrium Lithium Incorporation in LiFePO4. *Nat. Mater.* **2011**, *10* (8), 587–590.

(181) Nie, Z. X.; Ouyang, C. Y.; Chen, J. Z.; Zhong, Z. Y.; Du, Y. L.; Liu, D. S.; Shi, S. Q.; Lei, M. S. First Principles Study of Jahn – Teller Effects in Li x MnPO 4. *Solid State Commun.* **2010**, *150* (1–2), 40–44.

(182) Theil, S.; Fleischhammer, M.; Axmann, P.; Wohlfahrt-mehrens, M. Experimental Investigations on the Electrochemical and Thermal Behaviour of LiCoPO 4 -Based Cathode. *J. Power Sources* **2013**, *222*, 72–78.

(183) Surendra K. Martha, Ortal Haik, Ella Zinigrad, Ivan Exnar, Thierry Drezen, James H. Miners, D. A.

On the Thermal Stability of Olivine Cathode Materials for Lithium-Ion Batteries. *J. Electrochem. Soc.* **2011**, *158* (10), 1115–1122.

(184) Ong, S. P.; Jain, A.; Hautier, G.; Kang, B.; Ceder, G. Thermal Stabilities of Delithiated Olivine MPO4 (M = Fe, Mn) Cathodes Investigated Using First Principles Calculations. *Electrochem. commun.* **2010**, *12* (3), 427–430.

(185) Lu, Z.; Beaulieu, L. Y.; Donaberger, R. A.; Thomas, C. L.; Dahn, J. R. Synthesis, Structure, and Electrochemical Behavior of Li[Ni[Sub x]Li[Sub 1/3−2x/3]Mn[Sub 2/3−x/3]]O[Sub 2]. *J. Electrochem. Soc.* **2002**, *149* (6), A778.

(186) Thackeray, M. M.; Johnson, C. S.; Vaughey, J. T.; LiCurrent address: eVionyx Inc., Ha, N.; Hackney, S. A. Advances in Manganese-Oxide 'Composite' Electrodes for Lithium-Ion Batteries. *J. Mater. Chem.* **2005**, *15* (23), 2257.

(187) Zheng, J.; Myeong, S.; Cho, W.; Yan, P.; Xiao, J.; Wang, C.; Cho, J.; Zhang, J. Li- and Mn-Rich Cathode Materials : Challenges to Commercialization. *Adv. Energy Mater.* **2017**, 1–25.

(188) Sathiya, M.; Rousse, G.; Ramesha, K.; Laisa, C. P.; Vezin, H.; Sougrati, M. T.; Doublet, M.-L.; Foix, D.; Gonbeau, D.; Walker, W.; et al. Reversible Anionic Redox Chemistry in High-Capacity Layered-Oxide Electrodes. *Nat. Mater.* **2013**, *12* (9), 827–835.

(189) Yan, J.; Liu, X.; Li, B. Recent Progress in Li-Rich Layered Oxides as Cathode Materials for Li-Ion Batteries. *RSC Adv.* **2014**, *4*, 63268–63284.

(190) Croy, J. R.; Balasubramanian, M.; Gallagher, K. G.; Burrell, A. K. Review of the U.S. Department of Energy's "Deep Dive" Effort to Understand Voltage Fade in Li- and Mn-Rich Cathodes. *Acc. Chem. Res.* **2015**, *48* (11), 2813–2821.

(191) Boulineau, A.; Croguennec, L.; Delmas, C.; Weill, F. Reinvestigation of Li2MnO3 Structure: Electron Diffraction and High Resolution TEM. *Chem. Mater.* **2009**, *21* (18), 4216–4222.

(192) Yang, G.; Ji, H.; Gao, P.; Hong, A.; Ding, H.; Roy, S.; Pinto, J.; Jiang, X. Crystal Structure and Electrochemical Performances of Proton-Substituted Li2MnO3 and the Nanocomposites Treated by LiMnO2. *J. Electrochem. Soc.* **2011**, *158* (10), A1071–A1078.

(193) Armstrong, A. R.; Holzapfel, M.; Novák, P.; Johnson, C. S.; Kang, S. H.; Thackeray, M. M.; Bruce, P. G. Demonstrating Oxygen Loss and Associated Structural Reorganization in the Lithium Battery Cathode Li[Ni0.2Li0.2Mn 0.6]O2. *J. Am. Chem. Soc.* **2006**, *128* (26), 8694–8698.

(194) Armstrong, A. R.; Holzapfel, M.; Novak, P.; Johnson, C. S.; Kang, S.-H.; Thackeray, M. M.; Bruce, P. G. Demonstrating Oxygen Loss and Associated Structural Reorganization in the Lithium Battery Cathode Li Ni0.2Li0.2Mn0.6 O-2. *J. Am. Chem. Soc.* **2006**, *128* (26), 8694–8698.

(195) Hong, J.; Lim, H. D.; Lee, M.; Kim, S. W.; Kim, H.; Oh, S. T.; Chung, G. C.; Kang, K. Critical Role of Oxygen Evolved from Layered Li-Excess Metal Oxides in Lithium Rechargeable Batteries. *Chem. Mater.* **2012**, *24* (14), 2692–2697.

(196) Hu, E.; Bak, S. M.; Liu, Y.; Liu, J.; Yu, X.; Zhou, Y. N.; Zhou, J.; Khalifah, P.; Ariyoshi, K.; Nam, K. W.; et al. Utilizing Environmental Friendly Iron as a Substitution Element in Spinel Structured Cathode Materials for Safer High Energy Lithium-Ion Batteries. *Adv. Energy Mater.* **2016**, *6* (3), 1–7.

(197) Singer, A.; Zhang, M.; Hy, S.; Cela, D.; Fang, C.; Wynn, T. A.; Qiu, B.; Xia, Y.; Liu, Z.; Ulvestad, A.; et

al. Nucleation of Dislocations and Their Dynamics in Layered Oxide Cathode Materials during Battery Charging. *Nat. Energy* **2018**, *3*, 1–7.

(198) Chen, H.; Islam, M. S. Lithium Extraction Mechanism in Li-Rich Li 2 MnO 3 Involving Oxygen Hole Formation and Dimerization. *Chem. Mater.* **2016**, *28* (6656–6663).

(199) Chen, H.; Islam, M. S. Lithium Extraction Mechanism in Li-Rich Li2MnO3involving Oxygen Hole Formation and Dimerization. *Chem. Mater.* **2016**, *28* (18), 6656–6663.

(200) Pearce, P. E.; Perez, A. J.; Rousse, G.; Saubanère, M.; Batuk, D.; Foix, D.; McCalla, E.; Abakumov, A. M.; Van Tendeloo, G.; Doublet, M.-L.; et al. Evidence for Anionic Redox Activity in a Tridimensional-Ordered Li-Rich Positive Electrode β-Li2IrO3. *Nat. Mater.* **2017**, *16* (5), 580–586.

(201) Gu, M.; Belharouak, I.; Zheng, J.; Wu, H.; Xiao, J.; Genc, A.; Amine, K.; Thevuthasan, S.; Baer, D. R.; Zhang, J. G.; et al. Formation of the Spinel Phase in the Layered Composite Cathode Used in Li-Ion Batteries. *ACS Nano* **2013**, *7* (1), 760–767.

(202) Jiang, J.; Dahn, J. R. Electrochemical and Thermal Studies of Li[NixLi (1/3-2x/3)Mn(2/3-x/3)]O2 (x = 1/12, 1/4, 5/12, and 1/2). *Electrochim. Acta* **2005**, *50* (24), 4778–4783.

(203) Cho, J.; Kim, T.; Kim, C.; Lee, J.; Kim, Y.; Park, B. Comparison of Al2O3- and AlPO4-Coated LiCoO2 Cathode Materials for a Li-Ion Cell. *J. Power Sources* **2005**, *146*, 58–64.

(204) Konishi, H.; Hirano, T.; Takamatsu, D.; Gunji, A.; Feng, X.; Furutsuki, S. Effect of Composition of Transition Metals on Stability of Charged Li-Rich Layer-Structured Cathodes, Li1.2Ni0.2-XMn0.6-XCo2xO2(X=0, 0.033, and 0.067), at High Temperatures. *Electrochim. Acta* **2015**, *186*, 591–597.

(205) Konishi, H.; Hirano, T.; Takamatsu, D.; Gunji, A.; Feng, X.; Furutsuki, S. Evaluation of Stability of Charged Lithium-Rich Layer-Structured Cathode Material at Elevated Temperature. *Electrochim. Acta* **2015**, *169*, 310–316.

(206) Lin, C. K.; Piao, Y.; Kan, Y.; Bareño, J.; Bloom, I.; Ren, Y.; Amine, K.; Chen, Z. Probing Thermally Induced Decomposition of Delithiated Li 1.2-XNi0.15Mn0.55Co0.1O2 by in Situ High-Energy x-Ray Diffraction. *ACS Appl. Mater. Interfaces* **2014**, *6* (15), 12692–12697.

(207) Li, N.; He, Y. S.; Wang, X.; Zhang, W.; Ma, Z. F.; Zhang, D. Incorporation of Rubidium Cations into Li1.2Mn0.54Co0.13Ni0.13O2layered Oxide Cathodes for Improved Cycling Stability. *Electrochim. Acta* **2017**, *231*, 363–370.

(208) Wang, D.; Liu, M.; Wang, X.; Yu, R.; Wang, G.; Ren, Q.; Yang, X. Facile Synthesis and Performance of Na-Doped Porous Lithium-Rich Cathodes for Lithium Ion Batteries. *RSC Adv.* **2016**, *6* (62), 57310–57319.

(209) Yu, S.; Peng, C.; Li, Z.; Zhang, L.; Xiao, Q.; Lei, G.; Ding, Y. K-Doped Li-Rich Molybdenum-Based Oxide with Improved Electrochemical Properties for Lithium-Ion Batteries. *Arab. J. Sci. Eng.* **2017**, *42* (10), 4291–4298.

(210) Zheng, Z.; Guo, X. D.; Zhong, Y. J.; Hua, W. B.; Shen, C. H.; Chou, S. L.; Yang, X. S. Host Structural Stabilization of Li1.232Mn0.615Ni0.154O2through K-Doping Attempt: Toward Superior Electrochemical Performances. *Electrochim. Acta* **2016**, *188*, 336–343.

(211) Vu, D.; Lee, J. Na-Doped Layered LiNi0.8Co0.1Mn0.1O2 with Improved Rate Capability And. *J. Solid State Electrochem.* **2017**, *2*, 1165–1173.

(212) Liu, Y.; Ning, D.; Zheng, L.; Zhang, Q.; Gu, L.; Gao, R.; Zhang, J.; Franz, A.; Schumacher, G.; Liu, X. Improving the Electrochemical Performances of Li-Rich Li1.20Ni0.13Co0.13Mn0.54O2through a Cooperative Doping of Na+and PO43−with Na3PO4. *J. Power Sources* **2018**, *375* (August 2017), 1–10.

(213) Sun, Y.; Zhang, L.; Zhou, Y.; Shen, Y.; Hai, C.; Li, X.; Zeng, J.; Ren, X.; Ma, L.; Zhang, X.; et al. Study on Potassium Doped Modification of $Li_{1.2}Ni_{0.13}Co_{0.13}Mn_{0.54}O_2$ Materials Synthesized by Novel Method for Lithium Ion Battery. *J. Electrochem. Soc.* **2018**, *165* (2), A333–A338.

(214) Min, S. H.; Jo, M. R.; Choi, S. Y.; Kim, Y. Il; Kang, Y. M. A Layer-Structured Electrode Material Reformed by a PO4-O2Hybrid Framework toward Enhanced Lithium Storage and Stability. *Adv. Energy Mater.* **2016**, *6* (7), 1501717.

(215) Liu, H.; Cao, Q.; Fu, L. J.; Li, C.; Wu, Y. P.; Wu, H. Q. Doping Effects of Zinc on LiFePO4cathode Material for Lithium Ion Batteries. *Electrochem. commun.* **2006**, *8* (10), 1553–1557.

(216) Laisa, C. P.; Ramesha, R. N.; Ramesha, K. Enhanced Electrochemical Performance of Lithium Rich Layered Cathode Materials by Ca2+substitution. *Electrochim. Acta* **2017**, *256*, 10–18.

(217) Liu, A.; Li, J.; Shunmugasundaram, R.; Dahn, J. R. Synthesis of Mg and Mn Doped $LiCoO_2$ and Effects on High Voltage Cycling. *J. Electrochem. Soc.* **2017**, *164* (7), A1655–A1664.

(218) Bellitto, C.; Bauer, E. M.; Righini, G.; Green, M. A.; Branford, W. R.; Antonini, A.; Pasquali, M. The Effect of Doping LiMn2O4spinel on Its Use as a Cathode in Li-Ion Batteries: Neutron Diffraction and Electrochemical Studies. *J. Phys. Chem. Solids* **2004**, *65* (1), 29–37.

(219) Nayak, P. K.; Grinblat, J.; Levi, E.; Levi, M.; Markovsky, B.; Aurbach, D. Understanding the Influence of Mg Doping for the Stabilization of Capacity and Higher Discharge Voltage of Li- and Mn-Rich Cathodes for Li-Ion Batteries. *Phys. Chem. Chem. Phys.* **2017**, *19* (8), 6142–6152.

(220) Webin Luo; Li, X.; Dahn, J. R. Synthesis , Characterization , and Thermal Stability of Li[Ni1/3Mn1/3Co1/3-z(MnMg)z/2]O2. *Chem. Mater.* **2010**, *22* (10), 5065–5073.

(221) Iqbal, A.; Iqbal, Y.; Chang, L.; Ahmed, S.; Tang, Z.; Gao, Y. Enhanced Electrochemical Performance of La- and Zn-Co-Doped LiMn2O4 Spinel as the Cathode Material for Lithium-Ion Batteries. *J. Nanoparticle Res.* **2012**, *14* (10), 1206.

(222) Wenbin Luo, Fu Zhou, Xuemei Zhao, Zhonghua Lu, Xinhai Li, J. R. D. Synthesis , Characterization , and Thermal Stability of LiNi1/3Mn1/3Co1/3-ZMgzO2, LiNi1/3-ZMn1/3Co1/3MgzO2, and LiNi1/3Mn1/3-ZCo1/3MgzO2. *Chem. Mater.* **2010**, *22* (11), 1164–1172.

(223) Luo, Y.; Lu, T.; Zhang, Y.; Yan, L.; Mao, S. S.; Xie, J. Surface-Segregated, High-Voltage Spinel Lithium-Ion Battery Cathode Material LiNi0.5Mn1.5O4cathodes by Aluminium Doping with Improved High-Rate Cyclability. *J. Alloys Compd.* **2017**, *703*, 289–297.

(224) Hu, X.; Guo, H.; Peng, W.; Wang, Z.; Li, X.; Hu, Q. Effects of Nb Doping on the Performance of 0.5Li2MnO3·0.5LiNi1/3Co1/3Mn1/3O2cathode Material for Lithium-Ion Batteries. *J. Electroanal. Chem.* **2018**, *822* (January), 57–65.

(225) Li, M.; Zhou, Y.; Wu, X.; Duan, L.; Zhang, C.; Zhang, F.; He, D. The Combined Effect of CaF2coating and La-Doping on Electrochemical Performance of Layered Lithium-Rich Cathode Material. *Electrochim. Acta* **2018**, *275*, 18–24.

(226) Milad Ghorbanzadeh; Allahyari, E.; Reza Riahifar; Hadavi, S. M. M. Effect of Al and Zr Co-Doping on Electrochemical Performance of Cathode Li[Li0.2Ni0.13Co0.13Mn0.54]O2 for Li-Ion Battery. *J. Solid State Electrochem.* **2018**, *22*, 1155–1163.

(227) Guo, H.; Xia, Y.; Zhao, H.; Yin, C.; Jia, K.; Zhao, F.; Liu, Z. Stabilization Effects of Al Doping for Enhanced Cycling Performances of Li-Rich Layered Oxides. *Ceram. Int.* **2017**, *43* (16), 13845–13852.

(228) Ramesha, R. N.; Laisa, C. P.; Ramesha, K. Improving Electrochemical Stability by Transition Metal Cation Doping for Manganese in Lithium-Rich Layered Cathode, Li1.2Ni0.13Co0.13Mn0.54-XMxO2(M = Co, Cr and Fe). *Electrochim. Acta* **2017**, *249*, 377–386.

(229) Yu, R.; Wang, G.; Liu, M.; Zhang, X.; Wang, X.; Shu, H.; Yang, X.; Huang, W. Mitigating Voltage and Capacity Fading of Lithium-Rich Layered Cathodes by Lanthanum Doping. *J. Power Sources* **2016**, *335*, 65–75.

(230) Xu, G.; Xue, Q.; Li, J.; Li, Z.; Li, X.; Yu, T.; Li, J.; Wang, X.; Kang, F. Understanding the Enhanced Electrochemical Performance of Samarium Substituted Li[Li0.2Mn0.54 - XSmxCo0.13Ni0.13]O2cathode Material for Lithium Ion Batteries. *Solid State Ionics* **2016**, *293*, 7–12.

(231) Zhou, F.; Zhao, X.; Lu, Z.; Jiang, J.; Dahn, J. R. The Effect of Al Substitution on the Reactivity of Delithiated LiNi (0 . 5 − z) Mn (0 . 5 − z)A1 2 z O 2 with Nonaqueous Electrolyte Cell. *J. Electrochem. Soc.* **2008**, *11* (9), 155–157.

(232) Croguennec, L.; Bains, J.; Bre, J.; Tessier, C.; Levasseur, S.; Delmas, C. Effect of Aluminum Substitution on the Structure , Electrochemical Performance and Thermal Stability of Li11x(Ni0.40Mn0.40Co0.202zAlz)12xO2 L. *J. Electrochem. Soc.* **2011**, *158* (6), 664–670.

(233) Lin, H.; Liang, C.; Li, M.; Dai, C.; Xiong, Y. Effects of Aluminum Doping on Cobalt-Free Lithium–Iron–Nickel–Manganese–Oxygen Cathode Materials for Lithium-Ion Batteries. *Energy Technol.* **2017**, *5* (8), 1472–1483.

(234) Laisa, C. P.; Nanda Kumar, A. K.; Selva Chandrasekaran, S.; Murugan, P.; Lakshminarasimhan, N.; Govindaraj, R.; Ramesha, K. A Comparative Study on Electrochemical Cycling Stability of Lithium Rich Layered Cathode Materials Li1.2Ni0.13M0.13Mn0.54O2where M = Fe or Co. *J. Power Sources* **2016**, *324*, 462–474.

(235) Pan, L.; Xia, Y.; Qiu, B.; Zhao, H.; Guo, H.; Jia, K.; Gu, Q.; Liu, Z. Structure and Electrochemistry of B Doped Li(Li0.2Ni0.13Co0.13Mn0.54)1-XBxO2as Cathode Materials for Lithium-Ion Batteries. *J. Power Sources* **2016**, *327*, 273–280.

(236) Yu, R.; Zhang, Z.; Jamil, S.; Chen, J.; Zhang, X.; Wang, X.; Yang, Z.; Shu, H.; Yang, X. Effects of Nanofiber Architecture and Antimony Doping on the Performance of Lithium-Rich Layered Oxides: Enhancing Lithium Diffusivity and Lattice Oxygen Stability. *ACS Appl. Mater. Interfaces* **2018**, *10* (19), 16561–16571.

(237) Nayak, P. K.; Grinblat, J.; Levi, M.; Levi, E.; Kim, S.; Choi, J. W.; Aurbach, D. Al Doping for Mitigating the Capacity Fading and Voltage Decay of Layered Li and Mn-Rich Cathodes for Li-Ion Batteries. *Adv. Energy Mater.* **2016**, *6* (8), 1–13.

(238) Yan, W.; Xie, Y.; Jiang, J.; Sun, D.; Ma, X.; Lan, Z.; Jin, Y. Enhanced Rate Performance of Al-Doped Li-Rich Layered Cathode Material via Nucleation and Post-Solvothermal Method. *ACS Sustain.*

Chem. Eng. **2018**, *6* (4), 4625–4632.

(239) Yue, B.; Wang, X.; Wang, J.; Yao, J.; Zhao, X.; Zhang, H.; Yu, W.; Liu, G.; Dong, X. Au-Doped Li $_{1.2}$ Ni $_{0.7}$ Co $_{0.1}$ Mn $_{0.2}$ O $_{2}$ Electrospun Nanofibers: Synthesis and Enhanced Capacity Retention Performance for Lithium-Ion Batteries. *RSC Adv.* **2018**, *8* (8), 4112–4118.

(240) Zhao, L.; Wu, Q.; Wu, J. Improving Rate Performance of Cathode Material Li1.2Mn0.54Co0.13Ni0.13O2 via Niobium Doping. *J. Solid State Electrochem.* **2018**, *22*, 2141–2148.

(241) Wang, H.; Tan, T. A.; Yang, P.; Lai, M. O.; Lu, L. High-Rate Performances of the Ru-Doped Spinel Lini0.5Mn 1.5O4: Effects of Doping and Particle Size. *J. Phys. Chem. C* **2011**, *115* (13), 6102–6110.

(242) Myung, S.; Komaba, S.; Hosoya, K.; Hirosaki, N.; Miura, Y.; Kumagai, N. Synthesis of LiNi 0 . 5 Mn 0 . 5-x Ti x O 2 by an Emulsion Drying Method and Effect of Ti on Structure and Electrochemical Properties. *J. Solid State Electrochem.* **2005**, No. 4, 2427–2435.

(243) Kam, K. C.; Mehta, A.; Heron, J. T.; Doeff, M. M.; Radiation, S.; National, S.; Park, M. Electrochemical and Physical Properties of Ti-Substituted Layered Nickel Manganese Cobalt Oxide (NMC) Cathode Materials. *J. Electrochem. Soc.* **2012**, *159* (8), 1383–1392.

(244) Zhou, L.; Liu, J.; Huang, L.; Jiang, N.; Zheng, Q.; Lin, D. Sn-Doped Li1.2Mn0.54Ni0.13Co0.13O2 Cathode Materials for Lithium-Ion Batteries with Enhanced Electrochemical Performance. *J. Solid State Electrochem.* **2017**, *21* (12), 3467–3477.

(245) Lu, C.; Yang, S.; Wu, H.; Zhang, Y.; Yang, X.; Liang, T. Enhanced Electrochemical Performance of Li-Rich Li1.2Mn0.52Co0.08Ni0.2O2cathode Materials for Li-Ion Batteries by Vanadium Doping. *Electrochim. Acta* **2016**, *209*, 448–455.

(246) Wang, H.; Tan, T. A.; Yang, P.; Lai, M. O.; Lu, L. High-Rate Performances of the Ru-Doped Spinel LiNi 0.5 Mn 1.5 O 4 : Effects of Doping and Particle Size. *J. Phys. Chem. C* **2011**, *115* (13), 6102–6110.

(247) Zhao, Y.; Xia, M.; Hu, X.; Zhao, Z.; Wang, Y.; Lv, Z. Effects of Sn Doping on the Structural and Electrochemical Properties of Li<inf>1.2</Inf>Ni<inf>0.2</Inf>Mn<inf>0.8</Inf>O<inf>2</Inf> Li-Rich Cathode Materials. *Electrochim. Acta* **2015**, *174*, 1167–1174.

(248) Han, E.; Du, X.; Yang, P.; Han, Y. The Effects of Copper and Titanium Co-Substitution on LiNi0.6Co0.15Mn0.25O2 for Lithium Ion Batteries. *Ionics (Kiel).* **2018**, *24*, 393–401.

(249) Hoang, K. Doping Li-Rich Cathode Material Li2MnO3: Interplay between Lattice Site Preference, Electronic Structure, and Delithiation Mechanism. *Phys. Rev. Mater.* **2017**, *1* (7), 075404.

(250) Li, Q.; Li, G.; Fu, C.; Luo, D.; Fan, J.; Li, L. K+-Doped Li1.2Mn0.54Co0.13Ni0.13O2: A Novel Cathode Material with an Enhanced Cycling Stability for Lithium-Ion Batteries. *ACS Appl. Mater. Interfaces* **2014**, *6* (13), 10330–10341.

(251) Cho, W.; Myeong, S.; Kim, N.; Lee, S.; Kim, Y.; Kim, M.; Kang, S. J.; Park, N.; Oh, P.; Cho, J. Critical Role of Cations in Lithium Sites on Extended Electrochemical Reversibility of Co-Rich Layered Oxide. *Adv. Mater.* **2017**, *29* (21), 1605578.

(252) Yu, R.; Wang, X.; Fu, Y.; Wang, L.; Cai, S.; Liu, M.; Lu, B.; Wang, G.; Wang, D.; Ren, Q.; et al. Effect of Magnesium Doping on Properties of Lithium-Rich Layered Oxide Cathodes Based on a One-

Step Co-Precipitation Strategy. *J. Mater. Chem. A* **2016**, *4* (13), 4941–4951.

(253) Zhou, F.; Zhao, X.; Lu, Z.; Jiang, J.; Dahn, J. R. The Effect of Al Substitution on the Reactivity of Delithiated LiNi1/3Mn1/3Co(1/3-z)AlzO2 with Non-Aqueous Electrolyte. *Electrochem. Commun. J.* **2008**, *10*, 1168–1171.

(254) Luo, W.; Dahn, J. R. The Impact of Zr Substitution on the Structure , Electrochemical Performance and Thermal Stability of Li[Ni1/3Mn1/32zCo1/3Zrz]O2. *J. Electrochem. Soc.* **2011**, *158* (4), 428–433.

(255) Kapylou, A.; Song, J. H.; Missiul, A.; Ham, D. J.; Kim, D. H.; Moon, S.; Park, J. H. Improved Thermal Stability of Lithium-Rich Layered Oxide by Fluorine Doping. *ChemPhysChem* **2018**, *19* (1), 116–122.

(256) Liu, S.; Wang, Z.; Huang, Y.; Ni, Z.; Bai, J.; Kang, S.; Wang, Y.; Li, X. Fluorine Doping and Al2O3coating Co-Modified Li[Li0.20Ni0.133Co0.133Mn0.534]O2as High Performance Cathode Material for Lithium-Ion Batteries. *J. Alloys Compd.* **2018**, *731*, 636–645.

(257) Kong, F.; Liang, C.; Longo, R. C.; Yeon, D. H.; Zheng, Y.; Park, J. H.; Doo, S.-G. G.; Cho, K. Conflicting Roles of Anion Doping on the Electrochemical Performance of Li-Ion Battery Cathode Materials. *Chem. Mater.* **2016**, *28* (19), 6942–6952.

(258) Ming, L.; Zhang, B.; Cao, Y.; Zhang, J.-F.; Wang, C.-H.; Wang, X.-W.; Li, H. Effect of Nb and F Co-Doping on Li1.2Mn0.54Ni0.13Co0.13O2cathode Material for High-Performance Lithium-Ion Batteries. *Front. Chem.* **2018**, *6* (APR), 1–12.

(259) Guo, B.; Zhao, J.; Fan, X.; Zhang, W.; Li, S.; Yang, Z.; Chen, Z.; Zhang, W. Aluminum and Fluorine Co-Doping for Promotion of Stability and Safety of Lithium-Rich Layered Cathode Material. *Electrochim. Acta* **2017**, *236*, 171–179.

(260) Kang, Y.-J.; Kim, J.-H.; Sun, Y.-K. Structural and Electrochemical Study of Li–Al–Mn–O–F Spinel Material for Lithium Secondary Batteries. *J. Power Sources* **2005**, *146*, 237–240.

(261) Sun, Y. K.; Chen, Z.; Noh, H. J.; Lee, D. J.; Jung, H. G.; Ren, Y.; Wang, S.; Yoon, C. S.; Myung, S. T.; Amine, K. Nanostructured High-Energy Cathode Materials for Advanced Lithium Batteries. *Nat. Mater.* **2012**, *11* (11), 942–947.

(262) Li, J.; Doig, R.; Camardese, J.; Plucknett, K.; Dahn, J. R. Measurements of Interdiffusion Coefficients of Transition Metals in Layered Li-Ni-Mn-Co Oxide Core-Shell Materials during Sintering. *Chem. Mater.* **2015**, *27* (22), 7765–7773.

(263) Myung, S.-T.; Noh, H.-J.; Yoon, S.-J.; Lee, E.-J.; Sun, Y.-K. Progress in High-Capacity Core–Shell Cathode Materials for Rechargeable Lithium Batteries. *J. Phys. Chem. Lett.* **2014**, *5* (4), 671–679.

(264) Yoon, C. S.; Kim, S. J.; Kim, U.-H.; Park, K.; Ryu, H.; Kim, H.; Sun, Y. Microstructure Evolution of Concentration Gradient Li[Ni 0.75 Co 0.10 Mn 0.15]O 2 Cathode for Lithium-Ion Batteries. *Adv. Funct. Mater.* **2018**, *28*, 1802090.

(265) Park, K.-J.; Choi, M.-J.; Maglia, F.; Kim, S.-J.; Kim, K.-H.; Yoon, C. S.; Sun, Y.-K. High-Capacity Concentration Gradient Li[Ni 0.865 Co 0.120 Al 0.015]O 2 Cathode for Lithium-Ion Batteries. *Adv. Energy Mater.* **2018**, *8*, 1703612.

(266) Lim, B. B.; Yoon, S. J.; Park, K. J.; Yoon, C. S.; Kim, S. J.; Lee, J. J.; Sun, Y. K. Advanced

Concentration Gradient Cathode Material with Two-Slope for High-Energy and Safe Lithium Batteries. *Adv. Funct. Mater.* **2015**, *25* (29), 4673–4680.

(267) Sun, Y. K.; Kim, D. H.; Yoon, C. S.; Myung, S. T.; Prakash, J.; Amine, K. A Novel Cathode Material with a Concentrationgradient for High-Energy and Safe Lithium-Ion Batteries. *Adv. Funct. Mater.* **2010**, *20* (3), 485–491.

(268) Ju, J. W.; Lee, E. J.; Yoon, C. S.; Myung, S. T.; Sun, Y. K. Optimization of Layered Cathode Material with Full Concentration Gradient for Lithium-Ion Batteries. *J. Phys. Chem. C* **2014**, *118* (1), 175–182.

(269) Sun, Y. K.; Lee, B. R.; Noh, H. J.; Wu, H.; Myung, S. T.; Amine, K. A Novel Concentration-Gradient Li[Ni0.83Co0.07Mn0.10]O2cathode Material for High-Energy Lithium-Ion Batteries. *J. Mater. Chem.* **2011**, *21* (27), 10108–10112.

(270) Hou, P. Y.; Zhang, L. Q.; Gao, X. P. A High-Energy, Full Concentration-Gradient Cathode Material with Excellent Cycle and Thermal Stability for Lithium Ion Batteries. *J. Mater. Chem. A* **2014**, *2* (40), 17130–17138.

(271) Longo, R. C.; Liang, C.; Kong, F.; Cho, K. Core-Shell Nanocomposites for Improving the Structural Stability of Li-Rich Layered Oxide Cathode Materials for Li-Ion Batteries. *ACS Appl. Mater. Interfaces* **2018**, *10*, 19226–19234.

(272) Chong, S.; Wu, Y.; Chen, Y.; Shu, C.; Liu, Y. A Strategy of Constructing Spherical Core-Shell Structure of Li1.2Ni0.2Mn0.6O2@Li1.2Ni0.4Mn0.4O2cathode Material for High-Performance Lithium-Ion Batteries. *J. Power Sources* **2017**, *356*, 153–162.

(273) Ahn, J.; Kim, J. H.; Cho, B. W.; Chung, K. Y.; Kim, S.; Choi, J. W.; Oh, S. H. Nanoscale Zirconium-Abundant Surface Layers on Lithium- and Manganese-Rich Layered Oxides for High-Rate Lithium-Ion Batteries. *Nano Lett.* **2017**, *17* (12), 7869–7877.

(274) Sun, Y.; Myung, S.; Kim, M.; Prakash, J.; Amine, K. Synthesis and Characterization of Li[(Ni0.8Co0.1Mn0.1)0.8(Ni0.5Mn0.5)0.2]O2 with the Microscale Core - Shell Structure as the Positive Electrode Material for Lithium Batteries. *J. Am. Chem. Soc.* **2005**, *8* (7), 13411–13418.

(275) Vu, N. H.; Arunkumar, P.; Im, J. C.; Im, W. Bin. High Capacity Spinel @ Layered Li 1 . 5 MnTiO4+δ as Thermally Stable Core- Shell-Driven Cathode Materials for Lithium-Ion Batteries. *J. Alloys Compd.* **2017**, *704*, 459–468.

(276) Kalluri, S.; Yoon, M.; Jo, M.; Liu, H. K.; Dou, S. X.; Cho, J.; Guo, Z. Feasibility of Cathode Surface Coating Technology for High-Energy Lithium-Ion and Beyond-Lithium-Ion Batteries. *Adv. Mater.* **2017**, *29* (48), 1605807.

(277) Hu, L.; Brüner, P.; Grehl, T.; Brongersma, H. H.; Cabana, J. Control of Chemical Structure in Core-Shell Nanocrystals for the Stabilization of Battery Electrode/Electrolyte Interfaces. *Chem. Mater.* **2017**, *29* (14), 5896–5905.

(278) Zhang, X. D.; Shi, J. L.; Liang, J. Y.; Yin, Y. X.; Zhang, J. N.; Yu, X. Q.; Guo, Y. G. Suppressing Surface Lattice Oxygen Release of Li-Rich Cathode Materials via Heterostructured Spinel Li4Mn5O12Coating. *Adv. Mater.* **2018**, *30* (29), 1–8.

(279) Cho, Y.; Lee, S.; Lee, Y.; Hong, T.; Cho, J. Spinel-Layered Core-Shell Cathode Materials for Li-Ion Batteries. *Adv. Energy Mater.* **2011**, *1* (5), 821–828.

(280) Qiu, B.; Zhang, M.; Wu, L.; Wang, J.; Xia, Y.; Qian, D.; Liu, H.; Hy, S.; Chen, Y.; An, K.; et al. Gas–Solid Interfacial Modification of Oxygen Activity in Layered Oxide Cathodes for Lithium-Ion Batteries. *Nat. Commun.* **2016**, *7*, 12108.

(281) Cho, J.; Kim, Y.-W.; Kim, B.; Lee, J.-G.; Park, B. A Breakthrough in the Safety of Lithium Secondary Batteries by Coating the Cathode Material with AlPO4 Nanoparticles. *Angew. Chemie Int. Ed.* **2003**, *42* (14), 1618–1621.

(282) Cho, J. Correlation between AlPO 4 Nanoparticle Coating Thickness on LiCoO 2 Cathode and Thermal Stability. *Electrochim. Acta* **2003**, *48*, 2807–2811.

(283) Cho, J. Improved Thermal Stability of LiCoO2 by Nanoparticle AlPO4 Coating with Respect to Spinel Li 1.05 Mn1.95O4. *Electrochem. commun.* **2003**, *5*, 146–148.

(284) Appapillai, A. T.; Mansour, A. N.; Cho, J.; Shao-Horn, Y. Microstructure of LiCoO2 with and without "AlPO4" Nanoparticle Coating: Combined STEM and XPS Studies. *Chem. Mater.* **2007**, *19* (3), 5748–5757.

(285) Lu, Y.; Mansour, A. N.; Yabuuchi, N.; Shao-horn, Y. Probing the Origin of Enhanced Stability of " AlPO 4 " Nanoparticle Coated LiCoO 2 during Cycling to High Voltages : Combined XRD and XPS Studies. *Chem. Mater.* **2009**, *21*, 4408–4424.

(286) Xiao, B.; Wang, B.; Liu, J.; Kaliyappan, K.; Sun, Q.; Liu, Y.; Dadheech, G.; Balogh, M. P.; Yang, L.; Sham, T. K.; et al. Highly Stable Li1.2Mn0.54Co0.13Ni0.13O2enabled by Novel Atomic Layer Deposited AlPO4coating. *Nano Energy* **2017**, *34* (February), 120–130.

(287) Wang, Z.; Lu, H.-Q.; Yin, Y.-P.; Sun, X.-Y.; Bai, X.-T.; Shen, X.-L.; Zhuang, W.-D.; Lu, S.-G. FePO4-Coated Li[Li0.2Ni0.13Co0.13Mn0.54]O2 with Improved Cycling Performance as Cathode Material for Li-Ion Batteries. *Rare Met.* **2017**, *36* (11), 899–904.

(288) Lee, Y.; Lee, J. K. J.; Lee, K. Y.; Mun, J.; Lee, J. K. J.; Choi, W. Facile Formation of a Li3PO4coating Layer during the Synthesis of a Lithium-Rich Layered Oxide for High-Capacity Lithium-Ion Batteries. *J. Power Sources* **2016**, *315* (2016), 284–293.

(289) Wang, Z.; Luo, S.; Ren, J.; Wang, D.; Qi, X. Enhanced Electrochemical Performance of Li-Rich Cathode Li[Li0.2Mn0.54Ni0.13Co0.13]O2by Surface Modification with Lithium Ion Conductor Li3PO4. *Appl. Surf. Sci.* **2016**, *370* (2016), 437–444.

(290) Liu, H.; Chen, C.; Du, C.; He, X.; Yin, G.; Song, B.; Zuo, P.; Cheng, X.; Ma, Y.; Gao, Y. Lithium-Rich $Li_{1.2}Ni_{0.13}Co_{0.13}Mn_{0.54}O_2$ Oxide Coated by Li_3PO_4 and Carbon Nanocomposite Layers as High Performance Cathode Materials for Lithium Ion Batteries. *J. Mater. Chem. A* **2015**, *3* (6), 2634–2641.

(291) Wu, F.; Zhang, X.; Zhao, T.; Li, L.; Xie, M.; Chen, R. Surface Modification of a Cobalt-Free Layered $Li[Li_{0.2}Fe_{0.1}Ni_{0.15}Mn_{0.55}]O_2$ Oxide with the $FePO_4$ /Li_3PO_4 Composite as the Cathode for Lithium-Ion Batteries. *J. Mater. Chem. A* **2015**, *3* (18), 9528–9537.

(292) Qiao, Q. Q.; Zhang, H. Z.; Li, G. R.; Ye, S. H.; Wang, C. W.; Gao, X. P. Surface Modification of Li-Rich Layered Li(Li0.17Ni0.25Mn0.58)O2 Oxide with Li–Mn–PO4 as the Cathode for Lithium-Ion Batteries. *J. Mater. Chem. A* **2013**, *1* (17), 5262.

(293) Ding, F.; Li, J.; Deng, F.; Xu, G.; Liu, Y.; Yang, K.; Kang, F. Surface Heterostructure Induced by PrPO4Modification in Li1.2[Mn0.54Ni0.13Co0.13]O2Cathode Material for High-Performance

Lithium-Ion Batteries with Mitigating Voltage Decay. *ACS Appl. Mater. Interfaces* **2017**, *9* (33), 27936–27945.

(294) Liu, W.; Oh, P.; Liu, X.; Myeong, S.; Cho, W.; Cho, J. Countering Voltage Decay and Capacity Fading of Lithium-Rich Cathode Material at 60 °c by Hybrid Surface Protection Layers. *Adv. Energy Mater.* **2015**, *5* (13), 1–11.

(295) Kweon, H.; Park, J.; Seo, J.; Kim, G.; Jung, B.; Lim, H. S. Effects of Metal Oxide Coatings on the Thermal Stability and Electrical Performance of LiCoCO 2 in a Li-Ion Cell. *J. Power Sources* **2004**, *126*, 156–162.

(296) Scott, I. D.; Jung, Y. S.; Cavanagh, A. S.; Yan, Y.; Dillon, A. C.; George, S. M.; Lee, S. H. Ultrathin Coatings on Nano-LiCoO2 for Li-Ion Vehicular Applications. *Nano Lett.* **2011**, *11* (2), 414–418.

(297) Du, K.; Xie, H.; Hu, G.; Peng, Z.; Cao, Y.; Yu, F. Enhancing the Thermal and Upper Voltage Performance of Ni-Rich Cathode Material by a Homogeneous and Facile Coating Method: Spray-Drying Coating with Nano-Al2O3. *ACS Appl. Mater. Interfaces* **2016**, *8* (27), 17713–17720.

(298) Kang, J.; Han, B. First-Principles Study on the Thermal Stability of LiNiO2 Materials Coated by Amorphous Al2O3 with Atomic Layer Thickness. *ACS Appl. Mater. Interfaces* **2015**, *7* (21), 11599–11603.

(299) Jung, S. C.; Han, Y. K. How Do Li Atoms Pass through the Al2O3 Coating Layer during Lithiation in Li-Ion Batteries? *J. Phys. Chem. Lett.* **2013**, *4* (16), 2681–2685.

(300) Jung, S. C.; Kim, H. J.; Choi, J. W.; Han, Y. K. Sodium Ion Diffusion in Al2O3: A Distinct Perspective Compared with Lithium Ion Diffusion. *Nano Lett.* **2014**, *14* (11), 6559–6563.

(301) Su, Y.; Cui, S.; Zhuo, Z.; Yang, W.; Wang, X.; Pan, F. Enhancing the High-Voltage Cycling Performance of LiNi0.5Mn0.3Co0.2O2 by Retarding Its Interfacial Reaction with an Electrolyte by Atomic-Layer-Deposited Al2O3. *ACS Appl. Mater. Interfaces* **2015**, *7* (45), 25105–25112.

(302) Yan, P.; Zheng, J.; Zhang, X.; Xu, R.; Amine, K.; Xiao, J.; Zhang, J. G.; Wang, C. M. Atomic to Nanoscale Investigation of Functionalities of an Al2O3 Coating Layer on a Cathode for Enhanced Battery Performance. *Chem. Mater.* **2016**, *28* (3), 857–863.

(303) Fang, X.; Lin, F.; Nordlund, D.; Mecklenburg, M.; Ge, M.; Rong, J.; Zhang, A.; Shen, C.; Liu, Y.; Cao, Y.; et al. Atomic Insights into the Enhanced Surface Stability in High Voltage Cathode Materials by Ultrathin Coating. *Adv. Funct. Mater.* **2017**, *27* (7), 1–9.

(304) Teranishi, T.; Yoshikawa, Y.; Yoneda, M.; Kishimoto, A.; Halpin, J.; O'Brien, S.; Modreanu, M.; Povey, I. M. Aluminum Interdiffusion into $LiCoO_2$ Using Atomic Layer Deposition for High Rate Lithium Ion Batteries. *ACS Appl. Energy Mater.* **2018**, acsaem.8b00496.

(305) Zhou, A.; Lu, Y.; Wang, Q.; Xu, J.; Wang, W.; Dai, X.; Li, J. Sputtering TiO2on LiCoO2composite Electrodes as a Simple and Effective Coating to Enhance High-Voltage Cathode Performance. *J. Power Sources* **2017**, *346*, 24–30.

(306) Zhang, C.; Su, J.; Wang, T.; Yuan, K.; Chen, C.; Liu, S.; Huang, T.; Wu, J. H.; Lu, H.; Yu, A. Significant Improvement on Electrochemical Performance of LiMn2O4 at Elevated Temperature by Atomic Layer Deposition of TiO2 Nanocoating. *ACS Sustain. Chem. Eng.* **2018**, *6*, 7890–7901.

(307) Cho, H.-M.; Chen, M. V.; MacRae, A. C.; Meng, Y. S. Effect of Surface Modification on Nano-

Structured LiNi $_{0.5}$ Mn $_{1.5}$ O $_{4}$ Spinel Materials. *ACS Appl. Mater. Interfaces* **2015**, *7* (30), 16231–16239.

(308) Qiu, B.; Wang, J.; Xia, Y.; Wei, Z.; Han, S.; Liu, Z. Enhanced Electrochemical Performance with Surface Coating by Reactive Magnetron Sputtering on Lithium-Rich Layered Oxide Electrodes. *ACS Appl. Mater. Interfaces* **2014**, *6* (12), 9185–9193.

(309) Zhao, J.; Wang, Y. Ultrathin Surface Coatings for Improved Electrochemical Performance of Lithium Ion Battery Electrodes at Elevated Temperature. *J. Phys. Chem. C* **2012**, *116* (22), 11867–11876.

(310) Dai, X.; Wang, L.; Xu, J.; Wang, Y.; Zhou, A.; Li, J. Improved Electrochemical Performance of LiCoO2 Electrodes with ZnO Coating by Radio Frequency Magnetron Sputtering. *ACS Appl. Mater. Interfaces* **2014**, *6* (18), 15853–15859.

(311) Sun, Y.-K.; Hong, K.-J.; Prakash, J. The Effect of ZnO Coating on Electrochemical Cycling Behavior of Spinel LiMn[Sub 2]O[Sub 4] Cathode Materials at Elevated Temperature. *J. Electrochem. Soc.* **2003**, *150* (7), A970.

(312) Laskar, M. R.; Jackson, D. H. K.; Xu, S.; Hamers, R. J.; Morgan, D.; Kuech, T. F. Atomic Layer Deposited MgO: A Lower Overpotential Coating for Li[Ni0.5Mn0.3Co0.2]O2 Cathode. *ACS Appl. Mater. Interfaces* **2017**, *9*, 11231–11239.

(313) Jin, Y.; Lee, S.; Lim, H.; Moon, B.; Han, K.; Kim, J.; Song, J.; Yu, J.; Cho, W.; Park, M. Amorphous Li-Zr-O Layer Coating on the Surface of High-Ni Cathode Materials for Lithium Ion Batteries. *Electrochim. Acta* **2018**, *282*, 311–316.

(314) Li, Y. C.; Zhao, W. M.; Xiang, W.; Wu, Z. G.; Yang, Z. G.; Xu, C. L.; Xu, Y. Di; Wang, E. H.; Wu, C. J.; Guo, X. D. Promoting the Electrochemical Performance of LiNi0.8Co0.1Mn0.1O2cathode via LaAlO3coating. *J. Alloys Compd.* **2018**, *766*, 546–555.

(315) Zhang, S.; Gu, H.; Tang, T.; Du, W.; Gao, M.; Liu, Y.; Jian, D.; Pan, H. In Situ Encapsulation of the Nanoscale Er2O3phase to Drastically Suppress Voltage Fading and Capacity Degradation of a Li- and Mn-Rich Layered Oxide Cathode for Lithium Ion Batteries. *ACS Appl. Mater. Interfaces* **2017**, *9* (39), 33863–33875.

(316) Zhou, A.; Wang, W.; Liu, Q.; Wang, Y.; Yao, X.; Qing, F.; Li, E.; Yang, T.; Zhang, L.; Li, J. Stable, Fast and High-Energy-Density LiCoO2cathode at High Operation Voltage Enabled by Glassy B2O3modification. *J. Power Sources* **2017**, *362*, 131–139.

(317) Han, B.; Paulauskas, T.; Key, B.; Peebles, C.; Park, J. S.; Klie, R. F.; Vaughey, J. T.; Dogan, F. Understanding the Role of Temperature and Cathode Composition on Interface and Bulk: Optimizing Aluminum Oxide Coatings for Li-Ion Cathodes. *ACS Appl. Mater. Interfaces* **2017**, *9* (17), 14769–14778.

(318) Meng, H.; Li, L.; Liu, J.; Han, X.; Zhang, W.; Liu, X.; Xu, Q. Surface Modification of Li-Rich Layered Li[Li0.17Ni0.17Co0.10Mn0.56]O2oxide with LiV3O8as a Cathode Material for Li-Ion Batteries. *J. Alloys Compd.* **2017**, *690*, 256–266.

(319) Deng, Y.; Mou, J.; Wu, H.; Jiang, N.; Zheng, Q.; Lam, K. H.; Xu, C.; Lin, D. A Superior Li2SiO3-Composited LiNi0.5Mn1.5O4Cathode for High-Voltage and High-Performance Lithium-Ion Batteries. *Electrochim. Acta* **2017**, *235*, 19–31.

(320) Zhou, A.; Dai, X.; Lu, Y.; Wang, Q.; Fu, M.; Li, J. Enhanced Interfacial Kinetics and High-Voltage/High-Rate Performance of LiCoO2Cathode by Controlled Sputter-Coating with a Nanoscale Li4Ti5O12Ionic Conductor. *ACS Appl. Mater. Interfaces* **2016**, *8* (49), 34123–34131.

(321) Chen, C.; Geng, T.; Du, C.; Zuo, P.; Cheng, X.; Ma, Y.; Yin, G. Oxygen Vacancies in SnO2surface Coating to Enhance the Activation of Layered Li-Rich Li1.2Mn0.54Ni0.13Co0.13O2cathode Material for Li-Ion Batteries. *J. Power Sources* **2016**, *331*, 91–99.

(322) Fu, Q.; Du, F.; Bian, X.; Wang, Y.; Yan, X.; Zhang, Y.; Zhu, K.; Chen, G.; Wang, C.; Wei, Y. Electrochemical Performance and Thermal Stability of Li1.18Co0.15Ni0.15Mn0.52O2 Surface Coated with the Ionic Conductor Li3VO4. *J. Mater. Chem. A* **2014**, *2* (20), 7555–7562.

(323) Cheng, H.-M.; Wang, F.-M.; Chu, J. P.; Santhanam, R.; Rick, J.; Lo, S.-C. Enhanced Cycleabity in Lithium Ion Batteries: Resulting from Atomic Layer Depostion of Al2O3 or TiO2 on LiCoO2 Electrodes. *J. Phys. Chem. C* **2012**, *116*, 7629–7637.

(324) Shim, J.-H.; Lee, S.; Park, S. S. Effects of MgO Coating on the Structural and Electrochemical Characteristics of LiCoO2 as Cathode Materials for Lithium Ion Battery. *Chem. Mater.* **2014**, *26* (8), 2537–2543.

(325) Wu, F.; Liu, J.; Li, L.; Zhang, X.; Luo, R.; Ye, Y.; Chen, R. Surface Modification of Li-Rich Cathode Materials for Lithium-Ion Batteries with a PEDOT:PSS Conducting Polymer. *ACS Appl. Mater. Interfaces* **2016**, *8* (35), 23095–23104.

(326) Liu, Z.; Hu, P.; Ma, J.; Qin, B.; Zhang, Z.; Mou, C.; Yao, Y.; Cui, G. Conformal Poly(Ethyl α-Cyanoacrylate) Nano-Coating for Improving the Interface Stability of LiNi0.5Mn1.5O4. *Electrochim. Acta* **2017**, *236*, 221–227.

(327) Xue, P.; Gao, D.; Chen, S.; Zhao, S.; Wang, B.; Li, L. Improved High-Temperature Capacity Retention of the LiMn2O4cathode Lithium-Ion Battery by Ion Exchange Polymer Coating. *RSC Adv.* **2014**, *4* (95), 52624–52628.

(328) Park, J. S.; Mane, A. U.; Elam, J. W.; Croy, J. R. Amorphous Metal Fluoride Passivation Coatings Prepared by Atomic Layer Deposition on LiCoO2 for Li-Ion Batteries. *Chem. Mater.* **2015**, *27* (6), 1917–1920.

(329) Xie, J.; Sendek, A. D.; Cubuk, E. D.; Zhang, X.; Lu, Z.; Gong, Y.; Wu, T.; Shi, F.; Liu, W.; Reed, E. J.; et al. Atomic Layer Deposition of Stable LiAlF4Lithium Ion Conductive Interfacial Layer for Stable Cathode Cycling. *ACS Nano* **2017**, *11* (7), 7019–7027.

(330) Sun, Y. K.; Han, J. M.; Myung, S. T.; Lee, S. W.; Amine, K. Significant Improvement of High Voltage Cycling Behavior AlF3-Coated LiCoO2 Cathode. *Electrochem. commun.* **2006**, *8* (5), 821–826.

(331) Zhou, Y.; Lee, Y.; Sun, H.; Wallas, J. M.; George, S. M.; Xie, M. Coating Solution for High-Voltage Cathode: AlF_3 Atomic Layer Deposition for Freestanding $LiCoO_2$ Electrodes with High Energy Density and Excellent Flexibility. *ACS Appl. Mater. Interfaces* **2017**, *9* (11), 9614–9619.

(332) Hu, E.; Yu, X.; Lin, R.; Bi, X.; Lu, J.; Bak, S.; Nam, K. W.; Xin, H. L.; Jaye, C.; Fischer, D. A.; et al. Evolution of Redox Couples in Li- and Mn-Rich Cathode Materials and Mitigation of Voltage Fade by Reducing Oxygen Release. *Nat. Energy* **2018**, *3* (August), 690.

(333) Chen, M.; Kou, K.; Tu, M.; Hu, J.; Du, X.; Yang, B. Conducting Reduced Graphene Oxide Wrapped LiFePO4/C Nanocrystal as Cathode Material for High-Rate Lithium Secondary Batteries. *Solid*

State Ionics **2017**, *310* (August), 95–99.

(334) Lai, C.-H.; Ashby, D. S.; Lin, T. C.; Lau, J.; Dawson, A.; Tolbert, S. H.; Dunn, B. S. Application of Poly(3-Hexylthiophene-2,5-Diyl) as a Protective Coating for High Rate Cathode Materials. *Chem. Mater.* **2018**, *30*, 2589–2599.

(335) Lee, Y. S.; Shin, W. K.; Kannan, A. G.; Koo, S. M.; Kim, D. W. Improvement of the Cycling Performance and Thermal Stability of Lithium-Ion Cells by Double-Layer Coating of Cathode Materials with Al2O3 Nanoparticles and Conductive Polymer. *ACS Appl. Mater. Interfaces* **2015**, *7* (25), 13944–13951.

(336) Chen, S.; He, T.; Su, Y.; Lu, Y.; Bao, L.; Chen, L.; Zhang, Q.; Wang, J.; Chen, R.; Wu, F. Ni-Rich $LiNi_{0.8}Co_{0.1}Mn_{0.1}O_2$ Oxide Coated by Dual-Conductive Layers as High Performance Cathode Material for Lithium-Ion Batteries. *ACS Appl. Mater. Interfaces* **2017**, *9* (35), 29732–29743.

(337) Ha, J.; Park, S.-K.; Yu, S.-H.; Jin, A.; Jang, B.; Bong, S.; Kim, I.; Sung, Y.-E.; Piao, Y. A Chemically Activated Graphene-Encapsulated LiFePO4 Composite for High-Performance Lithium Ion Batteries. *Nanoscale* **2013**, *5* (18), 8647.

(338) Kim, I. T.; Knight, J. C.; Celio, H.; Manthiram, A. Enhanced Electrochemical Performances of Li-Rich Layered Oxides by Surface Modification with Reduced Graphene Oxide/AlPO4 Hybrid Coating. *J. Mater. Chem. A* **2014**, *2* (23), 8696–8704.

(339) Xu, H.; Chang, J.; Sun, J.; Gao, L. Graphene-Encapsulated LiFePO4nanoparticles with High Electrochemical Performance for Lithium Ion Batteries. *Mater. Lett.* **2012**, *83*, 27–30.

(340) Shim, J.-H.; Kim, Y.-M.; Park, M.; Kim, J.; Lee, S. Reduced Graphene Oxide-Wrapped Nickel-Rich Cathode Materials for Lithium Ion Batteries. *ACS Appl. Mater. Interfaces* **2017**, *9* (22), 18720–18729.

(341) Chen, K. S.; Xu, R.; Luu, N. S.; Secor, E. B.; Hamamoto, K.; Li, Q.; Kim, S.; Sangwan, V. K.; Balla, I.; Guiney, L. M.; et al. Comprehensive Enhancement of Nanostructured Lithium-Ion Battery Cathode Materials via Conformal Graphene Dispersion. *Nano Lett.* **2017**, *17* (4), 2539–2546.

(342) Oh, P.; Ko, M.; Myeong, S.; Kim, Y.; Cho, J. A Novel Surface Treatment Method and New Insight into Discharge Voltage Deterioration for High-Performance 0.4Li2MnO3-0.6LiNi1/3Co1/3Mn1/3O2cathode Materials. *Adv. Energy Mater.* **2014**, *4* (16), 1400631.

(343) Balakrishnan, P. G.; Ramesh, R.; Prem Kumar, T. Safety Mechanisms in Lithium-Ion Batteries. *J. Power Sources* **2006**, *155* (2), 401–414.

(344) Mi, C.; Li, B.; Buck, D.; Ota, N. Advanced Electro-Thermal Modeling of Lithium-Ion Battery System for Hybrid Electric Vehicle Applications. *VPPC 2007 - Proc. 2007 IEEE Veh. Power Propuls. Conf.* **2007**, *46256*, 107–111.

(345) Chen, Z.; Qin, Y.; Ren, Y.; Lu, W.; Orendorff, C.; Roth, E. P.; Amine, K. Multi-Scale Study of Thermal Stability of Lithiated Graphite. *Energy Environ. Sci.* **2011**, *4* (10), 4023.

(346) Ribière, P.; Grugeon, S.; Morcrette, M.; Boyanov, S.; Laruelle, S.; Marlair, G. Investigation on the Fire-Induced Hazards of Li-Ion Battery Cells by Fire Calorimetry. *Energy Environ. Sci.* **2012**, *5* (1), 5271–5280.

(347) Martha, S. K.; Haik, O.; Zinigrad, E.; Exnar, I.; Drezen, T.; Miners, J. H.; Aurbach, D. On the Thermal

Stability of Olivine Cathode Materials for Lithium-Ion Batteries. *J. Electrochem. Soc.* **2011**, *158* (10), A1115.

(348) Veluchamy, A.; Doh, C.-H.; Kim, D.-H.; Lee, J.-H.; Shin, H.-M.; Jin, B.-S.; Kim, H.-S.; Moon, S.-I. Thermal Analysis of LixCoO2 Cathode Material of Lithium Ion Battery. *J. Power Sources* **2009**, *189* (1), 855–858.

(349) Hu, E.; Bak, S. M.; Senanayake, S. D.; Yang, X. Q.; Nam, K. W.; Zhang, L.; Shao, M. Thermal Stability in the Blended Lithium Manganese Oxide - Lithium Nickel Cobalt Manganese Oxide Cathode Materials: An in Situ Time-Resolved X-Ray Diffraction and Mass Spectroscopy Study. *J. Power Sources* **2015**, *277*, 193–197.

(350) Konishi, H.; Yuasa, T.; Yoshikawa, M. Thermal Stability of Li1−yNixMn(1−x)/2Co(1−x)/2O2 Layer-Structured Cathode Materials Used in Li-Ion Batteries. *J. Power Sources* **2011**, *196*, 6884–6888.

(351) He, Y. B.; Tang, Z. Y.; Song, Q. S.; Xie, H.; Xu, Q.; Liu, Y. G.; Ling, G. W. The Thermal Stability of Fully Charged and Discharged LiCoO2 Cathode and Graphite Anode in Nitrogen and Air Atmospheres. *Thermochim. Acta* **2008**, *480* (1–2), 15–21.

(352) Choi, D.; Xiao, J.; Choi, Y. J.; Hardy, J. S.; Vijayakumar, M.; Bhuvaneswari, M. S.; Liu, J.; Xu, W.; Wang, W.; Yang, Z.; et al. Thermal Stability and Phase Transformation of Electrochemically Charged/Discharged LiMnPO4 Cathode for Li-Ion Batteries. *Energy Environ. Sci.* **2011**, *4* (11), 4560.

(353) Hwang, S.; Kim, S. M.; Bak, S. M.; Kim, S. Y.; Cho, B. W.; Chung, K. Y.; Lee, J. Y.; Stach, E. A.; Chang, W. Using Real-Time Electron Microscopy To Explore the Effects of Transition-Metal Composition on the Local Thermal Stability in Charged Li<inf>x</Inf>Ni<inf>y</Inf>Mn<inf>z</Inf>Co<inf>1-y-Z</Inf>O<inf>2</Inf> Cathode Materials. *Chem. Mater.* **2015**, *27*, 3927–3935.

(354) Wang, Q. S.; Sun, J. H.; Chen, C. H.; Zhou, X. M. Thermal Properties and Kinetics Study of Charged LiCoO2 by TG and C80 Methods. *J. Therm. Anal. Calorim.* **2008**, *92* (2), 563–566.

(355) Chebiam, R. V; Prado, F.; Manthiram, A. Structural and Chemical Characterization of Chemically Delithiated Li1-XCoO2 (0<=x=<1). In *ECS Trans.*; 2000; Vol. 2000–2, p 21.

(356) Zou, M.; Yoshio, M.; Gopukumar, S.; Yamaki, J. I. Synthesis of High-Voltage (4.5 V) Cycling Doped LiCoO2 for Use in Lithium Rechargeable Cells. *Chem. Mater.* **2003**, *15* (25), 4699–4702.

(357) Menetrier, M.; Saadoune, I.; Levasseur, S.; Delmas, C.; Demas, C. The Insulator–Metal Transition upon Lithium Deintercalation from LiCoO2: Electronic Properties and 7Li NMRstudy. *J. Mater. Chem.* **1999**, *9*, 1135–1140.

(358) Levasseur, S.; Ménétrier, M.; Shao-Horn, Y.; Gautier, L.; Audemer, A.; Demazeau, G.; Largeteau, A.; Delmas, C. Oxygen Vacancies and Intermediate Spin Trivalent Cobalt Ions in Lithium-Overstoichiometric LiCoO2. *Chem. Mater.* **2003**, *15* (1), 348–354.

(359) Mizushima, K.; Jones, P. C.; Wiseman, P. J.; Goodenough, J. B. B. LiCoO2: A New Cathode Material for Batteries of High Energy Density. *Mat. Res. Bull.* **1980**, *15* (6), 783–789.

(360) Park, Y. S.; Lee, S. M. Effects of Particle Size on the Thermal Stability of Lithiated Graphite Anode. *Electrochim. Acta* **2009**, *54* (12), 3339–3343.

(361) Takahashi, Y.; Kijima, N.; Dokko, K.; Nishizawa, M. Structure and Electron Density Analysis of

Electrochemically and Chemically Delithiated LiCoO 2 Single Crystals. **2007**, *180*, 313–321.

(362) Kresse, G.; Joubert, D. From Ultrasoft Pseudopotentials to the Projector Augmented-Wave Method. *Phys. Rev. B* **1999**, *59* (3), 11–19.

(363) Blöchl, P. E. Projector Augmented-Wave Method. *Phys. Rev. B* **1994**, *50* (24), 17953–17979.

(364) Kresse, G.; Hafner, J. Ab Initio Molecular Dynamics for Liquid Metals. *Phys. Rev. B* **1993**, *47* (1), 558–561.

(365) Kresse, G.; Hafner, J. Ab Initio Molecular-Dynamics Simulation of the Liquid-Metal–Amorphous-Semiconductor Transition in Germanium. *Phys. Rev. B* **1994**, *49* (20), 14251–14269.

(366) Kresse, G.; Furthmüller, J.; Furthm??ller, J. Efficiency of Ab-Initio Total Energy Calculations for Metals and Semiconductors Using a Plane-Wave Basis Set. *Comput. Mater. Sci.* **1996**, *6* (1), 15–50.

(367) Kresse, G.; Furthmüller, J. Efficient Iterative Schemes for Ab Initio Total-Energy Calculations Using a Plane-Wave Basis Set. *Phys. Rev. B* **1996**, *54*, 11169–11186.

(368) Perdew, J. P.; Burke, K.; Ernzerhof, M. Generalized Gradient Approximation Made Simple. *Phys. Rev. Lett.* **1996**, *77*, 3865–3868.

(369) Dudarev, S.; Botton, G.; Savrasov, S.; Humphreys, C.; Sutton, A. Electron-Energy-Loss Spectra and the Structural Stability of Nickel Oxide: An LSDA+ U Study. *Phys. Rev. B* **1998**, *57* (3), 1505–1509.

(370) Zhou, F.; Cococcioni, M.; Marianetti, C. A.; Morgan, D.; Ceder, G. First-Principles Prediction of Redox Potentials in Transition-Metal Compounds with LDA + U. *Phys. Rev. B - Condens. Matter Mater. Phys.* **2004**, *70* (23), 1–8.

(371) Nosé, S. A Molecular Dynamics Method for Simulations in the Canonical Ensemble. *Mol. Phys.* **1984**, *52* (2), 255–268.

(372) Zhao, Y.; Feltes, T. E.; Regalbuto, J. R.; Meyer, R. J.; Klie, R. F. In Situ Electron Energy Loss Spectroscopy Study of Metallic Co and Co Oxides. *J. Appl. Phys.* **2010**, *108* (6).

(373) Wang, Z. L.; Yin, J. S.; Jiang, Y. D. EELS Analysis of Cation Valence States and Oxygen Vacancies in Magnetic Oxides. *Micron* **2000**, *31* (5), 571–580.

(374) Bak, S. M.; Nam, K. W.; Chang, W.; Yu, X.; Hu, E.; Hwang, S.; Stach, E. A.; Kim, K. B.; Chung, K. Y.; Yang, X. Q. Correlating Structural Changes and Gas Evolution during the Thermal Decomposition of Charged LixNi0.8Co0.15Al 0.05O2 Cathode Materials. *Chem. Mater.* **2013**, *25* (3), 337–351.

(375) He, Y. B.; Tang, Z. Y.; Song, Q. S.; Xie, H.; Xu, Q.; Liu, Y. G.; Ling, G. W. The Thermal Stability of Fully Charged and Discharged LiCoO2 Cathode and Graphite Anode in Nitrogen and Air Atmospheres. *Thermochim. Acta* **2008**, *480* (1–2), 15–21.

(376) Veluchamy, A.; Doh, C. H.; Kim, D. H.; Lee, J. H.; Shin, H. M.; Jin, B. S.; Kim, H. S.; Moon, S. I. Thermal Analysis of LixCoO2 Cathode Material of Lithium Ion Battery. *J. Power Sources* **2009**, *189* (1), 855–858.

(377) Katayama, N.; Watanabe, I.; Yamaki, J. Thermal Stability of LiXCoO2 Cathode in Li-Ion Cell. In *The Electrochemical Society*; 2011; Vol. 19, p 6740.

(378) Kriston, A.; Adanouj, I.; Ruiz, V.; Pfrang, A. Quantification and Simulation of Thermal

Decomposition Reactions of Li-Ion Battery Materials by Simultaneous Thermal Analysis Coupled with Gas Analysis. *J. Power Sources* **2019**, *435* (July), 226774.

(379) Sanchez-Santolino, G.; Tornos, J.; Bruno, F. Y.; Cuellar, F. A.; Leon, C.; Santamaria, J.; Pennycook, S. J.; Varela, M. Characterization of Surface Metallic States in SrTiO3 by Means of Aberration Corrected Electron Microscopy. *Ultramicroscopy* **2013**, *127*, 109–113.

(380) Maram, P. S.; Costa, G. C. C.; Navrotsky, A. Experimental Confirmation of Low Surface Energy in LiCoO2 and Implications for Lithium Battery Electrodes. *Angew. Chemie - Int. Ed.* **2013**, *52* (46), 12139–12142.

(381) Qian, D.; Hinuma, Y.; Chen, H.; Du, L. S.; Carroll, K. J.; Ceder, G.; Grey, C. P.; Meng, Y. S. Electronic Spin Transition in Nanosize Stoichiometric Lithium Cobalt Oxide. *J. Am. Chem. Soc.* **2012**, *134* (14), 6096–6099.

(382) Doughty, D.; Roth, E. P. A General Discussion of Li Ion Battery Safety. *Electrochem. Soc. Interface* **2012**, *21* (2), 37–44.

(383) Pesaran, A. Battery Thermal Management in EVs and HEVs : Issues and Solutions. *Adv. Automot. Batter. Conf.* **2001**, No. January 2001, 10.

(384) Rezvanizaniani, S. M.; Liu, Z.; Chen, Y.; Lee, J. Review and Recent Advances in Battery Health Monitoring and Prognostics Technologies for Electric Vehicle (EV) Safety and Mobility. *J. Power Sources* **2014**, *256*, 110–124.

(385) Doughty, D. H.; Ph, D. Vehicle Battery Safety Roadmap Guidance. **2012**, No. October.

(386) Lisbona, D.; Snee, T. A Review of Hazards Associated with Primary Lithium and Lithium-Ion Batteries. *Process Saf. Environ. Prot.* **2011**, *89* (6), 434–442.

(387) Zaghib, K.; Charest, P.; Guerfi, A.; Shim, J.; Perrier, M.; Striebel, K. Safe Li-Ion Polymer Batteries for HEV Applications. *J. Power Sources* **2004**, *134* (1), 124–129.

(388) Xue, L.; Savilov, S. V; Lunin, V. V; Xia, H. Self-Standing Porous LiCoO 2 Nanosheet Arrays as 3D Cathodes for Flexible Li-Ion Batteries. *Adv. Funct. Mater.* **2018**, *10*, 1705836.

(389) Xiao, B.; Sun, X. Surface and Subsurface Reactions of Lithium Transition Metal Oxide Cathode Materials : An Overview of the Fundamental Origins and Remedying Approaches. *Adv. Energy Mater.* **2018**, *8*, 1802057.

(390) Tebbe, J. L.; Holder, A. M.; Musgrave, C. B. Mechanisms of LiCoO2 Cathode Degradation by Reaction with HF and Protection by Thin Oxide Coatings. *ACS Appl. Mater. Interfaces* **2015**, *7* (43), 24265–24278.

(391) Kalluri, S.; Yoon, M.; Jo, M.; Park, S.; Myeong, S.; Kim, J.; Dou, S. X.; Guo, Z.; Cho, J. Surface Engineering Strategies of Layered LiCoO2Cathode Material to Realize High-Energy and High-Voltage Li-Ion Cells. *Adv. Energy Mater.* **2017**, *7* (1).

(392) Dai, X.; Zhou, A.; Xu, J.; Lu, Y.; Wang, L.; Fan, C.; Li, J. Extending the High-Voltage Capacity of LiCoO2 Cathode by Direct Coating of the Composite Electrode with Li2CO3 via Magnetron Sputtering. *J. Phys. Chem. C* **2016**, *120* (1), 422–430.

(393) Qian, J.; Liu, L.; Yang, J.; Li, S.; Wang, X.; Zhuang, H. L.; Lu, Y. Electrochemical Surface Passivation of LiCoO2 Particles at Ultrahigh Voltage and Its Applications in Lithium-Based Batteries. *Nat.*

Commun. **2018**, *9* (4918).

(394) Chen, Z.; Qin, Y.; Amine, K. Role of Surface Coating on Cathode Materials for Lithium-Ion Batteries. *J. Mater. Chem.* **2010**, *20*, 7606–7612.

(395) Kirkland, N. T.; Schiller, T.; Medhekar, N.; Birbilis, N. Exploring Graphene as a Corrosion Protection Barrier. *Corros. Sci.* **2012**, *56*, 1–4.

(396) Chen, S.; Brown, L.; Levendorf, M.; Cai, W.; Ju, S. Y.; Edgeworth, J.; Li, X.; Magnuson, C. W.; Velamakanni, A.; Piner, R. D.; et al. Oxidation Resistance of Graphene-Coated Cu and Cu/Ni Alloy. *ACS Nano* **2011**, *5* (2), 1321–1327.

(397) Lanza, M.; Wang, Y.; Sun, H.; Tong, Y.; Duan, H. Morphology and Performance of Graphene Layers on As-Grown and Transferred Substrates. *Acta Mech.* **2014**, *225* (4–5), 1061–1073.

(398) Hu, J.; Ji, Y.; Shi, Y. A Review on the Use of Graphene as a Protective Coating against Corrosion. *Ann. Mater. Sci. Eng.* **2014**, *1* (3), 1–16.

(399) Prasai, D.; Tuberquia, J. C.; Harl, R. R.; Jennings, G. K.; Bolotin, K. I. Graphene: Corrosion-Inhibiting Coating. *ACS Nano* **2012**, *6* (2), 1102–1108.

(400) Bunch, J. S.; Verbridge, S. S.; Alden, J. S.; van der Zande, A. M.; Parpia, J. M.; Craighead, H. G.; McEuen, P. L.; Der, A. M. Van; Parpia, J. M.; Craighead, H. G.; et al. Impermeable Atomic Membranes from Graphene Sheets. *Nano Lett.* **2008**, *8* (8), 2458–2462.

(401) Cui, Y.; Kundalwal, S. I.; Kumar, S. Gas Barrier Performance of Graphene/Polymer Nanocomposites. *Carbon N. Y.* **2016**, *98*, 313–333.

(402) Nair, R. R.; H. A. Wu; Jayaram, P. A.; Grigorieva, I. V.; Geim, A. K. Unimpeded Permeation of Water Through Helium-Leak–Tight Graphene-Based Membranes. *Science (80-.).* **2012**, *335* (January), 442–444.

(403) Guo, F.; Silverberg, G.; Bowers, S.; Kim, S. P.; Datta, D.; Shenoy, V.; Hurt, R. H. Graphene-Based Environmental Barriers. *Environ. Sci. Technol.* **2012**, *46* (14), 7717–7724.

(404) Yan, N.; Capezzuto, F.; Buonocore, G. G.; Lavorgna, M.; Xia, H.; Ambrosio, L. Gas-Barrier Hybrid Coatings by the Assembly of Novel Poly(Vinyl Alcohol) and Reduced Graphene Oxide Layers through Cross-Linking with Zirconium Adducts. *ACS Appl. Mater. Interfaces* **2015**, *7* (40), 22678–22685.

(405) Zhu, J.; Lim, J.; Lee, C. H.; Joh, H. I.; Kim, H. C.; Park, B.; You, N. H.; Lee, S. Multifunctional Polyimide/Graphene Oxide Composites via in Situ Polymerization. *J. Appl. Polym. Sci.* **2014**, *131* (9), 1–7.

(406) Pei, S.; Cheng, H. M. The Reduction of Graphene Oxide. *Carbon N. Y.* **2012**, *50* (9), 3210–3228.

(407) Zhu, Y.; Murali, S.; Cai, W.; Li, X.; Suk, J. W.; Potts, J. R.; Ruoff, R. S. Graphene and Graphene Oxide: Synthesis, Properties, and Applications. *Adv. Mater.* **2010**, *22* (35), 3906–3924.

(408) Gómez-Navarro, C.; Weitz, R. T.; Bittner, A. M.; Scolari, M.; Mews, A.; Burghard, M.; Kern, K. Electronic Transport Properties of Individual Chemically Reduced Graphene Oxide Sheets. *Nano Lett.* **2007**, *7* (11), 3499–3503.

(409) Eda, G.; Fanchini, G.; Chhowalla, M. Large-Area Ultrathin Films of Reduced Graphene Oxide as a

Transparent and Flexible Electronic Material. *Nat. Nanotechnol.* **2008**, *3* (5), 270–274.

(410) Yang, S.; Feng, X.; Ivanovici, S.; M??llen, K. Fabrication of Graphene-Encapsulated Oxide Nanoparticles: Towards High-Performance Anode Materials for Lithium Storage. *Angew. Chemie - Int. Ed.* **2010**, *49* (45), 8408–8411.

(411) Chem, J. M.; Liscio, A.; Veronese, P.; Treossi, E.; Suriano, F.; Rossella, F.; Bellani, V.; Rizzoli, R.; Samorı, P. Charge Transport in Graphene – Polythiophene Blends as Studied by Kelvin Probe Force Microscopy and Transistor Characterization. *J. Mater. Chem.* **2011**, *21*, 2924–2931.

(412) Wen, Y.; He, K.; Zhu, Y.; Han, F.; Xu, Y.; Matsuda, I.; Ishii, Y.; Cumings, J.; Wang, C. Expanded Graphite as Superior Anode for Sodium-Ion Batteries. *Nat. Commun.* **2014**, *5* (May), 1–10.

(413) Zheng, J.; Ren, Z.; Guo, P.; Fang, L.; Fan, J. Diffusion of Li + Ion on Graphene: A DFT Study. *Appl. Surf. Sci.* **2011**, *258* (5), 1651–1655.

(414) Yao, F.; Güneş, F.; Ta, H. Q.; Lee, S. M.; Chae, S. J.; Sheem, K. Y.; Cojocaru, C. S.; Xie, S. S.; Lee, Y. H. Diffusion Mechanism of Lithium Ion through Basal Plane of Layered Graphene. *J. Am. Chem. Soc.* **2012**, *134* (20), 8646–8654.

(415) Zhou, L. J.; Hou, Z. F.; Wu, L. M.; Zhang, Y. F. First-Principles Studies of Lithium Adsorption and Diffusion on Graphene with Grain Boundaries. *J. Phys. Chem. C* **2014**, *118* (48), 28055–28062.

(416) Lin, L. C.; Grossman, J. C. Atomistic Understandings of Reduced Graphene Oxide as an Ultrathin-Film Nanoporous Membrane for Separations. *Nat. Commun.* **2015**, *6*.

(417) Ven, A. Van Der; Aydinol, M. K.; Ceder, G. First-Principles Evidence for Stage Ordering in Li,Co02. *J. Electrochem. Soc.* **1998**, *145* (6), 2149–2155.

(418) Wang, H.; Rus, E.; Sakuraba, T.; Kikuchi, J.; Abruña, H. D. CO 2 and O 2 Evolution at High Voltage Cathode Materials of Li-Ion Batteries: A Di Ff Erential Electrochemical Mass Spectrometry Study. *Anal. Chem.* **2014**, *86*, 6197–6201.

(419) Qiu, X.; Zhuang, Q.; Zhang, Q.; Cao, R. Electrochemical and Electronic Properties of LiCoO 2 Cathode Investigated by Galvanostatic Cycling and EIS. *Phys. Chem. Chem. Phys.* **2012**, *14*, 2617–2630.

(420) Jung, Y. S.; Cavanagh, A. S.; Dillon, A. C.; Groner, M. D.; George, S. M.; Lee, S. Enhanced Stability of LiCoO 2 Cathodes in Lithium-Ion Batteries Using Surface Modification by Atomic Layer Deposition. *J. Electrochem. Soc.* **2010**, *157* (1), 75–81.

(421) Edstr, K.; Gustafsson, T.; Thomas, J. O. The Cathode – Electrolyte Interface in the Li-Ion Battery. *Electrochim. Acta* **2004**, *50*, 397–403.

(422) Hwang, B. J.; Chen, C. Y.; Cheng, M. Y.; Santhanam, R.; Ragavendran, K. Mechanism Study of Enhanced Electrochemical Performance of ZrO 2 -Coated LiCoO 2 in High Voltage Region. *J. Power Sources* **2010**, *195* (13), 4255–4265.

(423) Dai, X.; Zhou, A.; Xu, J.; Lu, Y.; Wang, L.; Fan, C.; Li, J. Extending the High-Voltage Capacity of LiCoO 2 Cathode by Direct Coating of the Composite Electrode with Li 2 CO 3 via Magnetron Sputtering. *J. Phys. Chem. C* **2016**.

(424) Späth, T.; Becker, D.; Schulz, N.; Hausbrand, R. Understanding the SEI Formation at Pristine Li-Ion Cathodes : Chemisorption and Reaction of DEC on LiCoO 2 Surfaces Studied by a Combined SXPS

/ HREELS Approach. *Adv. Mater. Interfaces* **2017**, *1700567*, 1–9.

(425) Yao, F.; Gu, F.; Ta, H. Q.; Lee, S. M.; Chae, S. J.; Sheem, K. Y. Diffusion Mechanism of Lithium Ion through Basal Plane of Layered Graphene. *J. Am. Chem. Soc.* **2012**, No. 134, 8646–8654.

(426) Yong, S.; Shyuan, K.; Kartom, S.; Ramli, W.; Daud, W. Graphene Production via Electrochemical Reduction of Graphene Oxide : Synthesis and Characterisation. *Chem. Eng. J.* **2014**, *251*, 422–434.

(427) Rocha, D. P.; Dornellas, R. M.; Cardoso, R. M.; Narciso, L. C. D.; Silva, M. N. T.; Nossol, E.; Richter, E. M.; Munoz, R. A. A. Chemical Chemically versus Electrochemically Reduced Graphene Oxide : Improved Amperometric and Voltammetric Sensors of Phenolic Compounds on Higher Roughness Surfaces. *Sensors Actuators B. Chem.* **2018**, *254*, 701–708.

(428) Wang, Z.; Zhou, X.; Zhang, J.; Boey, F.; Zhang, H. Direct Electrochemical Reduction of Single-Layer Graphene Oxide and Subsequent Functionalization with Glucose Oxidase. *J. Phys. Chem. C* **2009**, *113*, 14071–14075.

(429) Ramesha, G. K.; Sampath, S. Electrochemical Reduction of Oriented Graphene Oxide Films : An in Situ Raman Spectroelectrochemical Study. *J. Phys. Chem. C* **2009**, *113*, 7985–7989.

(430) Shao, Y.; Wang, J.; Engelhard, M.; Wang, C.; Lin, Y. Facile and Controllable Electrochemical Reduction of Graphene Oxide and Its Applications. *J. Mater. Chem.* **2010**, *20*, 743–748.

(431) Xia, H.; Lu, L.; Meng, Y. S.; Ceder, G. Phase Transitions and High-Voltage Electrochemical Behavior of LiCoO2 Thin Films Grown by Pulsed Laser Deposition. *J. Electrochem. Soc.* **2007**, *154* (4), A337.

(432) Karki, K.; Huang, Y.; Hwang, S.; Gamalski, A. D.; Whittingham, M. S.; Zhou, G.; Stach, E. A. Tuning the Activity of Oxygen in LiNi0.8Co0.15Al0.05O2 Battery Electrodes. *ACS Appl. Mater. Interfaces* **2016**, *8*, 27762–27771.

(433) Karki, K.; Huang, Y.; Hwang, S.; Gamalski, A. D.; Whittingham, M. S.; Zhou, G.; Stach, E. A. Tuning the Activity of Oxygen in $LiNi_{0.8}Co_{0.15}Al_{0.05}O_2$ Battery Electrodes. *ACS Appl. Mater. Interfaces* **2016**, *8* (41), 27762–27771.

(434) Paier, J.; Hirschl, R.; Marsman, M.; Kresse, G. The Perdew-Burke-Ernzerhof Exchange-Correlation Functional Applied to the G2-1 Test Set Using a Plane-Wave Basis Set. *J. Chem. Phys.* **2005**, *122* (23), 0–13.

(435) Hammer, B.; Hansen, L. B.; Nørskov, J. K. Improved Adsorption Energetics within Density-Functional Theory Using Revised Perdew-Burke-Ernzerhof Functionals. *Phys. Rev. B - Condens. Matter Mater. Phys.* **1999**, *59* (11), 7413–7421.

(436) Aykol, M.; Kim, S.; Wolverton, C. Van Der Waals Interactions in Layered Lithium Cobalt Oxides. *J. Phys. Chem. C* **2015**, *119* (33), 19053–19058.

(437) Dixit, M.; Markovsky, B.; Schipper, F.; Aurbach, D.; Major, D. T. Origin of Structural Degradation during Cycling and Low Thermal Stability of Ni-Rich Layered Transition Metal-Based Electrode Materials. *J. Phys. Chem. C* **2017**, *121* (41), 22628–22636.

(438) Qiu, B.; Zhang, M.; Xia, Y.; Liu, Z.; Meng, Y. S. Understanding and Controlling Anionic Electrochemical Activity in High-Capacity Oxides for Next Generation Li-Ion Batteries. *Chem. Mater.* **2017**, *29*, 908–915.

(439) Yan, J.; Liu, X.; Li, B. Recent Progress in Li-Rich Layered Oxides as Cathode Materials for Li-Ion

Batteries. *RSC Adv.* **2014**, *4*, 63268–63284.

(440) Nayak, P. K.; Erickson, E. M.; Schipper, F.; Penki, T. R.; Munichandraiah, N.; Adelhelm, P.; Sclar, H.; Amalraj, F.; Markovsky, B.; Aurbach, D. Review on Challenges and Recent Advances in the Electrochemical Performance of High Capacity Li- and Mn-Rich Cathode Materials for Li-Ion Batteries. *Adv. Energy Mater.* **2018**, *8*, 1–16.

(441) Pan, H.; Zhang, S.; Chen, J.; Gao, M.; Liu, Y.; Zhu, T.; Jiang, Y. Li- and Mn-Rich Layered Oxide Cathode Materials for Lithium-Ion Batteries: A Review from Fundamentals to Research Progress and Applications. *Mol. Syst. Des. Eng.* **2018**, *3*, 748–803.

(442) Croy, J. R.; Balasubramanian, M.; Gallagher, K. G.; Burrell, A. K. Review of the U.S. Department of Energy ' s " Deep Dive " Effort to Understand Voltage Fade in Li- and Mn-Rich Cathodes. *Acc. Chem. Res.* **2015**, *48*, 2813–2821.

(443) Croy, J. R.; Gallagher, K. G.; Balasubramanian, M.; Chen, Z.; Ren, Y.; Kim, D.; Kang, S.; Dees, D. W.; Thackeray, M. M. Examining Hysteresis in Composite x Li 2 MnO 3 · (1 − x)LiMO 2 Cathode Structures. *J. Phys. Chem. C* **2013**, *117*, 6525–6536.

(444) Teufl, T.; Pritzl, D.; Mendez, M. A.; Solchenbach, S. State of Charge Dependent Resistance Build-Up in Li- and Mn-Rich Layered Oxides during Lithium Extraction and Insertion. *J. Electrochem. Soc.* **2019**, *166*, 1275–1284.

(445) Gowda, S. R.; Dees, D. W.; Jansen, A. N.; Gallagher, K. G. Examining the Electrochemical Impedance at Low States of Charge in Lithium- and Manganese-Rich Layered Transition-Metal Oxide Electrodes. *J. Electrochem. Soc.* **2015**, *162*, 1374–1381.

(446) Seo, D.-H.; Lee, J.; Urban, A.; Malik, R.; Kang, S.; Ceder, G. The Structural and Chemical Origin of the Oxygen Redox Activity in Layered and Cation-Disordered Li-Excess Cathode Materials. *Nat. Chem.* **2016**, *8*, 692–697.

(447) Croy, J. R.; Iddir, H.; Gallagher, K.; Johnson, C. S.; Benedek, R. First-Charge Instabilities of Layered-Layered Lithium-Ion-Battery Materials. *Phys. Chem. Chem. Phys.* **2015**, No. 17, 24382–24391.

(448) Lee, P.; Wu, S.; Wang, C.; Song, Y.; Liu, R. The Origin of Capacity Fade in the Li 2 MnO 3 · Li M O 2 (M = Li, Ni, Co, Mn) Microsphere Positive Electrode: An Operando Neutron Di Ff Raction and Transmission X - Ray Microscopy Study. *JACS* **2016**, *2*, 2–11.

(449) Liu, H.; Chen, Y.; Hy, S.; An, K.; Venkatachalam, S.; Qian, D. Operando Lithium Dynamics in the Li-Rich Layered Oxide Cathode Material via Neutron Diffraction. *Adv. Energy Mater.* **2016**, *6*, 1–7.

(450) Mu, L.; Lin, R.; Xu, R.; Han, L.; Xia, S.; Sokaras, D.; Steiner, J. D.; Weng, T.; Nordlund, D.; Doe, M. M.; et al. Oxygen Release Induced Chemomechanical Breakdown of Layered Cathode Materials. *Nano Lett* **2018**, *18*, 3241–2149.

(451) Yano, A.; Shikano, M.; Ueda, A.; Sakaebe, H.; Ogumi, Z. LiCoO 2 Degradation Behavior in the High-Voltage Phase Transition Region and Improved Reversibility with Surface Coating. *J. Electrochem. Soc.* **2017**, *164*, 6116–6122.

(452) Yan, P.; Zheng, J.; Liu, J.; Wang, B.; Cheng, X.; Zhang, Y.; Sun, X.; Wang, C.; Zhang, J. Tailoring Grain Boundary Structures and Chemistry of Ni-Rich Layered Cathodes for Enhanced Cycle Stability of Lithium-Ion Batteries. *Nat. Energy* **2018**, *3*, 600–605.

(453) Gallagher, K. G.; Croy, J. R.; Balasubramanian, M.; Bettge, M.; Abraham, D. P.; Burrell, A. K.; Thackeray, M. M. Electrochemistry Communications Correlating Hysteresis and Voltage Fade in Lithium- and Manganese-Rich Layered Transition-Metal Oxide Electrodes. *Electrochem. commun.* **2013**, *33*, 96–98.

(454) Dogan, F.; Long, B. R.; Croy, J. R.; Gallagher, K. G.; Iddir, H.; Russell, J. T.; Balasubramanian, M.; Key, B. Re-Entrant Lithium Local Environments and Defect Driven Electrochemistry of Li- and Mn-Rich Li-Ion Battery Cathodes. *JACS* **2015**, *137*, 2328–2335.

(455) Lu, Z.; Chen, Z.; Dahn, J. R. Lack of Cation Clustering in Li[NixLi1/3-2x/3Mn2/3-x/3]O2 (0 < x e 1/2) and Li[CrxLi(1-x)/3Mn(2-2x)/3]O2 (0 < x < 1). *Chem. Mater.* **2003**, *15*, 3214–3220.

(456) Gu, M.; Belharouak, I.; Genc, A.; Wang, Z.; Wang, D.; Amine, K.; Gao, F.; Zhou, G.; Thevuthasan, S.; Baer, D. R.; et al. Conflicting Roles of Nickel in Controlling Cathode Performance in Lithium Ion Batteries. *Nano Lett.* **2012**, *12*, 5186–5191.

(457) Wen, J. G.; Bareño, J.; Lei, C. H.; Kang, S. H.; Balasubramanian, M.; Petrov, I.; Abraham, D. P. Analytical Electron Microscopy of Li 1 . 2 Co 0 . 4 Mn 0 . 4 O 2 for Lithium-Ion Batteries. *Solid State Ionics* **2011**, *182*, 98–107.

(458) Thackeray, M. M.; Kang, S. H.; Johnson, C. S.; Vaughey, J. T.; Hackney, S. A. Comments on the Structural Complexity of Lithium-Rich Li1+xM1-XO2 Electrodes (M = Mn, Ni, Co) for Lithium Batteries. *Electrochem. commun.* **2006**, *8*, 1531–1538.

(459) Thackeray, M. M.; Kang, S.-H.; Johnson, C. S.; Vaughey, J. T.; Benedek, R.; Hackney, S. a. Li2MnO3-Stabilized LiMO2 (M = Mn, Ni, Co) Electrodes for Lithium-Ion Batteries. *J. Mater. Chem.* **2007**, *17*, 3112.

(460) Koga, H.; Croguennec, L.; Mannessiez, P.; Ménétrier, M.; Weill, F.; Bourgeois, L.; Duttine, M.; Suard, E.; Delmas, C. Li 1.20Mn 0.54Co 0.13Ni 0.13O 2 with Different Particle Sizes as Attractive Positive Electrode Materials for Lithium-Ion Batteries: Insights into Their Structure. *J. Phys. Chem. C* **2012**, *116*, 13497–13506.

(461) Long, B. R.; Rinaldo, S. G.; Gallagher, K. G.; Dees, D. W.; Trask, S. E.; Polzin, B. J.; Jansen, A. N.; Abraham, D. P.; Bloom, I.; Croy, J. R.; et al. Enabling High-Energy , High-Voltage Lithium-Ion Cells : Standardization of Coin-Cell Assembly , Electrochemical Testing , and Evaluation of Full Cells. **2016**, *163*, 2999–3009.

(462) Kohn, W.; Sham, L. J. Self-Consistent Equations Including Exchange and Correlation Effects. *Phys. Rev.* **1965**, *140*, 1133–1138.

(463) Perdew, J.; Chevary, J.; Vosko, S.; Jackson, K.; Pederson, M.; Singh, D.; Fiolhais, C. Atoms, Molecules, Solids, and Surfaces: Applications of the Generalized Gradient Approximation for Exchange and Correlation. *Phys. Rev. B* **1992**, *46*, 6671–6687.

(464) Perdew, J. P.; Burke, K.; Ernzerhof, M. Generalized Gradient Approximation Made Simple. *Phys. Rev. Lett.* **1996**, *77*, 3865–3868.

(465) Sun, H.; Zhao, K. Electronic Structure and Comparative Properties of LiNi x Mn y Co z O 2 Cathode Materials. *J. Phys. Chem. C* **2017**, *121*, 6002–6010.

(466) Gilbert, J. A.; Bareño, J.; Spila, T.; Trask, S. E.; Miller, D. J.; Polzin, B. J.; Jansen, A. N.; Abraham, D. P. Cycling Behavior of NCM523 / Graphite Lithium-Ion Cells in the 3 – 4 . 4 V Range : Diagnostic

Studies of Full Cells and Harvested Electrodes. *J. ofThe Electrochem. Soc.* **2017**, *164* (1), 6054–6065.

(467) Gilbert, J. A.; Shkrob, I. A.; Abraham, D. P. Transition Metal Dissolution , Ion Migration , Electrocatalytic Reduction and Capacity Loss in Lithium-Ion Full Cells. *J. ofThe Electrochem. Soc.* **2017**, *164*, 389–399.

(468) Watanabe, S.; Kinoshita, M.; Hosokawa, T.; Morigaki, K. Capacity Fading of LiAl y Ni 1 À x À y Co x O 2 Cathode for Lithium-Ion Batteries during Accelerated Calendar and Cycle Life Tests (Effect of Depth of Discharge in Charge e Discharge Cycling on the Suppression of the Micro-Crack Generation of LiAl y Ni 1. *J. Power Sources* **2014**, *260*, 50–56.

(469) Tornheim, A.; Sharifi-asl, S.; Garcia, J. C.; Bareño, J.; Iddir, H. Effect of Electrolyte Composition on Rock Salt Surface Degradation in NMC Cathodes during High-Voltage Potentiostatic Holds. *Nano Energy* **2019**, *55* (August 2018), 216–225.

(470) Croy, J. R.; Hanlon, D. C. O.; Shari, S.; Murphy, M.; Mane, A.; Lee, C.; Trask, S. E.; Shahbazian-yassar, R.; Balasubramanian, M. Insights on the Stabilization of Nickel-Rich Cathode Surfaces: Evidence of Inherent Instabilities in the Presence of Conformal Coatings. *Chem. Mater.* **2019**, *31*, 3891–3899.

Appendixes

Atomic Scale Analysis of the Modified Layered Oxide Cathodes *(Collaborative Efforts with Argonne National Laboratory)*

Introduction

The cumulative understandings derived from the extensive research on identifying the degradation mechanisms of Li-ion battery cathode materials suggests that surface structure of the cathodes plays a dominant role in defining the structural stability and electrochemical properties of the cathodes. Additionally, it has been identified that chemical composition and atomic interactions within the crystal structure has large implications on the structural stability of the cathodes. Therefore, as discussed in Chapter 3.3 coating strategies and chemical composition modifications have been vigorously followed to improve the properties of the cathode materials. In this chapter our contribution to the collaborative researches on various aspects of Li-ion battery cathode materials is presented.

STEM/EELS Characterization of Ni-rich Surfaces in LCMO Cathodes

(Used as a Part of the Following Article: Croy, J. R.; Hanlon, D. C. O.; Shari, S.; Murphy, M.; Mane, A.; Lee, C.; Trask, S. E.; Shahbazian-yassar, R.; Balasubramanian, M. Insights on the

Stabilization of Nickel-Rich Cathode Surfaces: Evidence of Inherent Instabilities in the Presence of Conformal Coatings. Chem. Mater. 2019, 31, 3891–3899. Reproduced with permission[470]. Copyright 2019, American Chemical Society.)

One of the main challenges associated with understanding the behavior and degradation mechanism of cathode materials is the complexity of the Li-ion battery degradation, since numerous mechanisms and reactions are happening at each electrochemical cell, making the deconvolution and isolation of the subject of study nearly impossible. On the other hand, environmental sensitivity of the Li-ion battery components, inevitable local variation in the behavior of battery materials and rapid kinetics of reactions are other issues associated with studying the battery materials, which imply the necessity of *in-operando* techniques. One of the most successfully developed *in-operando* techniques is synchrotron X-ray absorption spectroscopy (XAS) and X-ray diffraction (XRD). These techniques allow for characterization of individual battery components during electrochemical cycling under operational circumstances. Therefore, the results can reveal many aspects of the battery operation with minimum experimental artifacts. However, the results do not contain any spatial information as the X-ray interacts with the surface as well as the bulk of materials. To solve this issue, researchers at Argonne National Laboratory (ANL) have developed a surface doping technique in which Ni dopants are placed only at the top surface areas in $Li(Mn_xCo_{1-x})O_2$ structure. During the electrochemical cycling, the surface doped Ni-cations will participate in the electrochemical redox reaction and will oxidize from 2+ to 4+ during charge and reduce to 2+ again during discharge. The change in the Ni valence state can be captured by *in-operando* XAS analysis. However, if the cathode surface undergoes degradation and phase transition, the redox activity will be halted at the surface, which can be detected through sequential analysis of XAS results of Ni cations at each cycle. Using such innovative materials design, the effectivity of the surface coating can be gauged. By performing

the same experimental procedure on the coated particles, the contribution of the coating layers on the surface stability of the cathodes can be gauged. *Figure 63* schematically illustrates the described idea in this research.

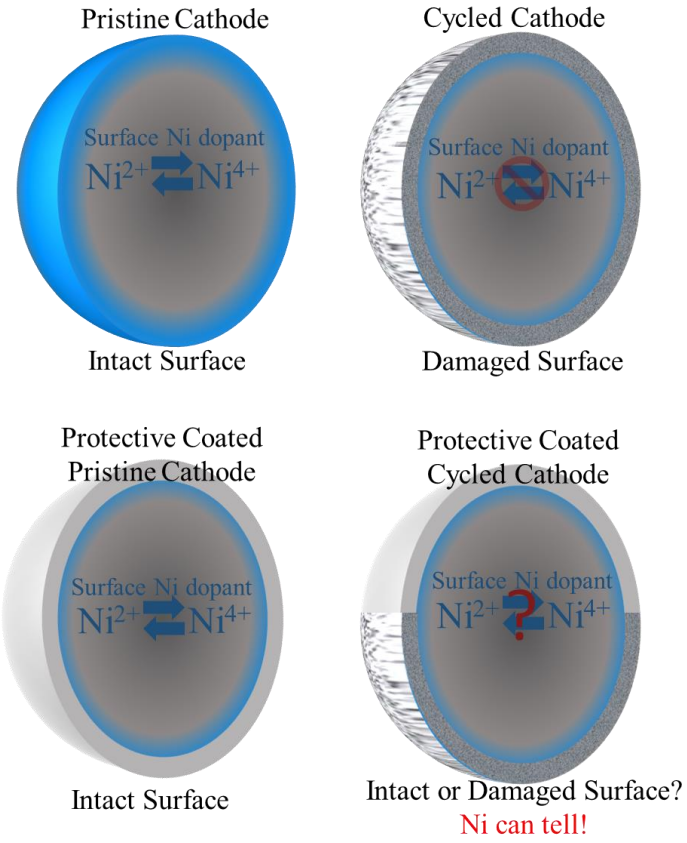

Figure 63. Schematic illustration of the cathodes with surface doping structure and its effect on *in-operando* evaluation of the coatings' effectiveness.

We have contributed to this research by identifying the atomic structure of the cathode surface after introducing Ni dopant cations, concentration of the dopant in the cathode particles' surface and length of dopant diffusion into the surface through STEM/EELS analysis. Moreover, identification of the ALD deposited alumina layers was carried out by STEM/EDS analysis. After surface treating the LNMO cathodes with nickel nitrate, heat treatment is carried out to allow for Ni diffusion into the surface and formation of Ni-doped surface. Two types of samples have been

synthesized based on the various heat treatment temperatures, at 900 °C and at 600 °C. Both samples are characterized using STEM/EELS analysis to evaluate the doping conditions at various temperatures. *Figure 64* demonstrates the STEM/EELS results from the sample heat treated at 900°C. *Figure 64A* shows a morphological image from a particle agglomerate with clean and defined crystalline facets. An EELS line scan is captured from the top 100 nm area of the facet that is shown in *Figure 64B*. As can be seen from the EELS spectra plotted in *Figure 64C*, a very weak Ni signal can be detected at the top 80 nm of the surface, which fades gradually throughout the particle thickness. The sum spectrum which is shown at top in black allows for better visualization of the Ni L edge, but it does not contain any spatial information. Based on EDS analysis, Ni constitutes about 1%wt of this particle agglomerate.

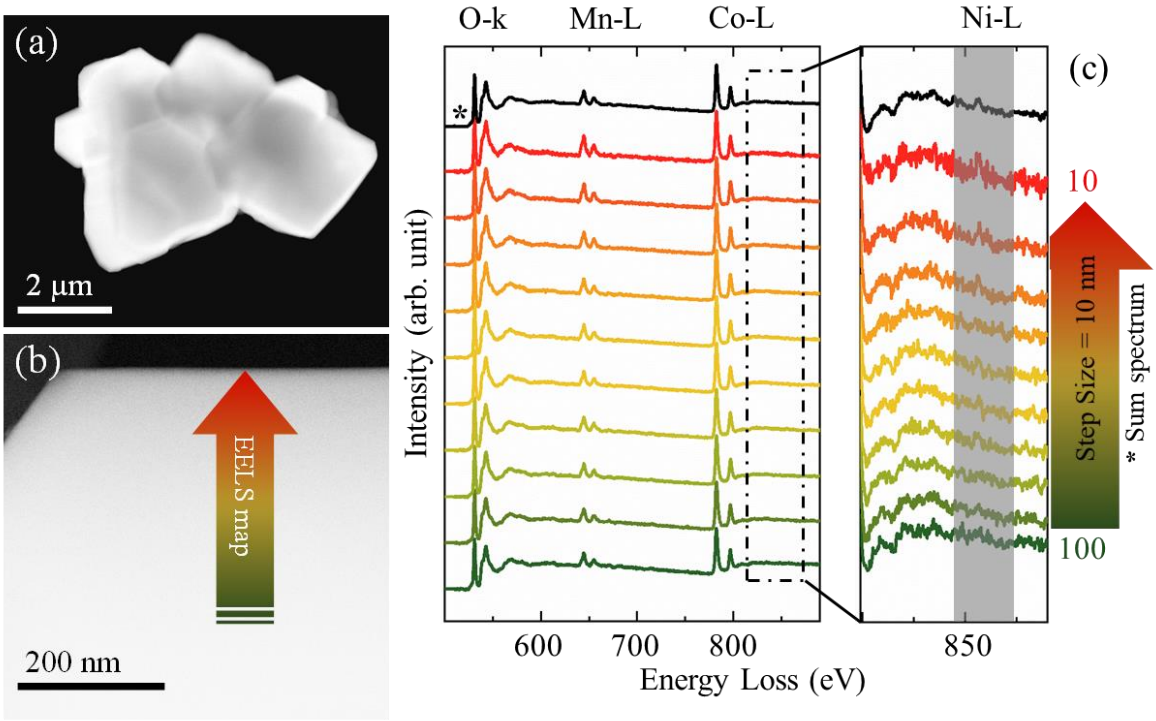

Figure 64. (a) Low-magnification HAADF image of the Ni-900 °C particles. (b) Low-magnification HAADF image from the surface of a Ni-900 °C particle. (c) EELS map data from

the region marked with an arrow in (b). The “sum spectrum” (*, black line at top) is the summation of all spectra from the mapped area.

Next, we analyzed the sample that was heat treated at 600 °C. *Figure 65A* demonstrates the low magnification HAADF image from the surface of sample. Atomic resolution HAADF image shown in *Figure 65B* demonstrates that the sample has retained its original layered structure after introducing the Ni dopants. *Figure 65C* demonstrates the EELS spectra acquired as a function of distance from the particle surface. The results show that the Ni dopants have diffused to the top 30 nm when heat treated at 600 °C. Also based on the higher intensity of the Ni signal in this sample, they have a higher concentration at the top surface. Based on the equal concentration of Ni in both samples obtained from EDS analysis (1%wt Ni), the significant change in diffusion length of Ni dopants denotes to the effect of heat treatment temperature on the diffusion rate of Ni dopants. Therefore the 600°C is chosen for *in-operando* XAS analysis that is discussed in detail in this publication[470]. Finally, the 600 °C sample was coated with an atomically thin alumina layer, to investigate the effectiveness of the coating on suppressing or delaying the surface degradation of the cathode samples. EDS map analysis was carried out on the surface of the samples to evaluate and confirm the uniformity and the thickness of the ALD coating layer (*Figure 66*).

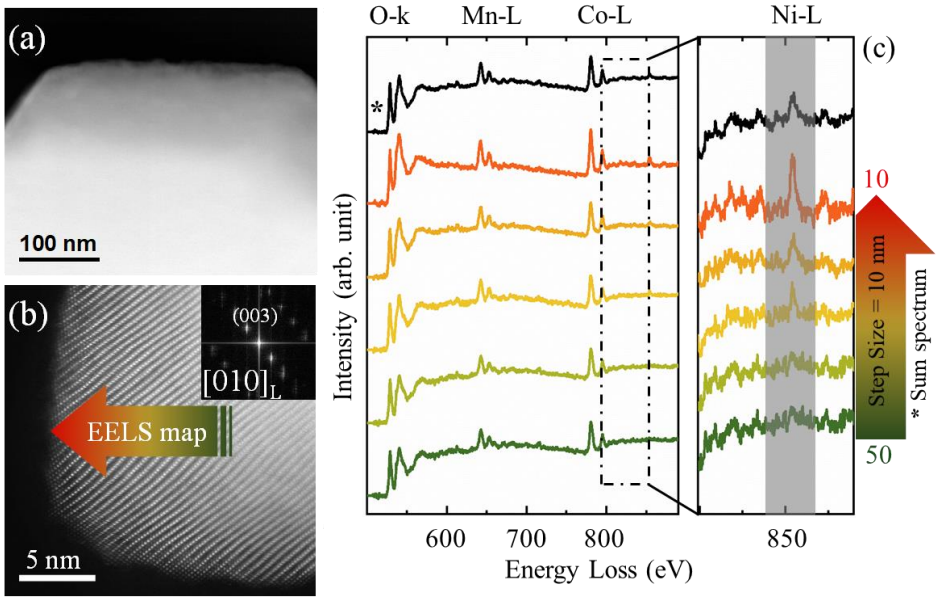

Figure 65. (a) Low-magnification HAADF image from the surface of a Ni-600 °C particle. (b) Atomic resolution image and the corresponding FTT (inset) from the surface of a Ni-600 °C particle. (c) EELS map data from the region marked with an arrow in (b). The "sum spectrum" (*, black line at top) is the summation of all spectra from the mapped area.

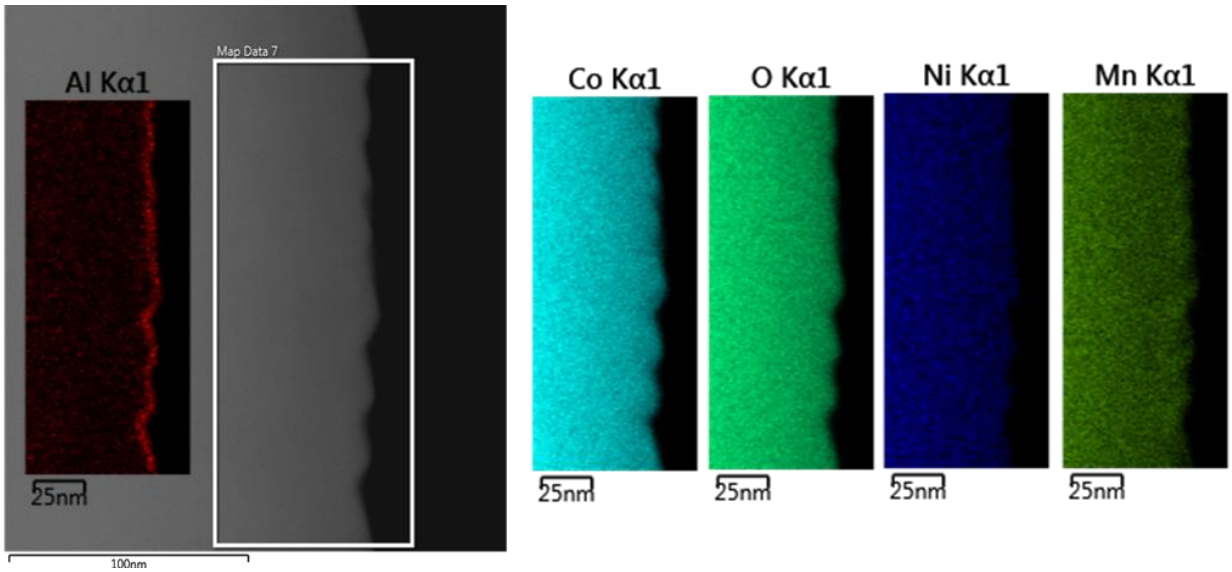

Figure 66. (a) HAADF image of the surface of a Ni-600 °C electrode coated with Al2O3 via ALD, with the Al EDS map shown as inset. (b) EDS map data for Co, O, Ni, and Mn.

Atomic Resolution Analysis of the Dispersion of W Dopant in $LiCoO_2$ Structure

As discussed in Chapter 3.3, introducing dopants in considered as a solution to improve the structural stability of layered oxide cathodes. In this research we utilized atomic resolution STEM analysis to study the atomic arrangement of W-doped $LiCoO_2$. High angle annular dark field imaging (z-contrast imaging technique) that can distinguish between Co and W atoms is utilized in our investigation. The sample is composed of $LiCoO_2$ sample that is ALD coated with AlWF layers and then heat treated to induce the diffusion of W and Al layers into the structure (*Figure 67*).

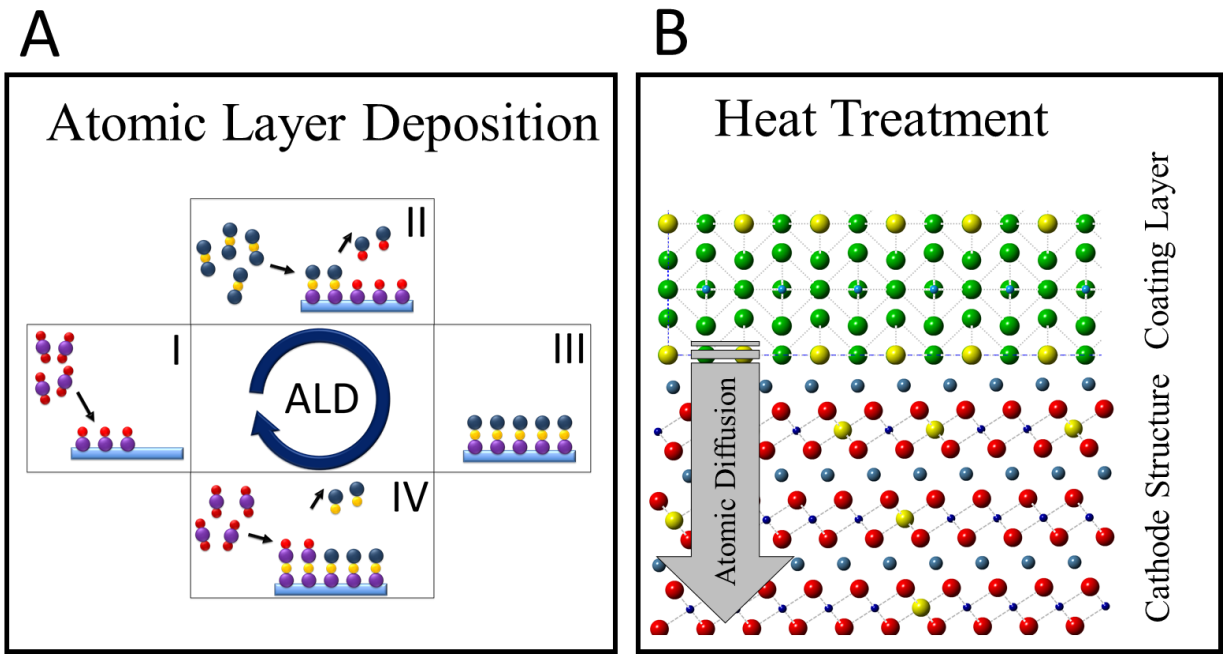

Figure 67. Schematic depiction of ALD Coating and subsequent heat treatment procedure that was utilized to dope the cathode samples. (A) Coating layers of AlWF was deposited through ALD process. (B) The Coating is then heat treated to induce the diffusion of coating elements into the cathode structure.

EDS analysis is then carried out on the particles after the thermal treatment of the ALD coated cathode particles at 550 °C and 750 °C. The results demonstrate that by heat treating the sample

at 550 °C a large concentration of Al and W layers remain on the surface of the particle and W and Al signals at the bulk area remain very weak (*Figure 68A*). However, the sample that is exposed to the heat treatment process at 750 °C demonstrates a different structure. In this sample, the coating is decomposed, and the W atoms have diffused into the substrate structure while Al is still highly concentrated on the substrate (*Figure 68B*).

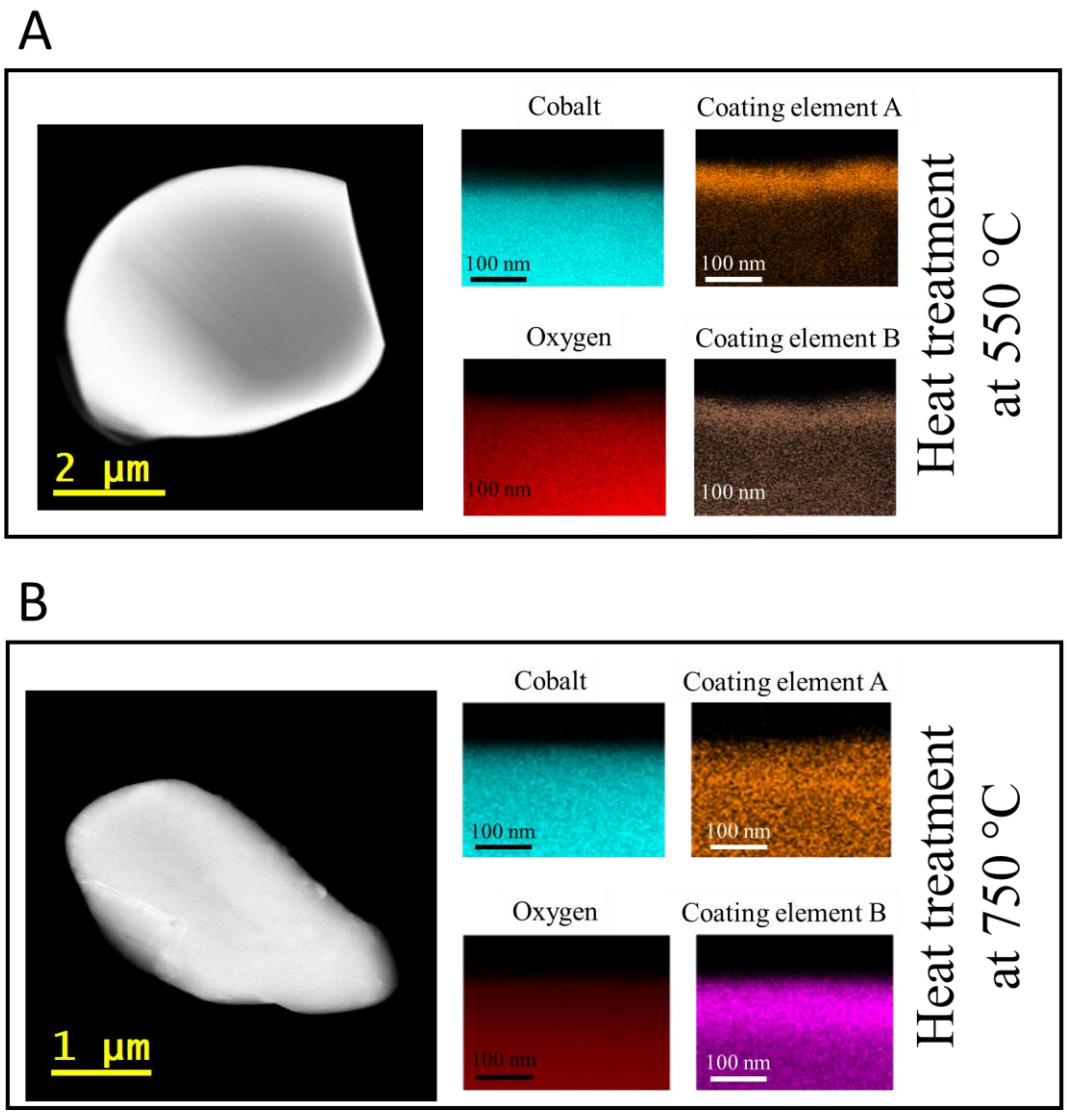

Figure 68. Morphological HAADF images and EDS analysis from the AlWF@LCO sample that is heat treated at (A) 550 °C and (B) at 750 °C.

This sample further investigated with atomic resolution imaging. Interestingly, our results indicate that, W atoms prefer to occupy distinct Co layers and form $LiWO_2$ slabs inside the $LiCoO_2$ matrix. As shown in *Figure 69A* the mid-magnification HAADF demonstrates bright-contrast line within the structure of $LiCoO_2$. HAADF imaging mode which is known as a z-contrast imaging technique, can distinguish between the elements with large variation in atomic number. In this image the bright line corresponds to the heavy W atoms while the matrix has a lower contrast corresponding to Co. Image *Figure 69B* demonstrates atomic resolution image where the distinct W slabs are resolved. Intensity profile as well as the EDS line scan are shown in the inset of this image which confirms the formation of W rich slabs within the structure of $LiCoO_2$ and depicts the heterogenous dispersion of the W dopants.

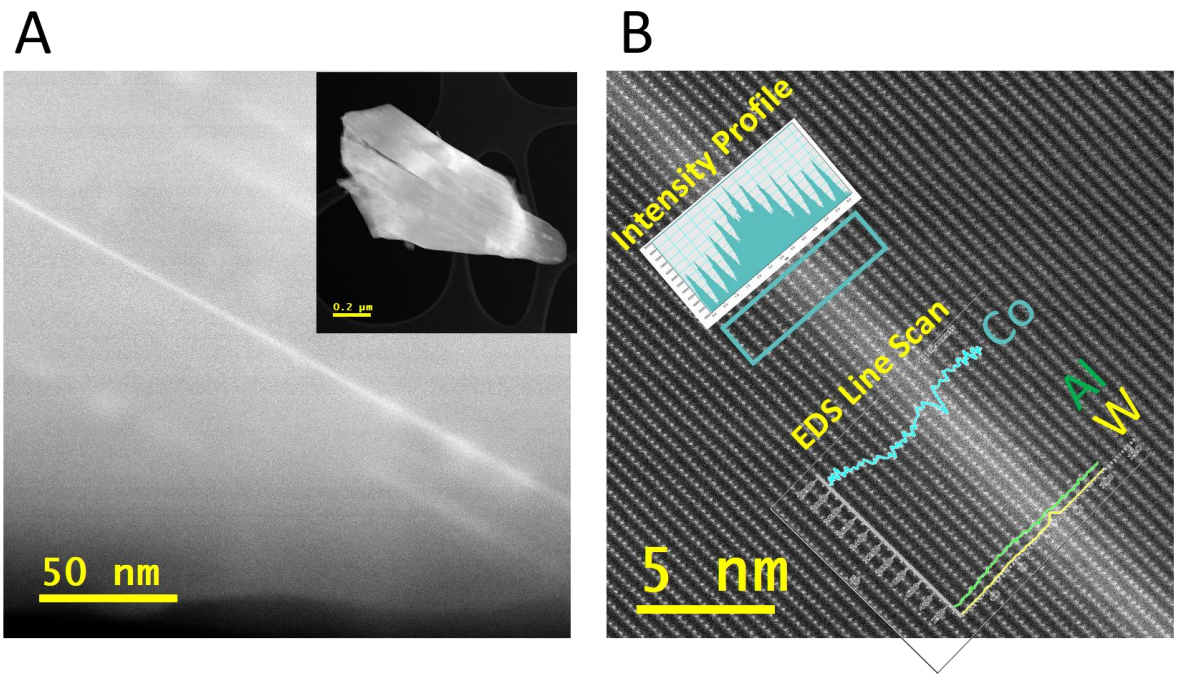

Figure 69. (A) Mid-magnification HAADF image from the AlWF@LCO sample heat treated at 750 °C. The bright line corresponds to local increase in the average atomic number. (B) atomic resolution HAADF image with intensity profile and EDS line maps as insets demonstrating the formation of WO_2 slabs within the structure of LCO in this structure.

In summary, we investigated the atomic diffusion and arrangement of Al and W elements in the Li-ion battery cathodes structure. Firstly, we observed that preferred diffusion of W into the substrate structure upon heat treating of a coating composed of two metallic ions. Interestingly, based on the HAADF z-contrast imaging the diffused ion is not dispersed homogenously in the crystal structure and forms distinct slabs within the layered matrix of $LiCoO_2$. These preliminary results demonstrate the importance of atomic resolution investigation of doped cathode particles to ensure the homogenous distribution of the dopants to improve the effectiveness of such structural modification approaches.

Investigation of the Effect of Composition on the Cationic Migration of NMC Cathodes
(Used as a Part of the Article: Zhu, J.; Sharifi-Asl, S.; Hong j.; Iddir, H.; Croy, J.; Shahbazian-Yassar, R.; Chen, G. Atomic-Level Understanding of Surface Reconstruction Based on Li[NixMnyCo1-x-y]O2 Single-Crystal Studies, Under Submission)

One of the most bewildering issues in the research of Li-ion battery cathode materials is the effect of chemical composition on the structural stability and electrochemical properties of such materials. As discussed in Chapter 3.2, it is known that there is a considerable difference in the electrochemical activity and atomic stability of different constituting transition metals in the layered oxide cathodes. For instance, it is suggested that Ni and Co are the redox active centers in the NMC cathodes, while Mn ions do not participate in the redox reaction and contribute to the structural stability of the material during cycling. So, when the NMC cathodes are charged, oxidation of Ni^{2+} to Ni^{4+} initially compensates for the charge process, followed by Co^{3+} to Co^{4+} redox reaction. It is known that Mn^{4+} cations do not participate in the charge compensation process and retain their coordination and only contribute to the stability of the cathodes structure. Therefore, composition tuning of NMC cathode materials and its effect on the degradation mechanism of the cathode particles have been studied by various methods including electron

microscopy. In this research, we have contributed to the atomic scale analysis of the single particle $Li(Ni_xMn_yCo_z)O_2$ cathodes with two different compositions namely x:y:z= 3:3:3 & x:y:z= 6:2:2.

Figure 70 demonstrates the chemical composition analysis carried out using EDS mapping on both samples that confirms the chemical composition of the 622 and 333 samples respectively.

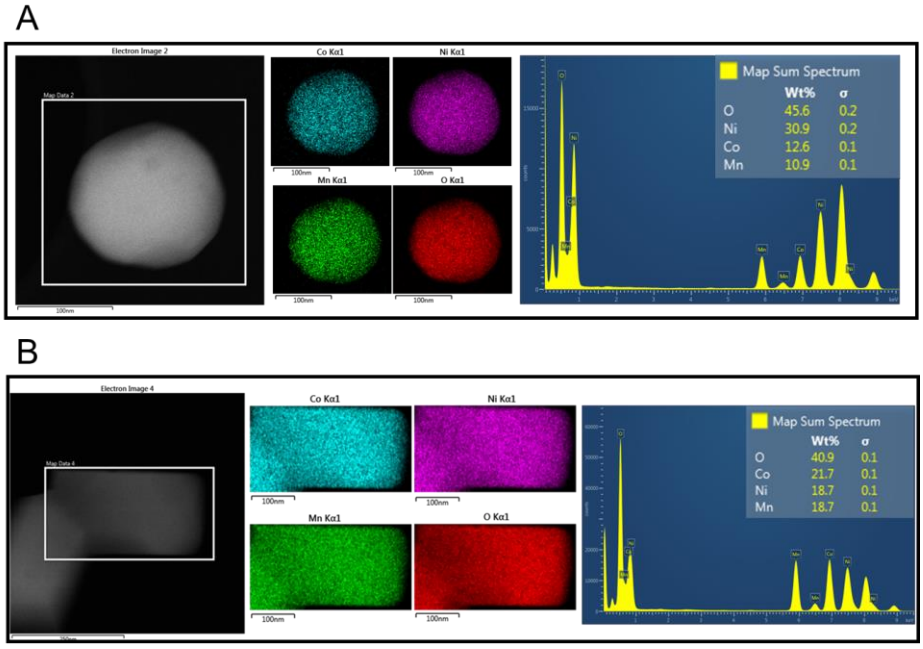

Figure 70. EDS maps illustrating the homogeneity and chemical composition of (A) 622 and (B) 333 particles.

Next, morphological and atomic resolution imaging was carried out to confirm the hexagonal R3m crystal structure in both samples. As demonstrated in *Figure 71* the considerable change in the chemical composition of the sample does not induce any change in the particle morphology and the atomic structure. Both samples contain ~1nm surface reconstruction layer in the pristine, uncycled condition.

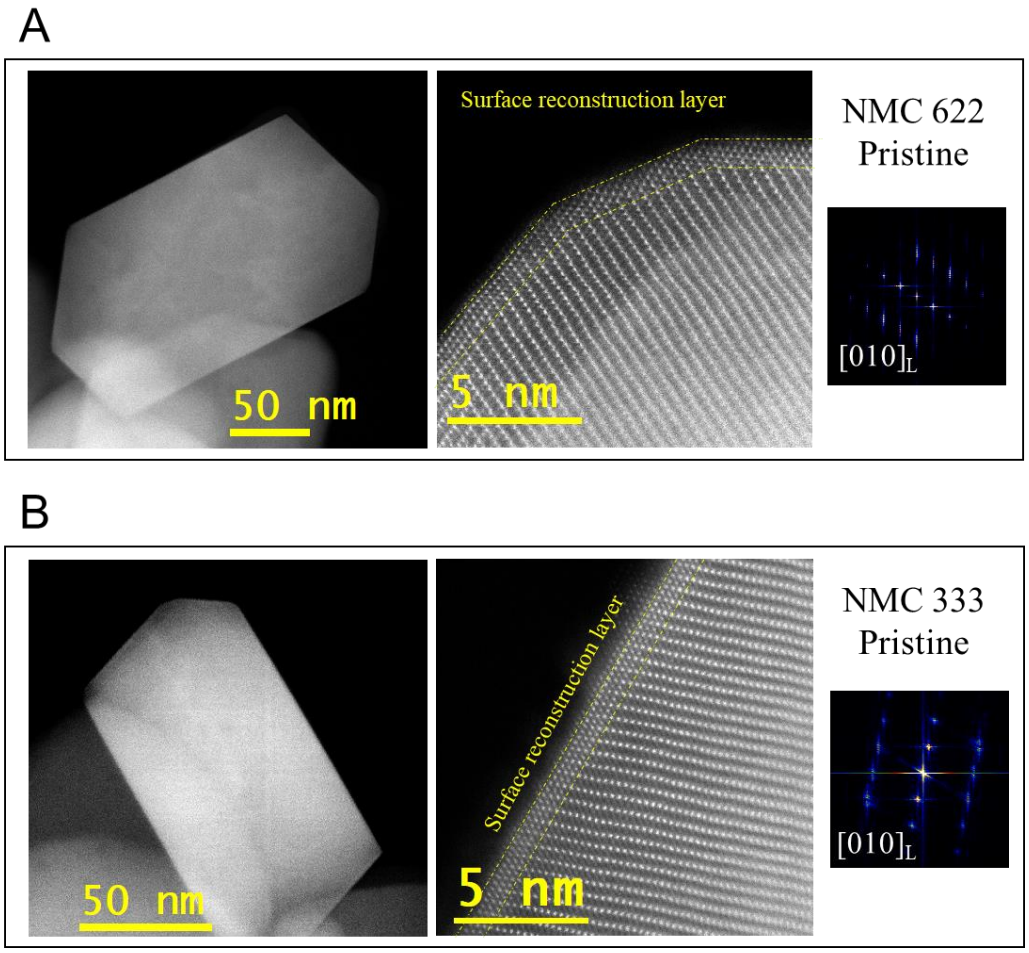

Figure 71. Morphological and atomic resolution STEM images from the (A) uncycled 622 and (B) uncycled 333 NMC samples. Despite the large variation in the composition, sample morphology, the atomic structure and the thickness of the surface reconstruction layer has remained unchanged in both samples.

The electrochemically cycled samples were also investigated through atomic scale imaging. The results demonstrated the 333 sample has a superior structural stability compared to the 622 sample. *Figure 72* demonstrates atomic resolution HAADF images from (*A*) 622 and (*B*) 333 samples after electrochemical cycling. It can be clearly observed that the thickness of the surface reconstruction layer has increased from ~ 1nm to ~1.5 nm and 3.5 nm for the 333 and 622 samples respectively.

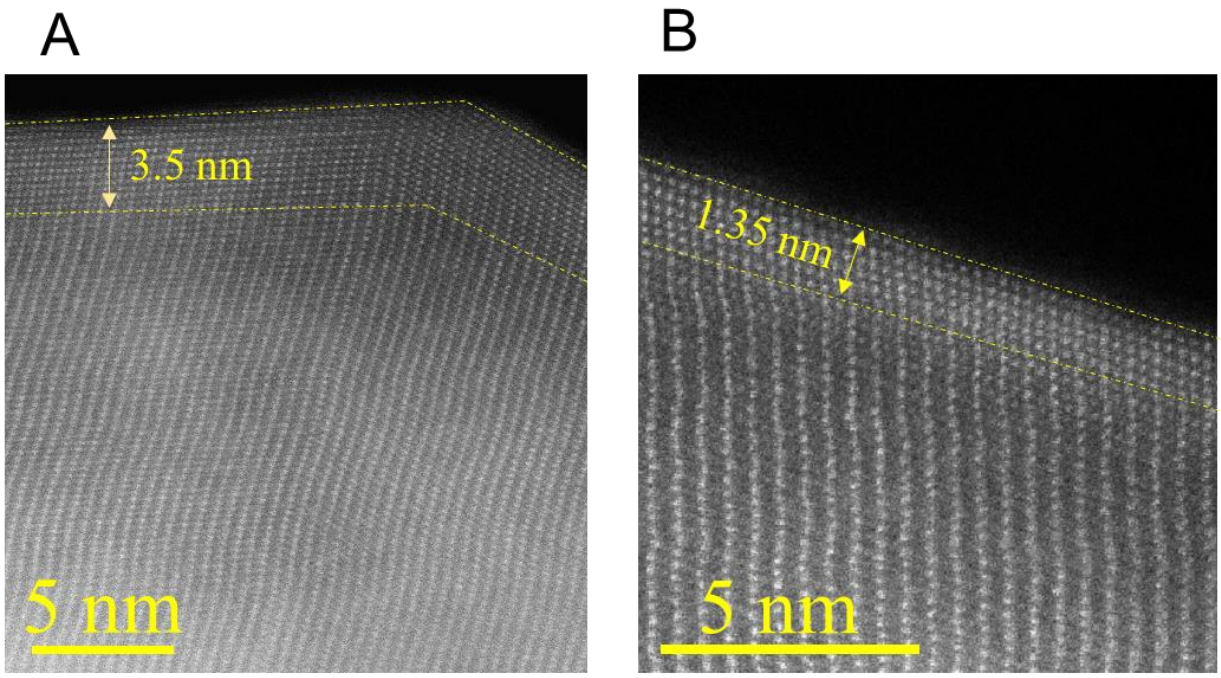

Figure 72. Atomic resolution HAADF images from the surface structure of (A) cycled 622 and (B) cycled 333 NMC particles. The results demonstrate that the surface reconstruction layer thickness has increased from ~ 1nm to ~1.5 nm and 3.5 nm for the 333 and 622 samples respectively.

In addition, atomic resolution imaging was carried out in the bulk areas of the samples. The results demonstrate that the extent of cationic migration (i.e. formation of point defects as a result of migration of transition metals to Li octahedral sites) is significantly larger in 622 samples. From HAADF and ABF images shown in *Figure 73A* it can be observed that there are many bright atoms located in the Li sites (indicated with the arrows) in the 622 sample. On the other hand, there is no indication of transition metal migration into the Li octahedral sites in the 333 sample as can be observed in the *Figure 73B*.

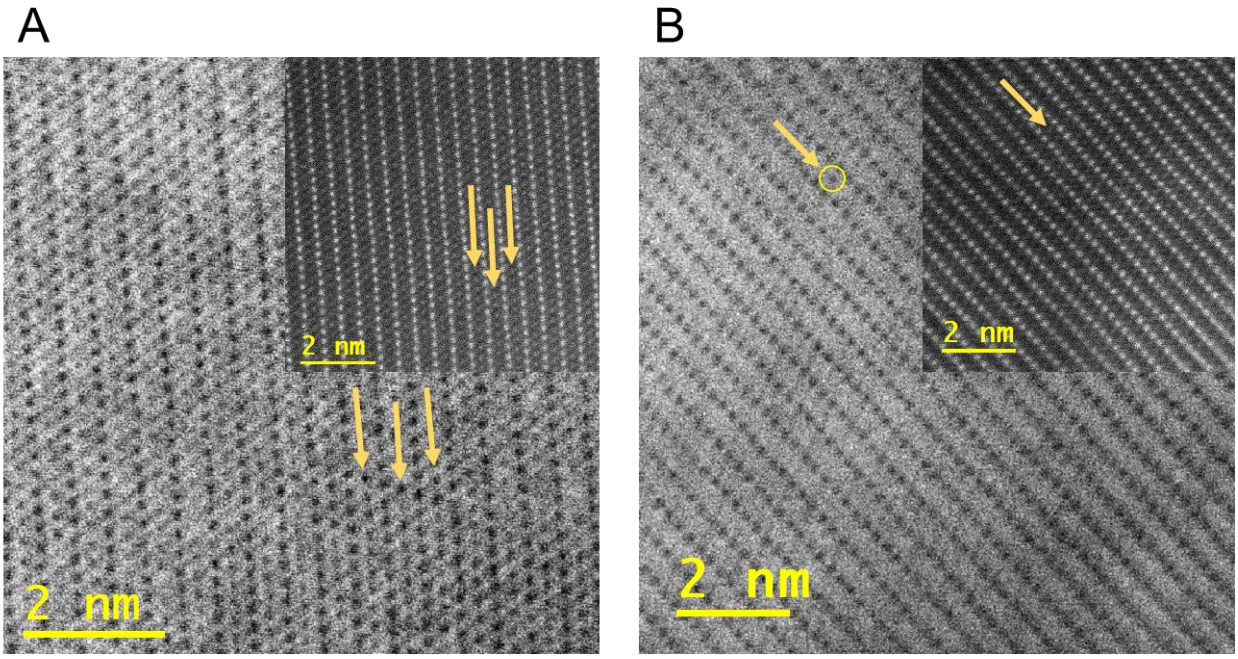

Figure 73. Atomic resolution ABF images with the corresponding HAADF inset images from the bulk structure of (A) cycled 622 and (B) cycled 333 NMC particles. As can be clearly observed, the extent of cationic migration is considerably larger in the 622 sample. The arrows indicated the Li octahedral sites that are highly occupied by the transition metals based on the high contrast resolved in the ABF images.

Investigation of the Effect of Electrolyte on the NMC Degradation Mechanism

(Used as a Part of the Following Article: Tornheim, A.; Sharifi-asl, S.; Garcia, J. C.; Bareño, J.; Iddir, H. Effect of Electrolyte Composition on Rock Salt Surface Degradation in NMC Cathodes during High-Voltage Potentiostatic Holds. Nano Energy 2019, 55 (August 2018), 216–225. Reproduced with permission[469]. Copyright 2019, Elsevier.)

Surface degradation of Li-ion battery materials that is known to be a significant contributor to cell degradation, is controlled and influenced by many parameters including electrochemical cycling conditions, particle morphology and composition and the other cell components such as the liquid electrolyte. In this research, the effect of electrolyte composition on the surface degradation of cathode materials were investigated. We have contributed to this research by atomic resolution STEM analysis as well as EELS spectroscopy to analyze the surface structure of NM cathodes ($Li(Ni_xMn_yCo_z)O2$ with the composition of x:y:z= 5:3:2) that were cycled with three different electrolytes. The three electrolytes used in this study were 1) baseline electrolyte (1.2M LiPF6 in 3:7 EC:EMC) referred to as Gen2. 2) the baseline Gen2 electrolyte with 10wt% tris(2,2,2-trifluoroethyl)phosphite (TTFP), an additive typically used with high voltage cathodes; and 3) a high voltage fluorinated electrolyte called FE-3 (1MLiPF6 in 3:7 DFEC and carbonate HFDEC). Cells were exposed to potentiostatic holds at 4.6 V (vs Li/Li^+) for 60 hrs to intentionally induce rapid degradation. Then STEM/EELS analysis was carried out on the cycled samples to analyze and compare the effect of the electrolyte composition.

Figure 74, *Figure 75* and *Figure 76* demonstrate STEM/EELS results from the near-surface areas of NMC particles cycled with the baseline Gen2, baseline Gen2 + 10% TTFP and the fluorinated FE-3 electrolyte, respectively. In each figure, atomic resolution images illustrate areas with local rock-salt ($Fm\bar{3}m$) and spinel ($Fd\bar{3}m$) crystal structures together with the original layered ($R\bar{3}m$) structure.

Figure 74 demonstrate the results obtained from the sample cycled with the baseline Gen2 electrolyte. Surface and sub-surface areas in the particle shown in *Figure 74A* are imaged. The

atomic structure of the surface areas (*Figure 74B*) correspond to the spinel phase, while the layered structure is retained based on the atomic resolution image shown in panel C. EELS line scan perpendicular to particle surface is collected as illustrated in panel A. The spectra are plotted as a function of distance to particle surface. Variation in the oxygen fine structure can be clearly observed, which correlates with the valence state of transition metals and is associated with the structural degradation as discussed in Chapter 4. The EELS quantification is carried out based on the oxygen fine structure and is presented below.

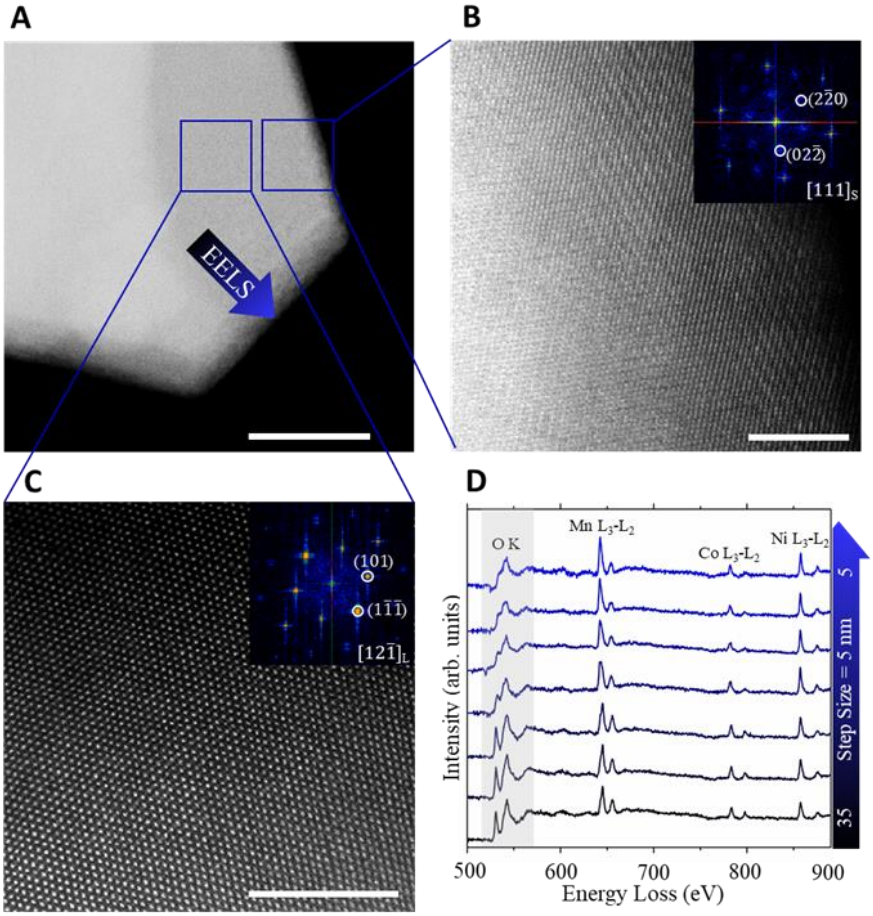

Figure 74. HAADF-STEM micrographs (a-c) and EELS scan spectra (d) from an NMC particle cycled in Gen2 electrolyte, without additives. (a) Low magnification image of the particle, 50 nm scale bar. (b) Atomic resolution image of the surface region indicated in (a), 5 nm scale bar. (c)

Atomic resolution image of the deeper region indicated in (a), 5 nm scale bar. (d) Spectra from EELS line scan (40 nm range, 5 nm steps) on the area indicated in (a).

Figure 75 shows the results obtained from the sample cycled with the baseline Gen2+10% TTFP electrolyte. The regions close to the surface of the particles shown in *Figure 75A* shows a clear stained contrast that is absent in the bulk of the particle, which is due to local changes of density, resulting from oxygen release and structural degradation. The higher magnification image (5 nm scale bar) of the surface area shown in *Figure 75B* shows a hexagonal atomic structure that can be indexed either as the $\{20\bar{2}\}_{RS}$ spots expected in the $[111]_{RS}$ Z.A., the $\{1\bar{2}0\}_{L}$ spots of the $[001]_{L}$ Z.A., or the $\{40\bar{4}\}_{S}$ spots of the $[111]_{S}$ Z.A.. The spots in the inner hexagon can only be indexed as the $\{20\bar{2}\}_{S}$ spots of the spinel structure; or ½ spinel super reflections on the L or RS parent structures. The outer hexagon spots arise from the overall hexagonal arrangement of atomic columns described above. Although the phase identification of the degraded particle is complicated due to structural similarities, EELS analysis that contains information about the valence state of the transition metals can be used as a more reliable technique to better gauge the degradation extent of the sample structure. EELS line scan was collected under the same condition as with the previous sample and the results are demonstrated in the panel D.

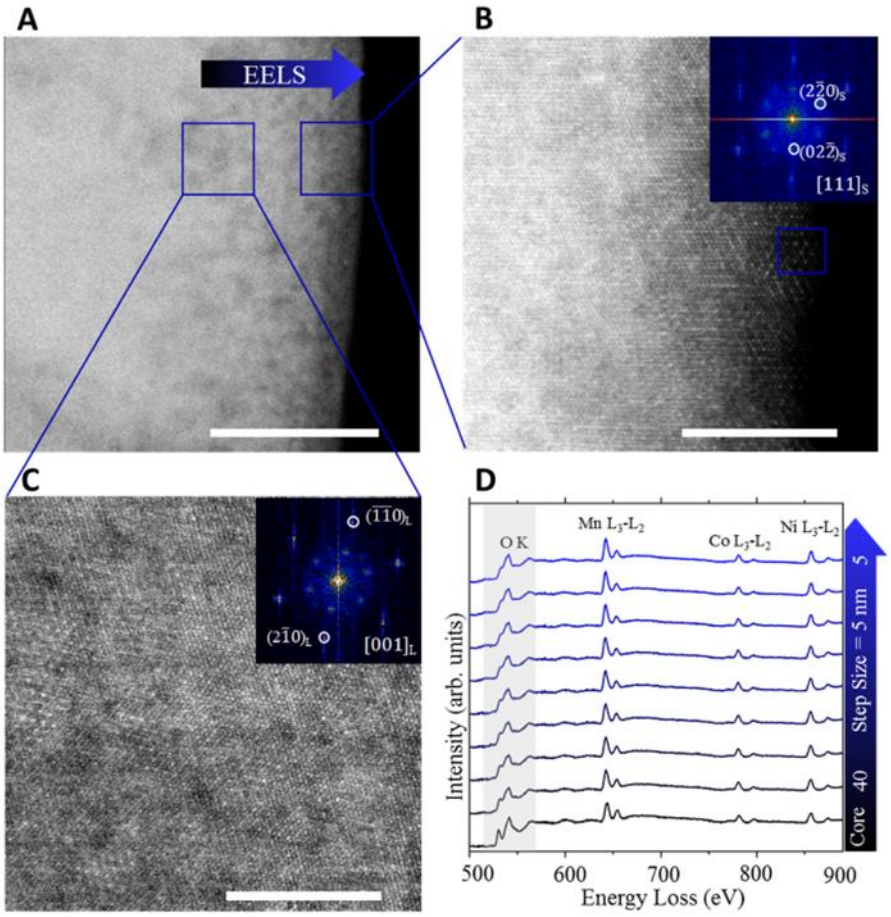

Figure 75. Figure 5. HAADF-STEM micrographs (a-c) and EELS scan spectra (d) from an NMC particle cycled in Gen2+TTFP electrolyte. (a) Low magnification image of the particle, 50 nm scale bar. (b) Atomic resolution image of the surface region, 5 nm scale bar. (c) Atomic resolution image of the deeper region indicated in (a), 5 nm scale bar. (d) Spectra from EELS line scan (40 nm range, 5 nm steps) on the area indicated in (a).

Figure 76 shows the STEM/EELS results from the NMC sample cycled in the FE-3 electrolyte. *Figure 76A* and *Figure 76B* show atomic resolution images from the surface and subsurface areas from a particle that can be indexed as the $[12\bar{1}]_L$ Z.A. The FFT inset in Figure 7.5.3B clearly shows $\{\bar{1}11\}_S$ that is present together with the layered structure. The top left corner of the *Figure 76B* shows a reconstructed color-coded image for a clear demonstration of dual spinel/hexagonal structure of the sample. The details of color-coded image reconstruction are

described in Chapter 4. *Figure 76C* shows the atomic structure of another particle from the side view, along the $[110]_L$ Z.A.. The alternating sequence of TM and Li planes can be clearly observed (labeled "Li^+ Transport channels" in the image). A surface area of ~5 nm thickness is labeled as "Cation Disordered Area" in the image, showing the presence of the migrated TM atoms to Li sites. The top-right FFT inset that is obtained from the whole field of view, corresponds to the hexagonal layered structure. However, the bottom-right FFT inset, obtained from the "Cation Disordered Area", lacks any superspots characteristic of either a layered or spinel structure, and can be indexed as a $[\bar{1}10]_{RS}$ Z.A.. *Figure 76D* presents the EELS spectra, acquired as a line scan perpendicular to particle surface. Compared to the EELS spectra from the previous samples, the O-K edge fine structure undergoes smaller changes and the subtle changes are more confined to the surface. *Figure 77*, which plots the difference in energy ΔE between the O-K pre- and main peaks as a function of distance to the surface for the particles cycled in the three electrolytes of interest.

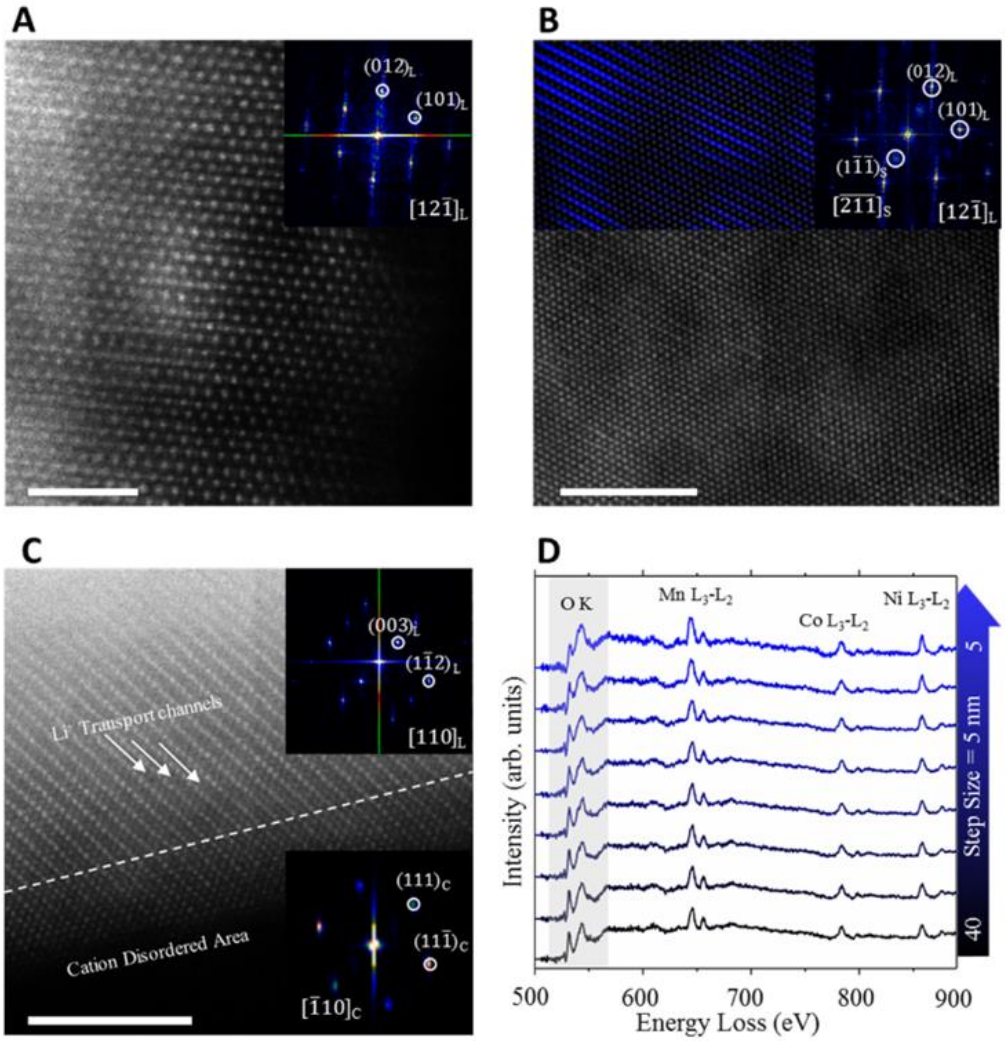

Figure 76. HAADF-STEM micrographs (a-c) and EELS scan spectra (d) from NMC particles cycled in FE-3 electrolyte. (a) Atomic resolution image of a surface region, 2 nm scale bar. (b) Atomic resolution image of region adjacent to the surface, 5 nm scale bar. (c) Atomic resolution, side view of a surface region, 5 nm scale bar. (d) Spectra from EELS line scan (40 nm range, 5 nm steps) approaching the surface of the particle. See text for inset details.

Figure 77 demonstrates the EELS quantification based on the O-K edge. The O-K edges consist of a pre-peak and a main peak, with the pre-peak appearing at lower energy loss than the main peak. Both pre- and main-peaks are due to transitions between O 1s and two kinds of O 2p states; O 2p states hybridized with metal 3d states for the pre peak and O 2p states hybridized with metal 4sp states for the main peak. Correspondingly, metal L edges show two peaks, L3 and L2,

corresponding to transitions from $2p_{3/2}$ and $2p_{1/2}$ metal orbitals, respectively, to metal 3d orbitals. While all these edges are useful to determine oxidation state of the transition metals, we focus our analysis on changes to the O-K edge. Because the the EELS spectrum from multi-metal NMC cathodes are complex, quantification of the changes in the valence state of transition metals based on the Mn, Ni and Co L edges were not persuaded. In particular, we used the energy difference between the pre- and main-peaks of the O-K edge, determined from fitting a Gaussian to each peak, as an indication of the local oxidation state of the metals.

Accordingly, the ΔE values between the pre- and main-peaks of the O-K edge for the particles cycled in Gen2 and FE-3 electrolytes is $\simeq$ 11.5 eV at the core regions, which are maintained up to a distance of ~25 nm from the surface. At this point, the ΔE value of the Gen2-cycled sample reduces to $\simeq$ 7 eV at 10 nm below the surface, and retains this value up to the surface. However, the FE-3 cycled sample shows a more stable electronic structure over the same depth range, and the ΔE value decreases only to $\simeq$ 10.5 eV. However, the Gen2 + TTFP cycled particle has a lower $\Delta E \simeq$ 10.5 eV at the core of the particle that reduces rapidly to $\simeq$ 7 eV at 25 nm depth all the way to the surface. As can be seen in *Figure 77*, this low ΔE region is greatest and extends deeper in the sample cycled in Gen2 + 10% TTFP electrolyte than in the sample cycled in Gen2 electrolyte. Detailed discussions about the mechanism of various rate of degradation of particles cycled with different electrolytes that was identified through STEM/EELS analysis, can be found in this publication[469].

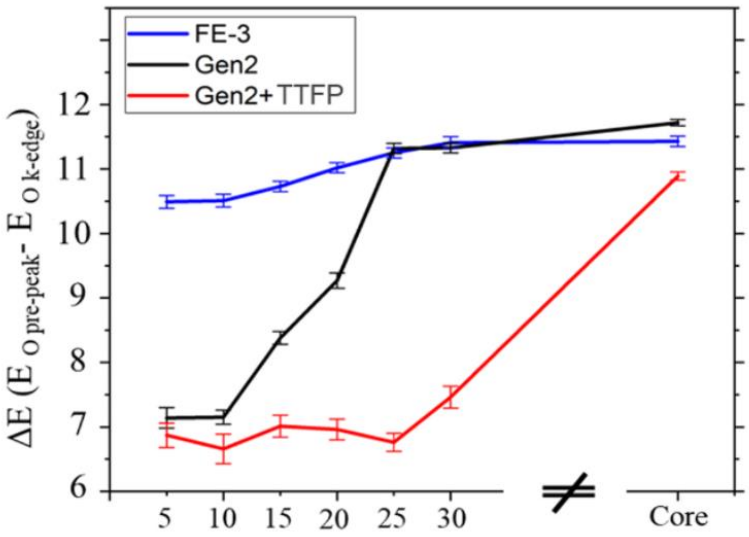

Figure 77. EELS analysis results from NMC samples cycled with various electrolytes. Energy difference between the O-K edge and its pre-peak is plotted as a function of distance from the surface.

Supplemental Movies:

Supplemental Movie 1: Ronchigram mode TEM recording from a graphene-coated $Li_{0.5}CoO_2$ particle captured during an in-situ heating experiment at 300°C, which illustrates the effect of graphene-coating on the structural stability of the cathode.

Copyright Permissions

Title: Challenges for Rechargeable Li Batteries
Author: John B. Goodenough, Youngsik Kim
Publication: Chemistry of Materials
Publisher: American Chemical Society
Date: Feb 1, 2010
Copyright © 2010, American Chemical Society

Logged in as:
Soroosh Sharifi-Asl
UIC
Account #:
3001171421
LOGOUT

PERMISSION/LICENSE IS GRANTED FOR YOUR ORDER AT NO CHARGE

This type of permission/license, instead of the standard Terms & Conditions, is sent to you because no fee is being charged for your order. Please note the following:

- Permission is granted for your request in both print and electronic formats, and translations.
- If figures and/or tables were requested, they may be adapted or used in part.
- Please print this page for your records and send a copy of it to your publisher/graduate school.
- Appropriate credit for the requested material should be given as follows: "Reprinted (adapted) with permission from (COMPLETE REFERENCE CITATION). Copyright (YEAR) American Chemical Society." Insert appropriate information in place of the capitalized words.
- One-time permission is granted only for the use specified in your request. No additional uses are granted (such as derivative works or other editions). For any other uses, please submit a new request.

If credit is given to another source for the material you requested, permission must be obtained from that source.

BACK CLOSE WINDOW

JOHN WILEY AND SONS LICENSE TERMS AND CONDITIONS

Oct 21, 2019

This Agreement between UIC -- Soroosh Sharifi-Asl ("You") and John Wiley and Sons ("John Wiley and Sons") consists of your license details and the terms and conditions provided by John Wiley and Sons and Copyright Clearance Center.

License Number	4693861113166
License date	Oct 21, 2019
Licensed Content Publisher	John Wiley and Sons
Licensed Content Publication	Advanced Energy Materials
Licensed Content Title	Narrowing the Gap between Theoretical and Practical Capacities in Li-Ion Layered Oxide Cathode Materials
Licensed Content Author	Anton Van der Ven, Y. Shirley Meng, M. Stanley Whittingham, et al
Licensed Content Date	Jul 4, 2017
Licensed Content Volume	7
Licensed Content Issue	20
Licensed Content Pages	33
Type of use	Dissertation/Thesis
Requestor type	University/Academic
Format	Electronic
Portion	Figure/table
Number of figures/tables	3
Original Wiley figure/table number(s)	Figure 2, Figure 5, Figure 6
Will you be translating?	No
Title of your thesis / dissertation	Atomic Scale Study of Oxygen Loss and Structural Degradation in Oxide Cathodes and a Mitigation strategy
Expected completion date	Dec 2019
Expected size (number of pages)	200
Requestor Location	UIC 847 W Taylor Stree SEL-E 3295 CHICAGO, IL 60607 United States Attn: UIC
Publisher Tax ID	EU826007151
Total	0.00 USD
Terms and Conditions	

TERMS AND CONDITIONS

This copyrighted material is owned by or exclusively licensed to John Wiley & Sons, Inc. or one of its group companies (each a"Wiley Company") or handled on behalf of a society with

JOHN WILEY AND SONS LICENSE TERMS AND CONDITIONS

Oct 21, 2019

This Agreement between UIC -- Soroosh Sharifi-Asl ("You") and John Wiley and Sons ("John Wiley and Sons") consists of your license details and the terms and conditions provided by John Wiley and Sons and Copyright Clearance Center.

License Number	4693871067468
License date	Oct 21, 2019
Licensed Content Publisher	John Wiley and Sons
Licensed Content Publication	Angewandte Chemie International Edition
Licensed Content Title	Direct Atomic-Resolution Observation of Two Phases in the Li1.2Mn0.567Ni0.166Co0.067O2 Cathode Material for Lithium-Ion Batteries
Licensed Content Author	Haijun Yu, Ryo Ishikawa, Yeong-Gi So, et al
Licensed Content Date	Apr 24, 2013
Licensed Content Volume	52
Licensed Content Issue	23
Licensed Content Pages	5
Type of use	Dissertation/Thesis
Requestor type	University/Academic
Format	Print and electronic
Portion	Figure/table
Number of figures/tables	1
Original Wiley figure/table number(s)	Figure 3
Will you be translating?	No
Title of your thesis / dissertation	Atomic Scale Study of Oxygen Loss and Structural Degradation in Oxide Cathodes and a Mitigation strategy
Expected completion date	Dec 2019
Expected size (number of pages)	200
Requestor Location	UIC 847 W Taylor Stree SEL-E 3295 CHICAGO, IL 60607 United States Attn: UIC
Publisher Tax ID	EU826007151
Total	0.00 USD
Terms and Conditions	

TERMS AND CONDITIONS

This copyrighted material is owned by or exclusively licensed to John Wiley & Sons, Inc. or one of its group companies (each a"Wiley Company") or handled on behalf of a society with

SPRINGER NATURE LICENSE TERMS AND CONDITIONS

Oct 24, 2019

This Agreement between UIC -- Soroosh Sharifi-Asl ("You") and Springer Nature ("Springer Nature") consists of your license details and the terms and conditions provided by Springer Nature and Copyright Clearance Center.

License Number	4695440787049
License date	Oct 24, 2019
Licensed Content Publisher	Springer Nature
Licensed Content Publication	Springer eBook
Licensed Content Title	The Instrument
Licensed Content Author	David B. Williams, C. Barry Carter
Licensed Content Date	Jan 1, 2009
Type of Use	Thesis/Dissertation
Requestor type	academic/university or research institute
Format	print and electronic
Portion	figures/tables/illustrations
Number of figures/tables/illustrations	1
Will you be translating?	no
Circulation/distribution	1000 - 1999
Author of this Springer Nature content	no
Title	Atomic Scale Study of Oxygen Loss and Structural Degradation in Oxide Cathodes and a Mitigation strategy
Institution name	n/a
Expected presentation date	Dec 2019
Portions	Figure 9.23
Requestor Location	UIC 847 W Taylor Stree SEL-E 3295 CHICAGO, IL 60607 United States Attn: UIC
Total	0.00 USD
Terms and Conditions	

Springer Nature Customer Service Centre GmbH Terms and Conditions

This agreement sets out the terms and conditions of the licence (the **Licence**) between you and **Springer Nature Customer Service Centre GmbH** (the **Licensor**). By clicking 'accept' and completing the transaction for the material (**Licensed Material**), you also confirm your acceptance of these terms and conditions.

JOHN WILEY AND SONS LICENSE TERMS AND CONDITIONS

Oct 24, 2019

This Agreement between UIC -- Soroosh Sharifi-Asl ("You") and John Wiley and Sons ("John Wiley and Sons") consists of your license details and the terms and conditions provided by John Wiley and Sons and Copyright Clearance Center.

License Number	4695441408901
License date	Oct 24, 2019
Licensed Content Publisher	John Wiley and Sons
Licensed Content Publication	Advanced Energy Materials
Licensed Content Title	Oxygen Release Degradation in Li-Ion Battery Cathode Materials: Mechanisms and Mitigating Approaches
Licensed Content Author	Soroosh Sharifi-Asl, Jun Lu, Khalil Amine, et al
Licensed Content Date	Apr 29, 2019
Licensed Content Volume	9
Licensed Content Issue	22
Licensed Content Pages	19
Type of use	Dissertation/Thesis
Requestor type	Author of this Wiley article
Format	Print and electronic
Portion	Full article
Will you be translating?	No
Title of your thesis / dissertation	Atomic Scale Study of Oxygen Loss and Structural Degradation in Oxide Cathodes and a Mitigation strategy
Expected completion date	Dec 2019
Expected size (number of pages)	200
Requestor Location	UIC 847 W Taylor Stree SEL-E 3295 CHICAGO, IL 60607 United States Attn: UIC
Publisher Tax ID	EU826007151
Total	0.00 USD
Terms and Conditions	

TERMS AND CONDITIONS

This copyrighted material is owned by or exclusively licensed to John Wiley & Sons, Inc. or one of its group companies (each a"Wiley Company") or handled on behalf of a society with which a Wiley Company has exclusive publishing rights in relation to a particular work (collectively "WILEY"). By clicking "accept" in connection with completing this licensing transaction, you agree that the following terms and conditions apply to this transaction (along with the billing and payment terms and conditions established by the Copyright

JOHN WILEY AND SONS LICENSE TERMS AND CONDITIONS

Oct 24, 2019

This Agreement between UIC -- Soroosh Sharifi-Asl ("You") and John Wiley and Sons ("John Wiley and Sons") consists of your license details and the terms and conditions provided by John Wiley and Sons and Copyright Clearance Center.

License Number	4695460389173
License date	Oct 24, 2019
Licensed Content Publisher	John Wiley and Sons
Licensed Content Publication	Advanced Functional Materials
Licensed Content Title	Combining In Situ Synchrotron X-Ray Diffraction and Absorption Techniques with Transmission Electron Microscopy to Study the Origin of Thermal Instability in Overcharged Cathode Materials for Lithium-Ion Batteries
Licensed Content Author	Xiao-Qing Yang, Kyung-Yoon Chung, Yimei Zhu, et al
Licensed Content Date	Jun 19, 2012
Licensed Content Volume	23
Licensed Content Issue	8
Licensed Content Pages	17
Type of use	Dissertation/Thesis
Requestor type	University/Academic
Format	Print and electronic
Portion	Figure/table
Number of figures/tables	1
Original Wiley figure/table number(s)	Figure 2
Will you be translating?	No
Title of your thesis / dissertation	Atomic Scale Study of Oxygen Loss and Structural Degradation in Oxide Cathodes and a Mitigation strategy
Expected completion date	Dec 2019
Expected size (number of pages)	200
Requestor Location	UIC 847 W Taylor Stree SEL-E 3295 CHICAGO, IL 60607 United States Attn: UIC
Publisher Tax ID	EU826007151
Total	0.00 USD
Terms and Conditions	

TERMS AND CONDITIONS

This is not an invoice. Please go to manage account to access your order history and invoices.

CUSTOMER INFORMATION

Billing Address

Soroosh Sharifi-Asl
UIC
847 W Taylor Stree
SEL-E 3295
Chicago, IL 60607
United States

+1 (312) 483-0215
sshari25@uic.edu

Customer Location

Soroosh Sharifi-Asl
UIC
847 W Taylor Stree
SEL-E 3295
Chicago, IL 60607
United States

PO Number (optional)

N/A

Payment options

Invoice

PENDING ORDER CONFIRMATION

Total Due: 0.00 USD

Confirmation Number: Pending

Order Date: 24-Oct-2019

1. Journal of the Electrochemical Society

0.00 USD

Order license ID	Pending
ISSN	1945-7111
Type of Use	Republish in a thesis/dissertation
Publisher	Electrochemical Society
Portion	Image/photo/illustration

LICENSED CONTENT

Publication Title	Journal of the Electrochemical Society	Country	United States of America
Author/Editor	Electrochemical Society.	Rightsholder	Electrochemical Society, Inc.
Date	12/31/1947	Publication Type	e-Journal

Language	English	URL	http://www.scitation.org/jES

REQUEST DETAILS

Portion Type	Image/photo/illustration	Distribution	Worldwide
Number of images / photos / illustrations	1	Translation	Original language of publication
Format (select all that apply)	Print, Electronic	Copies for the disabled?	No
Who will republish the content?	Academic institution	Minor editing privileges?	No
Duration of Use	Life of current edition	Incidental promotional use?	No
Lifetime Unit Quantity	Up to 19,999	Currency	USD
Rights Requested	Main product		

NEW WORK DETAILS

Title	Atomic Scale Study of Oxygen Loss and Structural Degradation in Oxide Cathodes and a Mitigation strategy	Institution name	UIC
		Expected presentation date	2019-12-15
Instructor name	Soroosh Sharifi-Asl		

ADDITIONAL DETAILS

Order reference number	N/A	The requesting person / organization to appear on the license	Soroosh Sharifi-Asl

REUSE CONTENT DETAILS

Title, description or	Atomic Scale Study of	Title of the	N/A

ELSEVIER LICENSE
TERMS AND CONDITIONS

Oct 24, 2019

This Agreement between UIC -- Soroosh Sharifi-Asl ("You") and Elsevier ("Elsevier") consists of your license details and the terms and conditions provided by Elsevier and Copyright Clearance Center.

License Number	4695470032976
License date	Oct 24, 2019
Licensed Content Publisher	Elsevier
Licensed Content Publication	Journal of Power Sources
Licensed Content Title	Impact of active material surface area on thermal stability of LiCoO2 cathode
Licensed Content Author	Jan Geder,Harry E. Hoster,Andreas Jossen,Jürgen Garche,Denis Y.W. Yu
Licensed Content Date	Jul 1, 2014
Licensed Content Volume	257
Licensed Content Issue	n/a
Licensed Content Pages	7
Start Page	286
End Page	292
Type of Use	reuse in a thesis/dissertation
Intended publisher of new work	other
Portion	figures/tables/illustrations
Number of figures/tables/illustrations	1
Format	both print and electronic
Are you the author of this Elsevier article?	No
Will you be translating?	No
Original figure numbers	Figure 4
Title of your thesis/dissertation	Atomic Scale Study of Oxygen Loss and Structural Degradation in Oxide Cathodes and a Mitigation strategy
Expected completion date	Dec 2019
Estimated size (number of pages)	200
Requestor Location	UIC 847 W Taylor Stree SEL-E 3295 CHICAGO, IL 60607 United States Attn: UIC
Publisher Tax ID	98-0397604

SPRINGER NATURE LICENSE TERMS AND CONDITIONS

Oct 24, 2019

This Agreement between UIC -- Soroosh Sharifi-Asl ("You") and Springer Nature ("Springer Nature") consists of your license details and the terms and conditions provided by Springer Nature and Copyright Clearance Center.

License Number	4695510699901
License date	Oct 24, 2019
Licensed Content Publisher	Springer Nature
Licensed Content Publication	Nature Chemistry
Licensed Content Title	The structural and chemical origin of the oxygen redox activity in layered and cation-disordered Li-excess cathode materials
Licensed Content Author	Dong-Hwa Seo, Jinhyuk Lee, Alexander Urban, Rahul Malik, ShinYoung Kang et al.
Licensed Content Date	May 30, 2016
Licensed Content Volume	8
Licensed Content Issue	7
Type of Use	Thesis/Dissertation
Requestor type	academic/university or research institute
Format	print and electronic
Portion	figures/tables/illustrations
Number of figures/tables/illustrations	1
High-res required	no
Will you be translating?	no
Circulation/distribution	5000 - 9999
Author of this Springer Nature content	no
Title	Atomic Scale Study of Oxygen Loss and Structural Degradation in Oxide Cathodes and a Mitigation strategy
Institution name	n/a
Expected presentation date	Dec 2019
Portions	Figure 4
Requestor Location	UIC 847 W Taylor Stree SEL-E 3295 CHICAGO, IL 60607 United States Attn: UIC
Total	0.00 USD
Terms and Conditions	

SPRINGER NATURE LICENSE TERMS AND CONDITIONS

Oct 24, 2019

This Agreement between UIC -- Soroosh Sharifi-Asl ("You") and Springer Nature ("Springer Nature") consists of your license details and the terms and conditions provided by Springer Nature and Copyright Clearance Center.

License Number	4695520863481
License date	Oct 24, 2019
Licensed Content Publisher	Springer Nature
Licensed Content Publication	Nature Materials
Licensed Content Title	Nanostructured high-energy cathode materials for advanced lithium batteries
Licensed Content Author	Yang-Kook Sun, Zonghai Chen, Hyung-Joo Noh, Dong-Ju Lee, Hun-Gi Jung et al.
Licensed Content Date	Oct 7, 2012
Licensed Content Volume	11
Licensed Content Issue	11
Type of Use	Thesis/Dissertation
Requestor type	academic/university or research institute
Format	print and electronic
Portion	figures/tables/illustrations
Number of figures/tables/illustrations	1
High-res required	no
Will you be translating?	no
Circulation/distribution	5000 - 9999
Author of this Springer Nature content	no
Title	Atomic Scale Study of Oxygen Loss and Structural Degradation in Oxide Cathodes and a Mitigation strategy
Institution name	n/a
Expected presentation date	Dec 2019
Portions	Figure 1
Requestor Location	UIC 847 W Taylor Stree SEL-E 3295 CHICAGO, IL 60607 United States Attn: UIC
Total	0.00 USD
Terms and Conditions	

JOHN WILEY AND SONS LICENSE TERMS AND CONDITIONS

Oct 24, 2019

This Agreement between UIC -- Soroosh Sharifi-Asl ("You") and John Wiley and Sons ("John Wiley and Sons") consists of your license details and the terms and conditions provided by John Wiley and Sons and Copyright Clearance Center.

License Number	4695521051692
License date	Oct 24, 2019
Licensed Content Publisher	John Wiley and Sons
Licensed Content Publication	Advanced Energy Materials
Licensed Content Title	Spinel-Layered Core-Shell Cathode Materials for Li-Ion Batteries
Licensed Content Author	Jaephil Cho, Taeeun Hong, Yongseok Lee, et al
Licensed Content Date	Jul 19, 2011
Licensed Content Volume	1
Licensed Content Issue	5
Licensed Content Pages	8
Type of use	Dissertation/Thesis
Requestor type	University/Academic
Format	Print and electronic
Portion	Figure/table
Number of figures/tables	1
Original Wiley figure/table number(s)	Figure 1
Will you be translating?	No
Title of your thesis / dissertation	Atomic Scale Study of Oxygen Loss and Structural Degradation in Oxide Cathodes and a Mitigation strategy
Expected completion date	Dec 2019
Expected size (number of pages)	200
Requestor Location	UIC 847 W Taylor Stree SEL-E 3295 CHICAGO, IL 60607 United States Attn: UIC
Publisher Tax ID	EU826007151
Total	0.00 USD
Terms and Conditions	

TERMS AND CONDITIONS

This copyrighted material is owned by or exclusively licensed to John Wiley & Sons, Inc. or one of its group companies (each a"Wiley Company") or handled on behalf of a society with which a Wiley Company has exclusive publishing rights in relation to a particular work

Title: First-Principles Study on the Thermal Stability of LiNiO2 Materials Coated by Amorphous Al2O3 with Atomic Layer Thickness

Author: Joonhee Kang, Byungchan Han

Publication: Applied Materials

Publisher: American Chemical Society

Date: Jun 1, 2015

PERMISSION/LICENSE IS GRANTED FOR YOUR ORDER AT NO CHARGE

This type of permission/license, instead of the standard Terms & Conditions, is sent to you because no fee is being charged for your order. Please note the following:

- Permission is granted for your request in both print and electronic formats, and translations.
- If figures and/or tables were requested, they may be adapted or used in part.
- Please print this page for your records and send a copy of it to your publisher/graduate school.
- Appropriate credit for the requested material should be given as follows: "Reprinted (adapted) with permission from (COMPLETE REFERENCE CITATION). Copyright (YEAR) American Chemical Society." Insert appropriate information in place of the capitalized words.
- One-time permission is granted only for the use specified in your request. No additional uses are granted (such as derivative works or other editions). For any other uses, please submit a new request.

If credit is given to another source for the material you requested, permission must be obtained from that source.

BACK | CLOSE WINDOW

JOHN WILEY AND SONS LICENSE TERMS AND CONDITIONS

Oct 24, 2019

This Agreement between UIC -- Soroosh Sharifi-Asl ("You") and John Wiley and Sons ("John Wiley and Sons") consists of your license details and the terms and conditions provided by John Wiley and Sons and Copyright Clearance Center.

License Number	4695521314181
License date	Oct 24, 2019
Licensed Content Publisher	John Wiley and Sons
Licensed Content Publication	Advanced Energy Materials
Licensed Content Title	A Novel Surface Treatment Method and New Insight into Discharge Voltage Deterioration for High-Performance 0.4Li2MnO3–0.6LiNi1/3Co1/3Mn1/3O2 Cathode Materials
Licensed Content Author	Jaephil Cho, Youngsik Kim, Seungjun Myeong, et al
Licensed Content Date	Jun 23, 2014
Licensed Content Volume	4
Licensed Content Issue	16
Licensed Content Pages	9
Type of use	Dissertation/Thesis
Requestor type	University/Academic
Format	Print and electronic
Portion	Figure/table
Number of figures/tables	1
Original Wiley figure/table number(s)	Figure 1
Will you be translating?	No
Title of your thesis / dissertation	Atomic Scale Study of Oxygen Loss and Structural Degradation in Oxide Cathodes and a Mitigation strategy
Expected completion date	Dec 2019
Expected size (number of pages)	200
Requestor Location	UIC 847 W Taylor Stree SEL-E 3295 CHICAGO, IL 60607 United States Attn: UIC
Publisher Tax ID	EU826007151
Total	0.00 USD
Terms and Conditions	

TERMS AND CONDITIONS

This copyrighted material is owned by or exclusively licensed to John Wiley & Sons, Inc. or one of its group companies (each a"Wiley Company") or handled on behalf of a society with

JOHN WILEY AND SONS LICENSE TERMS AND CONDITIONS

Oct 24, 2019

This Agreement between UIC -- Soroosh Sharifi-Asl ("You") and John Wiley and Sons ("John Wiley and Sons") consists of your license details and the terms and conditions provided by John Wiley and Sons and Copyright Clearance Center.

License Number	4695521457789
License date	Oct 24, 2019
Licensed Content Publisher	John Wiley and Sons
Licensed Content Publication	Advanced Functional Materials
Licensed Content Title	Anti-Oxygen Leaking LiCoO2
Licensed Content Author	Soroosh Sharifi-Asl, Fernando A. Soto, Tara Foroozan, et al
Licensed Content Date	Apr 5, 2019
Licensed Content Volume	29
Licensed Content Issue	23
Licensed Content Pages	12
Type of use	Dissertation/Thesis
Requestor type	Author of this Wiley article
Format	Print and electronic
Portion	Full article
Will you be translating?	No
Title of your thesis / dissertation	Atomic Scale Study of Oxygen Loss and Structural Degradation in Oxide Cathodes and a Mitigation strategy
Expected completion date	Dec 2019
Expected size (number of pages)	200
Requestor Location	UIC 847 W Taylor Stree SEL-E 3295 CHICAGO, IL 60607 United States Attn: UIC
Publisher Tax ID	EU826007151
Total	0.00 USD
Terms and Conditions	

TERMS AND CONDITIONS

This copyrighted material is owned by or exclusively licensed to John Wiley & Sons, Inc. or one of its group companies (each a"Wiley Company") or handled on behalf of a society with which a Wiley Company has exclusive publishing rights in relation to a particular work (collectively "WILEY"). By clicking "accept" in connection with completing this licensing transaction, you agree that the following terms and conditions apply to this transaction (along with the billing and payment terms and conditions established by the Copyright Clearance Center Inc., ("CCC's Billing and Payment terms and conditions"), at the time that

Vita

Soroosh Sharifi-Asl

Electron Microscopy Scientist

Department of Mechanical Engineering, University of Illinois at Chicago
842 W Taylor St, Chicago, IL 60607
sshari25@uic.edu, +1 312 5455749

SUMMARY

- PhD candidate with 5 years' experience on failure analysis of nanomaterials using electron microscopy.
- Expertise in TEM, STEM and related techniques such as SAEDP, HRTEM, EDS, ADF/ABF and EELS.
- Skilled in materials synthesis (e.g CVD and PLD) and characterization techniques such as XRD, XPS, AFM, TA, SEM, FIB.
- Successful records in project leadership and proven ability in team-work and collaborative research with other groups and institutions.

EDUCATION

2015-2019 **Ph.D. Mechanical Engineering** (*Graduation Date: Nov 2019*)
University of Illinois at Chicago, Chicago, IL (Advisor: Prof. Reza Shahbazian-Yassar)

2012-2014 **M.Sc. Materials Science and Engineering**
University of Tehran, Tehran, Iran

2007-2012 **B.Sc. Materials Engineering**
International University of Imam Khomeini, Qazvin, Iran

TECHNICAL SKILLS

- **Electron Microscopy and Analysis Techniques: (>500 hours experience)**
  - Spherical aberration corrected scanning transmission electron microscope (AC-STEM): JEOL JEM-ARM200CF
  - Transmission electron microscopy and electron diffraction analysis (TEM/ SAEDP): JEOL JEM-3010
  - Energy dispersive spectroscopy (EDS): (Oxford X-max 100TLE)
  - Electron energy loss spectroscopy (EELS) and energy filtered TEM (EFTEM): (Gatan Enfina 1000 & GIF Quantum)
- **TEM Results Post Processing Techniques:**
  - STEM/TEM image simulation (Kirkland multislice STEM/TEM simulation)
  - Electron crystallography and phase identification (SAEDP analysis by Crystal Maker and Single Crystal)
  - Geometrical phase analysis (GPA) for strain analysis in HRTEM images
- **In-situ TEM Techniques:**
  - Gatan heating/cooling holders, DENS solutions Wildfire heating holder, Nano-factory (STM-TEM) holder, Protochips Fusion heating holder.
- **Materials Synthesis and Preparation:**
  - Chemical vapor deposition (CVD MTI OTF-1200X)
  - Graphene encapsulation of cathode particles through surface charge modification
- **Materials Characterization:**
  - Scanning Electron Microscopy (Hitachi S4800-II cFEG SEM)
  - Focused ion-beam (FIB) lamella preparation and cross-sectional analysis (FEI Helios Nano-lab FIB)
  - X-ray diffraction (Siemens Bruker D-5000 powder diffractometer XRD)
  - Raman spectroscopy (Horiba LabRamHR evolution confocal Raman microscope)
  - X-ray photoelectron spectroscopy **(**Kratos AXIS-165 XPS X-ray photoelectron spectroscopy XPS)
  - Atomic force microscopy (Bruker-Nano Dimension Icon atomic force microscope)
  - Metallography techniques: grinding, polishing, wet etching
- **Thermal Analysis:**
  - TA Instruments SDT Q600 (Simultaneous TGA/DSC), TA Instruments Q500 TGA, TA Instruments Q2000 DSC
  - Gas chromatography and mass spectroscopy Thermal analysis with (NETZSCH STA/Agilent Technologies GC-MS)

CERTIFICATES

Apr. 2016 EELS and EFTEM Analysis Training School, Gatan Inc, CA

Jan. 2016 Winter School on High Resolution Electron Microscopy, Arizona State University, AZ

Jun. 2016 Next Generation Electrochemistry (NGenE), University of Illinois at Chicago, IL

Soroosh Sharifi-Asl

Electron Microscopy Scientist

RESEARCH EXPERIENCE

- **In-situ heating TEM study of $LiCoO_2$ cathodes**
  - Atomic resolution imaging of $LiCoO_2$ phase transitions subsequent to thermal decomposition
  - Quantification of oxygen release from $LiCoO_2$ by in-situ heating electron energy loss spectroscopy analysis
- **In-situ cycling TEM study of all-solid-state Li-ion battery**
  - FIB lamella preparation and mounting on DENS solutions in-situ MEMS chip
  - Failure and degradation analysis of the layered heterostructure of Li-ion battery through in-situ STEM/EELS
- **Atomic resolution analysis of the grain boundary structures in the nano-composite Li-rich NMC cathode materials**
  - Identification of the dual phase monoclinic/hexagonal structure of Li-rich cathodes by atomic resolution imaging
  - Strain analysis of the grain interphase by Geometric Phase Analysis (GPA)
  - Chemical composition quantification and metal-oxygen debonding at the grain interphase by EDS/EELS analysis
- **Analysis of the modified cathode materials by atomic layer coatings/dopants (Argonne National Lab contract)**
  - Revealing the non-homogenous distribution of W dopants in the $LiCoO_2$ structure by Z contrast HAADF imaging
  - Quantification of the diffusion rate of Ni in the surface of $LiCoO_2$ using EELS analysis
- **Graphene-encapsulation of $LiCoO_2$ cathodes to mitigate the oxygen release and thermal runaway**
  - Surface functionalization of $LiCoO_2$ by silane coupling agents to promote self-assembly of graphene/$LiCoO_2$ particles
  - TEM, XPS and Raman analysis of the graphene coated $LiCoO_2$ samples to study the graphene coating layer
  - Electrochemical cycling and impedance spectroscopy of graphene coated $LiCoO_2$ samples
  - Thermal analysis testing of graphene coated $LiCoO_2$ samples
- **CVD growth and characterization of Zn_4Sb_3 nanowires as an ultra-fast, highly reversible Na-ion cathode material**

HONORS / AWRDS

Dec. 2018	Faydor Litvin graduate award (Awarded to top 3 PhD candidates in MIE department at UIC)
Apr. 2018	Provost/Deiss award for graduate research (Awarded to top 10 graduate students at UIC)
Apr. 2017	Argonne national laboratory (ANL) funding ($150K funding for a 3-year collaboration contract)
Jun. 2016	Poster award in Microscopy and Microanalysis (M&M) 2017 conference
Jan. 2016	Winter School on High Resolution Electron Microscopy scholarship

LEADERSHIP

Since 2018	Vice president of MIE Graduate Association (MIEGA)
Since 2017	Vice president of ECS student chapter at UIC
2016-2017	Student liaison for Midwest Microscopy and Microanalysis Society (M3S)

SELECTED PUBLICATIONS

[1] (*FIRST AUTHORED*) S. Sharifi-Asl, F. A. Soto, A. Nie, Y. Yuan, H. Asayesh-Ardakani, T. Foroozan, V. Yurkiv, B. Song, F. Mashayek, R. Klie, K. Aamine, J. Lu, P. Balbuena, R. Shahbazian-Yassar, "Facet-dependent Thermal Instability in $LiCoO_2$" **Nano Lett.** 2017, 17(4) 2165-2171.

[2] (*FIRST AUTHORED*) S. Sharifi-Asl, F. A Soto, T. Foroozan, M. Asadi, Y. Yuan, R. Deivanayagam, R. Rojaee, B. Song, X. Bi, K. Amine, J. Lu, A. Salehi-khojin, P. B Balbuena, R.Shahbazian-Yassar, "Anti-Oxygen Leaking $LiCoO_2$" **Adv. Funct. Mater.** 2019, 1901110.

[3] (*FIRST AUTHORED*) S. Sharifi-ASl, K. Amine, J. Lu, R. Shahbazian-Yassar. "Thermal Stability of Oxide Cathode Materials: Mechanisms and Mitigation Approaches" **Adv. Energy Mater.** 2019, 1900551.

[4] (*FIRST AUTHORED*) S. Sharifi-Asl, A. Gutierrez, V. Yurkiv, J. Croy, M. Balasubramanian, F. Mashayek, R. Shahbazian-Yassar, "Revealing the Atomic Structure of Grain Boundaries in Li-rich Cathode Materials" Nano Lett. 2020, 20, 2, 1208-1217.

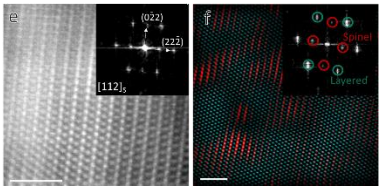

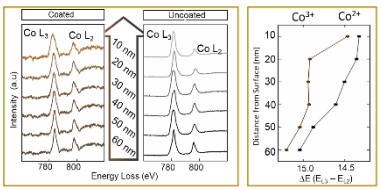

SELECTED PUBLICATIONS

[5] A. Nie, L. Gan, Y. Cheng, X. Tao, Y. Yuan, S. Sharifi-Asl, K. He, H. Asayesh-Ardakani, V. Vasiraju, J. Lu, F. Mashayek, R. Klie, S. Vaddiraju, U. Schwingenschlögl, and R. Shahbazian-Yassar, "Ultrafast and Highly Reversible Sodium Storage in Zinc-Antimony Intermetallic Nanomaterials" **Adv. Funct. Mater.** 2016, 26, pp. 543–552.

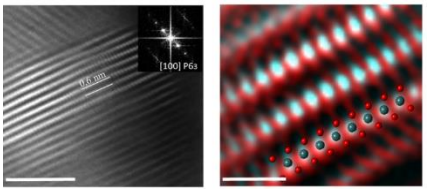

[6] P. Abbasi, M. Asadi, C. Liu, S. Sharifi-Asl, B. Sayahpour, A. Behranginia, P. Zapol, R. Shahbazian-Yassar, L. A. Curtiss, A. Salehi-khojin, "Tailoring the Edge Structure of Molybdenum Disulfide toward Electrocatalytic Reduction of Carbon Dioxide" **ACS Nano** 2016, 11 (1) pp. 453-460.

[7] Y. Yuan, C. Zhan, K. He, H. Chen, W. Yao, S. Sharifi-Asl, B. Song, Z. Yang, A. Nie, X. Lou, H. Wang, S. M. Wood, K. Amine, M. S. Islam, J. Lu, R. Shahbazian-Yassar, "The influence of large cations on the electrochemical properties of tunnel-structured metal oxides" **Nat. Commun.** 2016, 7, 13374.

[8] T. Foroozan, F. A. Soto, V. Yurkiv, S. Sharifi-Asl, R. Deivanayagam, Z. Huang, R. Rojaee, F.Mashayek, P. B. Balbuena, R. Shahbazian-Yassar, "Synergistic Effect of Graphene Oxide for Impeding the Dendritic Plating of Li" **Adv. Funct. Mater.** 2018, 28 (15), 1705917.

[9] P. Rohani, S. Banerjee, S. Sharifi-Asl, M. Malekzadeh, R. Shahbazian-Yassar, S. JL Billinge, M. T Swihart, Synthesis and Properties of Plasmonic Boron-Hyperdoped Silicon Nanoparticles" **Adv. Funct. Mater.** 2019, 29 (8), 1807788.

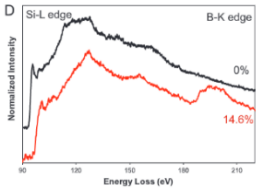

[10] J. R. Croy, D. O'Hanlon, S. Sharifi-Asl, M. Murphy, A. Mane, C.-Wook Lee, S. E Trask, R. Shahbazian-Yassar, M. Balasubramanian, "Insights on the Stabilization of Nickel-Rich Cathode Surfaces: Evidence of Inherent Instabilities in the Presence of Conformal Coatings" **Chem. Mater.** 2019, 31 (11) 3891-3899.

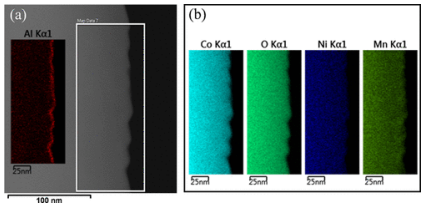

SELECTED PRESENTATIONS

[1] (*AWARDED*) In-situ TEM Investigation on Thermal Stability and Oxygen Release Behavior of Charged and Discharged $LiCoO_2$, Microscopy & Microanalysis Meeting, June 2016, Columbus, OH.

[2] Surface Nano-Coating as a Novel Approach to Improve the Structural Stability of Layered Oxide Cathodes in Li-ion Batteries, Materials Research Society, April 2017 Phoenix, AZ.

[3] Investigation of the Effect of Graphene-encapsulation on the O_2 Release Phenomenon from Li_xCoO_2, Studied by In-situ Heating STEM/EELS, Microscopy & Microanalysis Meeting, August 2018, Baltimore, NY.

[4] Aberration-Corrected Scanning Transmission Electron Microscopy of Single Crystals and Chemically Gradient NMC Cathodes, Microscopy & Microanalysis Meeting, August 2018, Baltimore, NY.

[5] Revealing the Atomic Arrangement of Dopant Elements in the Layered Oxide Cathode Structures, Materials Research Society, Nov 2018, Boston, MA.

[6] Strained Phase Boundaries in Li-rich Cathodes; An Atomic Resolution Study, Microscopy & Microanalysis Meeting, August 2019, Portland, OR.

WEBPAGES

Google Scholar: https://scholar.google.com/citations?user=3sCdbaEAAAAJ&hl=en

Linked-In: http://www.linkedin.com/in/soroosh-sharifiasl